The Spectroscopy of the Formyl Radical

by

George William Adamson

B.S. University of California, Riverside (1988)

Submitted to the Department of Chemistry
in Partial Fulfillment of the Requirements
for the Degree of

Doctor of Philosophy

at the

Massachusetts Institute of Technology

September 1994

Signature of Author____
Department of Chemistry
6 July 1994

Certified by____
Robert W. Field
Professor of Chemistry
Thesis Supervisor

Accepted by____
Dietmar Seyferth, Chairman
Departmental Committee on Graduate Students

This thesis has been examined by a committee of the Department of Chemistry as Follows:

Professor Robert J. Silbey ____
Chairman

Professor Robert W. Field ____
Thesis Supervisor

Professor Robert G. Griffin ________ ______

The Spectroscopy of the Formyl Radical

by

George William Adamson

Submitted to the Department of Chemistry
6 July 1994 in Partial Fulfillment
of the Requirements for the Degree of
Doctor of Philosophy

ABSTRACT

Fluorescence-excitation and stimulated emission pumping (SEP) spectroscopies were used to study the properties of photolytically generated, gas phase, formyl radical (HCO). This work focused on the ground doublet electronic state, between 4 000 - 11 200cm^{-1} of energy, and the second excited doublet electronic state, between 38 590 - 38 750cm^{-1} of energy. From the fluorescence-excitation spectrum the rotational, centrifugal distortion, and spin-rotational constants were determined for the vibrationless level of the second excited doublet electronic state. From the stimulated emission pumping spectrum vibrational term values, rotational constants, spin-rotational constants, and rotational linewidths were determined for ground electronic state vibrational levels—both above and below the dissociation limit for formyl radical dissociating to hydrogen atom and carbon monoxide. The systematics of the dissociation lifetimes, inferred from the observed rotational linewidths, for rovibrational levels of the ground electronic state were studied. The dissociating lifetimes were found to be strongly correlated with bending vibrational excitation and the amount of angular momentum about the minimum inertial axis of formyl radical. The observed dissociation lifetimes indicates the need for an upward adjustment of the currently accepted dissociation limit and barrier height.

thesis supervisor: Robert W. Field
title: Professor of Chemistry

Acknowledgments

One of my first memories of MIT is of some one finishing their thesis and writing the acknowledgments. Now it is my turn—weird. So many people have helped and given me fond memories. Truly, all you get to keep are your memories. I hope I get to thank them all. I'll begin with those who helped from outside MIT.

First and foremost (better sit down), I would like to thank my long term friend—thirteen years—and now wife Kikuye Branstrator Adamson for all her help and patience. She has most importantly given me a "home" to go to when I'm done.

Next, I would like to thank my family. They have humored me for a very long time. A much longer time for them I'm sure. I could not begin to list what they have done for me but I am grateful. The two most important lessons were: "All you can do is your best" and "You can only loose when you quit". And Mom, when I used to swipe the tape and glue I really was doing an "experiment".

Finally, I thank my grandparents. I unfortunately lost all of them during my visit at MIT. I sorely miss the resource of there wisdom and knowledge and look forward to being with them again.

With few exceptions, the group of people who inhabit the basement of MIT (and some other places as well) are a good group of people. It has been a privilege and a joy to work and live with them. I extend special thanks to Nicole Harris for her help above and beyond the call of duty in helping me exit MIT. She has always provided a refreshingly lucid view of reality and a willingness to

discuss anything. She is blessed with an amazing poise and calm as evidenced when we discovered, after eating dinner, that Durgin Park does not take credit cards. I also thank Chris Gittins for patiently sharing both a laser and an apartment with me for nearly my entire time at the Basement. He also endured, a not so pleasant, front row seat to the many turns my life has taken during graduate school and even manage to talk me into staying. How, I do not quite know, but I will forgive him—someday.

Recently, I have had the pleasure of many discussion with a person who is wise beyond her years, Amy Stevens Miller. Anything you want from Trader Joe's? I also had the privilege not only to share lab space but also to teach with a truly magnificent teacher, Jonathan O'Brien. I wish him luck finding all of my stashes of spare parts. Last but in no way not least, I thank the stray bear who showed up one night many years ago looking for the Field labs. She has always been there to go get more coffee than I could drink and to discuss recipes for deserts that my mouth still waters over. I wish Stephani "Ursus" Solina the best of luck and for a speedy return to the Sunshine State.

The undergraduates, Peter Mao and James Boiani, deserve special thanks for being patient with me and for keeping me company on long nights with the laser. They are already top notch researchers.

Lastly, I thank the members of the Porter Square Theater Group for the many excellent gourmet meals and the many sanity breaks spent in good company. They also taught me the lesson that the first course run in a season should not be a red one. Adieu.

Dedication

I dedicate this thesis with much gratitude to my beloved Kikuye, without whose love and friendship this would not have been possible.

You'll say, "Oh, my God; did it have to end this way?"
And then you'll say, "Why did it have to end this way?"
And then you'll have to say, "Yes, I understand why; but
--oh my God, why did it have to end this way?"

Theodore Sturgeon, San Diego 1980

Table of Contents

Chapter 1: Introduction

Chapter 2: Experimental

Chapter 3: Results and Analysis: Fluorescence Excitation and First SEP Experiment

Chapter 4: Results and Analysis: Second SEP Experiment

Chapter 5: Discussion

Chapter 6: Fabricated Equipment and Experimental Details

Appendices:

Chapter 1

Introduction

1.1 Introduction to Formyl Radical.

Spectroscopic techniques are powerful tools for the study of chemical reactions. The simplest of all chemical reactions to study is a unimolecular dissociation. For any chemical reaction, including unimolecular dissociation, to occur a molecule must first acquire sufficient internal energy to react. A molecule usually acquires this energy through collisions with other molecules but direct absorption of radiation can also provide the needed energy, as in photo-initiated reactions.

Typically covalently bound molecules at energies necessary to cause a chemical reaction have a density of vibrational states of several hundred states per wavenumber (cm^{-1}). At such a high density of states it is virtually impossible to place traditional spectroscopic labels on individual vibrational levels undergoing dissociation [1]. The study of individual dissociating vibrational states is difficult because experimental techniques only observe the dissociating state indirectly. Usually, one observes states that are coupled through perturbations to another state and this second state is the actual state that can undergo the dissociation [2].

The spectroscopic study of the formyl radical (HCO) by stimulated emission pumping (SEP) described here overcomes both of the typical limitations by allowing the direct observation of isolated spectroscopically assignable vibrational states undergoing dissociation in the ground state of a covalently bound molecule. In this SEP experiment the lifetime (dissociation rate) for vibrational levels of HCO was determined by measuring the homogeneous linewidths of the SEP transitions terminating on rovibronic levels of the $\tilde{X}\,^2A'$-state. These rovibronic levels were assigned traditional rotational and vibrational spectroscopic labels. The observation of these rovibronic levels were possible because the HCO radical has one of the lowest dissociation energies of any covalently bound molecule (D_0^0 ~5050cm^{-1} for HCO($\tilde{X}\,^2A'$ (0,0,0))$\rightarrow$CO($\tilde{X}\,^1S^+$ v = 0, J = 0) + H(1^2S)) [3,21,22,23]. This implies that there are only 15 bound vibrational levels in the ground state ($\tilde{X}\,^2A'$) of HCO [4,20].

Above the dissociation limit the lifetime for HCO vibrational levels increases relatively slowly so that up to energies of 16 000cm^{-1} above the $\tilde{X}\,^2A'$-state zero-point level the SEP linewidths are sufficiently narrow to be experimentally observed [3,16,17]. The energy of the highest vibrational level observed in this set of SEP spectra is ~10 800cm^{-1}. The highest vibrational level observed was limited by the tuning range of the dye laser used in the SEP experiment [4,16,17].

The ground state potential energy surface of HCO has been reasonably well characterized both theoretically and experimentally [3,5,6,7,11,16,17,20]. Table 1.1-1 lists the energies, molecular constants and geometries of the three lowest doublet electronic states of HCO. In the ground state ($\tilde{X}\,^2A'$), HCO is bent with a bond angle of 124.95°, a C-H distance of 1.125 Å, and a CO distance of 1.175 Å [9].

The classical limit for dissociation ($HCO \rightarrow H + CO$) is approximately (D_0^0) 5058cm^{-1} determined from the Dunning *ab initio* potential surface [20,24,25] and is experimentally determined to lie at 4883cm^{-1} [21,22]. On the Dunning *ab initio* potential surface the H—CO saddle point occurs at a C-H distance of ~1.75 Å, a CO bond length of 1.15 Å and a bond angle of ~150° [3,20]. The top of the H—CO saddle point is at an energy of 5757cm^{-1} above the HCO zero-point producing a small barrier to dissociation [20,24,25]. The vibrational density of states at energies just above the dissociation barrier is only 7 per 1000cm^{-1} [3]. In Figure 1.1-2, all ground state vibrational levels for HCO below 12 000cm^{-1} are plotted and the levels observed by SEP are indicated.

The stimulated emission pumping (SEP) technique is a double resonance technique that allows the observation of rovibrational levels of HCO both above and below the dissociation barrier. In the SEP experiment the first laser (the PUMP) excites the HCO into an excited electronic state, then a second laser (the DUMP) stimulates emission back to a vibrationally excited state of the ground state [10]. Both vibrational and rotational selectivity was possible with SEP providing complete control over which vibrational mode the energy was initially placed. The double resonance nature of SEP also made the rotational assignment of the observed transitions unambiguous.

Since observation of a single spectroscopically assignable dissociating level of HCO using SEP was possible, it was possible to pose and answer the question: does altering the distribution of energy amongst the three vibration degrees of freedom (rotations can be included as well) affect the dissociation rate? The answer to this question is yes, dissociation exhibits mode specificity. The dissociation rate (lifetime) is strongly affected by the initial rovibrational distribution of energy in HCO. The dissociation rate was also strongly affected by the amount of angular momentum about the a-inertial axis (approximately the CO bond axis, K_a''), see Section 5.1. The comprehensive explanation as to why these effects occur is more difficult to provide. However, the homogeneous SEP linewidths and molecular constants, measured in this work provide a substantial set of experimental data with which to test future more rigorous theoretical models.

The mode numbering convention used in this thesis is the same as in Reference (14). In that Reference the $\tilde{X}\,^2A'$-state vibrational modes are labeled (ν_1=CH stretch, ν_2=CO stretch, ν_3=bend) and the $\tilde{B}\,^2A'$-state vibrational modes are labeled (ν_1=CH stretch, ν_2=bend, ν_3=CO stretch). The choice of mode numbering was based upon the order of descending magnitude of the mode frequency, and not upon the character of the mode (i.e. stretch or bend) [19]. Vibrational transitions are labeled by their mode number with the superscript referring to the number of quanta in the upper state and the subscript to the number of quanta in the lower state (the rotation implies: $1_{v''}^{v'}2_{v''}^{v'}3_{v''}^{v'} \Rightarrow v_1 = v' \leftarrow v''$, $v_2 = v' \leftarrow v''$, $v_3 = v' \leftarrow v''$).

The rotational labeling convention used in this thesis is the same as in Reference (14). For rotational levels where single spin-rotation levels are not specified, the levels have the standard label for a near prolate symmetric top ($N_{K_a K_c}$). For rotational levels where the individual spin-rotational J levels ($J = N \pm 1/2$) are specified, the levels are labeled by $(N_{K_a K_c} J)$. Rotational transitions are labeled by ${}^{\Delta K_a}\Delta N(N''_{K_a'' K_c''})$. Even when spin-rotation was resolvable the change in J was not specified, since only transitions where $\Delta J = \Delta N$ were observed in this work.

In order to apply SEP to HCO there were some experimental obstacles that had to be first overcome; the experimental details of recording SEP spectra and fluorescence excitation spectra of photolytically generated transient species are described in Chapter 2. The first excited electronic state of HCO ($\tilde{A}\ ^2A'$) has been studied extensively [9]. However, this state was unsuitable for use as the intermediate state in a fluorescence dip detected SEP experiment. The $\tilde{A}$-state has a fluorescence quantum yield of about 10^{-4} and a lifetime of about 30ps which would make the sensitivity of an SEP experiment low (at least for detection schemes that monitor fluorescence). The second excited doublet electronic state ($\tilde{B}\ ^2A'$) in HCO has also been observed [11,12,13,14]. Better known from its emission spectrum, the "hydrocarbon flame bands," the $\tilde{B}$-state turned out to have a fluorescence quantum yield of almost 1 and a lifetime on the order of about 50ns for its zero-point level, making it well suited for use as the intermediate state in our SEP experiment. Prior to being used as an SEP intermediate, a detailed rotational analysis of the $\tilde{B}$-state origin band had to be performed. This rotational analysis is discussed in Section 3.1.

The most important consideration was the production of HCO. A method to produce a high partial pressure of HCO while maintaining a low total pressure in order to minimize collision effects was desired. The method chosen was laser flash photolysis of acetaldehyde, which converted most of the acetaldehyde into HCO and worked at relatively low pressures (200-500mTorr neat precursor) [15]. In order to perfect details of recording SEP spectra of a photolytically generated species, an initial SEP apparatus was built and used (see Section 2.2 and Section 3.2).

Using the experience gained with this initial SEP apparatus and to exploit a new laser system, the second SEP apparatus was built (see Section 2.3 and Chapter 4). With the second SEP apparatus a systematic determination of the dissociation rates for single assigned rovibrational eigenstates of HCO was recorded. These systematic SEP measurement are described in Chapter 4 and discussed in Chapter 5. A calculation of the relative direction rotational transition dipole moment from intensities is described in Appendix I. The use of axis switching transitions to determine the absolute direction is also discussed in Appendix I.

1.2 References

1. W. F. Polik, D. R. Guyer, and C. B. Moore, *J. Chem. Phys.* **92**, 3453 (1990); W. F. Polik, D. R. Guyer, W. Miller, C. B. Moore, *J. Chem. Phys.* **92**, 3471 (1990); Y. S. Choi, P. Teal, C. B. Moore, *J. Opt. Soc. Am. B*, 7, 1829-1834 (1990).
2. S. H. Kable, J.-C. Loison, P. L. Houston and I. Burak, *J. Chem. Phys.* **92**, 6332 (1990); J.-C. Loison, S. H. Kable, P.L. Houston and I. Burak, *J. Phys. Chem.* **94**, 1796 (1991).
3. R. N. Dixon, *J. Chem. Soc. Faraday Trans.* **88**, 2575-2586 (1992).
4. D. W. Neyer, X. Luo, and P. L. Houston, *J. Chem. Phys.* **98** (1993).
5. B. Gadzy and J. M. Bowman in "Adv. Mol. Vibr. and Dynamics", J. M. Bowman and M. A. Ratner, ed. Vol. 1 B, JAI, Greenwich, CT (1992); K. T. Lee, J. M. Bowman, *J. Chem. Phys.* **86**, 215-225 (1987); S. W. Cho, A. F. Wagner, B. Gadzy and J. M. Bowman, *J. Chem. Phys.* 96, 2799-2812 (1992).
6. S. K. Gray, *J. Chem. Phys.* 96, 6543 (1992).
7. K. Tanaka and E. R. Davidson, *J. Chem. Phys.* **70**, 2904-2913 (1979).
8. P. J. Bruna, R. J. Buenker, S. D. Peyerimhoff, *J. Mol. Struct.* **32**, 217-233 (1976); J. M. Bowman, J. S. Bitman and L. B. Harding, *J. Chem. Phys.* **85**, 911 (1986).
9. J. M. Brown and D. A. Ramsay, *Can. J. Phys.* **53**, 2232 (1975).
10. Y. Chen, S. D. Halle, D. M. Jonas, J. L. Kinsey, and R. W. Field, *J. Opt. Soc. Am. B*, 7, 1805-1815 (1990).
11. A. D. Sappey and D. R. Crosley, *J. Chem. Phys.* **93**, 7601-7608 (1990).

12. D. W. Neyer, X. Luo, and P. L. Houston, Private Communication. (1992).

13. T. Gejo, M. Takayanagi, T. Nishiya, T. Kono, and, I. Hanazaki *Chem. Phys. Lett.* **218**, 343-348 (1994).

14. G. W. Adamson, X. Zhao, and R. W. Field, *J. Mol. Spectrosc.* **160**, 11-38 (1993).

15. B. M. Stone, M. Noble, and E. K. C. Lee, *Chem. Phys. Lett.* **118**, 83-87 (1985).

16. R. N. Dixon, *Trans. Faraday Soc.* **65**, 3141-3149 (1969).

17. R. N. Dixon, *J. Mol. Spectrosc.* **30**, 248-252 (1969).

18. T. A. Cool and X. M. Song, *J. Chem. Phys.* **96**, 8675-8683 (1992).

19. R. S. Mulliken, *J. Chem. Phys.* **23**, 1997-2011 (1955).

20. S. W. Cho, W. L. Hase and K. N. Swamy, *J. Phys. Chem.* **94**, 7371-7377 (1990).

21. K. K. Murray, T. M. Miller, D. G. Leopold and W. C. Lineberger, *J. Chem. Phys.* **84**, 2520-2525 (1986).

22. J. M. Dyke, N. B. H. Jonathan, A. Morris and M. J. Winter, *J. Chem. Soc, Faraday Trans. 2*, **77**, 667 (1981).

23. J. S. Francisco, A. N. Goldstein and I. H. Williams, *J. Chem. Phys.* **89**, 3044-3049 (1988).

24. T. H. Dunning, *J. Chem. Phys.* **73**, 2304-2309 (1980).

25. J. M. Bowman, J. S. Bitman and L. B. Harding, *J. Chem. Phys.* **85**, 911-921 (1986).

1.3 Chapter 1 Figure and Table Captions

Table 1.1-1 The Energies, Geometries and Important Constants for the Three Lowest Electronic States of HCO. The table lists the vibration, rotation, and structure constants for each of the three lowest electronic states [9,16,17].

Figure 1.1-2 HCO $\tilde{X}\,^2A'$-State Vibrational Levels with v_1(CH-stretch) < 2 Calculated to Lie Below 12 000cm^{-1} in Energy. Plot showing all vibrational levels for HCO with v_1(CH-stretch) < 2calculated from a simple anharmonic expansion. The levels observed in this SEP work are marked. The constants for this expansion were taken from Reference (17) and from refitting the observed dispersed fluorescence levels in Reference (11). In this plot each vertical stack of levels is a bending progression built upon a fix quantity of CO-stretch and CH-stretch. Horizontal lines denote the energy of the dissociation limit [20,24,25] and origin of the $\tilde{A}$-state [9].

Table 1.1-1 The Energies, Geometries and Important Constants for the Three Lowest Doublet Electronic States of HCO

Electronic	Vibrational Constants ①				Rotational Constants ①			Geometry ②		
State	T_{000}	ν_1	ν_2	ν_3	A	B	C	r_{CH}	r_{CO}	θ
$\tilde{X}\,^2A'$ ③	0.0	2488	1080.7	1861	24.29	1.4937	1.3988	1.08	1.19	119.5
$\tilde{A}\,^2A''$ ③	9297	3319	805.4	1812.2	⑥	1.3389	⑥	1.064	1.186	180
$\tilde{B}\,^2A'$ ④	38695	2597⑤	1382⑤	1065⑤	16.04	1.192	1.108	1.16⑦	1.36⑦	111⑦

① - All units in cm^{-1} ② - Bond lengths in Angstroms and bond angles in degrees

③ - Values from Reference (9) ④ - Values from Reference (14) except as noted

⑤ - Values from Reference (18) ⑥ - The $\tilde{A}\,^2A''$-state is linear

⑦ - Values from Reference (16)

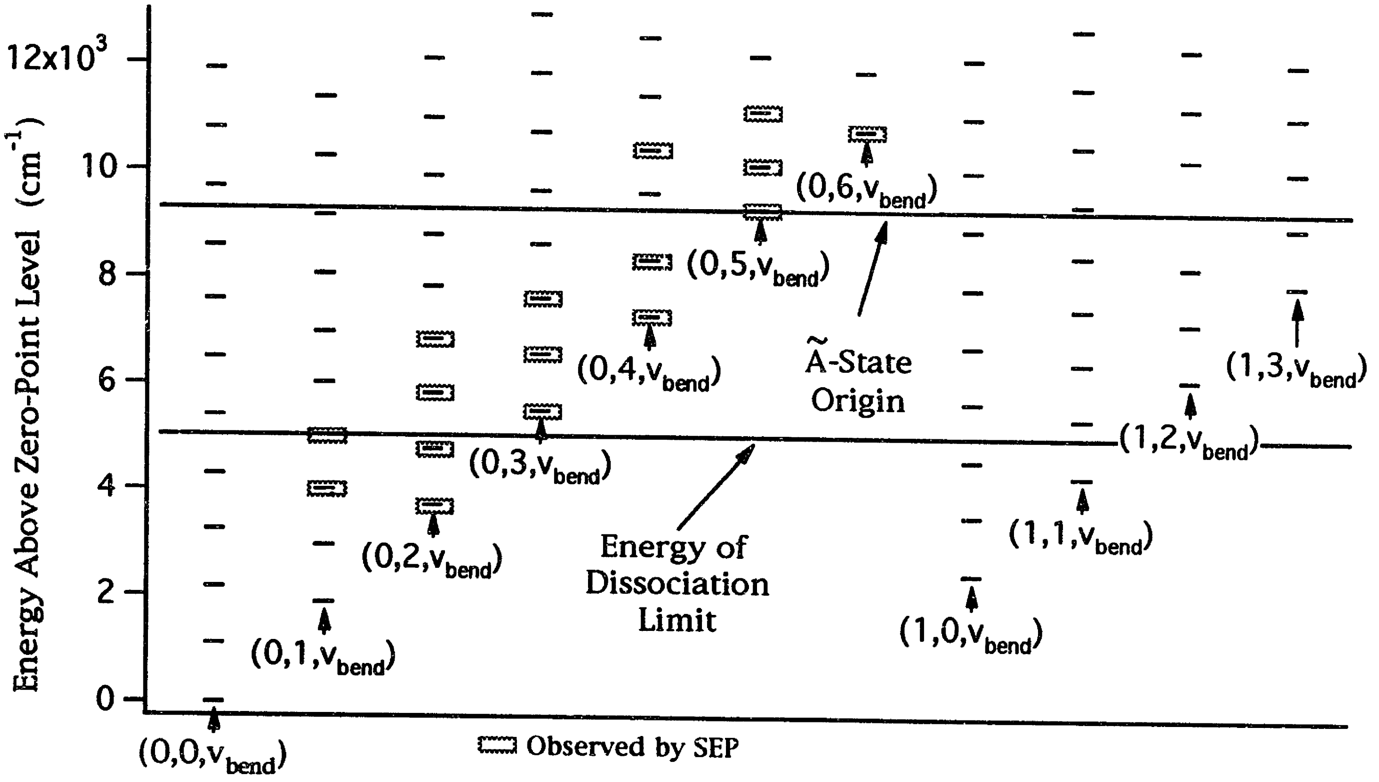

Figure 1.1-2 HCO Ground State Vibrational Levels with v_1(CH-Stretch) < 2 Calculated to Lie Below 12,000cm^{-1} in Energy

Chapter 2

Experimental

2.1 Fluorescence Excitation Apparatus

In the fluorescence excitation experiment, the HCO radical was generated by photolyzing acetaldehyde (Aldrich Chemical Company 99%) using 308nm laser light in a brass flow cell. This experimental technique was similar to that used by Stone et al. to observe the $\tilde{A}$-state of HCO by fluorescence excitation [1]. The apparatus, used in the current fluorescence excitation experiment to observe the $\tilde{B}$-state of HCO, is diagrammed in Figure 2.1-1.

The gas handling system used with the flow cells of all three experiments (Section 2.1, 2.2, 2.3) is detailed in Figure 2.1-2. The gas handling system was constructed from 1/4" copper refrigeration tubing, brass bellows valves (NuPro) and brass fittings (SwageLok). The sample bulb containing the liquid acetaldehyde was Pyrex glass with an all Teflon stopcock (AceGlass, 0-5mm). The Teflon stopcock was needed because O-rings made of Viton dissolved in liquid acetaldehyde. However, Viton O-rings were unaffected by low pressure gaseous acetaldehyde.

In the fluorescence excitation experiment the servo pressure controller (see Section 2.3) was not used. Instead the sample bulb was immersed in a dry-ice/methanol bath (T = 80K). The vapor pressure of acetaldehyde at this bath temperature was 2-3 Torr. The cell pressure was monitored by a capacitance manometer (MKS Baratron, 10 Torr, model 220B) which was attached directly to the cell.

In order to set the flow rate of precursor through the cell, the cell was first evacuated to 2-5 mTorr using a mechanical pump (Sargent-Welch 1397, aldehyde resistant metal vanes). The cell was flooded several times with acetaldehyde to purge the cell and also to degas the liquid precursor sample. The vacuum pump was next closed off from the cell and the sample bulb was opened. The micrometer adjusted needle valve was then set to produce the desired rate of pressure increase (dP/dt) in the cell. After the desired flow rate was set, the vacuum pump was opened to the cell again and the pumping rate adjusted using the fine adjust throttle valve thus establishing the final cell pressure.

In the fluorescence excitation experiment, the total pressure of neat acetaldehyde in the cell was typically 1 Torr and flowing at a rate of 75 ℓ·Torr/min. The photolysis cell volume was approximately 32mℓ and the volume (1cm X 65cm) of the photolysis laser beam inside the cell was 1mℓ. Mixing the neat acetaldehyde with inert buffer gases (argon, nitrogen, and helium) was tried but no conditions could be found where these dilutions produced a higher density of HCO radical than the photolysis of neat acetaldehyde. Atmospheric leaks into the flow cell were observed to markedly reduce the yield of HCO.

The 308nm photolysis laser light was produced by a xenon chloride excimer laser (Lambda Physik, EMG-201). The pulse energy of the laser operated at 20Hz was 100mJ. Half of the rectangular (1cm X 2cm) excimer laser beam was split off by a large 90° fused silica prism. The rest of the beam was discarded onto a beam dump. The now square (1cm X 1cm) photolysis beam was focused slightly before reaching the center of the fluorescence excitation cell with a +132cm focal length fused silica spherical lens. The corners of the square photolysis beam were clipped by an iris located just in front of the entrance window of the fluorescence excitation cell. This was a fused silica window mounted normal to the laser beam.

A doubled dye laser (Lambda Physik, FL3002E), pumped at 20Hz by the tripled output of a Nd:YAG laser (Molectron, MY34/20), was used unfocused (0.2cm spot diameter) as the excitation laser (0.2mJ/pulse of ultraviolet excitation energy). The fundamental output of the dye laser was doubled by a β-BaB$_2$O$_4$ (BBO) doubling crystal (CSK Company, 55°). The doubling crystal was mounted to allow for the automatic angle tuning of the crystal as the dye laser was scanned (see Section 6.2). The frequency doubled dye laser output was separated from the fundamental by a pair of 60° fused silica prisms. The doubled excitation light entered the fluorescence excitation cell through a fused silica window mounted at Brewster's angle. It was found that a cell, with one window mounted at Brewster's angle and the other mounted normal to the laser beam, produced the least amount of scattered laser light.

The left over dye laser fundamental radiation was sent through an iodine absorption cell and onto a photodiode. This arrangement allowed the absorption spectrum of iodine gas (35° C) to be simultaneously recorded along with the HCO fluorescence excitation spectrum, thus providing absolute frequency calibration (see Section 3.1).

The resultant HCO $\tilde{B}\,^2A' \rightarrow \tilde{X}\,^2A'$ side fluorescence was imaged onto a photomultiplier tube (Hamamatsu R928) by f/1.5 collection optics. These collection optics, used in the fluorescence excitation experiment and in both SEP experiments, consisted of two 51mm diameter fused silica lenses glued into a length of aluminum pipe. The first lens, a 51mm focal length plano-convex line was mounted 51mm from the laser beams with the planar side toward the fluorescence region. This first lens served to collimate the HCO fluorescence. The second lens, a 76mm focal length bi-convex lens, was mounted 25mm from the first lens and served to image the fluorescence onto the PMT, which was mounted 76mm from the second lens. To align the PMT and collection optics with the sample cell a HeNe laser beam was first passed through the cell overlapped with the excitation laser. A paper card (Oxford Index Card 3" X 5") was inserted into the cell to scatter the HeNe laser light. The lenses were then adjusted to image the scattered laser beam onto the photocathode of the PMT.

A colored glass filter (Schott UG-11) and a high reflector coated for 325nm at 45° (Acton Research Corp.) were used at normal incidence to minimize scattered light from the excitation laser while the fluorescence excitation spectra were being recorded. The excitation laser pulse was delayed by 6 microseconds relative to the photolysis laser pulse in order to suppress detection of the acetaldehyde fluorescence produced by the photolysis laser and to allow the HCO photofragment to thermalize. Strong fluorescence was observed for 1-10 microseconds after the photolysis pulse. The output of the photomultiplier tube was sent through a preamplifier with 20dB gain (see Section 6.1). The output of the preamplifier was input to a boxcar integrator (Stanford Research Systems, SRS-250).

The output of the boxcar was then digitized (Data Translations, DT-2801) and stored on a personal computer.

Low resolution spectra were recorded with an undoubled laser linewidth of 0.6cm^{-1} FWHM. The high resolution spectra, 0.06cm^{-1} FWHM in the laser fundamental, were recorded by SF_6-pressure-scanning the dye laser with an intracavity etalon installed. These linewidths were estimated from the minimum resolvable linewidth in the iodine reference spectrum.

2.2 First SEP Apparatus

The basic design for the first fluorescence dip detected SEP apparatus was similar to that used previously in our group [2]. However, significant modifications were necessary to be able to record the SEP spectrum of a transient molecule produced by laser flash photolysis. The first SEP apparatus is shown in Figure 2.2-1 and Figure 2.2-2. Figure 2.2-3 shows a detail of the laser interaction region inside the SEP cell for the first and second SEP experiments. Finally, Figure 2.2-4 shows a block diagram of the detection electronics which are described in Section 6.1.

As in the fluorescence excitation experiment, HCO was produced by photolysis of acetaldehyde in a flow cell. The first SEP cell was fabricated from stainless steel with all windows made from fused silica. Care was taken when mounting the fused silica windows that no stress induced birefringence was produced. Birefringence in the cell windows scrambles the linear polarization of a laser beam passing through it and produces anomalous transition intensities in the SEP spectrum. The presence of stress induced birefringence was checked by a standard technique for observing stresses in glass. The cell windows were placed between crossed polarizers and then back illuminating them with a flashlight the stress reduced birefringence was then observable as bright bands.

In the first SEP experiment, the total pressure in the flow cell was maintained at 250 mTorr of neat acetaldehyde at a flow rate of 75 ℓ·Torr/min. The same gas handling equipment, Figure 2.1-2, and flow rate setting procedure was used for the SEP experiment as for the fluorescence excitation experiment. In the first SEP experiment the acetaldehyde sample bulb was placed in a water-ice bath (400 mTorr vapor pressure).

The same excimer laser (Lambda Physik EMG-201) used in the fluorescence excitation experiment was again used as the photolysis laser in the first SEP experiment. The beam path of the photolysis laser is described in Figure 2.2-1. A +100cm focal length fused silica cylindrical lens was used to focus the entire excimer laser beam on the center line of the arm which crosses the REFERENCE and SIGNAL sides of the SEP cell, as shown in the "Front" view of Figure 2.2-3. A metal baffle/slit assembly, located between the SIGNAL and REFERENCE sides of the SEP cell, allowed the photolysis beam to traverse both cells but minimized laser scatter between the two cells. Typically, 90mJ/pulse of 308nm at 20Hz was present in the cell for photolysis.

In the first SEP experiment, the Nd:YAG laser pulse was electronically delayed by 7 microseconds relative to the photolysis laser pulse. The tripled output of the Nd:YAG laser (355nm) was again used to pump a dye laser (Lambda Physik 3002E). The doubled output of this dye laser was separated from the dye laser fundamental by a pair of 60° fused silica prisms and focused with a +125cm focal length fused silica spherical lens (S1-UV, ESCO). The PUMP beam was then split by a broad band UV beam splitter (45%T,55%R,ESCO) to provide a separate PUMP beam for the SIGNAL and REFERENCE sides of the SEP cell, Figure 2.2-2. The pulse energy in each SIGNAL and REFERENCE PUMP beam was approximately 0.1mJ/pulse. These two PUMP beams were propagated perpendicularly to and spatially overlapped with the photolysis laser beam at the centers of the SIGNAL and REFERENCE sides of the SEP cell, Figure 2.2-3. The thickness of the photolysis laser beam, where the PUMP laser beam overlapped with it, was 0.1cm. The width of the photolysis laser beam was 3cm and the diameter of both PUMP laser beams was 0.05cm. A monitor etalon (0.21cm^{-1} FSR) and a short negative focal length lens provided a visual verification of the stable operation of the PUMP dye laser was running stably.

The doubled output of the same Nd:YAG laser (532nm) was used to pump another dye laser (modified, Molectron DL-16P), which, when frequency doubled and optically delayed by 20ns, served as the DUMP laser in the SEP experiment. The phase matching angle for the KD*P crystal which frequency doubled the DUMP laser beam was automatically tracked during an SEP scan. An improved version of this doubling crystal auto-tracker is described in Section 6.2. A pair of +15cm focal length lenses focused the DUMP laser beam so that the diameter of the DUMP beam at the center of the SEP cell was slightly larger than that of the PUMP laser beam. The DUMP laser was split into two beams by another beam splitter

(45%T, 55%R, ESCO), with one of the beams being counter-propagated and spatially overlapped with the PUMP and photolysis beam in the SIGNAL side of the SEP cell. The second DUMP laser beam was counter-propagated and spatially overlapped with the photolysis beam *but not spatially overlapped with the DUMP laser beam in the REFERENCE cell.* This arrangement compensated for fluorescence from acetaldehyde caused by the DUMP beam. In order to balance the total fluorescence intensity excited by the DUMP laser beam in the two sides of the SEP cell, a variable optical attenuator was inserted into the DUMP laser beam before it entered the REFERENCE side of the SEP cell. This variable attenuator consisted of two quartz microscope slides which were tipped so that the angle of incidence of the DUMP laser beam was easily adjustable. The first microscope slide was tilted so that the electric vector of the DUMP laser beam remained in the plane of the slide. Thus the reflected DUMP intensity increased monotonically from a minimum at normal incidence. The second microscope slide was maintained at the supplement of the angle of incidence on the first microscope slide. This second slide compensated for any displacement of the DUMP beam by the first microscope slide. The PUMP and DUMP beams were polarized parallel to each other. The doubled energy for both the PUMP and DUMP beams was typically 0.2mJ per pulse before the beam splitters.

A pair of f/1.5 fused silica collection optics, the same as that used in the florescence excitation experiment, were located below a plane defined by the laser beams. These lenses imaged the side fluorescence from the SIGNAL and REFERENCE sides of the SEP cell onto a matched pair of photomultiplier tubes (Hamamatsu R928). These tubes were matched by the supplier for blue sensitivity and the temporal response was matched in our lab (see Section 6.1). Fluorescence from the SIGNAL side of the SEP cell traversed a colored glass filter (Schott UG-11, 2mm thick) and a high reflector coated for 308nm at 45° (Acton Research Corp.) and that from the REFERENCE side of the SEP cell traversed another colored glass filter (Schott UG-11, 2mm thick) with a high reflector coated for 325nm at 45° (Acton Research Corp.). The filters were selected to minimize scattered light from the PUMP and DUMP lasers and to pass the long wavelength of the resultant $\tilde{B}\,^2A' \rightarrow \tilde{X}\,^2A'$ fluorescence.

A block diagram of the detection electronics is shown in Figure 2.2-4 and each component is described in Section 6.1. The output signals from the two photomultiplier tubes were individually preamplified and differentially amplified using a home built high speed discriminator (described in Section 6.1). The output of the differential amplifier was input to a boxcar integrator (Stanford Research Systems, SRS-250). The output of the boxcar was then digitized (Data Translations, DT-2801) and stored on a personal computer.

Both dye lasers were equipped with intracavity etalons. With these etalons the PUMP and DUMP lasers had line widths of 0.06cm^{-1} and 0.03cm^{-1} , respectively. During an SEP experiment the PUMP dye laser was locked on a specific $\tilde{B}\,^2A' \leftarrow \tilde{X}\,^2A'$ rotational transition. The DUMP laser was then pressure scanned with SF_6. A simultaneously recorded I_2 spectrum provided an absolute frequency standard (± 0.04 cm^{-1}) for the DUMP laser. Typically, the

DUMP laser would produce approximately a 30% [{I(DUMP off)-I(DUMP on)}/I(DUMP off)] decrease in SIGNAL cell fluorescence when the DUMP laser frequency was coincident with a downward transition.

2.3 Second SEP Apparatus

The second fluorescence-dip detected SEP apparatus was similar in design to the first SEP apparatus. The general layout of the SEP cell remained the same (see Figure 2.3-2). However, the doubly balanced feature of the previous experimental design was not used. As in the previous experiment, HCO was produced by the photolysis of acetaldehyde (Aldrich, 99%) in a flow cell, but the total cell pressure was maintained at 700mTorr of neat acetaldehyde flowing at approximately 50 ℓ-Torr/min. The pressure of the cell was stabilized by immersion of the precursor sample bulb in a regulated temperature bath (5°C to 25°C), the temperature of which was servo-controlled by the output of the cell's vacuum gauge (see Figure 2.1-2).

Photolytic production of HCO was accomplished with the quadrupled output (266nm) of a Nd:YAG laser (Quanta-Ray DCR-2) instead of the xenon chloride excimer laser radiation (308nm) used in the previous experiment (see Figure 2.3-1). The quadrupled output of the Nd:YAG laser was generated externally to the Nd:YAG laser (Cleveland Crystals, 266nm KD*P) and separated from the fundamental and first harmonic (532nm) by a dichroic mirror (CVI, 266nm, 45°) and a pellin-broca prism. The photolysis laser beam then traversed several meters before passing through a cylindrical telescope, which resulted in a ten times reduction in the height of the beam. The 266nm photolysis beam, upon entering the cell arm passing perpendicularly through the REFERENCE and SIGNAL SEP cells, was approximately a 1mm by 1cm oval with a total pulse energy of between 15mJ and 20mJ. The doughnut mode from the unstable resonator of the photolysis laser had filled in where the photolysis beam entered the cell. To partially compensate for the smaller absorption cross section of acetaldehyde at 266nm than 308nm [3], the photolysis beam was retroreflected back through the cell by a single flat dichroic mirror (CVI, 266nm, 0°). The final right angle turning prism, as well as both cell windows in the photolysis beam path, were made from magnesium fluoride.

The tripled output of another Nd:YAG laser (355nm, refurbished Quanta-Ray DCR-1A) pumped a dye laser (Lumonics HD-500), the doubled output of which served as the PUMP laser in the SEP experiment. The doubled output of this dye laser was separated from the dye laser fundamental by a two pairs of 60° fused silica prisms. The two Nd:YAG lasers were electrically synchronized so that the photolysis pulse preceded the PUMP laser pulse by 6 to 10 microseconds. Strong HCO fluorescence could be excited in the cell from 1 to 30 microseconds following the photolysis pulse. The PUMP beam was collimated by a telescope consisting of two +10cm focal length spherical lenses. At the focus of the telescope, a 100 micrometer sapphire pinhole (Richard H. Bird & Co.) was placed at the focus and served as a spatial filter. The PUMP beam was split by a dichroic beam splitter (CVI 50:50 260nm) to supply separate PUMP beams for the SIGNAL and REFERENCE cells.

The PUMP beams were overlapped perpendicularly with the major axis of the 1 by 10mm oval photolysis laser beam inside the respective SIGNAL and REFERENCE cells as illustrated in Figure 2.2-3.

The doubled output (532nm) of the second Nd:YAG laser pumped a second dye laser (Lumonics HD-350) which, when doubled and optically delayed by 6 nanoseconds relative to the PUMP pulse, served as the DUMP laser. The DUMP laser was frequency calibrated by simultaneously recording fringes from a solid etalon (Optics for Research, FSR 0.667cm^{-1}) and neon optogalvanic transitions in a Uranium hollow cathode lamp (Photron). A full description of the calibration procedure is given in Chapter 4.2. Another telescope, consisting of two +15cm focal length spherical lenses fitted with a 150 micrometer sapphire spatial filter (Richard H. Bird & Co.), collimated the output of the DUMP laser. The DUMP beam was counter-propagated relative to the PUMP beam and spatially overlapped with the PUMP beam in the SIGNAL side of the SEP cell. In the interaction region of the SIGNAL SEP cell, the diameter of the DUMP beam was 1.2mm, with typically 275 to 300 microJoules of pulse energy. The diameter of the PUMP beam was 1.0mm, with approximately 175 to 200 microJoules pulse energy. The duration of all dye laser pulses was measured to be 15 nanoseconds. The linewidth (FWHM) of the PUMP laser fundamental was 0.09cm^{-1} and that of the DUMP fundamental was 0.15cm^{-1}.

A pair of f/1.5 fused silica collection optics, identical to that used in the florescence excitation experiment, were located above the plane defined by the laser beams. These lenses imaged the side fluorescence from the SIGNAL and REFERENCE sides of the SEP cell onto a matched pair of photomultiplier tubes (Hamamatsu R106). This type of photomultiplier tube produced lower noise and responded better to UV than the tube used in the first two experiments. The photomultiplier tubes were shielded from scattered laser light by colored glass filters (Corion SB-300 and Schott UG-11, 2mm thick).

A block diagram of the detection electronics is shown in Figure 2.2-4, with each component being illustrated in Section 6.1. The output signals from the two photomultiplier tubes were individually preamplified and differentially amplified using a home built high speed discriminator (Figure 6.1-3). The output of the differential amplifier was input to a boxcar integrator (Stanford Research Systems, SRS-250). The output of the boxcar was digitized (Data Translations, DT-2801) and stored on a personal computer.

2.4 References

1. B. M. Stone, M. Noble, and E. K. C. Lee, *Chem. Phys. Lett.* **118**, 83-87 (1985).
2. Y. Chen, S. D. Halle, D. M. Jonas, J. L. Kinsey, and R. W. Field, *J. Opt. Soc. Am.* **B7**, 1805-1815 (1990).
3. R. J. Gill, W. D. Johnson and G. H. Atkinson, *Chemical Physics* **58**, 29-44 (1981).

2.5 Chapter 2 Figure Captions

Figure	
2.1-1	Fluorescence Excitation Spectroscopy: Optical Layout. Figure showing the optical layout of the photolysis and excitation lasers for the HCO $\tilde{B}\,^2A' \leftarrow \tilde{X}\,^2A'$ fluorescence excitation experimental apparatus.
2.1-2	Flow Cell Gas Handling System. Schematic displaying the plumbing for controlling the flow and pressure of the precursor gas. Used in all HCO experiments.
2.2-1	First SEP Apparatus: Photolysis Optical Layout. Diagram of the optical layout of the excimer photolysis laser used in the first HCO SEP experiment.
2.2-2	First SEP Apparatus: PUMP and DUMP Optical Layout. Diagram of the optical layout of the PUMP and DUMP lasers used in the first doubly balanced HCO SEP experiment.
2.2-3	First and Second SEP Apparatus: Laser Detail. Figure shows three cross-sectional views of the laser overlap region inside the sample cell of the first and second HCO SEP experiments.
2.2-4	First SEP Apparatus: Detection Electronics. Schematic displaying the detection electronics used in the first HCO SEP experiment. Each component is described fully in Chapter 6.
2.3-1	Second SEP Apparatus: Photolysis Optical Layout. Diagram of the optical layout of the Nd:YAG photolysis laser used in the first HCO SEP experiment.
2.3-2	Second SEP Apparatus: PUMP and DUMP Optical Layout. Diagram of the optical layout of the PUMP and DUMP lasers used in the first doubly balanced HCO SEP experiment.
2.3-3	Second SEP Apparatus: Detection Electronics. Schematic displaying the detection electronics used in the first HCO SEP experiment. Each component is described fully in Chapter 6.

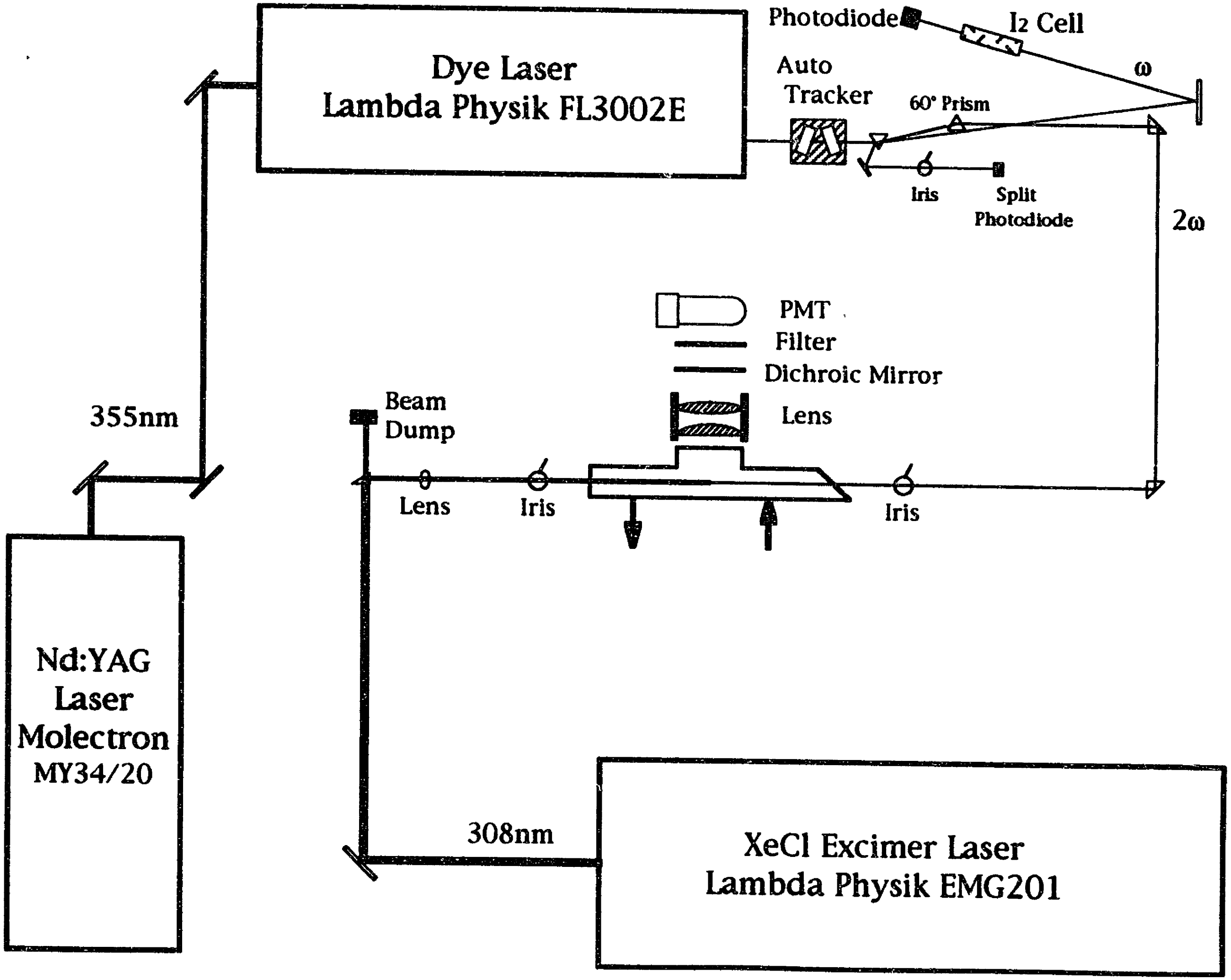

Figure 2.1-1 Fluorescence Excitation Spectroscopy: Optical Layout

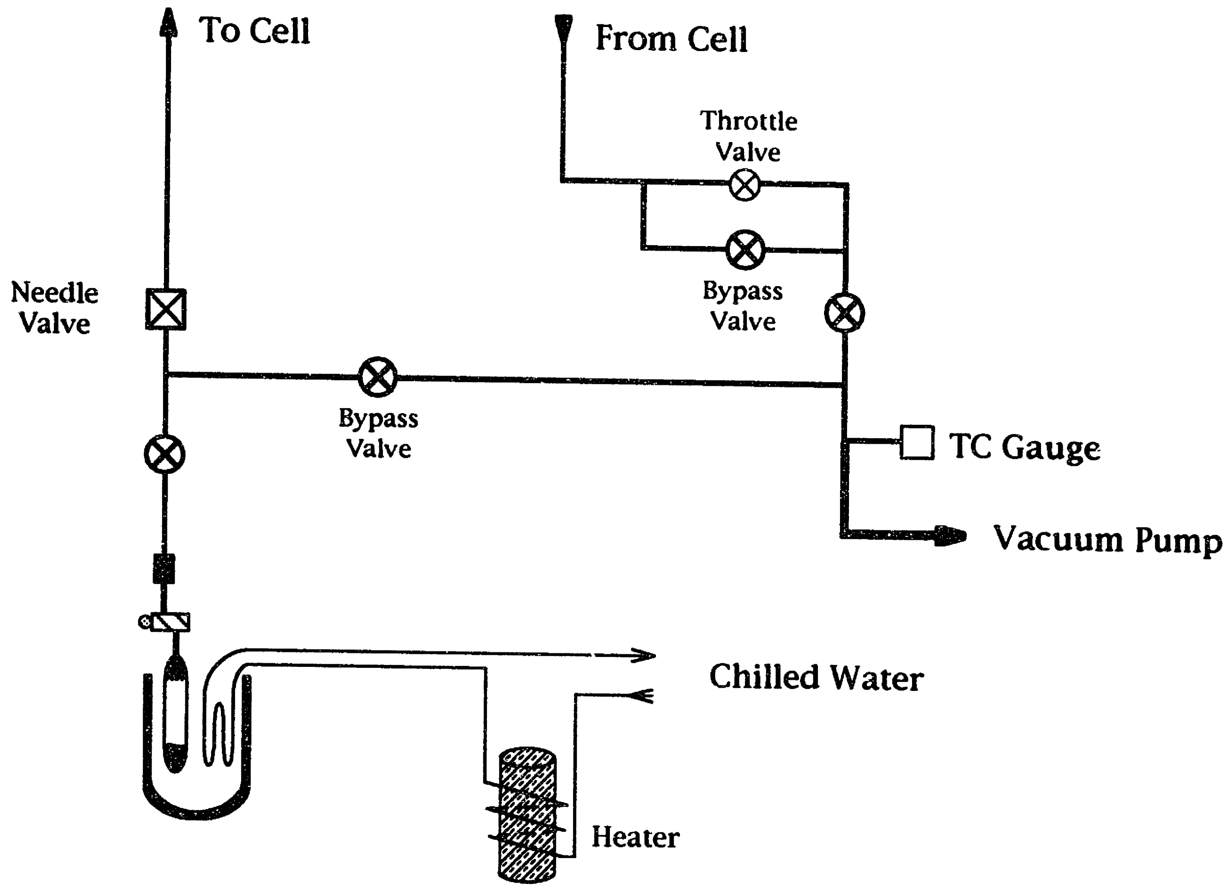

Figure 2.1-2 Flow Cell Gas Handling System

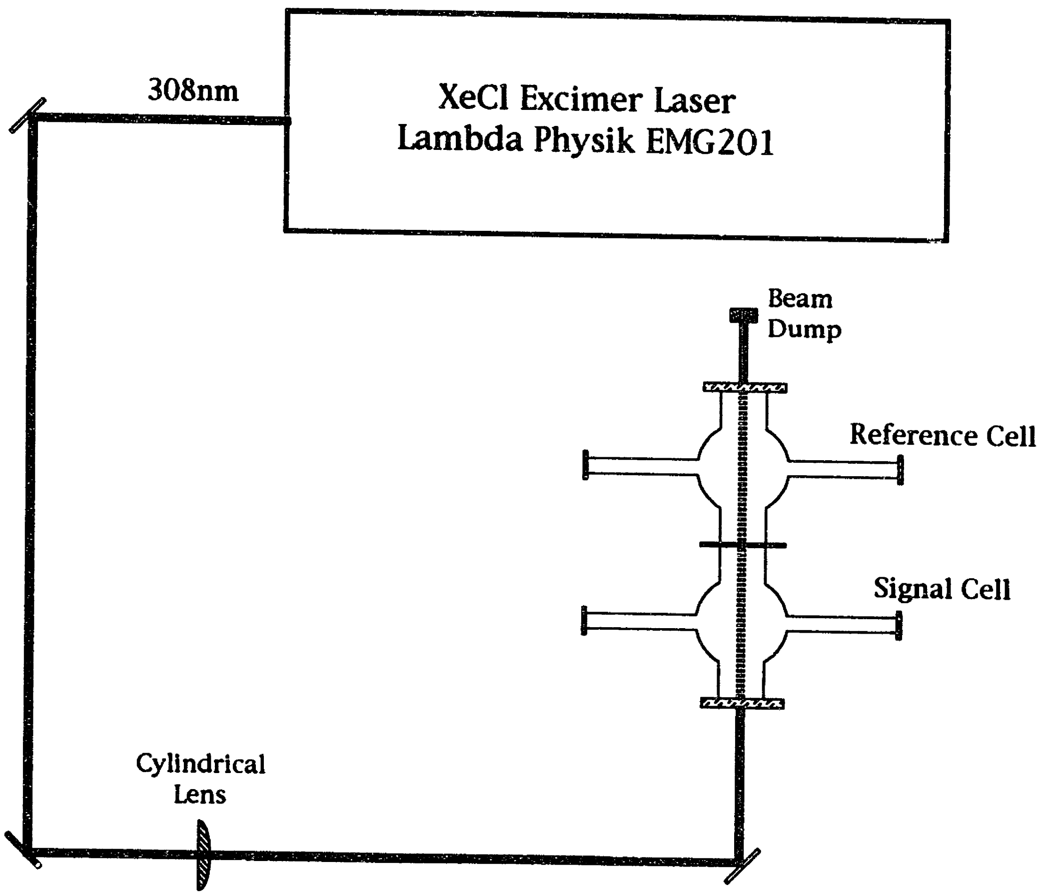

Figure 2.2-1 First SEP Apparatus: Photolysis Optical Layout

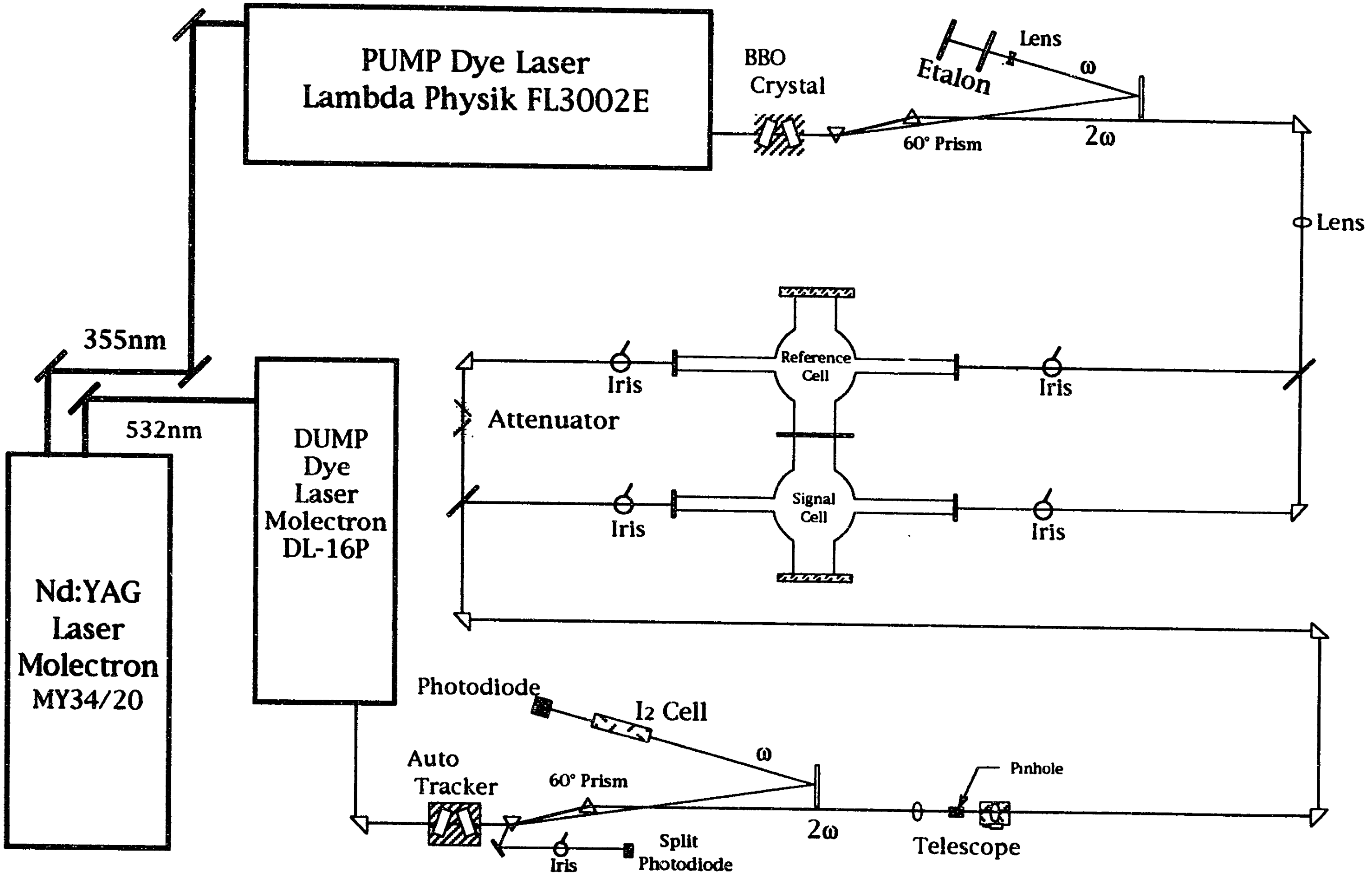

Figure 2.2-2 First SEP Apparatus: PUMP and DUMP Optical Layout

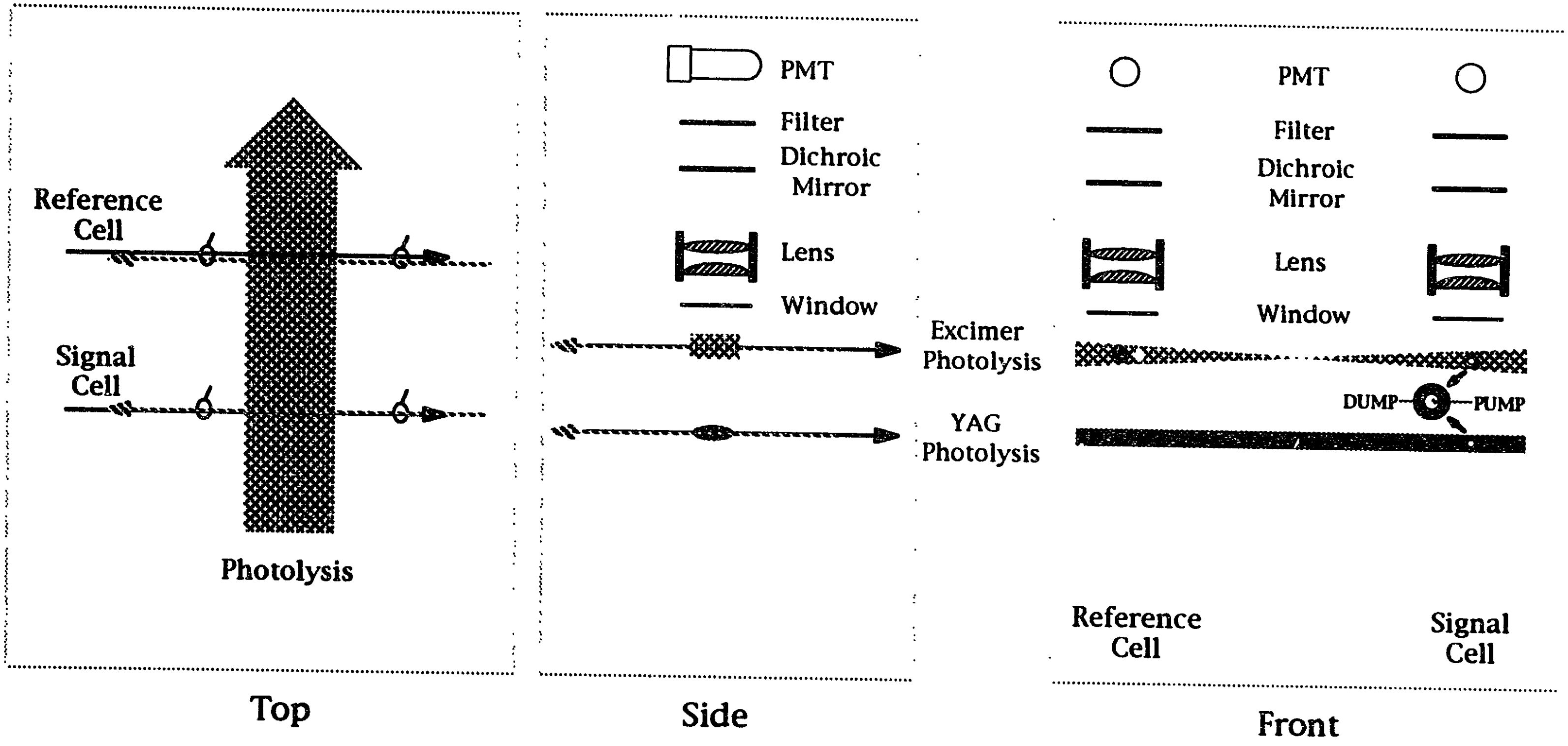

Figure 2.2-3 First and Second SEP Apparatus: Laser Detail

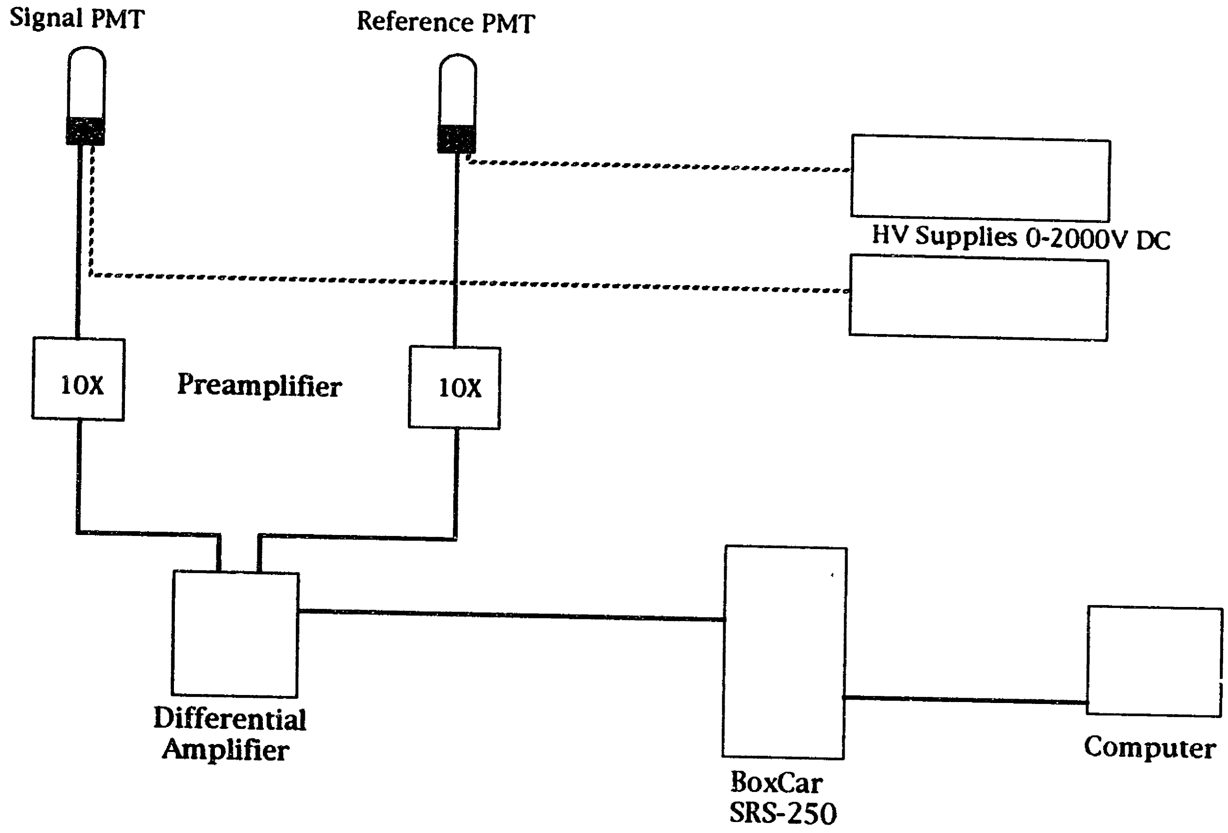

Figure 2.2-4 First SEP Apparatus: Detection Electronics

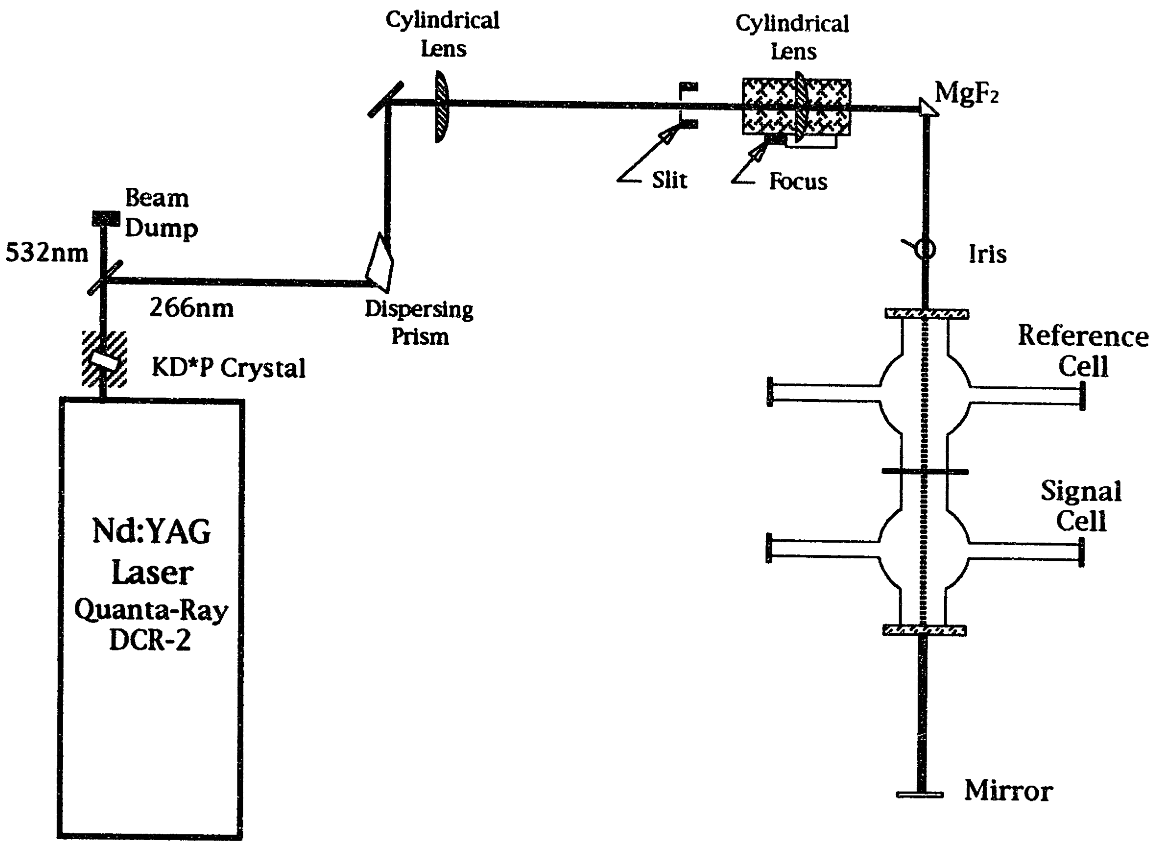

Figure 2.3-1 Second SEP Apparatus: Photolysis Optical Layout

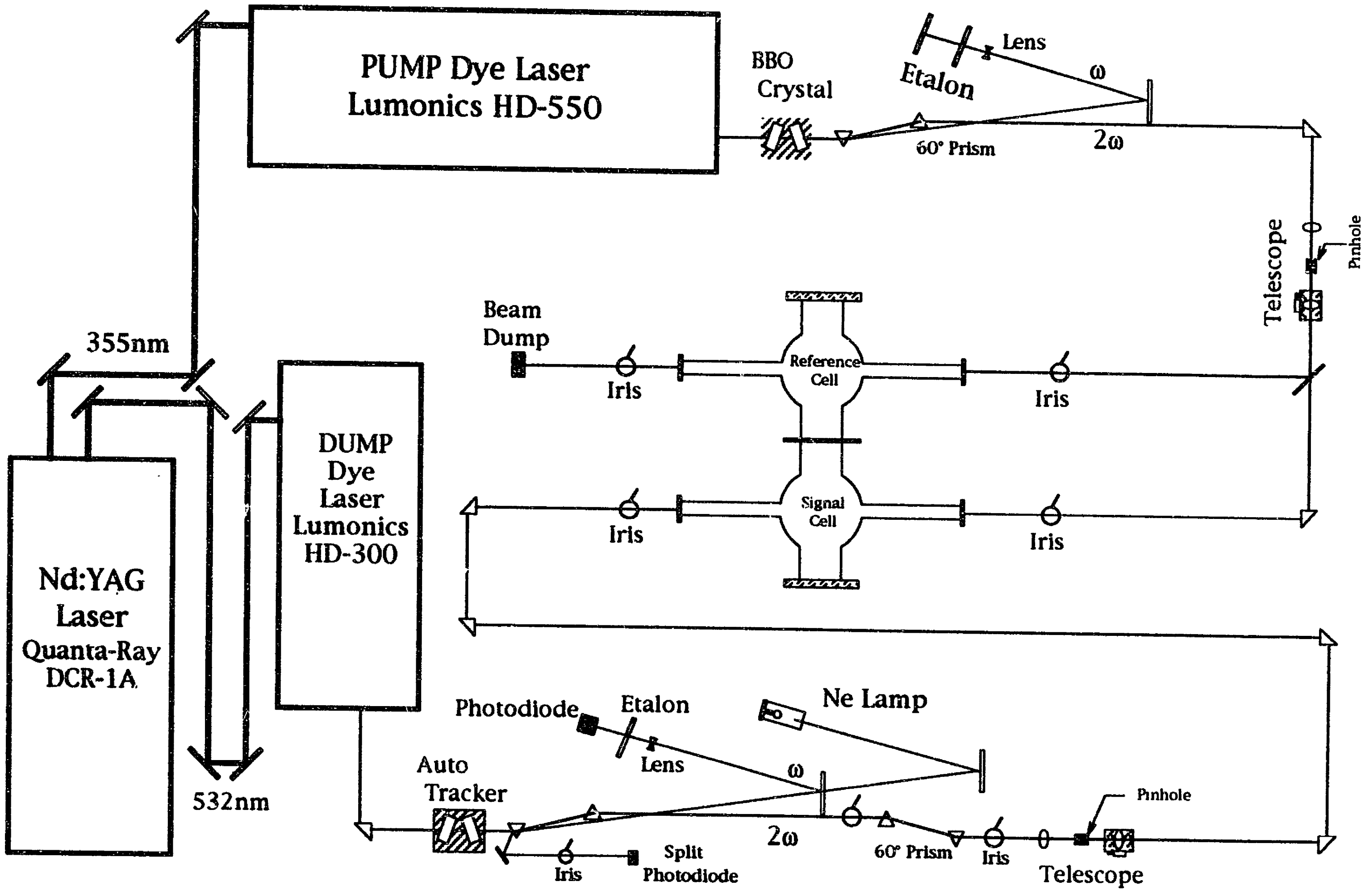

Figure 2.3-2 Second SEP Apparatus: PUMP and DUMP Optical Layout

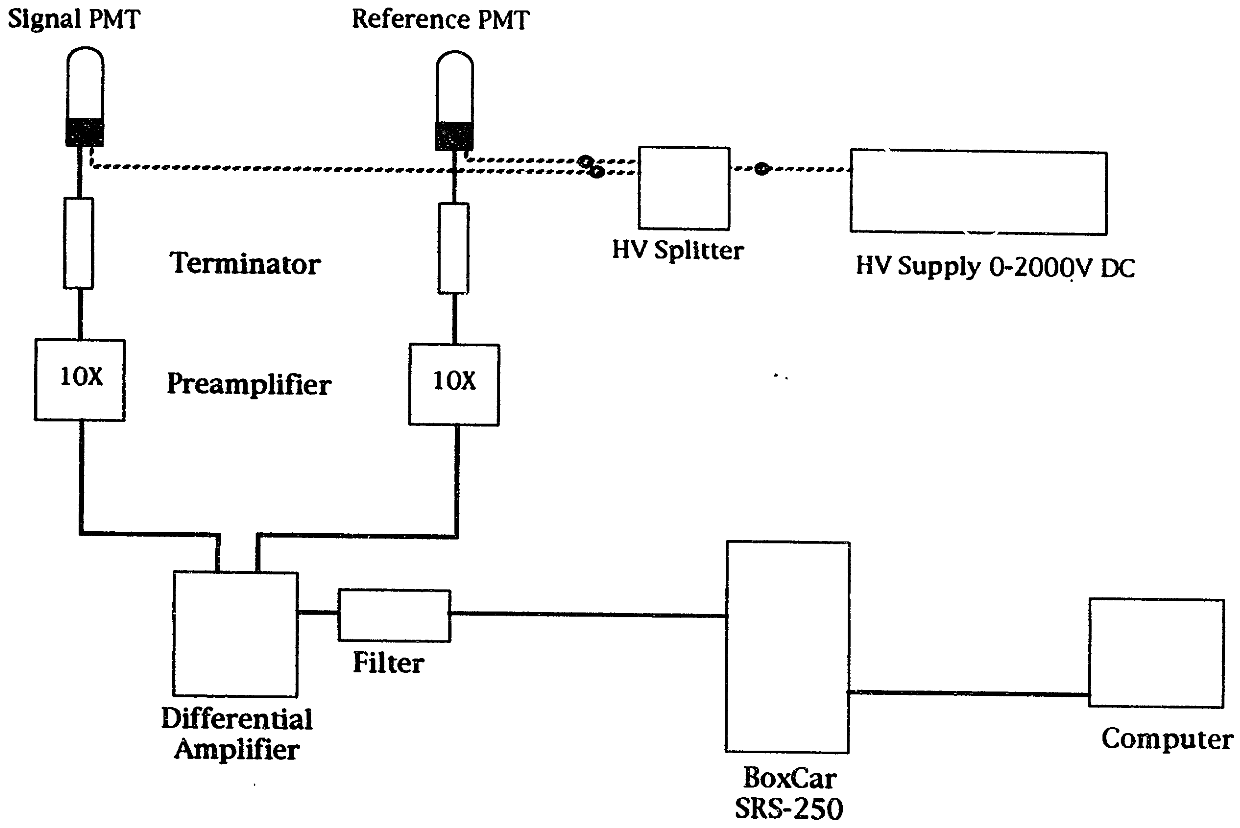

Figure 2.3-3 Second SEP Apparatus: Detection Electronics

CHAPTER 3

Results and Analysis: Fluorescence Excitation and First SEP Experiment

3.1 High-Resolution Fluorescence-Excitation Spectrum of the HCO $\tilde{B}\,^2A' \leftarrow \tilde{X}\,^2A'\,0_0^0$ Band

A high-resolution (0.06cm^{-1} FWHM laser fundamental) fluorescence-excitation spectrum of the $\tilde{B}\,^2A' \leftarrow \tilde{X}\,^2A'$ origin band was recorded between 258.06 and 259.40nm by SF$_6$-presure-scannning a Lambda Physik dye laser (FL-3002E) with an intracavity etalon installed. This high-resolution spectrum is shown in Figure 3.1-1. From this spectrum almost 400 line positions were measured and are shown as a stick spectrum in Figure 3.1-1. A complete table of the measured positions and intensities for these lines is provided in Table 3.1-3.

This high-resolution spectrum of the $\tilde{B}\,^2A' \leftarrow \tilde{X}\,^2A'\,0_0^0$ band was calibrated by simultaneously recording a molecular iodine (35°C) spectrum [1]. The measured line positions of the iodine absorption spectrum were fit to a linear function to produce a calibration curve for each pressure scan. It was found that the residuals of this calibration curve fit were reduced if each pressure scan was divided in half and the iodine absorption lines in each half of the pressure scan fit to separate linear functions. This procedure reduced the RMS deviation of the measured iodine absorption lines from a linear calibration function to 0.04cm^{-1}.

In the high-resolution spectrum of the $\tilde{B}\,^2A' \leftarrow \tilde{X}\,^2A'\,0_0^0$ band (shown in Figure 3.1-1 and Figure 3.1-2), the most striking features of the spectrum are the numerous, strong, a-type K_a

subbands ($\Delta K_a = 0$, ΔK_c = odd). The conclusion that these were actually a-type and not c-type subbands ($\Delta K_a = \pm 1$, ΔK_c = even) was based upon the observation of a subband with strong P- and R-branches but no Q-branch. Such a subband cannot occur for b-type or c-type transitions, where the Q-branch should have intensity comparable to the combined intensity of the P- and R-branches at room temperature. The P- and R-branches of the a-type subband observed here were assigned as ${}^{q}P_0$ and ${}^{q}R_0$ branches (${}^{\Delta K_a}\Delta N_{K_a''}$ branch notation). On the basis of this assignment, the ${}^{q}Q_0$ branch is rigorously parity-forbidden and is not observed. Our ${}^{q}P_0$ and ${}^{q}R_0$ assignment was confirmed (see Table 3.1-5) by comparing the current observed combination differences to the combination differences from the infrared flash kinetic work of Dane et al. [2]. This comparison conclusively establishes the rovibronic identity of the lower state of the hydrocarbon flame bands as HCO $\tilde{X}\ {}^2A'$ (0, 0, 0) $K_a = 0$ and proves that the N' and N'' rotational assignments are also correct [3].

Bent HAB-triatomic molecules must be planar and have the c-inertial axis perpendicular to the plane containing the nuclei. The transition dipole for $A' \leftrightarrow A'$ (or $A'' \leftrightarrow A''$) electric dipole transitions must lie in the molecular plane, while the transition dipole for $A' \leftrightarrow A''$ electric dipole transitions must be perpendicular to the molecular plane. $A' \leftrightarrow A'$ (or $A'' \leftrightarrow A''$) transitions may thus have nonzero projections of the transition dipole onto both the a- and the b-inertial axes (but not onto the c-axis), whereas with $A' \leftrightarrow A''$ transitions the transition dipole has only a projection onto the c-axis.

The conclusive identification of a-type bands from HCO $\tilde{X}\,^2A'$ thus proves Dixon's assignment of the electronic symmetry of the $\tilde{B}\,^2A'$-state [4]. The A' symmetry of the $\tilde{B}\,^2A'$ state also agrees with the *ab initio* calculation by Bruna et al. [5].

There are, however, many more lines in the $\tilde{B}\,^2A' \leftarrow \tilde{X}\,^2A'\,0_0^0$ band than can be accounted for by the $\Delta K_a = 0$, $\Delta K_c =$ odd selection rules of an a-type transition. The spectrum appears to contain many lines which follow b-type rotational selection rules, $\Delta K_a = \pm 1$, $\Delta K_c =$ odd. For HCO, the relative intensities of the $^qR_0$ a-type and $^rQ_0$ b-type branches indicate that the transition dipole moment is tipped approximately 31(4)° away from the a-inertial axis [11]. The numerical value of this tipping angle was determined from the average ratio of the intensities of the rotational lines, $^qR_0(N)$ and $^rQ_0(N)$ for $N = 2$ through 9. For the $^rQ_0(N)$ branch it was necessary to sum the intensities of both spin-rotation components to make a comparison with the intensities in the $^qR_0(N)$ branch, since the spin-rotation components ($\Delta N = \Delta J$) of the $^qR_0(N)$ branch are unresolved in our spectrum.

The molecular constants listed in Figure 3.1-6 for the $\tilde{B}\,^2A'$-state zero-point level were obtained by converting the measured $\tilde{B}\,^2A' \leftarrow \tilde{X}\,^2A'\,0_0^0$ rotational lines to term values, using the rotational constants for the $\tilde{X}\,^2A'$ zero-point level from Dane et al. [2]. The nonlinear least-squares fitting program was the same one used by Dane et al. [2] to fit the high-resolution rotation-vibration spectra of the HCO $\tilde{X}\,^2A'$-state and was provided by T. Sears, who has described this program in detail [7]. Absolute J assignments — i.e., $J = N + 1/2$ (F_2) versus $J = N - 1/2$ (F_1) — were based in part on the $\tilde{X}\,^2A'$-state spin-rotation constants of Reference (2) and Reference (10) and in part on the expected relative intensities of the two spin doublet components of each N', N'' line. At low N in the $^rQ_0$ branch, the $J = N + 1/2$ ($F_2 - F_2$) components should be more intense than the $J = N - 1/2$ ($F_1 - F_1$) component (at $N = 2$ the intensity ratio is predicted to be 1 : 0.75). In the $^rP_0$ and $^rR_0$ branches, the ($F_2 - F_2$) : ($F_1 - F_1$) relative intensity pattern is opposite to that in the $^rQ_0$ branch.

In the least-squares fit, most lines were assigned relative weights equal to the inverse of their full width squared. Badly blended lines, which occur mostly near the R-heads for each of the K_a subbands, were assigned zero weight in the fit. Table 3.1-4 shows the $\tilde{B}\,^2A' \leftarrow \tilde{X}\,^2A'\,0^0_0$ band with the line assignments, and in Table 3.1-5 the frequencies of 287 assigned rotational lines and their residuals are listed. The average residual was 0.04cm^{-1} with an RMS deviation of 0.06cm^{-1}. The following molecular constants for the $\tilde{B}\,^2A'$ (0, 0, 0) level were determined: T_{00}, A, $\bar{B} = (B+C)/2$, $(B-C)/4$, Δ_{KN}, Δ_N, κ, and μ. The rotational constants reported are standard for triatomic molecules and correspond to those reported in the most extensive high resolution ground state work [2,10]. The parameters Δ_{KN}, Δ_N are centrifugal distortion terms that were defined by Watson in his A-reduction of the asymmetric top Hamiltonian expressed in the I^r representation [8]. The parameters κ and μ [where $\kappa = \varepsilon_{aa} - 0.5\,(\varepsilon_{bb} + \varepsilon_{cc})$ and $\mu = 0.5\,(\varepsilon_{bb} + \varepsilon_{cc})$] are the spin-rotation parameters of the A-reduction of the spin-rotation Hamiltonian of Brown and

Sears [9,7] for doublet electronic states of asymmetric tops. The values of these parameters are listed in Table 3.1-6.

Using the above molecular parameters for the $\tilde{B}\,{}^2A'$ (0, 0, 0) level and molecular parameters for the $\tilde{X}\,{}^2A'$ zero-point level from Dane et al. [2], the transition energies for lines that had not been assigned in the spectrum were calculated. The calculated positions of the unassigned lines were then compared with the set of unassigned lines in Figure 3.1-1 in an attempt to extend the rotational assignments. No further convincing rotational assignments could be made using this procedure. The size of the apparent line shifts in the observed unassigned lines ranged from 0.2 to 1.0cm^{-1} with no apparent systematic trends. Additionally, no further subbands with $K_a' > 2$ could be identified.

3.2 First HCO Stimulated Emission Pumping Experiment

Partially to confirm that our spectra were downward SEP spectra rather than upward OODR spectra and also to confirm our rotational analysis of the $\tilde{B}\,{}^2A' \leftarrow \tilde{X}\,{}^2A'\,0^0_0$ ${}^qR_0$ branch, the $\tilde{B}\,{}^2A' \leftarrow \tilde{X}\,{}^2A'\,0^0_0$ PUMP and the $\tilde{B}\,{}^2A' \rightarrow \tilde{X}\,{}^2A'\,2^0_5$ DUMP bands were chosen for initial experiments. For each SEP scan the PUMP laser was locked onto the unresolved spin doublet components of a line in the ${}^qR_0$ (N) (N = 1 through 7) branch of the $\tilde{B}\,{}^2A' \leftarrow \tilde{X}\,{}^2A'\,0^0_0$ band. The SEP spectrum was recorded by monitoring the total spontaneous side fluorescence produced when the PUMP laser excited a single rovibronic level of the HCO $\tilde{B}\,{}^2A'$-state. The DUMP laser caused a decrease in the intensity of side fluorescence whenever it was tuned through resonance with a downward transition into the $\tilde{X}\ ^2A'$-state or an upward transition into another electronic state. This fluorescence dip occurred when the stimulated emission or absorption caused by the DUMP laser competed with the spontaneous emission from the selected $\tilde{B}\ ^2A'$-state rovibronic level, regardless of whether the final level was predissociated.

The direction, upward or downward, of the transition stimulated by the DUMP laser was determined by recording spectra from a set of intermediate states differing in N' by steps of two. Then, by comparing the spectra obtained from the $N' = N'' + 1$ and $N' = N'' - 1$ pair of intermediate levels, it was possible to determine whether the transition was to higher or lower energy. If the transition was downward, the lower frequency line, $P(N'')$, originating from the $N' = N'' - 1$ intermediate level and the higher frequency line, $R(N'')$, originating from the $N' = N'' + 1$ intermediate level, were separated by the known $\tilde{B}\ ^2A'$-state $\Delta_2F'(N'')$ combination difference. If the transition was upward, the higher frequency line, $R(N'' - 1)$, originating from the $N' = N'' - 1$ intermediate level and the lower frequency line, $P(N'' + 1)$, originating from the $N' = N'' + 1$ intermediate level, would be separated by the $\tilde{B}\ ^2A'$-state $\Delta_2F'(N'')$ combination difference.

Because $\tilde{B}\ ^2A'$-state rotational levels of known N, K_a , K_c quantum numbers were selected by the PUMP, it was not difficult to assign the rotational quantum numbers of the lower states observed in SEP spectra. Since the $\tilde{B}\ ^2A' \leftrightarrow \tilde{X}\ ^2A'$ transition follows a/b-hybrid rotational section rules, for each selected

${}^{q}R(N_{0N})$ PUMP transition five DUMP rotational lines per vibrational level were observed in the SEP spectrum. For a ${}^{q}R(2_{02})$ PUMP, the DUMP lines were ${}^{q}R(2_{02})$, ${}^{q}P(4_{04})$, ${}^{q}R(2_{12})$, ${}^{q}Q(3_{12})$, and ${}^{q}P(4_{14})$. The spin-rotation splitting in both the PUMP and the DUMP transitions was small, thus each of the five lines will appear as an unresolved spin doublet.

The SEP spectrum of the $\tilde{B}\,{}^{2}A' \rightarrow \tilde{X}\,{}^{2}A'\,2^{0}_{5}$ band, recorded via the $\tilde{B}\,{}^{2}A' \leftarrow \tilde{X}\,{}^{2}A'\,0^{0}_{0}\;{}^{q}R(7_{07})$ PUMP line, is shown in Figure 3.2-1. It shows clearly all five of the expected rotational transitions. Satisfactory agreement was found between the observed and the calculated relative intensities of the SEP rotational lines for both a-type and b-type subbands.

The rotational term values measured by SEP for the $\tilde{X}\,{}^{2}A'$-state $\{v_2$ (CO-stretch) $= 5\}$ level are listed in Table 3.2-2. The measured FWHM linewidths are also collected in Table 3.2-2. These SEP lines contain unresolved spin-rotation splittings.

The transition frequencies measured in our SEP spectrum and those reported in emission by Dixon for this band agree to within experimental accuracy [4]. The spin splitting of the PUMP transitions was not resolved and the spin-rotation splitting in the rotational levels of the ground state sampled by our SEP spectra is at most 0.05cm^{-1}, thus spin doublet components are unresolved in the SEP spectrum. However, the spin-rotation splitting is resolved for PUMP transitions in the ${}^{r}Q_{0}$ branch. These ${}^{r}Q_{0}$ PUMP transitions were used in Section 4.2 to observe single J'', N'', K_a'' levels of the $\tilde{X}\,{}^{2}A'$-state and to measure the homogeneous widths of these levels.

The fact that the $\tilde{B}\,^2A' \leftrightarrow \tilde{X}\,^2A'$ transition of HCO is of hybrid a/b character allows us to determine the A, B, and C rotational constants for each vibrational level of the $\tilde{X}\,^2A'$-state from a single SEP spectrum. For example, using the $^qR_0(2)$ PUMP transition, the $\tilde{B}\,^2A'$ -state 3_{03} level is populated, and SEP transitions sample the five following ground state N_{K_a,K_c} rotational levels: 2_{02}, 4_{04}, 2_{12}, 3_{12}, 4_{14}. The wavenumbers of each of the PUMP transitions were measured to within ±0.04cm^{-1}. The DUMP laser had a linewidth of 0.06cm^{-1} and was also calibrated against the iodine absorption spectrum, thus the absolute wavenumber of each SEP line was determined to ±0.04cm^{-1} [1]. The same procedure was used to fit the SEP spectra as was used to fit the fluorescence excitation spectrum. The molecular constants for the vibrational bands observed by SEP are listed in Table 3.2-3.

From the observed intensity ratio between $^qR_0$, $^qP_0$, and $^pR_1$, $^pQ_1$, $^pP_1$ SEP transitions in the $\tilde{B}\,^2A' \rightarrow \tilde{X}\,^2A'\,2^0_5$ band, the angle of the transition dipole moment relative to the a-inertial axis is found to be 35 (5)°. The tipping angle of the transition moment for the $\tilde{B}\,^2A' \rightarrow \tilde{X}\,^2A'\,2^0_5$ transition is essentially the same as the 31 (4)° found for the $\tilde{B}\,^2A' \leftarrow \tilde{X}\,^2A'\,0^0_0$ transition. The details of the calculation of the transition moment angle is discussed in Appendix I.

3.3 References

1. S. Gerstenkorn and P. Luc, "Atlas du Spectre d'Absorption de la Molecule d'Iode," Paris: CNRS (1978); S. Gerstenkorn and P. Luc, *Rev. Phys. Appl.* **14**, 791-798 (1979).
2. C. B. Dane, D. R. Lander, R. F. Curl, F. K. Tittel, Y. Guo, M. I. F. Ochsner, and C. B. Moore, *J. Chem. Phys.* **88**, 2121-2128 (1988).
3. G. Herzberg, "Electronic Spectra of Polyatomic Molecules," New York: Van Nostrand Reinhold (1966); Pages 244-245.
4. R. N. Dixon, *Trans. Faraday Soc.* **65**, 3141-3149 (1969).
5. P. J. Bruna, R. J. Buenker, and S. D. Peyerimhoff, *J. Mol. Struct.* **32**, 217-233 (1976).
6. E. E. Whiting, A. Schadee, J. B. Tatum, J. T. Hougen, and R. W. Nicholls, *J. Mol. Spectrosc.* **80**, 249-256 (1980).
7. T. J. Sears, *Comput. Phys. Rep.* **2**,1-32 (1984); T. J. Sears, *Comput. Phys. Commun.* **34**, 123-133 (1984).
8. J. K. G. Watson, "In Vibrational Spectra and Structure," (J. R. Durig, Ed.), Vol. 6, New York: Dekker (1977).
9. J. M. Brown and T. J. Sears, *J. Mol. Spectrosc.* **75**, 111-133 (1979).
10. J. M. Brown, H. E. Radford, and T. J. Sears, *J. Mol. Spectrosc.* **148**, 20-37 (1991).
11. J. T. Hougen, "The Calculation of Rotational Energy Levels and Rotational Line Intensities in Diatomic Molecules," Washington, D. C.: NBS Monograph 115 (1970).

3.4 Chapter 3 Figure and Table Captions

Figure 3.1-1A-D Fluorescence Excitation Spectrum $\tilde{B}\,{}^2A' \leftarrow \tilde{X}\,{}^2A'$ 0^0_0, Measured and Unassigned Line Positions. (A) Unassigned line positions plotted as a stick spectrum. (B) High resolution (0.06cm^{-1}) fluorescence excitation spectrum. (C) Measured line positions and intensities plotted as stick spectrum.

Figure 3.1-2A,B Fluorescence Excitation Spectrum $\tilde{B}\,{}^2A' \leftarrow \tilde{X}\,{}^2A'$ 0^0_0, and Assigned Line Positions. (A) High resolution (0.06cm^{-1}) fluorescence excitation spectrum. (B) Assigned line positions plotted as stick spectrum versus rotational quantum number.

Table 3.1-3A-E Table of Measured Lines and Intensities from the $\tilde{B}\,{}^2A' \leftarrow \tilde{X}\,{}^2A'$ 0^0_0 Fluorescence Excitation Spectrum. The table of all measured line positions and relative intensities for the fluorescence excitation spectrum. All energies reported in wavenumbers (cm^{-1}) and intensities in arbitrary units.

Table 3.1-4A-D Table of Assigned Lines from the $\tilde{B}\,{}^2A' \leftarrow \tilde{X}\,{}^2A'$ 0^0_0 Fluorescence Excitation Spectrum. The table lists all assigned lines used in the rotational fit of $\tilde{B}$-state origin band. All energies reported in wavenumbers (cm^{-1}) and intensities in arbitrary units.

Table 3.1-5 Table of $\tilde{X}\,^2A'$-State Rotational Combination Differences from $\tilde{B}\,^2A' \leftarrow \tilde{X}\,^2A'\ 0^0_0$ Band. Figure shows the $\tilde{X}$-state rotational combination differences proving that the "hydrocarbon flame bands" are from HCO. The combination differences were calculated with constants from Reference [2]. Uncertainties for the observed combination differences are the averages for the $J'' = N'' + 1/2$ and $J'' = N'' - 1/2$ spin-rotation components.

Table 3.1-6 Table of Molecular Constants for $\tilde{B}$-state Zero-Point Level. Table summarizes the constants from the rotational fit of the assigned fluorescence excitation line positions. $\tilde{X}$-state constants from reference [2] were used in the fit.

Figure 3.2-1 $\tilde{B}\,^2A' \rightarrow \tilde{X}\,^2A'\ 1^0_0 2^0_5 3^0_0$ SEP Spectra, ${}^qR(7_{07})$ Pump. Each line in this SEP spectrum is an unresolved spin-rotation doublet. The feature marked with a asterisk is an intentional 4% attenuation to calibrate the intensities. The polarizations of the PUMP and DUMP lasers were parallel.

Table 3.2-2 Table of Term Values and Widths from the $\tilde{B}\,^2A' \rightarrow \tilde{X}\,^2A'$ $1^0_0 2^0_5 3^0_0$ SEP Spectra, ^qR(NON) Pump. Table summarizing all observed SEP rotational transitions into the ground state vibrational level (0,5,0). The FWHM for each line is shown in parentheses.

* - blended, w - weak.

Table 3.2-3 Table of Molecular Constants for the $\tilde{X}\,^2A'$-state (0,5,0) Vibrational Level. Table shows constants from rotational fit to the observed SEP transitions.

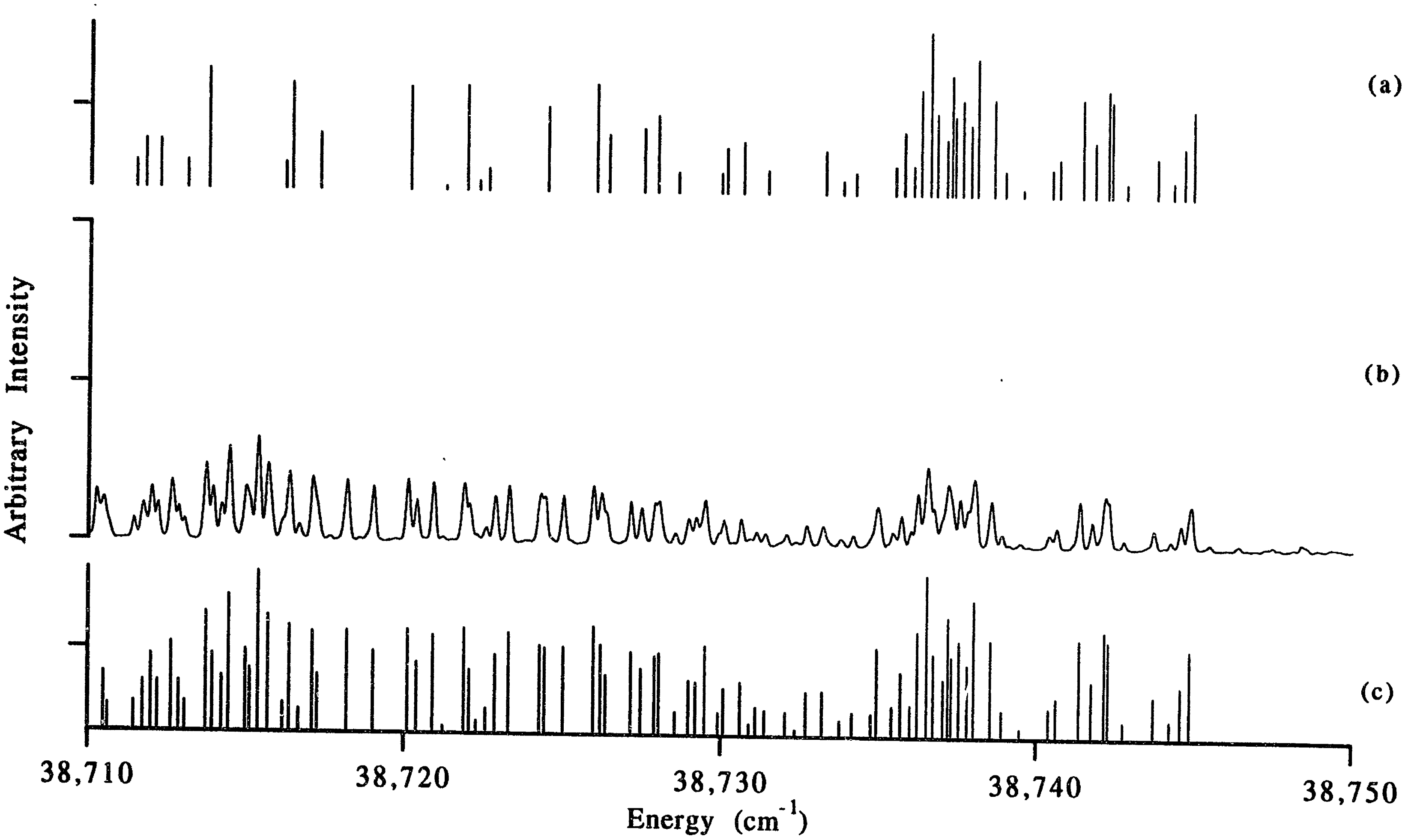

Figure 3.1-1A (a) Unassigned Line Positions
(b) Fluorescence Excitation Spectrum: HCO $\tilde{B} \leftarrow \tilde{X}$ Origin Band
(c) Measured Line Positions

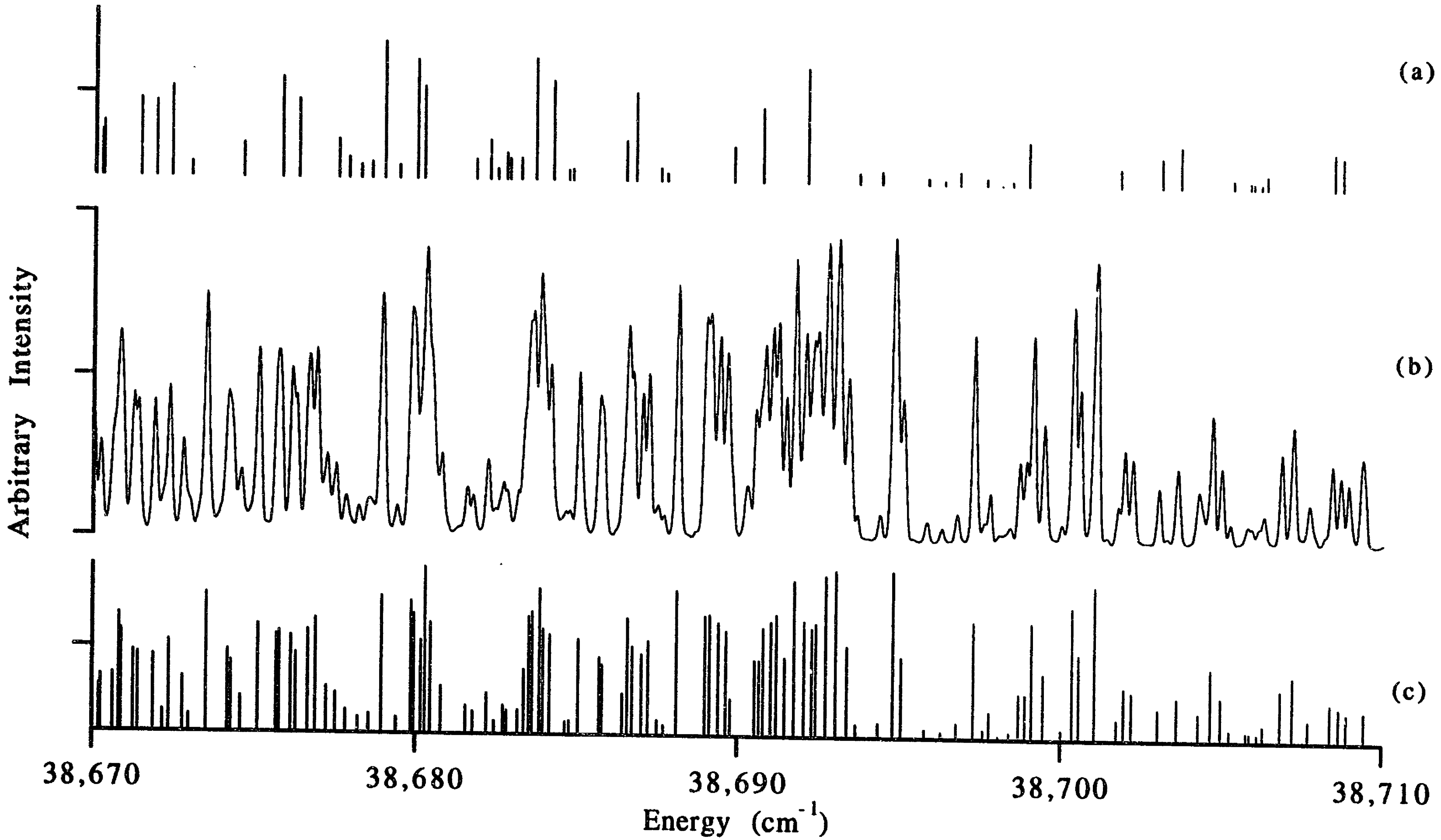

Figure 3.1-1B (a) Unassigned Line Positions
(b) Fluorescence Excitation Spectrum: HCO $\tilde{B} \leftarrow \tilde{X}$ Origin Band
(c) Measured Line Positions

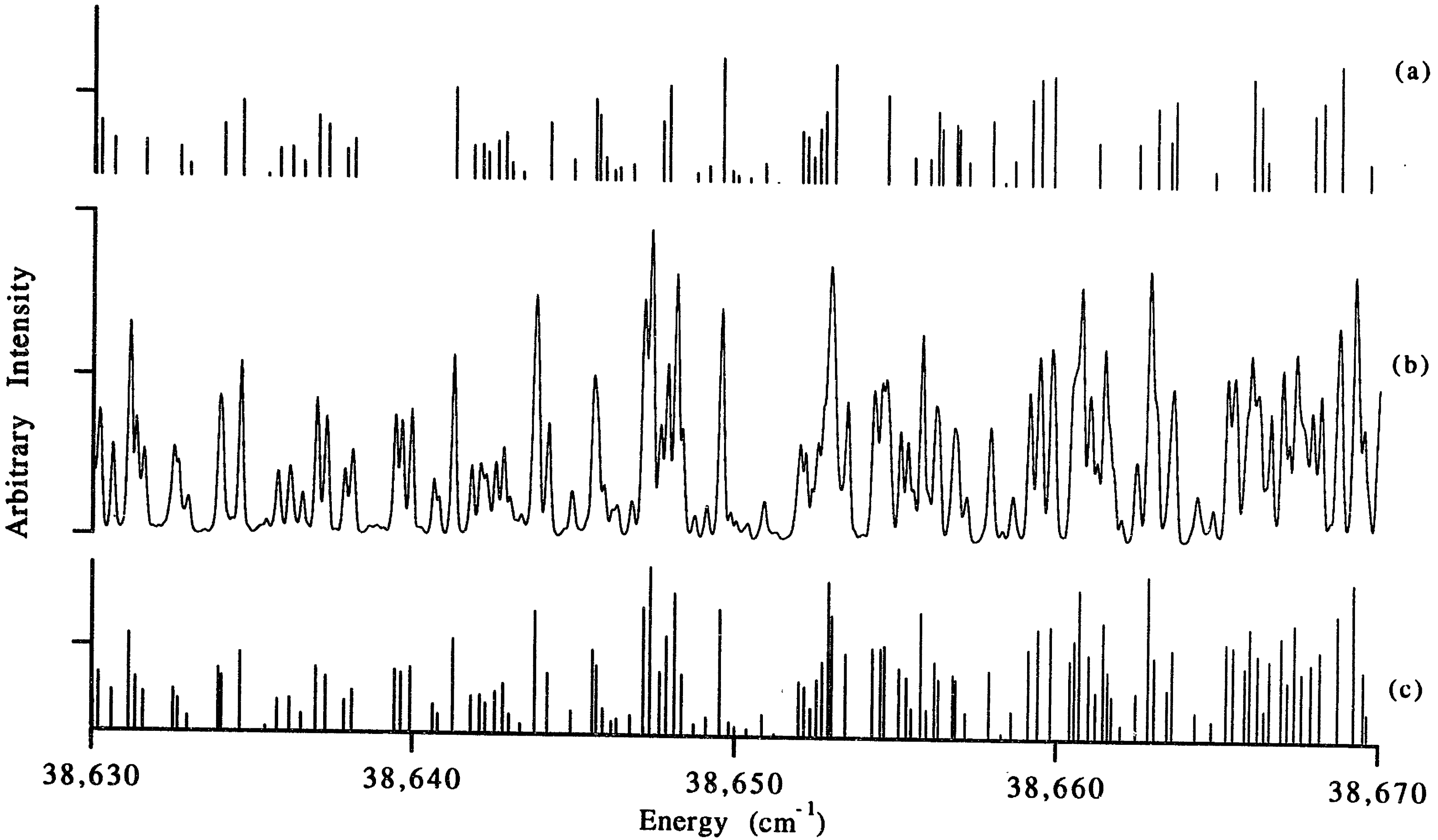

Figure 3.1-1C (a) Unassigned Line Positions
(b) Fluorescence Excitation Spectrum: HCO $\tilde{B} \leftarrow \tilde{X}$ Origin Band
(c) Measured Line Positions

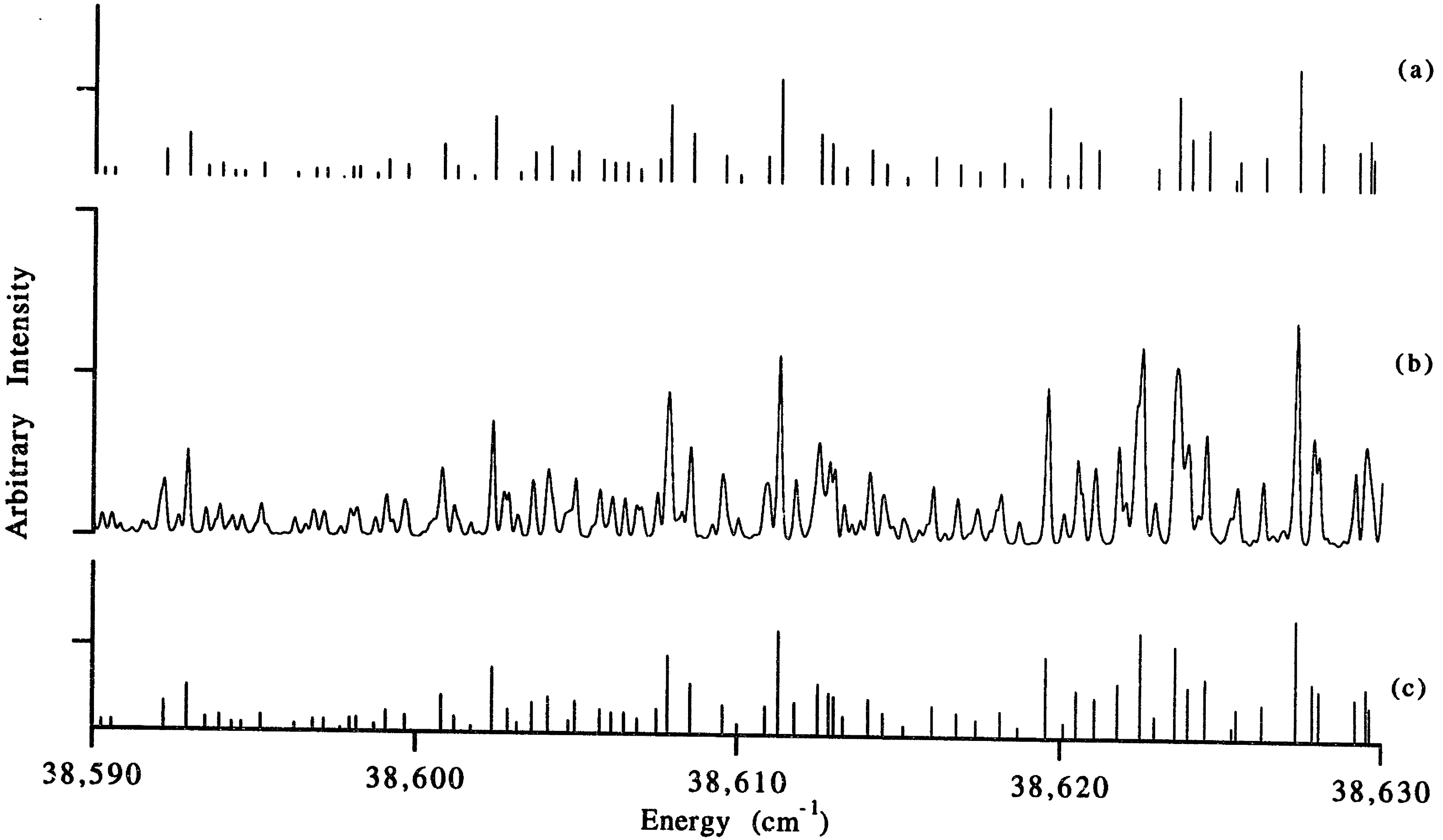

Figure 3.1-1D (a) Unassigned Line Positions
(b) Fluorescence Excitation Spectrum: HCO $\tilde{B} \leftarrow \tilde{X}$ Origin Band
(c) Measured Line Positions

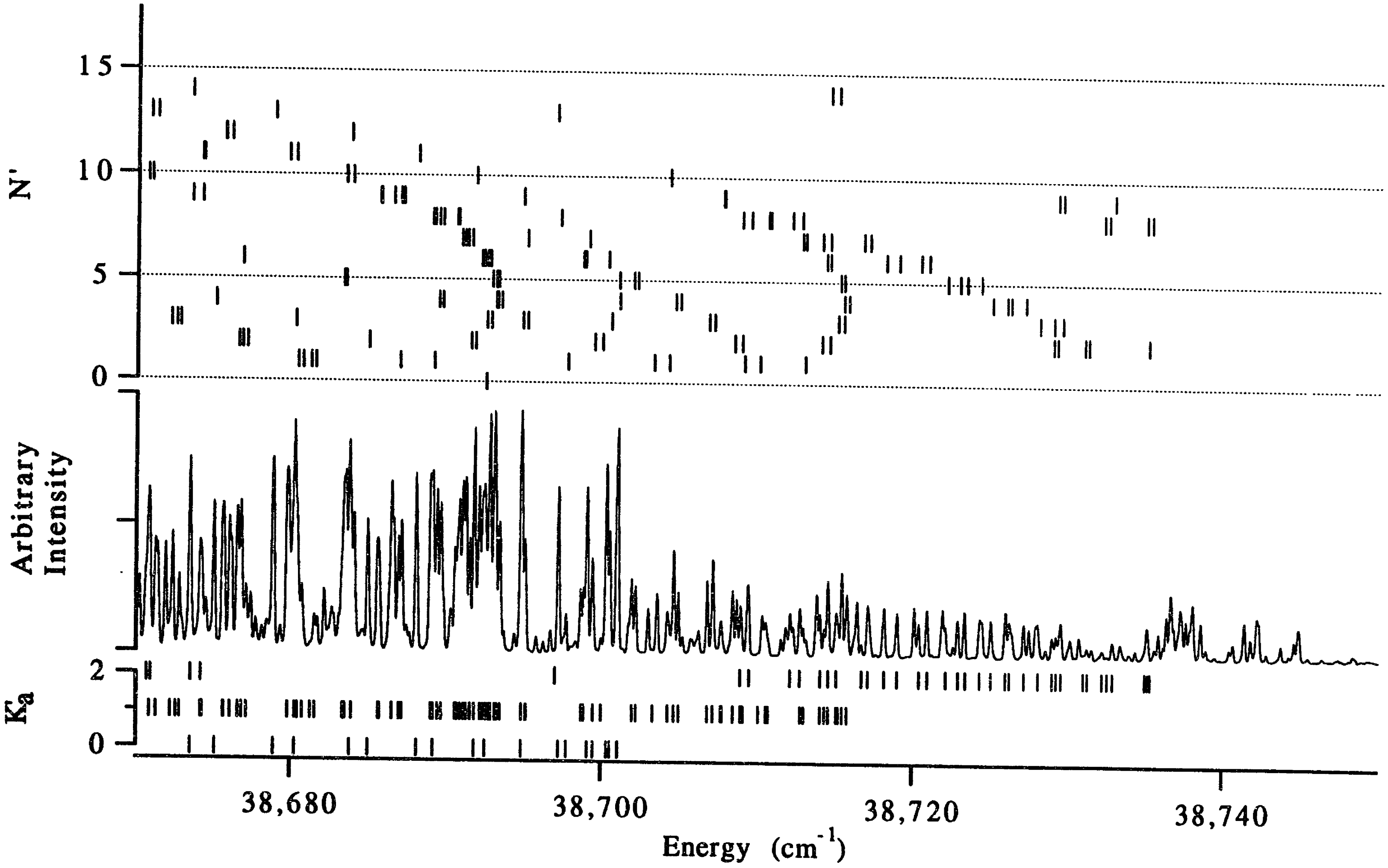

Figure 3.1-2A HCO $\tilde{B} \leftarrow \tilde{X}\ 0_0^0$ Fluorescence Excitation Spectrum and Assignments

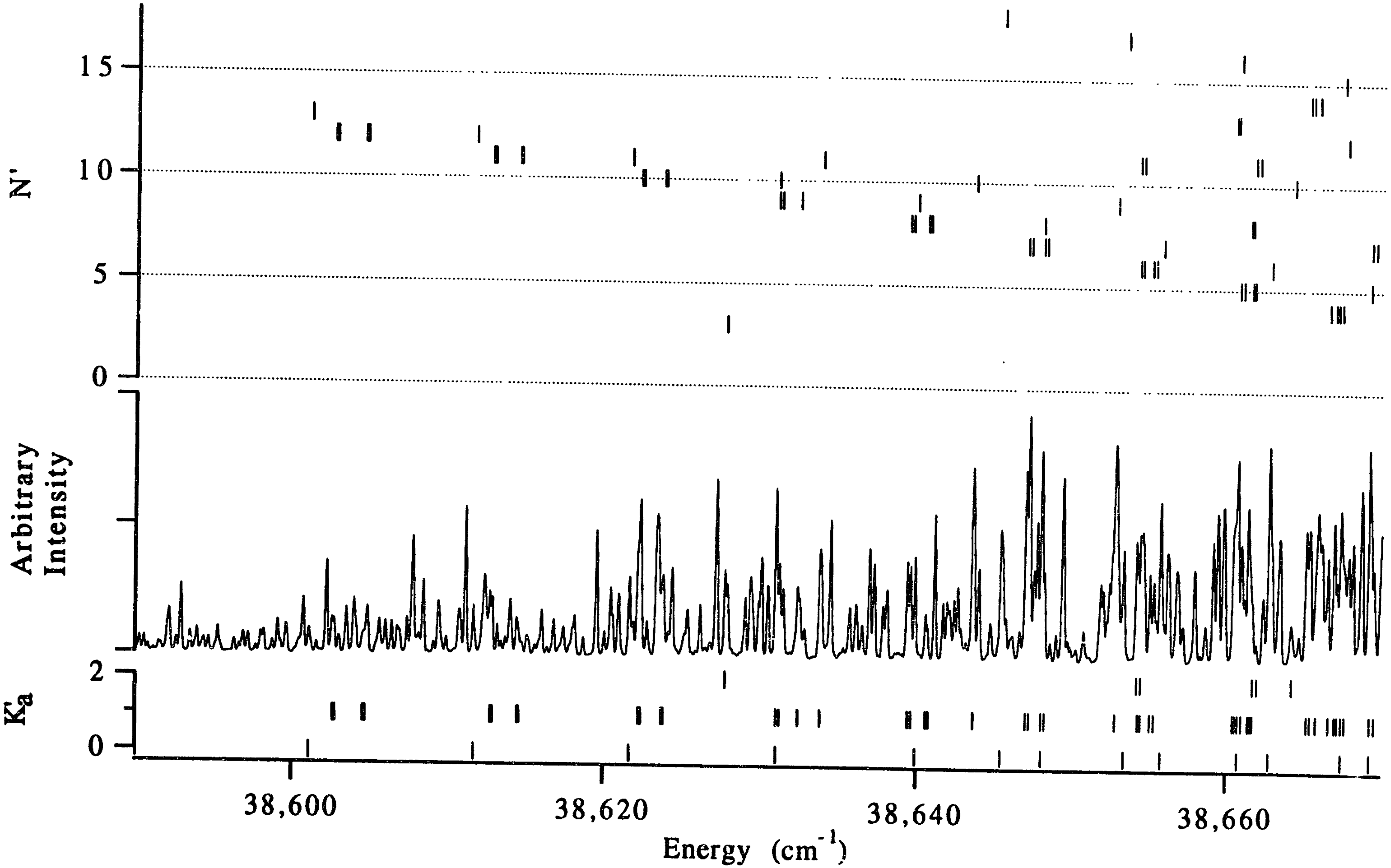

Figure 3.1-2B HCO $\tilde{B} \leftarrow \tilde{X}\ 0_0^0$ Fluorescence Excitation Spectrum and Assignments

Table 3.1-3A Table of Measured Line Positions and Intensities From the $\tilde{B}\,^2A' \leftarrow \tilde{X}\,^2A'\,0_0^0$ Fluorescence Excitation Spectrum

Energy cm^{-1}	Intensity	Energy cm^{-1}	Intensity	Energy cm^{-1}	Intensity
38 590.28	0.07	38 606.11	0.14	38 622.91	0.15
38 590.58	0.07	38 606.51	0.14	38 623.56	0.56
38 592.18	0.18	38 606.91	0.10	38 623.96	0.32
38 592.88	0.28	38 607.51	0.16	38 624.51	0.37
38 593.48	0.09	38 607.86	0.47	38 625.36	0.09
38 593.93	0.11	38 608.56	0.31	38 625.51	0.20
38 594.33	0.06	38 609.56	0.19	38 626.31	0.22
38 594.63	0.06	38 610.01	0.08	38 627.36	0.72
38 595.23	0.11	38 610.86	0.18	38 627.86	0.35
38 596.28	0.06	38 611.26	0.63	38 628.06	0.31
38 596.83	0.08	38 611.76	0.21	38 629.19	0.26
38 597.18	0.08	38 612.46	0.32	38 629.54	0.32
38 597.68	0.03	38 612.81	0.26	38 629.64	0.22
38 597.98	0.09	38 612.96	0.24	38 630.03	0.20
38 598.18	0.10	38 613.26	0.13	38 630.21	0.35
38 598.73	0.06	38 614.06	0.23	38 630.62	0.25
38 599.08	0.14	38 614.51	0.15	38 631.14	0.59
38 599.68	0.11	38 615.16	0.07	38 631.35	0.33
38 600.78	0.23	38 616.06	0.20	38 631.59	0.24
38 601.18	0.11	38 616.81	0.15	38 632.51	0.26
38 601.68	0.05	38 617.41	0.11	38 632.64	0.20
38 602.33	0.39	38 618.16	0.17	38 632.93	0.11
38 602.83	0.15	38 618.71	0.08	38 633.90	0.39
38 603.13	0.07	38 619.56	0.49	38 633.99	0.34
38 603.61	0.19	38 620.11	0.10	38 634.57	0.48
38 604.11	0.22	38 620.51	0.29	38 635.40	0.05
38 604.76	0.09	38 621.06	0.25	38 635.77	0.20
38 604.96	0.20	38 621.76	0.34	38 636.16	0.21
38 605.76	0.16	38 622.46	0.64		

Table 3.1-3B Table of Measured Line Positions and Intensities From the $\tilde{B}\,^2A' \leftarrow \tilde{X}\,^2A'\,0^0_0$ Fluorescence Excitation Spectrum

Energy cm^{-1}	Intensity	Energy cm^{-1}	Intensity	Energy cm^{-1}	Intensity
38 636.55	0.12	38 647.66	0.38	38 656.35	0.36
38 637.01	0.39	38 647.88	0.59	38 656.80	0.39
38 637.30	0.34	38 648.13	0.85	38 656.89	0.36
38 637.89	0.20	38 648.35	0.37	38 657.20	0.16
38 638.13	0.26	38 648.72	0.08	38 657.94	0.41
38 639.45	0.38	38 649.10	0.12	38 658.30	0.05
38 639.64	0.36	38 649.55	0.75	38 658.62	0.17
38 639.93	0.40	38 649.84	0.10	38 659.15	0.54
38 640.63	0.18	38 650.00	0.07	38 659.45	0.66
38 640.78	0.13	38 650.38	0.06	38 659.83	0.67
38 641.24	0.56	38 650.87	0.14	38 660.43	0.47
38 641.79	0.23	38 651.23	0.03	38 660.57	0.59
38 642.06	0.24	38 651.99	0.34	38 660.73	0.89
38 642.24	0.19	38 652.15	0.30	38 661.01	0.51
38 642.52	0.26	38 652.34	0.18	38 661.22	0.29
38 642.76	0.30	38 652.54	0.35	38 661.45	0.70
38 642.95	0.13	38 652.71	0.45	38 661.59	0.41
38 643.30	0.07	38 652.89	0.92	38 661.72	0.27
38 643.74	0.73	38 653.00	0.72	38 661.98	0.10
38 644.13	0.37	38 653.43	0.50	38 662.44	0.29
38 644.87	0.15	38 654.26	0.53	38 662.82	0.97
38 645.56	0.51	38 654.51	0.54	38 663.01	0.50
38 645.67	0.42	38 654.64	0.55	38 663.41	0.31
38 645.88	0.17	38 655.11	0.42	38 663.56	0.54
38 646.15	0.09	38 655.33	0.37	38 664.28	0.18
38 646.31	0.11	38 655.50	0.19	38 664.79	0.13
38 646.74	0.13	38 655.78	0.75	38 665.25	0.58
38 647.15	0.76	38 655.97	0.18	38 665.48	0.56
38 647.35	1.00	38 656.23	0.46		

Table 3.1-3C Table of Measured Line Positions and Intensities From the $\tilde{B}\,^2A' \leftarrow \tilde{X}\,^2A'\,0^0_0$ Fluorescence Excitation Spectrum

Energy cm^{-1}	Intensity	Energy cm^{-1}	Intensity	Energy cm^{-1}	Intensity
38 665.85	0.44	38 674.16	0.50	38 683.16	0.16
38 666.01	0.67	38 674.26	0.44	38 683.34	0.40
38 666.25	0.52	38 674.55	0.23	38 683.50	0.71
38 666.46	0.20	38 675.08	0.65	38 683.60	0.73
38 666.64	0.49	38 675.64	0.59	38 683.82	0.87
38 667.02	0.62	38 675.72	0.61	38 683.93	0.64
38 667.20	0.36	38 676.09	0.59	38 684.13	0.60
38 667.43	0.70	38 676.24	0.49	38 684.61	0.09
38 667.64	0.41	38 676.62	0.62	38 684.73	0.10
38 667.93	0.47	38 676.86	0.69	38 685.00	0.58
38 668.21	0.54	38 677.19	0.29	38 685.64	0.47
38 668.75	0.75	38 677.49	0.25	38 685.73	0.43
38 669.25	0.94	38 677.81	0.15	38 686.37	0.26
38 669.53	0.43	38 678.21	0.11	38 686.52	0.70
38 669.64	0.19	38 678.54	0.13	38 686.67	0.54
38 670.01	0.57	38 678.93	0.82	38 686.97	0.49
38 670.21	0.29	38 679.39	0.11	38 687.17	0.57
38 670.26	0.35	38 679.86	0.79	38 687.46	0.11
38 670.64	0.36	38 679.94	0.72	38 687.67	0.08
38 670.82	0.71	38 680.17	0.56	38 688.08	0.86
38 670.89	0.62	38 680.29	1.00	38 688.98	0.72
38 671.26	0.49	38 680.46	0.67	38 689.12	0.72
38 671.41	0.48	38 680.78	0.30	38 689.39	0.68
38 671.89	0.47	38 681.56	0.18	38 689.64	0.63
38 672.18	0.14	38 681.78	0.15	38 689.78	0.23
38 672.35	0.55	38 682.21	0.26	38 690.53	0.46
38 672.79	0.34	38 682.44	0.09	38 690.68	0.46
38 672.98	0.12	38 682.71	0.18	38 690.80	0.65
38 673.50	0.83	38 682.82	0.16		

Table 3.1-3D Table of Measured Line Positions and Intensities From the $\tilde{B}\,^2A' \leftarrow \tilde{X}\,^2A'\,0^0_0$ Fluorescence Excitation Spectrum

Energy cm^{-1}	Intensity	Energy cm^{-1}	Intensity	Energy cm^{-1}	Intensity
38 691.03	0.69	38 701.06	0.92	38 713.09	0.20
38 691.21	0.73	38 701.75	0.14	38 713.75	0.74
38 691.46	0.48	38 701.96	0.32	38 713.97	0.48
38 691.74	0.93	38 702.20	0.29	38 714.25	0.35
38 692.05	0.69	38 703.04	0.20	38 714.48	0.84
38 692.29	0.65	38 703.60	0.27	38 715.02	0.51
38 692.42	0.68	38 704.27	0.18	38 715.14	0.40
38 692.73	0.97	38 704.66	0.44	38 715.39	0.99
38 693.04	1.00	38 704.95	0.27	38 715.70	0.72
38 693.37	0.55	38 705.22	0.08	38 716.16	0.19
38 693.65	0.09	38 705.74	0.07	38 716.38	0.66
38 694.33	0.10	38 705.85	0.06	38 716.67	0.16
38 694.77	0.99	38 706.09	0.06	38 717.09	0.62
38 695.04	0.49	38 706.25	0.11	38 717.23	0.37
38 695.76	0.07	38 706.81	0.32	38 718.16	0.63
38 696.24	0.05	38 707.17	0.40	38 719.00	0.51
38 696.72	0.11	38 707.68	0.14	38 720.12	0.64
38 697.25	0.70	38 708.38	0.24	38 720.40	0.44
38 697.55	0.07	38 708.64	0.22	38 720.93	0.61
38 697.75	0.17	38 708.89	0.18	38 721.26	0.06
38 698.04	0.03	38 709.44	0.20	38 721.92	0.65
38 698.38	0.05	38 710.51	0.37	38 722.10	0.40
38 698.69	0.28	38 710.66	0.18	38 722.32	0.09
38 698.89	0.28	38 711.48	0.19	38 722.61	0.17
38 699.11	0.70	38 711.77	0.32	38 722.90	0.49
38 699.46	0.40	38 712.04	0.48	38 723.34	0.62
38 700.02	0.07	38 712.24	0.32	38 724.30	0.55
38 700.36	0.79	38 712.66	0.55	38 724.46	0.53
38 700.57	0.52	38 712.91	0.32		

Table 3.1-3E Table of Measured Line Positions and Intensities From the $\tilde{B}\,^2A' \leftarrow \tilde{X}\,^2A'\,0_0^0$ Fluorescence Excitation Spectrum

Energy cm^{-1}	Intensity
38 725.03	0.54
38 725.97	0.66
38 726.21	0.55
38 726.36	0.38
38 727.13	0.51
38 727.45	0.42
38 727.88	0.49
38 728.02	0.50
38 728.52	0.15
38 728.95	0.34
38 729.17	0.34
38 729.48	0.55
38 729.92	0.15
38 730.09	0.30
38 730.64	0.34
38 730.92	0.09
38 731.14	0.19
38 731.43	0.17
38 732.10	0.16
38 732.39	0.06
38 732.73	0.28
38 733.25	0.29
38 733.82	0.11
38 734.21	0.16
38 734.82	0.16
38 734.98	0.55
38 735.46	0.20
38 735.73	0.41
38 736.03	0.21
38 736.24	0.65
38 736.54	1.00
38 736.74	0.52
38 737.05	0.36
38 737.20	0.74
38 737.31	0.50
38 737.55	0.60
38 737.79	0.45
38 738.00	0.84
38 738.53	0.60
38 738.89	0.18
38 739.47	0.07
38 740.41	0.19
38 740.65	0.26
38 741.40	0.61
38 741.80	0.36
38 742.22	0.66
38 742.33	0.60
38 742.81	0.11
38 743.77	0.27
38 744.28	0.13
38 744.61	0.33
38 744.91	0.55

Table 3.1-4A Table of Assigned Lines From the the $\tilde{B}\,^2A' \leftarrow \tilde{X}\,^2A'\,0_0^0$ Fluorescence Excitation Spectrum

Upper State				Lower State				Energy	Obs. - Calc.
N	K_a	P	J	N	K_a	P	J	cm^{-1}	cm^{-1}
1	0	-	1.5	0	0	+	0.5	38 697.75	0.00
2	0	+	1.5	1	0	-	0.5	38 699.47	0.00
2	0	+	2.5	1	0	-	1.5	38 699.47	0.01
3	0	-	2.5	2	0	+	1.5	38 700.57	-0.01
3	0	-	3.5	2	0	+	2.5	38 700.57	-0.01
4	0	+	3.5	3	0	-	2.5	38 701.09	-0.01
4	0	+	4.5	3	0	-	3.5	38 701.09	-0.02
5	0	-	4.5	4	0	+	3.5	38 701.05	0.01
5	0	-	5.5	4	0	+	4.5	38 701.05	0.02
6	0	+	5.5	5	0	-	4.5	38 700.36	-0.01
6	0	+	6.5	5	0	-	5.5	38 700.36	-0.01
7	0	-	6.5	6	0	+	5.5	38 699.11	0.00
7	0	-	7.5	6	0	+	6.5	38 699.11	0.00
8	0	+	7.5	7	0	-	6.5	38 697.25	0.00
8	0	+	8.5	7	0	-	7.5	38 697.25	0.00
9	0	-	8.5	8	0	+	7.5	38 694.77	-0.03
9	0	-	9.5	8	0	+	8.5	38 694.77	-0.02
10	0	+	9.5	9	0	-	8.5	38 691.74	0.00
10	0	+	10.5	9	0	-	9.5	38 691.74	-0.00
11	0	-	10.5	10	0	+	9.5	38 688.08	0.00
11	0	-	11.5	10	0	+	10.5	38 688.08	0.00
12	0	+	11.5	11	0	-	10.5	38 683.83	0.01
12	0	+	12.5	11	0	-	11.5	38 683.83	0.01
13	0	-	12.5	12	0	+	11.5	38 678.95	-0.01
13	0	-	13.5	12	0	+	12.5	38 678.95	-0.01
14	0	+	13.5	13	0	-	12.5	38 673.49	0.00
14	0	+	14.5	13	0	-	13.5	38 673.49	0.00
15	0	-	14.5	14	0	+	13.5	38 667.43	0.01
15	0	-	15.5	14	0	+	14.5	38 667.43	0.02
16	0	+	15.5	15	0	-	14.5	38 660.73	0.00
16	0	+	16.5	15	0	-	15.5	38 660.73	0.00
17	0	-	16.5	16	0	+	15.5	38 653.43	0.00
17	0	-	17.5	16	0	+	16.5	38 653.43	0.00
18	0	+	17.5	17	0	-	16.5	38 645.52	-0.01
18	0	+	18.5	17	0	-	17.5	38 645.52	0.00
3	0	-	2.5	4	0	+	3.5	38 680.30	-0.03
3	0	-	3.5	4	0	+	4.5	38 680.30	-0.04
4	0	+	3.5	5	0	-	4.5	38 675.08	0.00
4	0	+	4.5	5	0	-	5.5	38 675.08	0.00
5	0	-	4.5	6	0	+	5.5	38 669.25	0.01
5	0	-	5.5	6	0	+	6.5	38 669.25	0.00
6	0	+	5.5	7	0	-	6.5	38 662.82	0.01
6	0	+	6.5	7	0	-	7.5	38 662.82	0.01
7	0	-	6.5	8	0	+	7.5	38 655.79	0.02
7	0	-	7.5	8	0	+	8.5	38 655.79	0.02
8	0	+	7.5	9	0	-	8.5	38 648.15	0.00
8	0	+	8.5	9	0	-	9.5	38 648.15	0.00
9	0	-	8.5	10	0	+	9.5	38 639.93	-0.01
9	0	-	9.5	10	0	+	10.5	38 639.93	-0.01
10	0	+	9.5	11	0	-	10.5	38 631.14	0.01
10	0	+	10.5	11	0	-	11.5	38 631.14	0.00
11	0	-	10.5	12	0	+	11.5	38 621.75	0.00
11	0	-	11.5	12	0	+	12.5	38 621.75	0.01
12	0	+	11.5	13	0	-	12.5	38 611.75	0.00

Table 3.1-4B Table of Assigned Lines From the the $\tilde{B}\,^2A' \leftarrow \tilde{X}\,^2A'\,0_0^0$ Fluorescence Excitation Spectrum

Upper State				Lower State				Energy	Obs. - Calc.
N	K_a	P	J	N	K_a	P	J	cm^{-1}	cm^{-1}
12	0	+	12.5	13	0	-	13.5	38 611.75	-0.01
13	0	-	12.5	14	0	+	13.5	38 601.16	-0.01
13	0	-	13.5	14	0	+	14.5	38 601.16	-0.01
14	0	+	13.5	15	0	-	14.5	38 590.02	-0.01
14	0	+	14.5	15	0	-	15.5	38 590.02	0.02
15	0	-	14.5	16	0	+	15.5	38 578.25	0.03
15	0	-	15.5	16	0	+	16.5	38 578.25	0.04
16	0	+	15.5	17	0	-	16.5	38 565.82	-0.02
16	0	+	16.5	17	0	-	17.5	38 565.82	-0.03
17	0	-	16.5	18	0	+	17.5	38 552.85	-0.01
17	0	-	17.5	18	0	+	18.5	38 552.85	-0.02
1	1	-	1.5	0	0	+	0.5	38 712.91	0.06
2	1	+	1.5	1	0	-	0.5	38 713.97	0.00
2	1	+	2.5	1	0	-	1.5	38 714.48	0.10
3	1	-	2.5	2	0	+	1.5	38 715.03	-0.02
3	1	-	3.5	2	0	+	2.5	38 714.34	0.07
4	1	+	3.5	3	0	-	2.5	38 715.40	0.06
4	1	+	4.5	3	0	-	3.5	38 715.70	-0.03
5	1	-	4.5	4	0	+	3.5	38 715.15	-0.02
5	1	-	5.5	4	0	+	4.5	38 715.40	0.06
6	1	+	5.5	5	0	-	4.5	38 714.25	-0.01
6	1	+	6.5	5	0	-	5.5	38 714.47	0.07
7	1	-	6.5	6	0	+	5.5	38 712.67	0.05
7	1	-	7.5	6	0	+	6.5	38 712.88	0.04
8	1	+	7.5	7	0	-	6.5	38 710.51	0.03
8	1	+	8.5	7	0	-	7.5	38 710.64	0.00
9	1	-	8.5	8	0	+	7.5	38 707.68	-0.04
9	1	-	9.5	8	0	+	8.5	38 707.74	-0.06
10	1	+	9.5	9	0	-	8.5	38 704.27	-0.07
10	1	+	10.5	9	0	-	9.5	38 704.27	0.00
1	1	+	0.5	1	0	-	0.5	38 709.06	-0.05
1	1	+	1.5	1	0	-	1.5	38 710.02	-0.02
2	1	-	1.5	2	0	+	1.5	38 708.41	-0.02
2	1	-	2.5	2	0	+	2.5	38 708.93	0.08
3	1	+	2.5	3	0	-	2.5	38 706.81	-0.06
3	1	+	3.5	3	0	-	3.5	38 707.16	0.00
4	1	-	3.5	4	0	+	3.5	38 704.66	-0.04
4	1	-	4.5	4	0	+	4.5	38 704.96	0.02
5	1	+	4.5	5	0	-	4.5	38 701.97	-0.02
5	1	+	5.5	5	0	-	5.5	38 702.21	0.04
6	1	-	5.5	6	0	+	5.5	38 698.71	-0.01
6	1	-	6.5	6	0	+	6.5	38 698.87	0.00
7	1	+	6.5	7	0	-	6.5	38 695.04	0.11
7	1	+	7.5	7	0	-	7.5	38 695.04	0.02
8	1	-	7.5	8	0	+	7.5	38 690.52	0.00
8	1	-	8.5	8	0	+	8.5	38 690.61	-0.03
9	1	+	8.5	9	0	-	8.5	38 685.64	0.05
9	1	+	9.5	9	0	-	9.5	38 685.73	0.03
10	1	-	9.5	10	0	+	9.5	38 680.16	0.03
10	1	-	10.5	10	0	+	10.5	38 680.26	0.04
11	1	+	10.5	11	0	-	10.5	38 674.16	0.06
11	1	+	11.5	11	0	-	11.5	38 674.26	-0.03
12	1	-	11.5	12	0	+	11.5	38 667.64	-0.06
12	1	-	12.5	12	0	+	12.5	38 667.64	-0.03
13	1	+	12.5	13	0	-	12.5	38 660.43	0.01

Table 3.1-4C Table of Assigned Lines From the the $\tilde{B}\,^2A' \leftarrow \tilde{X}\,^2A'\,0^0_0$ Fluorescence Excitation Spectrum

Upper State				Lower State				Energy	Obs. - Calc.
N	K_a	P	J	N	K_a	P	J	cm^{-1}	cm^{-1}
13	1	+	13.5	13	0	-	13.5	38 660.57	0.06
1	1	-	0.5	2	0	+	1.5	38 704.30	0.06
1	1	-	1.5	2	0	+	2.5	38 704.26	0.08
2	1	+	1.5	3	0	-	2.5	38 700.01	0.09
2	1	+	2.5	3	0	-	3.5	38 699.47	-0.03
3	1	-	2.5	4	0	+	3.5	38 695.09	0.09
3	1	-	3.5	4	0	+	4.5	38 694.77	-0.03
4	1	+	3.5	5	0	-	4.5	38 689.64	0.02
4	1	+	4.5	5	0	-	5.5	38 689.40	0.00
5	1	-	4.5	6	0	+	5.5	38 683.36	-0.04
5	1	-	5.5	6	0	+	6.5	38 683.50	-0.02
6	1	+	5.5	7	0	-	6.5	38 676.86	0.02
6	1	+	6.5	7	0	-	7.5	38 676.62	0.16
7	1	-	6.5	8	0	+	7.5	38 669.25	-0.13
7	1	-	7.5	8	0	+	8.5	38 669.53	0.03
8	1	+	7.5	9	0	-	8.5	38 661.45	0.04
8	1	+	8.5	9	0	-	9.5	38 661.58	0.04
9	1	-	8.5	10	0	+	9.5	38 652.89	0.02
9	1	-	9.5	10	0	+	10.5	38 652.89	0.07
10	1	+	9.5	11	0	-	10.5	38 643.74	-0.07
10	1	+	10.5	11	0	-	11.5	38 643.74	-0.01
11	1	-	10.5	12	0	+	11.5	38 633.90	0.05
11	1	-	11.5	12	0	+	12.5	38 633.90	0.03
2	1	+	1.5	1	1	-	0.5	38 691.45	-0.03
2	1	-	1.5	1	1	+	0.5	38 691.45	-0.06
2	1	+	2.5	1	1	-	1.5	38 691.45	0.09
2	1	-	2.5	1	1	+	1.5	38 691.74	0.10
3	1	+	2.5	2	1	-	1.5	38 692.73	0.09
3	1	-	2.5	2	1	+	1.5	38 692.44	-0.11
3	1	+	3.5	2	1	-	2.5	38 692.73	0.02
3	1	-	3.5	2	1	+	2.5	38 692.44	0.02
4	1	+	3.5	3	1	-	2.5	38 693.04	0.11
4	1	-	3.5	3	1	+	2.5	38 693.15	-0.06
4	1	+	4.5	3	1	-	3.5	38 693.04	0.00
4	1	-	4.5	3	1	+	3.5	38 693.38	0.11
5	1	+	4.5	4	1	-	3.5	38 693.04	-0.13
5	1	-	4.5	4	1	+	3.5	38 692.82	-0.01
5	1	+	5.5	4	1	-	4.5	38 693.18	-0.08
5	1	-	5.5	4	1	+	4.5	38 693.04	0.12
6	1	+	5.5	5	1	-	4.5	38 692.11	-0.03
6	1	-	5.5	5	1	+	4.5	38 693.50	-0.03
6	1	+	6.5	5	1	-	5.5	38 692.30	0.07
6	1	-	6.5	5	1	+	5.5	38 692.66	0.05
7	1	+	6.5	6	1	-	5.5	38 691.22	-0.07
7	1	-	6.5	6	1	+	5.5	38 690.81	-0.06
7	1	+	7.5	6	1	-	6.5	38 691.46	0.10
7	1	-	7.5	6	1	+	6.5	38 691.03	0.09
8	1	+	7.5	7	1	-	6.5	38 688.98	-0.02
8	1	-	7.5	7	1	+	6.5	38 689.41	-0.05
8	1	+	8.5	7	1	-	7.5	38 689.12	0.06
8	1	-	8.5	7	1	+	7.5	38 689.64	0.13
9	1	+	8.5	8	1	-	7.5	38 686.97	-0.05
9	1	-	8.5	8	1	+	7.5	38 686.52	-0.02
9	1	+	9.5	8	1	-	8.5	38 687.16	0.10
9	1	-	9.5	8	1	+	8.5	38 686.52	-0.07
10	1	+	9.5	9	1	-	8.5	38 683.49	0.00

Table 3.1-4D Table of Assigned Lines From the the $\tilde{B}\,^2A' \leftarrow \tilde{X}\,^2A'\,0_0^0$ Fluorescence Excitation Spectrum

Upper State				Lower State				Energy	Obs. - Calc.
N	K_a	P	J	N	K_a	P	J	cm^{-1}	cm^{-1}
10	1	-	9.5	9	1	+	8.5	38 683.49	-0.05
10	1	+	10.5	9	1	-	9.5	38 683.50	-0.04
10	1	-	10.5	9	1	+	9.5	38 683.93	-0.09
11	1	+	10.5	10	1	-	9.5	38 680.29	-0.05
11	1	-	10.5	10	1	+	9.5	38 679.86	0.02
11	1	+	11.5	10	1	-	10.5	38 680.29	-0.08
11	1	-	11.5	10	1	+	10.5	38 679.85	-0.04
12	1	+	11.5	11	1	-	10.5	38 676.10	0.01
12	1	-	11.5	11	1	+	10.5	38 675.64	0.04
12	1	+	12.5	11	1	-	11.5	38 675.67	0.02
12	1	-	12.5	11	1	+	11.5	38 676.10	-0.02
13	1	+	12.5	12	1	-	11.5	38 665.48	0.11
13	1	-	12.5	12	1	+	11.5	38 665.85	0.06
13	1	+	13.5	12	1	-	12.5	38 665.25	-0.08
13	1	-	13.5	12	1	+	12.5	38 665.85	0.04

Table 3.1-5 $\tilde{X}\,{}^2A'$-State Rotational Combination Differences from the $\tilde{B}\,{}^2A' \leftarrow \tilde{X}\,{}^2A'\,0^0_0$ Band

${}^qR_0(N'')$	${}^qP_0(N'')$	N"	Δ_2F'' (cm^{-1}) Calculated ①	Δ_2F'' (cm^{-1}) Observed ②
0	2	1	8.67	8.62
1	3	2	15.47	15.47
2	4	3	20.25	20.27
3	5	4	26.03	26.01
4	6	5	31.80	31.81
5	7	6	37.57	37.54
6	8	7	43.34	43.32
7	9	8	49.10	49.10
8	10	9	54.85	54.84
9	11	10	60.60	60.60
10	12	11	66.34	66.33
11	13	12	72.07	72.08
12	14	13	77.79	77.79

① - Calculated using constants from reference (2).

② - Uncertainties ±0.04 cm^{-1} . The combination differences observed here are the average of those for the J"=N"+1/2 and J"=N"-1/2 spin components.

Figure 3.1-6 $\tilde{B}$-state 0_0^0 Molecular Constants

Constant	Value	
T_{00}	38 695.453 (3)	cm^{-1}
A'	16.039 (5)	
(B'+C')/2	1.150 61 (4)	
(B'-C')/4	0.021 57 (6)	
Δ_N	4.6 (2) $\times 10^{-6}$	
Δ_{NK}	8.3 (6) $\times 10^{-4}$	
$\kappa+3\mu$	1.32 (2)	
2κ	2.62 (2)	cm^{-1}

Values in parenthesis are the standard deviation from the rotational constant fit

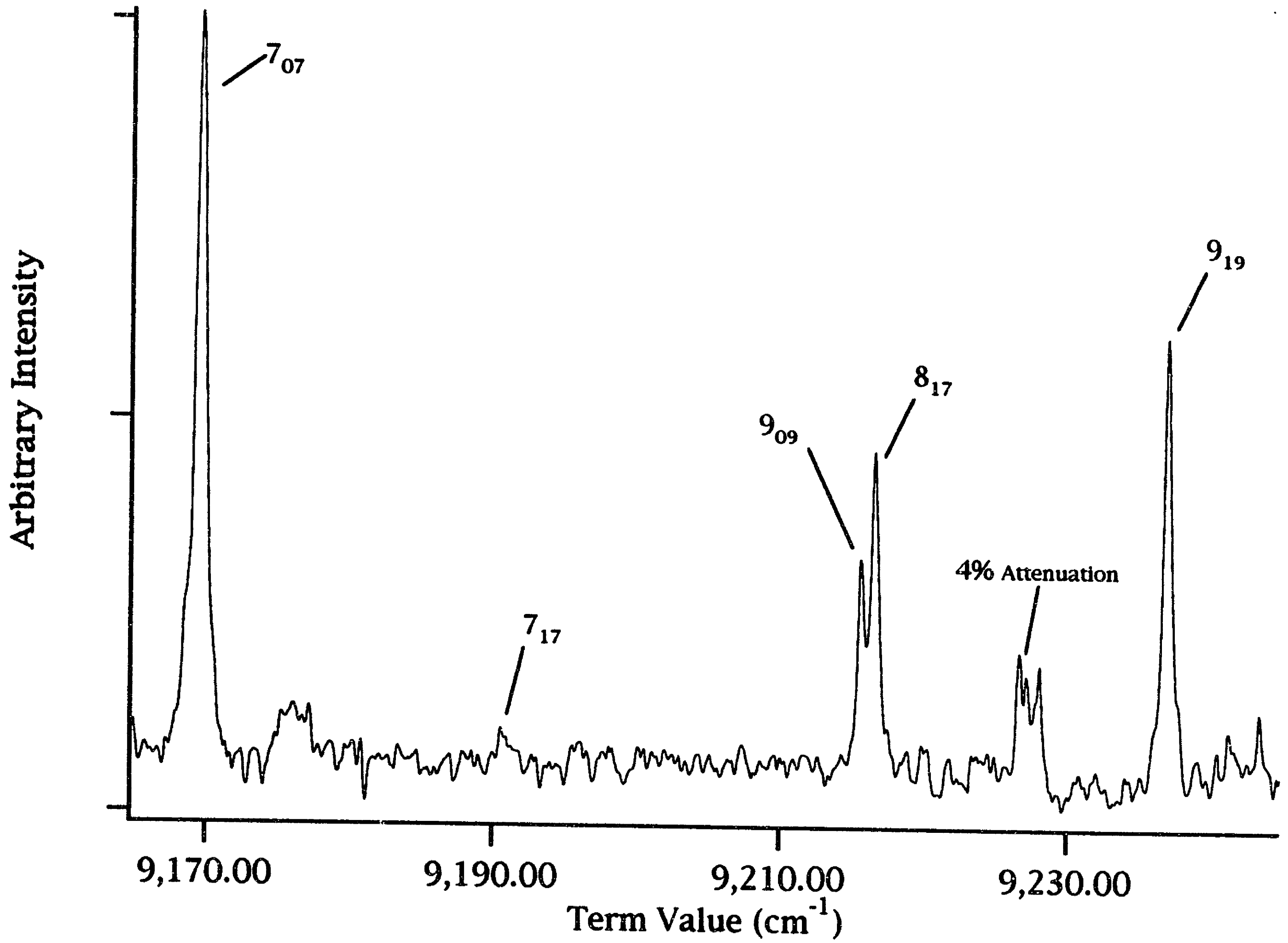

Figure 3.2-1 HCO $\tilde{B} \rightarrow \tilde{X}\ 2^0_5$ SEP Spectrum: PUMP $\tilde{B} \leftarrow \tilde{X}\ 0^0_0\ {}^qR(7_{07})$

Figure 3.2-2 Table of Measured Transitions and Widths (FWHM) from the First SEP Experiment

N''	$N''_{0}N''$		$N''_{1}N''-1$	$N''_{1}N''$	
	R-DUMP	P-DUMP	Q-DUMP	R-DUMP	P-DUMP
1	9 094.75	...	...	9 116.45	...
	(0.82)	...	...	(*)	...
2	9 100.15	...	9 122.73	9 122.51	...
	(0.72)	...	(0.87)	(0.60)	...
3	9 108.44	9 108.50	9 131.18	9 130.69	9 130.71
	(1.19*)	(0.87)	(0.72)	(0.60)	(0.72)
4	9 119.97	9 119.66	9 142.47	9 142.22	9 141.52
	(1.19*)	(0.90)	(1.19*)	(0.60)	(0.70)
5	9 133.48	9 133.45	9 156.26	9 155.36	9 155.21
	(1.02)	(0.75)	(1.19*)	(w)	(0.87)
6	9 150.16	9 150.16	9 173.50	9 171.49	9 171.57
	(0.92)	(0.67)	(0.62)	(w)	(0.67)
7	9 169.57	9 169.59	9 193.35	9 190.63	9 190.58
	(0.88)	(0.69)	(0.47)	(w)	(0.55)
8	...	9 191.58	9 215.61	...	9 212.41
	...	(0.50)	(0.50)	...	(0.57)
9	...	9 216.53	...	...	9 236.97
	...	(0.62)	...	...	(0.60)

*-Blended w-Weak ...-not measured

Figure 3.2-3 Table of $\tilde{X}\ ^2A'(0,5,0)$ Molecular Constants

Constant	Value
T_{00}	9 091.97(3) cm^{-1}
A	23.7(3)
(B+C)/2	1.384 (6)
(B-C)/4	0.0218 (6)
Δ_N	1.7(7) $x10^{-5}$ cm^{-1}

Values in parenthesis are the standard deviation from the rotational constant fit

CHAPTER 4

Results and Analysis: Second SEP Experiment

4.1 Second HCO Stimulated Emission Pumping Experiment: Spectra Recorded from a-Type PUMP Transitions $\tilde{B}\,^2A' \leftarrow \tilde{X}\,^2A'\,0_0^0\ ^qR(N_{0N})$

The second SEP apparatus (Section 2.3) allowed for the measurement of HCO SEP spectra to be performed more quickly than the first SEP apparatus (Section 2.2). The most significant difference between the two experiments was the addition of a new DUMP dye laser (Lumonics, HD-300) in the second SEP experiment. This dye laser was capable of being grating-scanned with a narrower laser linewidth (0.15cm^{-1}) than the dye laser used to produce the DUMP beam in the first SEP experiment (0.6cm^{-1}). By grating-scanning the Lumonics dye laser in the second SEP experiment, it was possible to record up to 140cm^{-1} of continuous high-resolution SEP spectrum. An example of an SEP spectrum recorded by pumping an a-type transition $\{\tilde{B}\,^2A' \leftarrow \tilde{X}\,^2A'\,0_0^0\ ^qR(N''_{0N''})$, specifically $N'' = 9\}$ is shown in Figure 4.1-1. These PUMP transitions following a-type rotational selection rules ($\Delta K_a = 0$, $\Delta K_c =$ odd) consisted of an unresolved spin-rotation doublet, thus both J' components for a given N' were populated; for example, for the transition $N' = 10 \leftarrow N'' = 9$ the two levels populated are $J' = 10.5$ and $J' = 9.5$. Table 4.1-2 summarizes all measured $\tilde{X}\,^2A'$-state rotational term values and line widths for each of the vibrational bands observed by SEP using PUMP transitions following a-type rotational selection rules. All term values are referenced to the zero point level (0, 0, 0) of the

$\tilde{X}\,^2A'$-state. A variety of different $\tilde{B}\,^2A' \leftarrow \tilde{X}\,^2A'\,0_0^0$ rotational transitions were used as PUMP transitions in the course of the SEP experiments. The frequencies for those $\tilde{B}\,^2A' \leftarrow \tilde{X}\,^2A'\,0_0^0$ transitions are listed in Table 4.1-3. The measurement of these frequencies is described in Section 3.1. Table 4.1-3 also contains a list of $\tilde{X}\,^2A'$-state rotational term values that were calculated with constants taken from Sears et al. [1,2].

A more efficient procedure was used to calibrate the DUMP dye laser frequency in the second SEP experiment than the calibration procedure used in the first SEP experiment. The slightly lower resolution of the DUMP dye laser in the second SEP experiment (lower resolution than the etalon scanning mode of the DUMP dye laser) made it difficult to use the iodine absorption spectrum as a frequency standard. Instead of the previous iodine calibration procedure, a procedure involving a monitor etalon and a neon optogalvanic lamp was employed [3,4]. The etalon fringes provided a linear frequency calibration for the SEP spectrum. The neon optogalvanic transitions provided absolute frequency calibration of the SEP spectrum.

For producing a calibrated spectrum linear in frequency, the performance of the etalon was comparable to the previous calibration scheme using an iodine absorption spectrum ($\pm 0.04\text{cm}^{-1}$ average deviation). To achieve this precision in the etalon-calibrated spectra, each recorded etalon fringe was individually fit to a Lorentzian function to obtain the fringe center. The spacings between these fringe centers were then fit to a cubic spline function to produce a relative calibration curve for the laser frequency. Even though the etalon provided a very good method of measuring relative frequencies in SEP spectra, the neon optogalvanic spectrum produced somewhat lower accuracy as an absolute frequency calibration. There were two reasons for this lower accuracy of the neon optogalvanic frequency calibration. First, no atlas exists for one-photon and two-photon optogalvanic transitions in neon at an accuracy comparable to that of the molecular iodine atlas [5]. Second, relatively few neon optogalvanic transitions were present in a single SEP scan — never more than four. Absolute frequency calibration was produced by fitting each neon optogalvanic line observed in an SEP scan to a Lorentzian function in order to determine the optogalvanic line center. The absolute frequency of the optogalvanic line was then taken from Table 4.1-4. These neon one-photon and two-photon optogalvanic transition energies, listed in Table 4.1-4, were calculated from a compilation of atomic energy levels by C. Moore [6].

An intermittent unwanted and unintended property was discovered in the data acquisition software which occasionally led to errors in the frequency calibration of SEP scans [7]. This unwanted and unintended property only became noticeable when the hard disk drive of the laboratory personal computer was nearly full. This unwanted and unintended property was caused by the operating system requiring more time to complete write requests on a nearly full hard disk. This unwanted and unintended property caused the data points of each scan to be digitized unevenly in time. To completely correct this unwanted and unintended property the laboratory's data acquisition software would need to be completely rewritten. A temporary solution to the unwanted and unintended property was to simultaneously record a linear voltage ramp during the SEP scans to provide a verification that all points were recorded uniformly in time. SEP scans that did not pass the linear voltage ramp test were discarded and measured again.

In order to determine the width and position of the observed SEP transitions, each SEP line was individually fit to a Lorentzian function: $I(\omega) = K_0 + K_1/[(\omega - K_2)^2 + K_3]$. The actual fitting was accomplished using a commercial data analysis software package, *Igor Pro* 2.0 [8]. Several examples of these fits are shown in Figure 4.1-5A through Figure 4.1-5E. These figures show the actual SEP data and the Lorentzian calculated from the fit to the data. Also shown on the same vertical scale is a plot of the difference between the actual SEP data and the calculated Lorentzian.

In the lineshape fits each point was equally weighted. This weighting scheme was used since the uncertainty for each point was taken to be a constant ($\sigma = 1$) and not the more usual value of the square root of the intensity ($\sigma = \sqrt{I(\omega)}$). This choice of weights was made because in an SEP spectrum the quantity measured is a small change in a large number of total photons observed and the square root weighting becomes effectively constant

($\sigma = \sqrt{I(\omega)} \approx \sqrt{I(\omega) - \delta}; I(\omega) >> \delta$) [9]. The major source of uncertainty comes not from the counting statistics of the photons but from the pulse to pulse fluctuations of the lasers and concentration fluctuations in the radical production.

In Table 4.1-2 the center position (K_2), the full width at half maximum (FWHM = $2 \cdot \sqrt{K_3}$) and the integrated intensity (area = $\pi \cdot K_1 / \sqrt{K_3}$) of the Lorentzian determined from the fit is reported. The uncertainty for the FWHM of each fit is also reported in Table 4.1-2. These uncertainties were estimated by first finding the RMS average value of the fit residual. Next the ratio of the amplitude for the fitted Lorentzian (Amplitude = K_1/K_3) and the RMS average for the fit residual was used to calculate a signal-to-noise ratio for that line. This estimate of the signal-to-noise ratio is approximately equal to the reciprocal of the standard deviation for the amplitude of the Lorentzian [21,22] and is also approximately equal to the square root of the more standard definition of a signal-to-noise ratio which is usually defined as the signal power divided by the noise power [23]. The signal-to-noise ratio used here typically ranged from 8 to 32 in the recorded SEP spectra. An estimate of the uncertainty in the width (FWHM) of the Lorentzian, reasonable for small uncertainties relative to the width, was then taken as the measured full width at half maximum divided by the signal-to-noise ratio.

Table 4.1-6 contains a list of molecular constants for the $\tilde{X}\,{}^2A'$-state vibrational levels observed by SEP. Tabulated are the rotational constants, linewidths (FWHM), and peak areas. In

Table 4.1-6 the uncertainties for the line widths are the standard deviation from the mean of all rotational line widths measured for that vibrational band. The procedure for the assignment of rotational quantum numbers to the observed SEP transitions and the procedure for fitting of the SEP transition frequencies to determine the rotational constants was identical to that used in the first SEP experiment, described in Section 3.2. The vibrational assignment was accomplished by comparing the observed term values with calculated values. These electronic ground state vibrational energies were calculated by taking the ground state vibrational constants determined by A. D. Sappey and D. R. Crosley [11] in dispersed fluorescence spectra and augmenting them with constants from R. N. Dixon [10,12]. The augmented set of vibrational constants was then used to calculate all vibrational energy levels below 16 000cm^{-1}. The vibrational assignments produced by this procedure did not differ significantly from those of A. D. Sappey and D. R. Crosley [11] or R. N. Dixon [10,12]. The vibrational assignments obtained this way were later confirmed by several *ab initio* calculations [13,14,15].

These vibrational assignments were also confirmed by comparing the observed and the expected changes with vibrational excitation of the A- and $\overline{B}$-rotational constants $\{\overline{B} = (B+C)/2\}$. The expected rotational constant trends are described more thoroughly below, but briefly: as the number of bending quanta (v_3) excited is increased the A-rotational constant is expected to increase, as observed in Figure 4.1-7. Contrastingly, as the number of CO stretching quanta (v_2) is increased the $\bar{B}$-rotational constant $\{\bar{B} = (B+C)/2\}$ is expected to decrease, as observed in Figure 4.1-8.

The discussion of the dependence of the $\bar{B}$-rotational constant on the number of quanta of CO stretch is more straight forward than the A-rotational constant discussion and is described first. The b- and c-inertial axes are both approximately perpendicular to the CO bond axis. The c-axis is exactly perpendicular to the CO bond axis and the b-axis is tipped ~4° toward the hydrogen [24]. Thus the $\bar{B}$-rotational constant describes rotation of the molecule perpendicular to the CO bond axis. Since the mass of the hydrogen is smaller than that of the carbon or oxygen the $\bar{B}$-rotational constant is approximately equal to the rigid-rotor expression for a rotational constant for just the carbon and oxygen. The rotational constant for a ridged rotor is defined as

$$B = \frac{\hbar}{4\pi\mu r_e^2}, \qquad (1)$$

where μ is the reduced mass and r_e is the equilibrium distance between the two masses [25]. In order to reproduce the decrease in the $\bar{B}$-rotational constant with increasing CO stretch the rotational constant for a rotor which can vibrate (stretch) must be calculated. This is accomplished by computing the expectation value of the rotational constant, $\langle B \rangle$, for each vibrational level of the rotor [25]. The calculation of the expectation value of $\langle B \rangle$ amounts to calculating the expectation value of $\frac{1}{r^2}$ for each vibrational level,

$$\langle B \rangle \propto \langle \varphi_v(r) | \frac{1}{r^2} | \varphi_v(r) \rangle . \qquad (2)$$

If the vibrational wavefunctions, $\varphi_v(r)$, in Equation (2) are wavefunctions for an anharmonic potential, then the wavefunction will have greater probability amplitude at the turning-point where the slope of the potential is less. For a CO stretching vibration this softer turning-point occurs on the longer bond length side of the potential ($r > r_e$). As the number of stretching quanta increases the probability amplitude of the wavefunction increases at the softer turning-point causing the expectation value of $\left\langle \frac{1}{r^2} \right\rangle$ to decrease. Consequently, the value of the rotational constant also decreases [25]. This is the observed trend in Figure 4.1-8.

The argument for determining the change in the A-rotational constant with bending excitation is similar to the argument for the change in the $\overline{B}$-rotational constant described above, in that the anharmonicity of the potential skews the probability amplitude of the vibrational wavefunction toward the softer turning-point. For the HCO bending vibrational mode this softer turning-point is at the nearly linear geometry [24,26,27]. Thus, as the number of quanta of bending excitation is increased, the probability amplitude of the bending wavefunction becomes increasingly skewed toward a bond angle of 180°.

The difference in the arguments for the determining the change in the $\overline{B}$- and A-rotational constants arises from slightly different procedure for calculating the expectation value for the A-rotational constant ($\langle A \rangle$), because the position variable which describes a bending vibration is the bond angle (θ) and not a length (r). The A-rotational constant describes rotations about the a-inertial axis which is approximately collinear with the CO bond. The a-inertial axis is tipped only ~4° from the CO bond [24]. The moment of inertia about the a-axis, and hence the A-rotational constant, is dominated by the distance of the hydrogen from the a-axis. It is this distance of the hydrogen from the a-axis that, when substituted into Equation (1) gives an approximate value for the A-rotational constant. Calculating the expectation value for the A-rotational constant is aided by noting that the distance of the hydrogen from the a-axis is equal to the CH-bond length times the sine of the supplement of the bond angle (θ). Similar to Equation (2) for a stretching vibration the expression for the expectation value of the A-rotational becomes

$$\langle \mathrm{A} \rangle \propto \langle \varphi_v(\theta) | \frac{1}{[\mathrm{r_{CH}} \cdot \sin(180-\theta)]^2} | \varphi_v(\theta) \rangle. \tag{3}$$

The expectation value of the A-rotational constant increases with increasing quanta of bending vibration since the probability amplitude of the bending vibrational wavefunctions shifts toward θ=180°. This increase of the A-rotational constant with increasing bending excitation is the observed trend in Figure 4.1-7.

4.2 Second HCO Stimulated Emission Pumping Experiment: Spectra Recorded from b-Type PUMP Transitions $\tilde{B}\,^2A' \leftarrow \tilde{X}\,^2A'\,0^0_0\,{}^rQ(N_{0N})$

An additional series of SEP spectra was also recorded using PUMP transitions following b-type rotational selection rules (ΔK_a = odd, ΔK_c = odd). This set of SEP spectra was recorded for two reasons. First, b-type PUMP transitions allowed the observation of $\tilde{X}\,^2A'$-state rotational levels with $K_a'' > 1$. And second, in the b-type PUMP transitions used here, the spin-rotation splitting was resolvable, thus allowing a single $\tilde{B}$-state J' level to be populated. By populating a single J' level, it was possible to measure homogeneous widths of the ground state without the inhomogeneous broadening caused by an unresolved spin-rotation splitting. An example of an SEP spectrum recorded by pumping a b-type transition $\{\tilde{B}\,^2A' \leftarrow \tilde{X}\,^2A'\,0^0_0\,{}^rQ(N''_{0N''}J'')$, specifically $N'' = 4$ and $J'' = N'' + 0.5\}$ is shown in Figure 4.2-1. Since the spin-rotation splitting was resolved in the b-type transitions, a single J' level could be populated. For example, in the transition ${}^rQ(N''_{0N''}J'')$ where $N'' = 4$ and $J'' = N'' + 0.5 = 4.5$, the single level populated is $J' = 4.5$, $N' = 4$, $K_a' = 1$, and $K_c' = 3$. Table 4.1-2 summarizes the measured $\tilde{X}\,^2A'$-state rotational term values and linewidths for each of the vibrational bands observed with SEP using PUMP transitions following b-type rotational selection rules, the levels: (0,2,0), (0,3,0), (0,3,2), (0,4,0), and (0,4,1). All term values are referenced to the zero point level (0,0,0) of the $\tilde{X}\,^2A'$-state.

A variety of different $\tilde{B}\,{}^2A' \leftarrow \tilde{X}\,{}^2A'\,0^0_0$ rotational transitions were used as PUMP transitions in the course of the SEP experiments. The frequencies for these $\tilde{B}\,{}^2A' \leftarrow \tilde{X}\,{}^2A'\,0^0_0$ transitions are listed in Table 4.1-3. The measurement of these frequencies is described in Section 3.1. Table 4.1-3 also contains a list of $\tilde{X}\,{}^2A'$-state rotational term values that were calculated with constants taken from Sears et al. [1,2].

The neon optogalvanic calibration procedure described in Section 4.1 was also used to calibrate the SEP spectra recorded with b-type PUMP transitions. The same lineshape fitting procedure as that described in Section 4.1 was used to analyze this second set of SEP spectra. Examples of these lineshape fits are shown in Figures 4.2-3A through 4.2-3F. These figures show the actual SEP spectra and the Lorentzian calculated from the fit to the spectra. Also shown on the same intensity scale is a plot of the difference between the actual spectrum and calculated Lorentzian. A comparison of the linewidths recorded in our SEP spectra with the widths obtained by other groups indicate that our linewidths are inhomogeneously power broadened [16, 17]. Table 4.2-4 contains a list of molecular constants for the $\tilde{X}\,{}^2A'$-state vibrational levels observed by SEP. These constants were determined by the same method described in Section 4.1. For comparison, Table 4.2 also lists the widths (Γ) for each vibrational level measured via a-type PUMP transitions (from Table 4.1-6).

The first thing to note is that the SEP widths measured via b-type PUMP transitions are 10-50% narrower than the corresponding width measured using a-type PUMP transitions. In effect the SEP linewidths measured using a-type PUMP transitions, where the spin rotation splitting is not resolved, are the sum of the homogeneous linewidth for a single spin-rotation component and the splitting between the two spin-rotation components, $(\Gamma_{observed} = \gamma_{J\ resolved} + \Delta_{Spin-Rot.\ Splitting})$. The inhomogeneous broadening caused by the spin-rotation splitting can be neglected when the width of the spin-rotation components and the splitting are much smaller than the laser linewidth or when the splitting is much larger than the laser linewidth and homogeneous width. The largest proportional error in the observed SEP linewidths would come for the case when both the homogeneous width and spin-rotation splitting were comparable to the laser linewidth. For this worst case, the observed error in the SEP linewidth would be 50%. In HCO, the spin-rotation splitting is comparable to the laser linewidth (see Section 3.1 and Table 4.2-4) producing a large inhomogeneous broadening.

Although, the inhomogeneous broadening by the spin-rotation could depend upon the vibrational state, this dependence is expected to be small for HCO. A comparison of the relative SEP linewidths observed for different vibrational levels is still valid. The most severe limitation for measuring narrow widths near the dissociation limit is the laser linewidth. Some possible experiments to overcome this limitation are discussed in Section 5.3.

It should be noted that, in the SEP spectra recorded from b-type PUMP transitions, an anomalously strong a-type Q-branch

($^{q}Q_{1}$) is observed. Only a single parity component of this Q-branch was observed, $^{q}Q(N''_{1\,N''}\, J'')$. This results because only a single parity component can be populated by a K_0^1 b-type PUMP transition since only a single parity component exists for all $K_a'' = 0$ levels. This type of Q-branch is expected to be extremely weak in a symmetric-top (see Figure 4.2-1 and Figure 4.2-3C). A mechanism that could possibly account for its appearance with intensity comparable to that of the a-type K_1^1 P- and R-branches in this SEP spectrum is rotational axis-switching [18,19]. The observed strength of this normally forbidden branch is consistent with the calculated axis switching angle for HCO of approximately +1.5° [20]. It would be possible to exploit the appearance of this Q-branch to determine the absolute sign of the angle the $\tilde{B}\,^2A' \rightarrow \tilde{X}\,^2A'$ transition moment makes with the inertial axis system of the molecule. The magnitude of this angle (referenced to the a-axis) was determined in Chapter 3 and the calculation is discussed in Appendix 1. The determination of the sign of the angle is also discussed in Appendix 1.

4.3 References

1. J. M. Brown, H. E. Radford, and T. J. Sears, *J. Mol. Spectrosc.* **148**, 20-37 (1991).
2. C. B. Dane, D. R. Lander, R. F. Curl, F. K. Tittel, Y. Guo, M. I. F. Ochsner, and C. B. Moore, *J. Chem. Phys.* **88**, 2121-2128 (1988).
3. A. Keller, R. Engleman and B. A. Palmer, *App. Opt.* **19**, 836-837; N. Dovichi, D. S. Moore and R. Keller, *App. Opt.* **21**, 1468-473.
4. C. J. Sansonetti, K. H. Weber, *J. Opt. Soc. Am. B*, **1**, 361-365.
5. S. Gerstenkorn and P. Luc, "Atlas du Spectre d'Absorption de la Molecule d'Iode," Paris: CNRS (1978); S. Gerstenkorn and P. Luc, *Rev. Phys. Appl.* **14**, 791-798 (1979).
6. C. E. Moore, "Atomic Energy Levels as Derived from Analyses of Optical Spectra", Vol 1, (U.S.)Washington D.C.: Nat. Stand. Ref. Data Ser., Nat. Bur. Stand (1971).
7. D. M. Watt, "Spec5.c", (Data aquisition software), Cambridge, MA: MIT (1989).
8. "Igor Pro 2.0", (Data analysis software), Lake Oswego, Oregon: Wavemetrics Inc. (1994).
9. P. R. Bevington, "Data Reduction and Error Analysis for the Physical Sciences, Ed. 1", New York: Mc Graw-Hill (1969); Chapter 6 and 8.
10. R. N. Dixon, *J. Mol. Spectrosc.* **30**, 248-252 (1969); R. N. Dixon.
11. A. D. Sappey and D. R. Crosley, *J. Chem. Phys.* **93**, 7601-7608 (1990).

12. R. N. Dixon, *Trans. Faraday Soc.* 65, 3141-3149 (1969).

13. R. N. Dixon, *J. Chem. Soc. Faraday Trans.* **88**, 2575-2586 (1992).

14. B. Gadzy and J. M. Bowman in "Adv. Mol. Vibr. and Dynamics" (J. M. Bowman and M. A. Ratner, ed. Vol. 1 B, JAI, Greenwich (1992)

15. R. Schinke, Private Comunication (1994).

16. D. W. Neyer, X. Luo, P. L. Houston, and I. Burak, *J. Chem. Phys.* **98**, 5095-5098 (1993).

17. E. Rohlfing, Private Comunication (1994).

18. G. W. Adamson, X. Zhao, and R. W. Field, *J. Mol. Spec.* 160, 11-38 (1993).

19. A. Held, B. B. Champagne, and D. W. Pratt, *J. Chem. Phys.* **95**, 8732-8743 (1991)

20. D. Jonas, Private Communication (1992).

21. W. Mendenhall, R. L. Scheaffer, and D. D. Wackerly, "Mathamatical Statistics with Applications, 3rd. Ed.", Boston:Duxbury Press, Chapter 11.

22. L. Ott, "An Introduction to Statistical Methods and Data Analysis, 3rd Ed.", Boston:PWS-Kent (1988), Chapter 12.

23. A. V. Oppenheim, A. A. Willsky, and I. T. Young, "Signals and Systems", Englewood Cliffs, NJ:Prentice-Hall (1983), Chapter 6.

24. S. W. Cho, W. L. Hase and K. N. Swamy, *J. Phys. Chem.* 94, 7371-7377 (1990).

25. C. Cohen-Tannoudji, B. Diu, and F. Laloë, "Quantum Mechanics, Volume 1", New York:John Wiley and Sons (1977), Chapter 7.

26. T. H. Dunning, *J. Chem. Phys.* **73**, 2304-2309 (1980).

27. J. M. Bowman, J. S. Bitman and L. B. Harding, *J. Chem. Phys.* **85**, 911-921 (1986).

4.4 Chapter 4 Figure and Table Captions

Figure 4.1-1 $\tilde{B}\,^2A' \rightarrow \tilde{X}\,^2A'$ $1^0_0 2^0_3 3^0_0$ SEP Spectra Recorded from the a-Type PUMP, $^qR(9_{09})$. Each line in this SEP spectrum is an unresolved spin-rotation doublet. The signal-to-noise ratio for this SEP spectrum is ~25. The polarizations of the PUMP and DUMP lasers were parallel.

Table 4.1-2 Table of Assigned Lines from the $\tilde{B}\,^2A' \rightarrow \tilde{X}\,^2A'$ $1^0_0 2^0_v 3^0_v$ SEP Spectra Recorded from $^qR(N''_{0N''})$ a-type PUMP Transitions. Tables listing PUMP transitions and rotational assignments for each of the vibrational bands observed. The assigned parity was calculated from $(-1)^{K_c}$. The term values, residuals from the rotational fit, Lorentzian linewidths, and integrated intensities are also listed.

Table 4.1-3 Table of Neon Optogalvanic Transitions Calculated from Tabulated Atomic Energy Levels. Neon Optogalvanic transitions were used to calibrate SEP spectra recorded in Chapter 4. These transition energies were calculated for one and two photon transitions from the neon atomic energy levels in Reference (6).

Table 4.1-4 Table of SEP PUMP Transitions and $\tilde{X}\,^2A'$-state Term Values. Transition energies for the various PUMP transitions used to record the SEP spectra in Chapter 4 are listed. These transitions were measured as described in Section 3.1. The ground state rotational term values were calculated with constants from Reference (1). The total energy of the $\tilde{B}$-state intermediate level is the sum of the term value and the transition energy.

Figure 4.1-5A-D Fits of SEP Line Shapes. The results of fitting each of the SEP lines observed in Figure 4.1-1 to a Lorentzian are shown. The original data, the calculated Lorentzian, and the fit residuals are plotted. The fitting function and determined parameters are also shown. Each line is labeled with the rotational level, $N''_{K''_a K''_c}$, for the $\tilde{X}\,^2A'$-state.

Table 4.1-6 Table of Molecular Constants and Widths for $\tilde{X}\,^2A'$-state Vibrational Levels. The results are from the rotational fits of the SEP spectra measured using a-type PUMP transitions. All constants have units of cm^{-1} and one sigma uncertainties are reported.

Figure 4.1-7 Dependence of the $\tilde{X}\,^2A'$-State A-Rotational Constant on number of Quanta of Bend (v_3). The A-rotational constants for vibrational levels of the $\tilde{X}\,^2A'$-state are plotted versus quanta of bend excited at constant CO stretch excitation.

Figure 4.1-8 Vibrational Dependence of the (B+C)/2 Rotational Constants on CO stretch (v_2). The (B+C)/2 rotational constants for vibrational levels of the $\tilde{X}\,^2A'$-state are plotted versus number of quanta of CO stretch excited at constant bend excitation.

Figure 4.2-1 The $\tilde{B}\,^2A' \rightarrow \tilde{X}\,^2A'$ $1^0_0 2^0_4 3^0_0$ SEP Spectrum from the b-Type PUMP $\tilde{B}\,^2A' \leftarrow \tilde{X}\,^2A'$ 0^0_0 $^rQ(4_{04}\ 4.5)$ [$N''_{K''_a K''_c}$ J'']. Each line in this SEP spectrum is a single $\Delta J = 0$ transition of a resolved spin-rotation doublet. The signal-to-noise ratio for this SEP spectrum is ~28. The polarizations of the PUMP and DUMP lasers were parallel.

Table 4.2-2 Table of Assigned Lines from the $\tilde{B}\,^2A' \rightarrow \tilde{X}\,^2A'$ $1^0_0 2^0_v 3^0_v$ SEP Spectra Recorded from b-Type $^rQ(N_{0N})$ PUMP Transitions. Tables listing PUMP transitions and rotational assignments for each of the vibrational bands observed. The assigned parity was calculated from $(-1)^{K_c}$. The term energies, residuals from the rotational fit, Lorentzian linewidth and the integrated intensities are also listed.

Figure 4.2-3 Fitting of Line Shapes, $K_a''=0, 1, 2$. The results of fitting to a Lorentzian each of the SEP lines observed in Figure 4.1-1 are shown. The original data, the calculated Lorentzian and the fit residuals are plotted on the same scale. The fitting function and determined parameters are also shown. Each line is labeled with the rotational level, $N''_{K_a''K_c''}\,J''$, for the $\tilde{X}\,^2A'$-state.

Table 4.2-4 Table of Molecular Constants, Including Spin-Rotation, and Widths for $\tilde{X}\,^2A'$-state Vibrational Levels. The results from the rotational fits of the SEP spectra measured using b-type PUMP transitions. All constants have units of cm^{-1} and the one sigma uncertainties reported. Constants from Figure 4.1-6 are included for comparison.

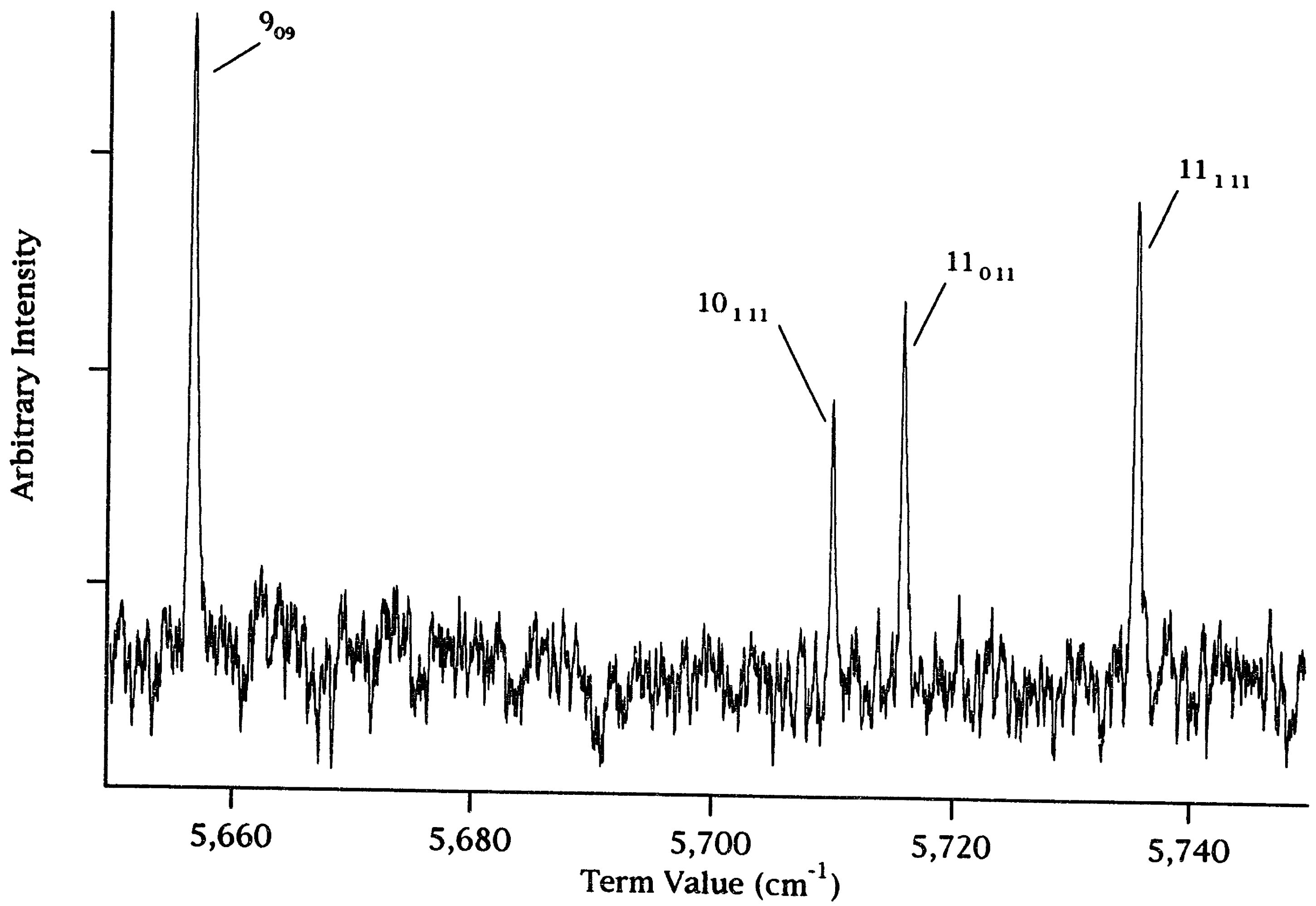

Figure 4.1-1 HCO $\tilde{B} \rightarrow \tilde{X}\ 2_3^0$ SEP Spectrum From the PUMP $\tilde{B} \leftarrow \tilde{X}\ 0_0^0\ {}^qR(9_{09})$

Table 4.1-2 Observed Transitions to $\tilde{X}\ ^2A'$ (0,1,2)

$^qR(N_{0N})$ PUMP	N"	K_a"	Parity	Term Value	Obs.-Calc.	Γ FWHM	Intensity (Area)	Notes
7_{07}	2	0	1	4,007.84	-0.03	0.48 (6)	878	
7_{07}	4	0	1	4,027.94	-0.03	0.4 (1)	300	
7_{07}	5	0	-1	4,042.35	0.03	0.46 (4)	1100	
7_{07}	7	0	-1	4,079.64	0.03	0.6 (1)	700	
8_{08}	8	0	1	4,102.48	-0.06	0.58 (6)	1100	
8_{08}	9	0	-1	4,128.37	0.03	0.55 (9)	760	
8_{08}	10	0	1	4,157.00	0.01	0.3 (2)	140	
9_{09}	11	0	-1	4,188.51	0.02	0.6 (1)	740	
9_{09}	4	1	1	4,055.10	0.04	0.5 (2)	413	
9_{09}	7	1	-1	4,105.72	0.03	0.46 (6)	830	
9_{09}	8	1	-1	4,132.41	0.06	0.3 (1)	186	
6_{06}	9	1	-1	4,153.50	0.00	0.64 (7)	1300	
6_{06}	9	1	1	4,158.64	-0.06	0.56 (9)	780	
6_{06}	10	1	1	4,181.53	-0.09	0.49 (8)	660	
6_{06}	11	1	-1	4,212.58	0.03	0.55 (7)	1014	

Units for Term Values, Residuals and Width are in cm^{-1}
and for Intensity is arbitrary.

Table 4.1-2 Observed Transitions to $\tilde{X}\ {}^2A'$ (0,1,3)

${}^{q}R(N_{0N})$ PUMP	N"	K_a"	Par-ity	Term Value	Obs.-Calc.	Γ FWHM	Intensity (Area)	Notes
3_{03}&4_{04}	5	0	-1	5,074.64	-0.02	0.7 (2)	740	Blend
3_{03}&4_{04}	6	0	1	5,091.85	-0.01	0.7 (2)	740	Blend
7_{07}	7	0	-1	5,111.90	-0.02	0.53 (7)	920	
6_{06}	8	0	1	5,134.84	0.01	0.6 (1)	710	
7_{07}	9	0	-1	5,160.61	0.02	0.53 (8)	750	
8_{08}	10	0	1	5,189.17	-0.04	0.5 (1)	620	
5_{05}	7	1	-1	5,141.08	0.02	0.6 (1)	600	
6_{06}	7	1	1	5,144.86	0.01	0.3 (2)	135	
7_{07}	8	1	-1	5,168.34	0.01	0.6 (2)	250	
6_{06}	8	1	1	5,163.46	-0.00	0.54 (7)	980	
7_{07}	9	1	-1	5,188.64	-0.01	0.59 (6)	1200	
8_{08}	9	1	1	5,194.73	-0.01	0.5 (1)	360	
8_{08}	10	1	1	5,216.65	-0.00	0.64 (8)	1100	

Units for Term Values, Residuals and Width are in cm^{-1} and for Intensity is arbitrary.

Table 4.1-2 Observed Transitions to $\tilde{X}\ ^2A'$ (0,2,0)

$^qR(N_{0N})$ PUMP	N"	K_a"	Par-ity	Term Value	Obs.-Calc.	Γ FWHM	Intensity (Area)	Notes
202	2	0	1	3,719.89	-0.04	0.73 (7)	1200	
202	4	0	1	3,739.82	-0.03	0.56 (5)	870	
505	5	0	-1	3,754.05	-0.02	0.64 (6)	1700	
505	7	0	-1	3,791.03	-0.00	0.69 (5)	1400	
808	8	0	1	3,813.73	-0.04	0.54 (4)	1100	
707	9	0	-1	3,839.43	0.08	0.74 (8)	750	
808	10	0	1	3,867.73	-0.02	0.6 (1)	633	
202	3	1	1	3,751.49	0.04	0.6 (1)	352	
202	4	1	1	3,762.15	0.05	0.70 (9)	626	
505	6	1	-1	3,794.75	-0.06	0.69 (9)	789	
505	7	1	-1	3,812.49	0.00	0.64 (7)	1600	
707	9	1	-1	3,860.10	0.04	0.63 (7)	998	
808	10	1	1	3,887.99	-0.06	0.57 (9)	633	

Units for Term Values, Residuals and Width are in cm^{-1}
and for Intensity is arbitrary.

Table 4.1-2 Observed Transitions to $\tilde{X}\ ^2A'$ (0,2,1)

$^qR(N_{0N})$ PUMP	N"	K_a"	Parity	Term Value	Obs.-Calc.	Γ FWHM	Intensity (Area)	Notes
5_{05}	5	0	-1	4 866.90	-0.04	0.87 (8)	3400	
6_{06}	6	0	1	4,883.97	-0.03	0.81 (8)	3100	
7_{07}	7	0	-1	4,903.86	-0.04	0.97 (8)	4200	
8_{08}	8	0	1	4,926.67	0.04	0.54 (6)	2000	
9_{09}	9	0	-1	4,952.27	0.07	1.00 (1)	4000	
10_{010}	10	0	1	4,980.57	-0.03	0.69 (6)	3000	
9_{09}	11	0	-1	5,011.87	0.04	0.70 (8)	3000	
10_{010}	12	0	1	5,045.88	-0.00	0.70 (1)	2300	
5_{05}	6	1	-1	4,909.92	-0.02	0.62 (1)	1200	
6_{06}	7	1	1	4,930.20	-0.01	0.60 (2)	1000	
7_{07}	8	1	-1	4,953.45	0.07	0.42 (8)	1100	
6_{06}	8	1	1	4,949.64	-0.02	0.70 (1)	2400	
7_{07}	9	1	-1	4,974.86	0.06	0.83 (6)	4100	
9_{09}	10	1	-1	5,008.44	0.03	0.40 (1)	650	
9_{09}	11	1	-1	5,033.48	0.05	0.59 (6)	2700	
10_{010}	11	1	1	5,040.18	-0.07	0.40 (1)	580	
10_{010}	12	1	1	5,066.85	-0.08	0.74 (8)	3100	

Units for Term Values, Residuals and Width are in cm^{-1} and for Intensity is arbitrary.

Table 4.1-2 Observed Transitions to $\tilde{X}\ ^2A'$ (0,2,2)

$^qR(N_{0N})$ PUMP	N"	K_a"	Par-ity	Term Value	Obs.-Calc.	Γ FWHM	Intensity (Area)	Notes
5_{05}	5	0	-1	5,758.41	0.02	0.46 (6)	1200	
6_{06}	6	0	1	5,775.44	0.00	0.50 (5)	1600	
7_{07}	7	0	-1	5,795.31	-0.01	0.46 (5)	1800	
9_{09}	9	0	-1	5,843.57	0.00	0.48 (6)	1200	
9_{09}	11	0	-1	5,903.11	-0.02	0.4 (1)	380	
5_{05}	7	1	-1	5,821.11	0.04	0.28 (5)	602	
6_{06}	7	1	1	5,824.26	-0.07	0.8 (2)	690	
7_{07}	8	1	-1	5,847.60	0.07	0.4 (1)	400	
6_{06}	8	1	1	5,843.32	-0.02	0.40 (8)	610	
9_{09}	9	1	-1	5,868.39	-0.01	0.43 (7)	400	
9_{09}	11	1	-1	5,926.85	0.01	0.34 (7)	540	

Units for Term Values, Residuals and Width are in cm^{-1}
and for Intensity is arbitrary.

Table 4.1-2 Observed Transitions to $\tilde{X}\ ^2A'$ (0,2,3)

$^qR(N_{0N})$ PUMP	N"	K_a"	Par-ity	Term Value	Obs.-Calc.	Γ FWHM	Intensity (Area)	Notes
5_{05}	5	0	-1	6,903.85	0.00	0.67 (7)	520	
6_{06}	6	0	1	6,920.91	0.02	0.54 (6)	620	
7_{07}	7	0	-1	6,940.76	-0.00	0.64 (5)	1200	
8_{08}	8	0	1	6,963.47	-0.00	0.66 (7)	1100	
9_{09}	9	0	-1	6,989.01	-0.01	1.0 (1)	700	
5_{05}	7	1	-1	6,969.46	-0.01	0.8 (1)	600	
6_{06}	7	1	1	6,973.02	0.01	0.7 (2)	210	
6_{06}	8	1	1	6,991.78	0.08	0.5 (2)	260	
7_{07}	9	1	-1	7,016.58	-0.13	0.61 (7)	500	
9_{09}	11	1	-1	7,075.09	0.05	0.8 (2)	320	

Units for Term Values, Residuals and Width are in cm^{-1}
and for Intensity is arbitrary.

Table 4.1-2 Observed Transitions to $\tilde{X}\ {}^{2}A'$ (0,3,0)

${}^{q}R(N_{0N})$ PUMP	N"	K_a"	Par-ity	Term Value	Obs.-Calc.	Γ FWHM	Intensity (Area)	Notes
5_{05}	5	0	-1	5,572.14	0.02	0.63 (4)	2300	
6_{06}	6	0	1	5,589.01	0.00	0.52 (3)	1900	
7_{07}	7	0	-1	5,608.69	-0.03	0.41 (4)	930	
8_{08}	8	0	1	5,631.29	0.03	0.55 (5)	1300	
9_{09}	9	0	-1	5,656.62	0.02	0.53 (5)	1500	
8_{08}	10	0	1	5,684.66	-0.09	0.7 (1)	910	
9_{09}	11	0	-1	5,715.71	0.01	0.51 (8)	730	
5_{05}	6	1	-1	5,612.51	-0.05	0.41 (5)	740	
5_{05}	7	1	-1	5,630.07	-0.02	0.47 (5)	1560	
6_{06}	7	1	1	5,632.61	0.03	0.58 (4)	1100	
6_{06}	8	1	1	5,652.27	0.02	0.56 (3)	2100	
7_{07}	9	1	-1	5,677.17	-0.01	0.38 (6)	583	
8_{08}	9	1	1	5,681.12	-0.08	0.5 (2)	300	
9_{09}	10	1	-1	5,709.89	0.07	0.35 (8)	380	
8_{08}	10	1	1	5,704.98	0.06	0.58 (8)	901	
9_{09}	11	1	-1	5,735.40	-0.03	0.57 (6)	1100	

Units for Term Values, Residuals and Width are in cm^{-1}
and for Intensity is arbitrary.

Table 4.1-2 Observed Transitions to $\tilde{X}\ {}^2A'$ (0,3,1)

$^{q}R(N_{0N})$ PUMP	N"	K_a"	Par-ity	Term Value	Obs.-Calc.	Γ FWHM	Intensity (Area)	Notes
5_{05}	5	0	-1	6,639.96	0.01	1.10 (8)	2300	
6_{06}	6	0	1	6,656.87	0.01	0.93 (4)	2500	
7_{07}	7	0	-1	6,676.55	-0.03	0.95 (6)	2300	
8_{08}	8	0	1	6,699.07	-0.05	1.00 (5)	2500	
9_{09}	9	0	-1	6,724.56	0.10	0.84 (4)	1900	
8_{08}	10	0	1	6,752.59	-0.02	0.85 (4)	1700	
9_{09}	11	0	-1	6,783.53	-0.03	0.78 (5)	1200	
5_{05}	6	1	-1	6,682.50	0.02	0.9 (1)	640	
5_{05}	7	1	-1	6,699.67	-0.05	0.92 (5)	1400	
6_{06}	7	1	1	6,702.64	0.06	0.66 (7)	330	
6_{06}	8	1	1	6,721.87	-0.00	0.86 (6)	1600	
8_{08}	9	1	1	6,751.29	-0.09	0.60 (8)	590	
9_{09}	10	1	-1	6,780.11	0.04	0.81 (7)	740	
8_{08}	10	1	1	6,774.42	-0.05	0.85 (7)	1700	
9_{09}	11	1	-1	6,804.98	0.07	0.99 (5)	1900	

Units for Term Values, Residuals and Width are in cm^{-1}
and for Intensity is arbitrary.

Table 4.1-2 Observed Transitions to $\tilde{X}\ ^2A'$ (0,3,2)

${}^qR(N_{0N})$ PUMP	N"	K_a"	Par-ity	Term Value	Obs.-Calc.	Γ FWHM	Intensity (Area)	Notes
5_{05}	5	0	-1	7,686.01	-0.00	0.66 (7)	770	
6_{06}	6	0	1	7,702.85	-0.05	0.59 (5)	730	
7_{07}	7	0	-1	7,722.68	0.06	0.75 (7)	940	
7_{07}	9	0	-1	7,770.54	0.08	0.64 (6)	600	
9_{09}	11	0	-1	7,829.43	-0.08	0.9 (1)	830	
5_{05}	7	1	-1	7,747.95	-0.00	0.49 (6)	460	
6_{06}	7	1	1	7,751.08	-0.07	0.5 (1)	230	
7_{07}	8	1	-1	7,774.22	0.07	0.8 (2)	350	
6_{06}	8	1	1	7,770.02	-0.02	0.62 (6)	550	
7_{07}	9	1	-1	7,794.92	0.04	0.75 (7)	990	
10_{010}	10	1	1	7,822.39	-0.09	0.9 (1)	390	
9_{09}	11	1	-1	7,852.92	0.08	0.8 (1)	960	

Units for Term Values, Residuals and Width are in cm^{-1}
and for Intensity is arbitrary.

Table 4.1-2 Observed Transitions to $\tilde{X}\ ^2A'$ (0,4,0)

$^qR(N_{0N})$ PUMP	N"	K_a"	Par-ity	Term Value	Obs.-Calc.	Γ FWHM	Intensity (Area)	Notes
5_{05}	5	0	-1	7,365.26	-0.06	0.72 (4)	1200	
6_{06}	6	0	1	7,382.08	0.01	0.67 (5)	990	
7_{07}	7	0	-1	7,401.63	0.02	0.82 (6)	1300	
8_{08}	8	0	1	7,423.91	-0.02	0.68 (6)	780	
9_{09}	9	0	-1	7,449.06	0.01	0.65 (4)	1000	
8_{08}	10	0	1	7,476.91	-0.02	0.45 (6)	380	
9_{09}	11	0	-1	7,507.63	0.03	0.6 (1)	440	
5_{05}	7	1	-1	7,422.80	-0.00	0.80 (7)	860	
6_{06}	7	1	1	7,425.36	0.03	1.0 (1)	780	
6_{06}	8	1	1	7,444.82	0.04	0.61 (7)	630	
7_{07}	9	1	-1	7,469.52	0.01	0.67 (9)	530	
9_{09}	10	1	-1	7,501.89	-0.06	0.4 (1)	150	
8_{08}	10	1	1	7,496.98	-0.00	0.45 (9)	380	
9_{09}	11	1	-1	7,527.14	-0.05	0.65 (6)	740	

Units for Term Values, Residuals and Width are in cm^{-1} and for Intensity is arbitrary.

Table 4.1-2 Observed Transitions to $\tilde{X}\ ^2A'$ (0,4,1)

${}^qR(N_{0N})$ PUMP	N"	K_a"	Parity	Term Value	Obs.-Calc.	Γ FWHM	Intensity (Area)	Notes
2_{02}	2	0	1	8,398.80	-0.30	2.8 (3)	1200	
2_{02}	4	0	1	8,418.73	0.03	2.3 (3)	960	
5_{05}	5	0	-1	8,432.64	-0.04	2.9 (3)	2400	
6_{06}	6	0	1	8,449.43	-0.02	2.0 (2)	2100	
7_{07}	7	0	-1	8,469.07	0.05	2.1 (2)	1830	
6_{06}	8	0	1	8,491.35	-0.03	1.9 (3)	1300	
7_{07}	9	0	-1	8,516.52	0.01	1.3 (2)	600	
9_{09}	11	0	-1	8,575.14	0.00	2.7 (4)	1400	
5_{05}	7	1	-1	8,491.21	-0.20	1.7 (1)	1200	
6_{06}	8	1	1	8,513.33	-0.01	1.8 (2)	1200	
7_{07}	9	1	-1	8,537.90	-0.10	1.5 (2)	890	
9_{09}	11	1	-1	8,595.64	0.11	1.7 (2)	1400	

Units for Term Values, Residuals and Width are in cm^{-1} and for Intensity is arbitrary.

Table 4.1-2 Observed Transitions to $\tilde{X}\ ^2A'$ (0,4,3)

$^qR(N_{0N})$ PUMP	N"	K_a"	Par-ity	Term Value	Obs.-Calc.	Γ FWHM	Intensity (Area)	Notes
2_{02}	2	0	1	10,457.11	0.21	1.8 (1)	3200	
1_{01}	3	0	-1	10,465.17	-0.11	2.3 (1)	2400	
2_{02}	4	0	1	10,476.80	0.34	2.2 (1)	2900	
5_{05}	5	0	-1	10,490.19	-0.23	1.79 (8)	5200	
6_{06}	6	0	1	10,507.17	-0.02	2.5 (1)	5200	
7_{07}	7	0	-1	10,526.45	-0.28	2.0 (1)	5678	
6_{06}	8	0	1	10,549.07	-0.00	1.7 (3)	3400	
9_{09}	9	0	-1	10,574.43	0.25	2.0 (2)	4700	
10_{010}	10	0	1	10,602.43	0.34	1.8 (3)	3600	
9_{09}	11	0	-1	10,632.75	-0.01	2.0 (2)	1800	
10_{010}	12	0	1	10,666.35	0.14	1.7 (1)	1600	
5_{05}	6	1	-1	10,537.09	0.00	1.1 (2)	560	
5_{05}	7	1	-1	10,553.99	0.04	1.8 (1)	3200	
6_{06}	8	1	1	10,575.98	0.11	1.8 (2)	2100	
7_{07}	9	1	-1	10,600.37	-0.15	2.0 (1)	3900	
8_{08}	10	1	1	10,627.91	-0.00	2.1 (3)	1400	
9_{09}	11	1	-1	10,658.04	0.00	1.9 (1)	3100	

Units for Term Values, Residuals and Width are in cm^{-1}
and for Intensity is arbitrary.

Table 4.1-2 Observed Transitions to $\tilde{X}\ ^2A'$ (0,5,1)

${}^qR(N_{0N})$ PUMP	N"	K_a"	Par-ity	Term Value	Obs.-Calc.	Γ FWHM	Intensity (Area)	Notes
7_{07}	7	0	-1	10,229.14	-0.01	3.0 (1)	9500	
9_{09}	9	0	-1	10,276.52	0.27	2.5 (1)	6400	
7_{07}	9	1	-1	10,297.98	-0.03	2.6 (1)	7200	
8_{08}	8	0	1	10,251.45	0.13	2.7 (1)	8500	
8_{08}	10	0	1	10,303.52	-0.43	3.6 (2)	8100	blend
8_{08}	9	1	1	10,303.52	0.06	3.6 (2)	8100	blend
8_{08}	10	1	1	10,325.18	0.03	2.2 (1)	5300	
9_{09}	11	1	-1	10,355.17	0.18	3.2 (1)	8400	
6_{06}	6	0	1	10,209.78	0.04	2.24 (8)	7100	
6_{06}	8	1	1	10,273.47	-0.11	2.5 (1)	5600	

Units for Term Values, Residuals and Width are in cm^{-1}
and for Intensity is arbitrary.

Table 4.1-2 Observed Transitions to $\tilde{X}\ ^2A'$ (0,6,0)

$^qR(N_{0N})$ PUMP	N"	K_a"	Par-ity	Term Value	Obs.-Calc.	Γ FWHM	Intensity (Area)	Notes
7_{07}	7	0	-1	10,912.89	0.05	1.84 (7)	6600	
7_{07}	9	0	-1	10,959.24	-0.18	1.89 (7)	7400	
7_{07}	7	1	-1	10,933.72	-0.01	1.5 (5)	650	
7_{07}	9	1	-1	10,979.56	-0.07	1.80 (9)	5300	
8_{08}	8	0	1	10,934.98	0.22	2.1 (1)	5300	
8_{08}	10	0	1	10,986.70	-0.11	1.8 (1)	3800	
8_{08}	10	1	1	11,006.68	0.05	1.9 (1)	3700	
9_{09}	9	0	-1	10,959.51	0.10	1.31 (6)	4500	
9_{09}	11	0	-1	11,016.88	-0.05	1.50 (9)	3400	
9_{09}	10	1	-1	11,011.41	0.13	1.2 (2)	910	
9_{09}	11	1	-1	11,036.39	0.07	1.7 (1)	4300	
6_{06}	6	0	1	10,893.75	0.11	2.0 (1)	4500	
6_{06}	8	0	1	10,934.62	-0.14	1.20 (6)	3400	
6_{06}	7	1	1	10,935.94	-0.16	1.8 (1)	3200	
6_{06}	8	1	1	10,955.31	-0.02	1.42 (8)	3900	

Units for Term Values, Residuals and Width are in cm^{-1}
and for Intensity is arbitrary.

Table 4.1-3 Table of PUMP Transition Energies and $\tilde{X}\,^2A'$-State Term Values

PUMP Transition	Transition Energy	$\tilde{X}\,^2A'$-State Term Value
${}^rQ(2_{02}\ 2.5)$	38 708.41 cm^{-1}	8.682 cm^{-1}
${}^rQ(3_{03}\ 3.5)$	38 706.81	17.360
${}^rQ(4_{04}\ 4.5)$	38 704.66	28.928
${}^rQ(5_{05}\ 5.5)$	38 701.97	43.385
${}^rQ(2_{02}\ 1.5)$	38 708.93	8.674
${}^rQ(3_{03}\ 2.5)$	38 707.16	17.349
${}^rQ(4_{04}\ 3.5)$	38 704.96	28.914
${}^rQ(5_{05}\ 4.5)$	38 702.21	43.368
${}^qR(0_{00})$	38 697.75	0.000
${}^qR(1_{01})$	38 699.47	2.893
${}^qR(2_{02})$	38 700.57	8.678
${}^qR(3_{03})$	38 701.09	17.354
${}^qR(4_{04})$	38 701.05	28.921
${}^qR(5_{05})$	38 700.36	43.376
${}^qR(6_{06})$	38 699.11	60.718
${}^qR(7_{07})$	38 697.25	80.945
${}^qR(8_{08})$	38 694.77	104.053
${}^qR(9_{09})$	38 691.74	130.041
${}^qR(10_{0\,10})$	38 688.08	158.903

Table 4.1-4 Table of Neon Optogalvanic Transitions Calculated from Atomic Energy Levels from Reference 6

12 042.623 cm^{-1}	12 044.413	12 092.796	12 094.317	12 104.123	12 119.821
12 287.066	12 298.393	12 314.091	12 369.076	12 585.957	12 595.763
12 611.461	12 726.944	12 753.138	12 942.059	13 251.844	13 266.388
13 349.476	13 378.835	13 439.155	13 798.509	13 935.511	14 162.198
14 177.896	14 215.956	14 232.881	14 427.151	14 789.731	14 883.402
14 969.798	14 995.365	15 028.721	15 149.743	15 302.960	15 364.944
15 512.323	15 615.210	15 662.306	15 739.093	15 782.381	15 798.016
15 834.237	15 856.584	15 884.412	15 953.481	16 003.963	16 079.761
16 088.575	16 109.566	16 116.853	16 142.636	16 153.067	16 171.144
16 190.171	16 219.822	16 274.031	16 312.835	16 399.231	16 458.154
16 484.758	16 534.933	16 579.176	16 659.500	16 695.714	16 730.282
16 732.818	16 758.501	16 769.309	16 816.678	16 890.331	16 905.406
16 926.029	16 936.471	16 937.397	16 996.623	17 022.867	17 035.650
17 082.027	17 176.923	17 202.776	17 223.399	17 343.007	17 354.535
17 391.639	17 480.044	17 570.398	17 655.010	17 673.388	17 686.171
17 971.684	18 049.937	18 066.158	18 195.256	18 348.563	18 398.738
18 450.001	18 470.127	18 511.460	18 571.023	18 599.586	18 608.805
18 651.507	18 689.189	18 709.893	18 717.575	18 753.789	18 769.211
18 845.777	18 869.134	18 933.827	18 955.530		

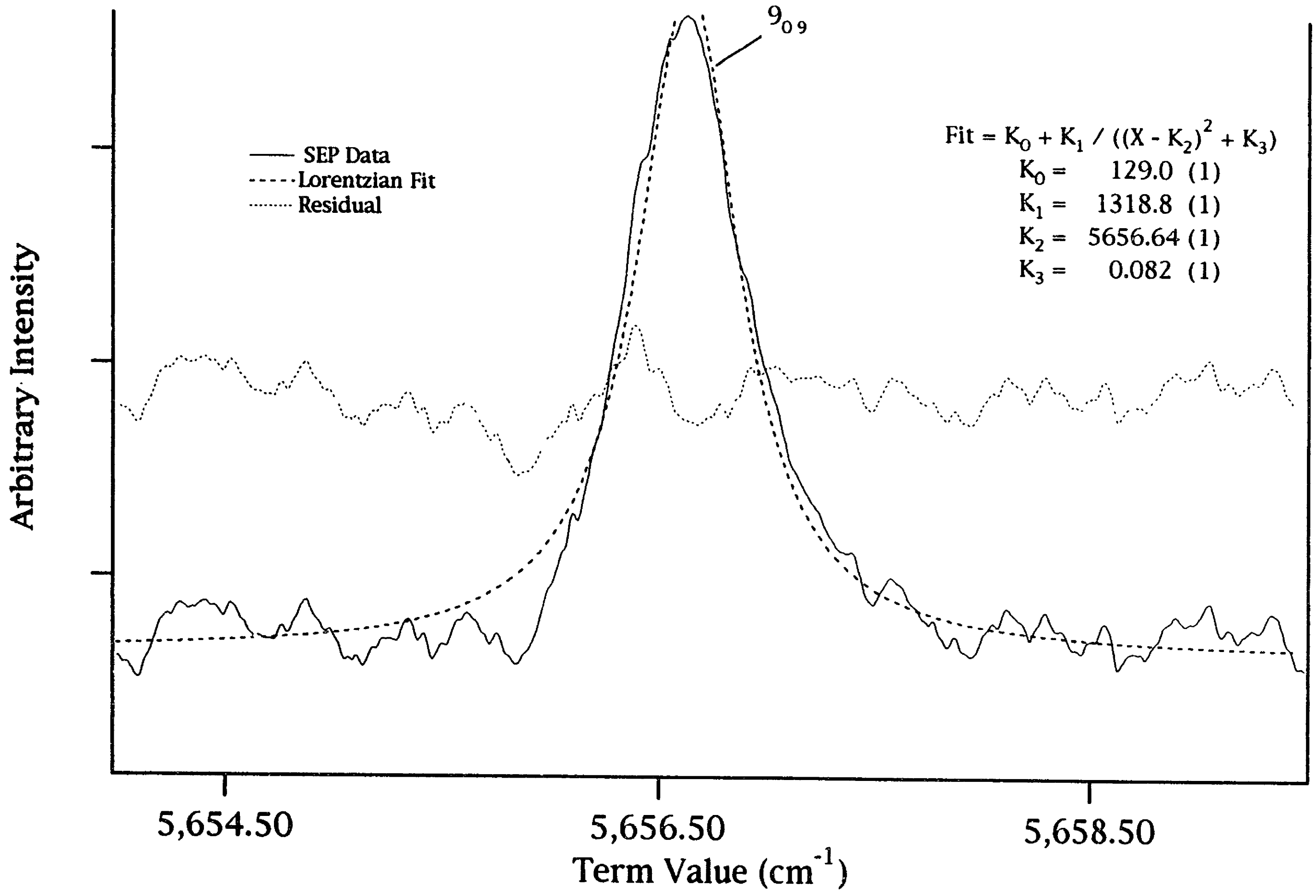

Figure 4.1-5A Line Shape Fit: HCO $\tilde{B} \rightarrow \tilde{X}\ 2_3^0$ SEP Spectrum From the PUMP $\tilde{B} \leftarrow \tilde{X}\ 0_0^0\ {}^qR(9_{09})$

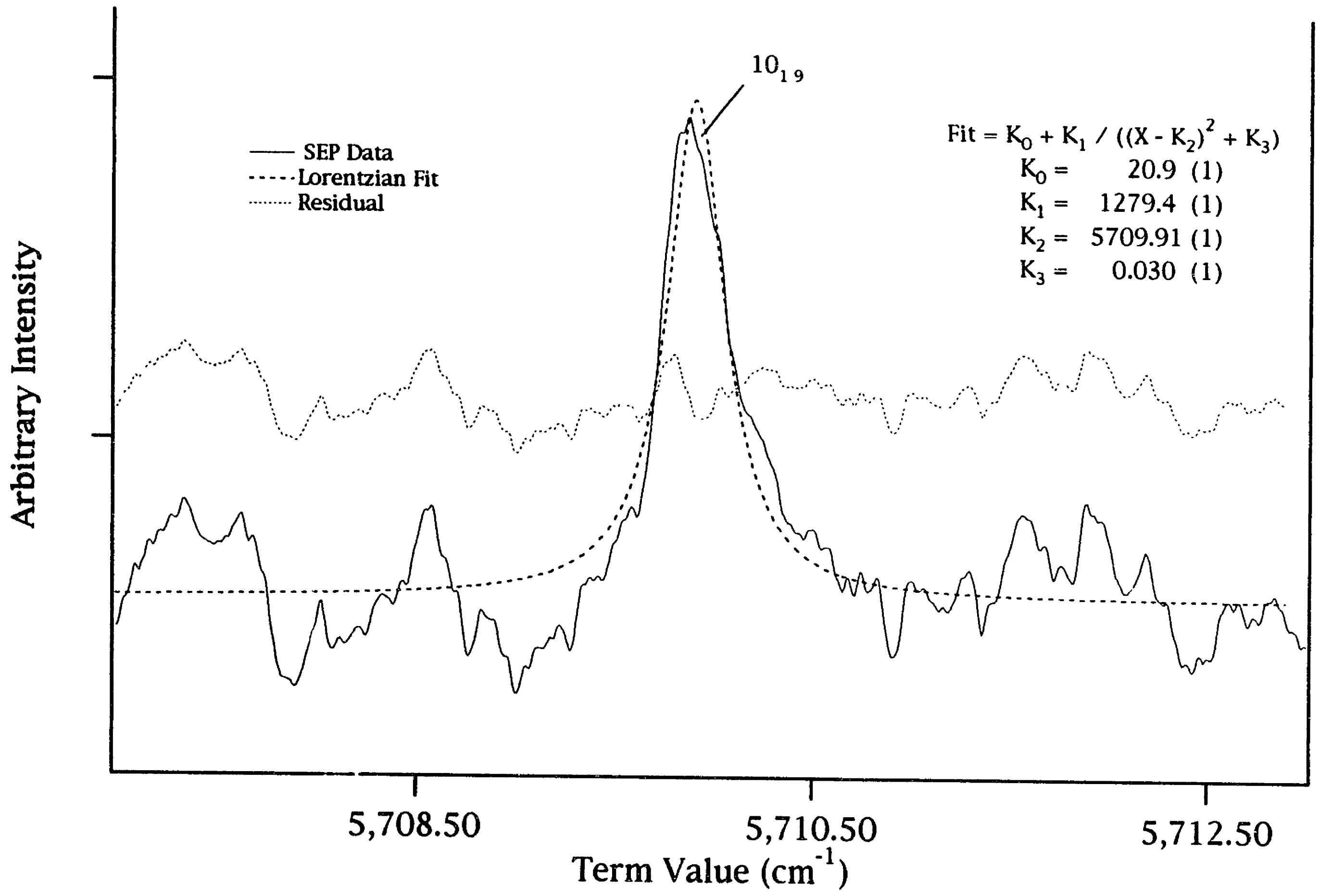

Figure 4.1-5B Line Shape Fit: HCO $\tilde{B} \rightarrow \tilde{X}\ 2_3^0$ SEP Spectrum
From the PUMP $\tilde{B} \leftarrow \tilde{X}\ 0_0^0\ {}^{q}R(9_{09})$

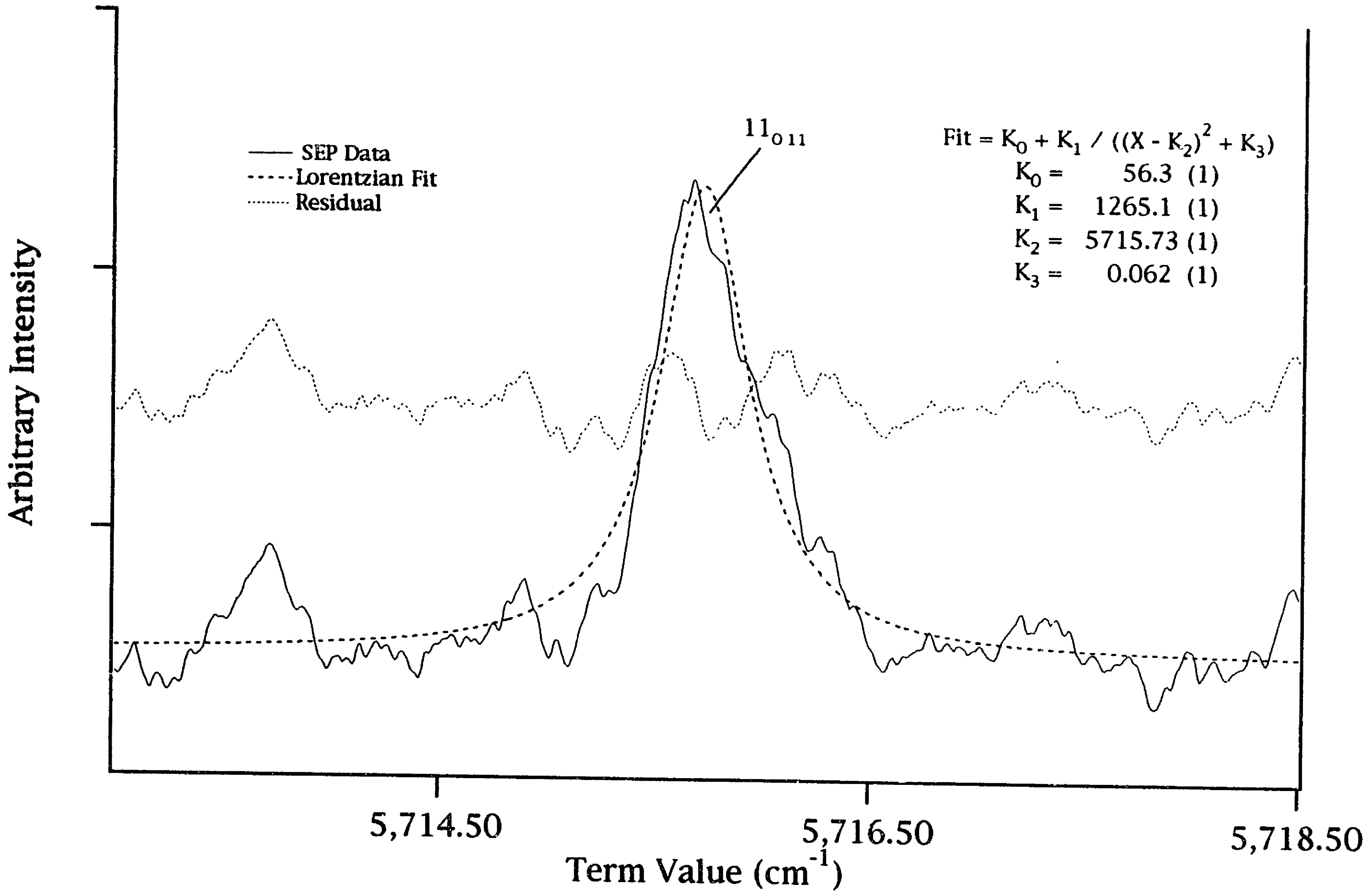

Figure 4.1-5C Line Shape Fit: HCO $\tilde{B} \rightarrow \tilde{X}\ 2_3^0$ SEP Spectrum
From the PUMP $\tilde{B} \leftarrow \tilde{X}\ 0_0^0\ {}^qR(9_{09})$

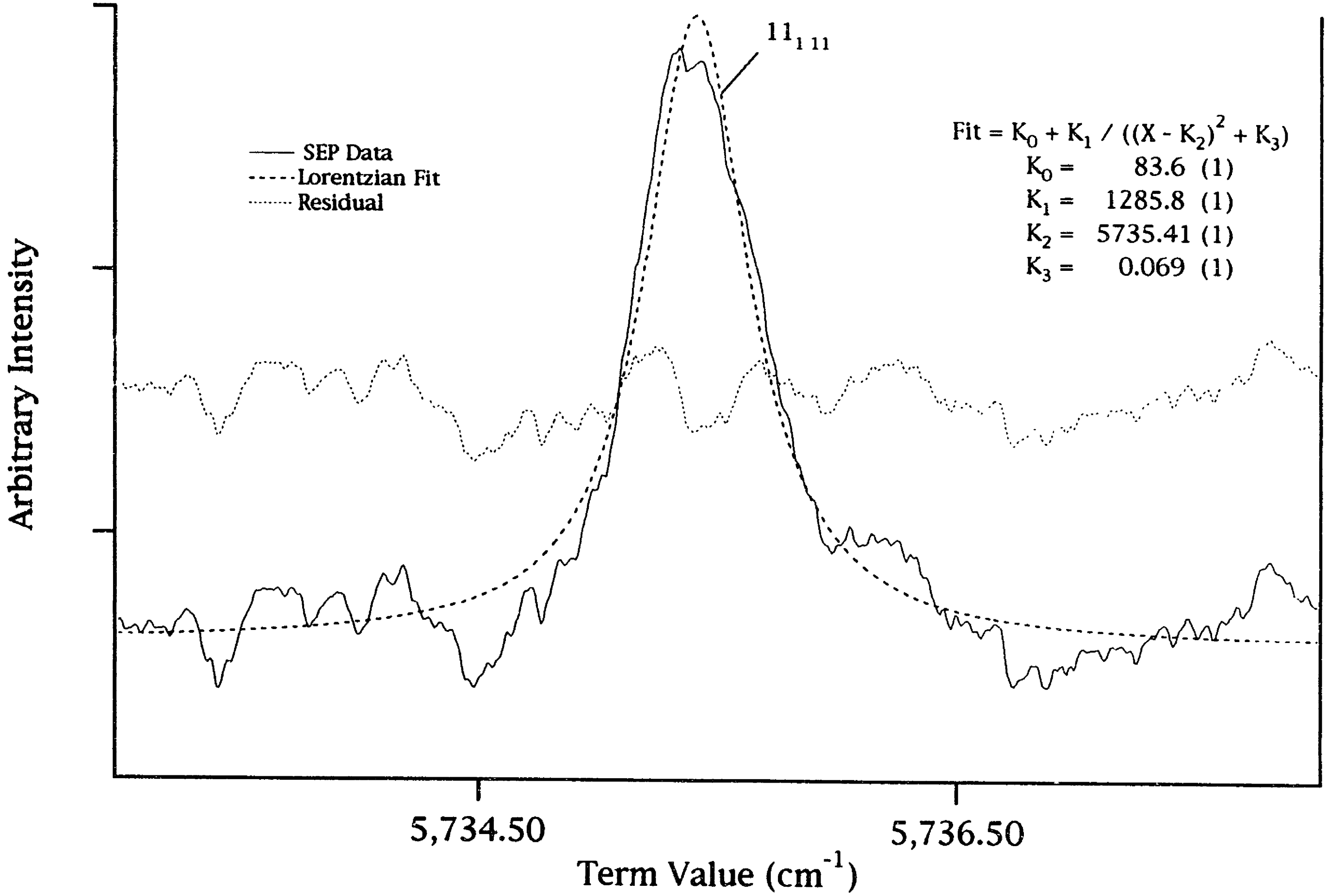

Figure 4.1-5D Line Shape Fit: HCO $\tilde{B} \rightarrow \tilde{X}\ 2_3^0$ SEP Spectrum
From the PUMP $\tilde{B} \leftarrow \tilde{X}\ 0_0^0\ {}^{q}R(9_{09})$

Table 4.1-6 Table of $\tilde{X}\,^2A'$-state Molecular Constants and Widths Measured with a-type PUMP Transitions

$(\nu_{CH},\nu_{CO},\nu_{bend})$	Term Value	Γ FWHM	A"	0.5*(B"+C")	0.25*(B"-C")
	cm^{-1}	cm^{-1}	cm^{-1}	cm^{-1}	cm^{-1}
(0,1,2)	3 999.27 (5)	0.50 (9)	29.10 (6)	1.4355 (8)	0.0289 (7)
(0,1,3)	5 031.65 (2)	0.53 (9)	32.43 (5)	1.4343 (2)	0.0338 (1)
(0,2,0)	3 711.40 (4)	0.64 (7)	24.13 (4)	1.4226 (5)	0.0229 (4)
(0,2,1)	4,824.27 (4)	0.7 (1)	26.26 (3)	1.4227 (4)	0.0258 (2)
(0,2,2)	5,715.76 (3)	0.41 (6)	28.77 (3)	1.4214 (4)	0.0291 (2)
(0,2,3)	6,861.22 (4)	0.65 (9)	31.86 (2)	1.4213 (8)	0.0316 (5)
(0,3,0)	5 529.81 (7)	0.50 (8)	23.94 (4)	1.4097 (7)	0.0223 (3)
(0,3,1)	6 597.65 (4)	0.85 (9)	25.95 (4)	1.4101 (4)	0.0255 (2)
(0,3,2)	7,643.74 (7)	0.7 (1)	28.31 (5)	1.4094 (8)	0.0285 (5)
(0,4,0)	7 323.43 (4)	0.63 (8)	23.83 (4)	1.3967 (4)	0.0226 (3)
(0,4,1)	8 390.71 (9)	2.1 (5)	25.35 (8)	1.3994 (9)	0.0286 (7)
(0,4,3)	10,448.51 (7)	1.9 (6)	30.1 (1)	1.3975 (9)	0.027 (3)
(0,5,0)	9,091.97 (3)	0.70 (1)	23.7 (3)	1.384 (6)	0.0218 (6)
(0,5,1)	10 151.5 (3)	2.8 (5)	25.8 (3)	1.388 (5)	0.030 (2)
(0,5,2)	11 196. (1)	30. (8)	26 (5)	1.39 (8)	[0.028]
(0,6,0)	10 836.1 (2)	1.7 (3)	23.43 (9)	1.371 (2)	0.0211 (8)

[ ] - Entry assumed and held fixed at the $\tilde{X}\,^2A'$ (0,0,0) level value.

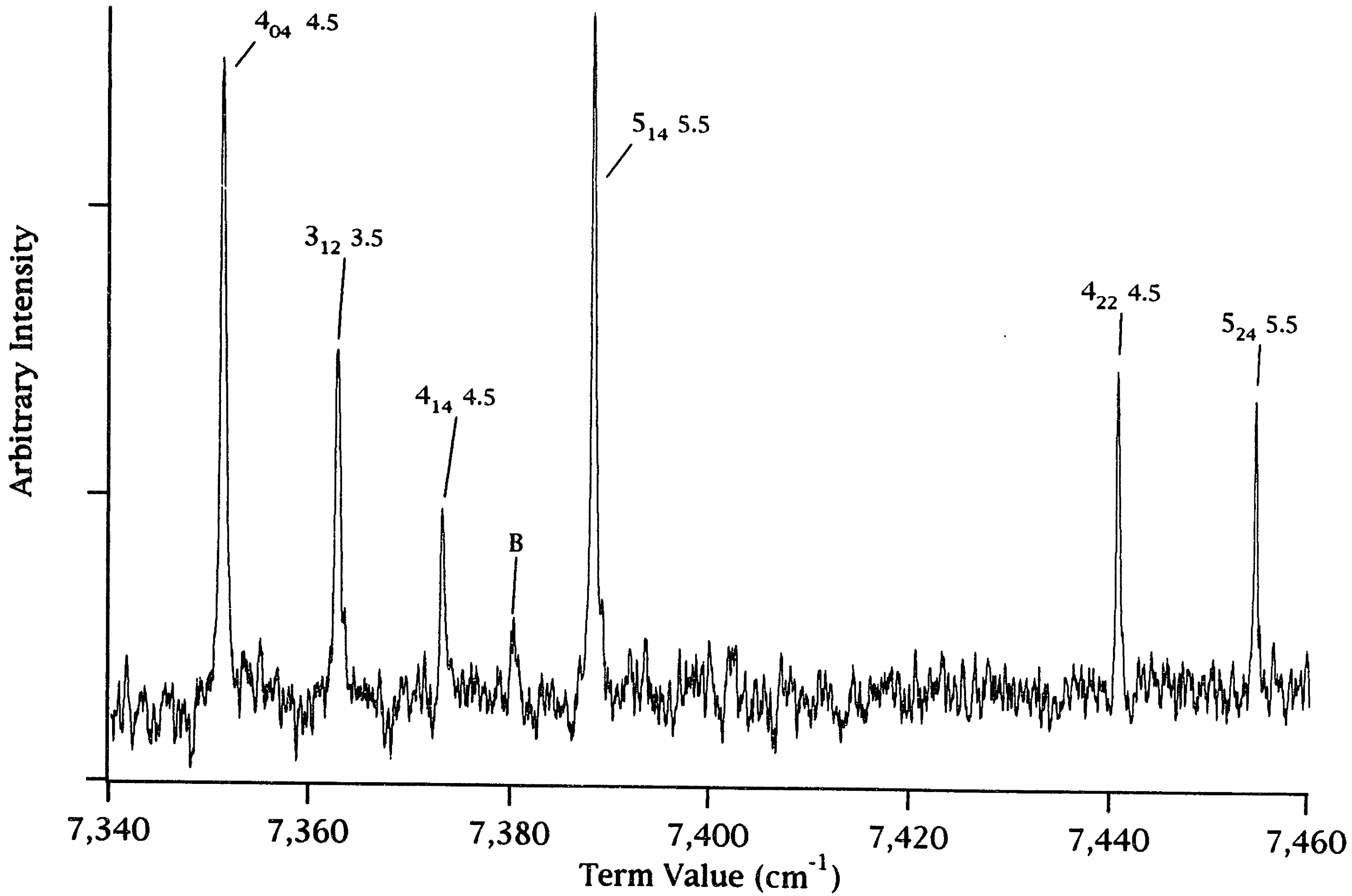

Figure 4.2-1 HCO $\tilde{B} \rightarrow \tilde{X}\ 2_4^0$ SEP Spectrum From the PUMP $\tilde{B} \leftarrow \tilde{X}\ 0_0^0\ {}^{r}Q(4_{04}\ 4.5)$

Table 4.2-2 Observed $\tilde{X}\ ^2A'$ (0,2,0) Term Values with Resolved Spin-Rotation Splitting

$^rQ(N_{0N}\ J)$ PUMP	N"	K_a"	Parity	J"	Term Value	Obs.-Calc.	Γ FWHM	Area	Notes
3_{03} 3.5	3	0	-1	3.5	3728.41 ①	0.0 ①	0.34 (4) ①	550 ②	
4_{04} 4.5	4	0	1	4.5	3739.82		0.03 (4)	480	
3_{03} 3.5	3	1	-1	3.5	3750.89		0.40 (8)	200	
5_{05} 5.5	5	0	-1	5.5	3754.04		0.39 (6)	790	
5_{05} 5.5	4	1	-1	4.5	3762.97		0.29 (5)	340	
4_{04} 4.5	5	1	1	5.5	3777.58		0.45 (9)	620	
5_{05} 5.5	6	1	-1	6.5	3794.91		0.45 (8)	680	

① - Units in cm^{-1}, ② - Arbitrary area units

Table 4.2-2 Observed $\tilde{X}\ {}^2A'$ (0,3,0) Term Values with Resolved Spin-Rotation Splitting

${}^rQ(N_{0N}\ J)$ PUMP	N"	K_a"	Parity	J"	Term Value	Obs.-Calc.	Γ FWHM	Area	Notes
3_{03} 3.5	3	0	-1	3.5	5546.66 ①	-0.09 ①	0.43 (9) ①	780 ②	
4_{04} 4.5	4	0	1	4.5	5558.00	-0.02	0.53 (5)	1490	
3_{03} 3.5	2	1	-1	2.5	5561.02	-0.01	0.23 (7)	300	
4_{04} 4.5	3	1	1	3.5	5569.58	0.01	0.48 (6)	840	
5_{05} 5.5	5	0	-1	5.5	5572.11	-0.02	0.32 (5)	940	
4_{04} 4.5	4	1	1	4.5	5580.12	0.07	0.5 (2)	640	
3_{03} 2.5	4	1	1	3.5	5580.95	0.02	0.38 (9)	580	
3_{03} 3.5	4	1	-1	4.5	5580.99	-0.02	0.28 (9)	520	
4_{04} 4.5	5	1	1	5.5	5595.36	0.00	0.51 (4)	1410	
5_{05} 4.5	6	1	-1	6.5	5612.58	-0.02	0.51 (6)	1090	
3_{03} 3.5	4	2	-1	4.5	5648.00	0.02	0.32 (7)	570	
4_{04} 4.5	4	2	1	4.5	5648.09	-0.06	0.38 (6)	790	
4_{04} 4.5	5	2	1	5.5	5662.13	0.01	0.39 (4)	570	
5_{05} 5.5	5	2	-1	5.5	5662.11	-0.02	0.43 (7)	690	
5_{05} 5.5	6	2	-1	6.5	5679.05	0.01	0.40 (8)	440	

① - Units in cm^{-1}, ② - Arbitrary area units

Table 4.2-2 Observed $\tilde{X}\ {}^2A'$ (0,3,2) Term Values with Resolved Spin-Rotation Splitting

${}^{r}Q(N_{0N}\ J)$ PUMP	N"	K_a"	Par-ity	J"	Term Value	Obs.-Calc.	Γ FWHM	Area	Notes
3_{03} 3.5	3	0	-1	3.5	7660.58 ①	-0.22 ①	0.53 (3) ①	2710 ②	
4_{04} 4.5	4	0	1	4.5	7671.99	-0.85	0.67 (7)	2020	
3_{03} 3.5	2	1	-1	2.5	7679.40	0.10	0.65 (4)	1930	
3_{03} 3.5	3	1	-1	3.5	7687.22	0.06	0.45 (4)	1270	
5_{05} 4.5	5	0	-1	4.5	7686.03	-0.12	0.68 (6)	2410	
5_{05} 5.5	5	0	-1	5.5	7685.98	-0.13	0.59 (4)	2960	
5_{05} 4.5	4	1	-1	3.5	7699.49	0.14	0.60 (7)	1360	
5_{05} 5.5	4	1	-1	4.5	7699.53	0.05	0.63 (5)	2570	
5_{05} 5.5	5	1	-1	5.5	7712.20	0.27	0.6 (1)	520	
4_{04} 4.5	5	1	1	5.5	7714.00	0.09	0.8 (1)	2220	
5_{05} 4.5	6	1	-1	5.5	7731.10	0.03	0.69 (9)	2070	
3_{03} 3.5	3	2	-1	3.5	7767.81	0.00	0.56 (6)	1130	
3_{03} 3.5	4	2	-1	4.5	7779.01	-0.05	0.40 (3)	1230	
5_{05} 4.5	5	2	-1	4.5	7792.83	-0.03	0.44 (8)	890	
5_{05} 5.5	5	2	-1	5.5	7793.11	-0.05	0.41 (4)	1280	
5_{05} 5.5	6	2	-1	6.5	7810.00	-0.04	0.54 (5)	1560	

① - Units in cm^{-1}, ② - Arbitrary area units

Table 4.2-2 Observed $\tilde{X}\ ^2A'$ (0,4,0) Term Values with Resolved Spin-Rotation Splitting

$^rQ(N_{0N}\ J)$ PUMP	N"	K_a"	Parity	J"	Term Value	Obs.-Calc.	Γ FWHM	Area	Notes
3_{03} 3.5	3	0	-1	3.5	7340.09 ①	-0.06 ①	0.58 (3) ①	1500 ②	
3_{03} 2.5	3	0	-1	2.5	7340.10	-0.05	0.61 (4)	1400	
4_{04} 4.5	4	0	1	4.5	7351.27	-0.05	0.62 (2)	2300	
3_{03} 2.5	2	1	-1	1.5	7354.17	0.04	0.52 (7)	620	
3_{03} 3.5	2	1	-1	2.5	7354.33	0.04	0.66 (5)	1100	
3_{03} 3.5	3	1	-1	3.5	7362.27	0.04	0.46 (6)	700	
4_{04} 4.5	3	1	1	3.5	7362.86	0.06	0.61 (4)	1300	
5_{05} 4.5	5	0	-1	4.5	7365.29	-0.01	0.61 (3)	1800	
5_{05} 5.5	5	0	-1	5.5	7365.31	0.01	0.66 (3)	1700	
4_{04} 4.5	4	1	1	4.5	7373.28	0.07	0.42 (8)	460	
3_{03} 2.5	4	1	-1	3.5	7374.09	0.02	0.61 (6)	880	
3_{03} 3.5	4	1	-1	4.5	7374.16	0.01	0.49 (3)	1300	
5_{05} 5.5	5	1	-1	5.5	7387.03	0.07	0.4 (1)	360	
4_{04} 4.5	5	1	1	5.5	7388.37	0.01	0.52 (2)	2000	
5_{05} 4.5	6	1	-1	6.5	7405.39	-0.01	0.50 (3)	1600	
3_{03} 2.5	3	2	-1	2.5	7429.19	-0.01	0.5 (1)	380	
3_{03} 3.5	3	2	-1	3.5	7429.60	-0.02	0.46 (6)	650	
3_{03} 2.5	4	2	-1	3.5	7440.37	-0.07	0.35 (9)	390	
3_{03} 3.5	4	2	-1	4.5	7440.74	-0.02	0.41 (6)	650	
4_{04} 4.5	4	2	1	4.5	7440.76	-0.01	0.36 (5)	670	
5_{05} 4.5	5	2	-1	4.5	7454.52	0.06	0.50 (7)	610	
4_{04} 4.5	5	2	1	5.5	7454.65	-0.06	0.35 (6)	590	
5_{05} 5.5	5	2	-1	5.5	7454.74	0.02	0.40 (6)	600	
5_{05} 4.5	6	2	-1	5.5	7471.25	0.00	0.40 (9)	440	
5_{05} 5.5	6	2	-1	6.5	7471.49	0.03	0.34 (6)	550	

① - Units in cm^{-1}, ② - Arbitrary area units

Table 4.2-2 Observed $\tilde{X}\ ^2A'$ (0,4,1) Term Values with Resolved Spin-Rotation Splitting

$^rQ(N_{0N}\ J)$ PUMP	N"	K_a"	Par-ity	J"	Term Value	Obs.-Calc.	Γ FWHM	Area	Notes
4_{04} 4.5	4	0	1	4.5	8418.49 ①	0.11 ①	2.5 (2) ①	8670 ②	
4_{04} 4.5	3	1	1	3.5	8431.58	0.06	2.0 (2)	5760	
5_{05} 5.5	5	0	-1	5.5	8432.37	0.07	2.8 (1)	5750	
4_{04} 4.5	4	1	1	4.5	8441.44	-0.16	1.7 (4)	1670	
5_{05} 5.5	4	1	-1	4.5	8442.90	-0.03	1.62 (7)	2890	
4_{04} 4.5	5	1	1	5.5	8457.09	-0.11	1.8 (1)	6540	
4_{04} 4.5	4	2	1	4.5	8513.93	0.00	0.94 (9)	1920	
5_{05} 5.5	5	2	1	5.5	8527.90	0.06	0.80 (6)	1900	
5_{05} 5.5	5	2	-1	5.5	8527.86	0.00	0.72 (6)	910	
5_{05} 5.5	6	2	-1	6.5	8544.56	0.01	0.89 (6)	1080	

① - Units in cm^{-1}, ② - Arbitrary area units

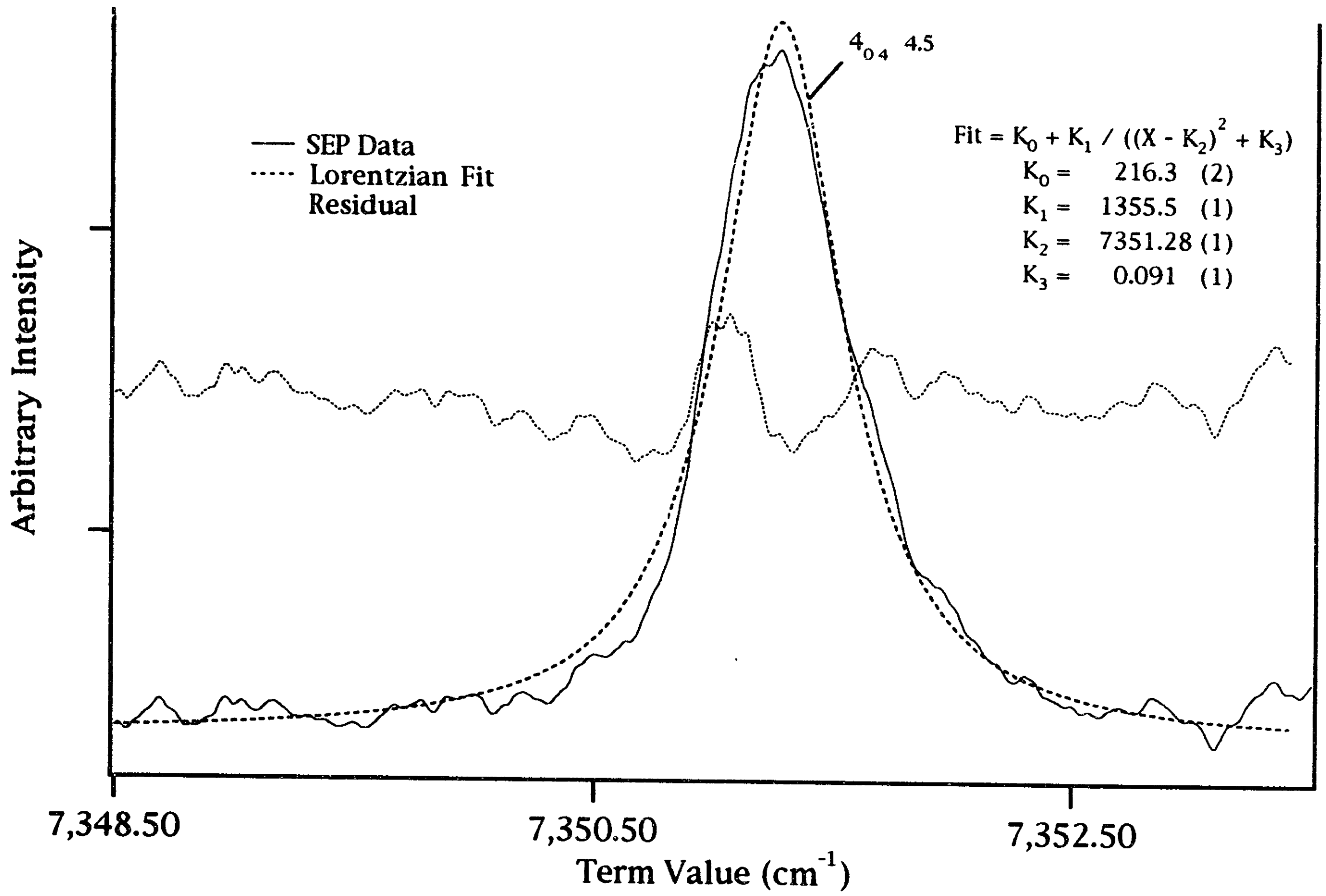

Figure 4.2-3A Line Shape Fit: HCO $\tilde{B} \rightarrow \tilde{X}\ 2_4^0$ SEP Spectrum from the PUMP $\tilde{B} \leftarrow \tilde{X}\ 0_0^0\ {}^rQ(4_{04}\ 4.5)$

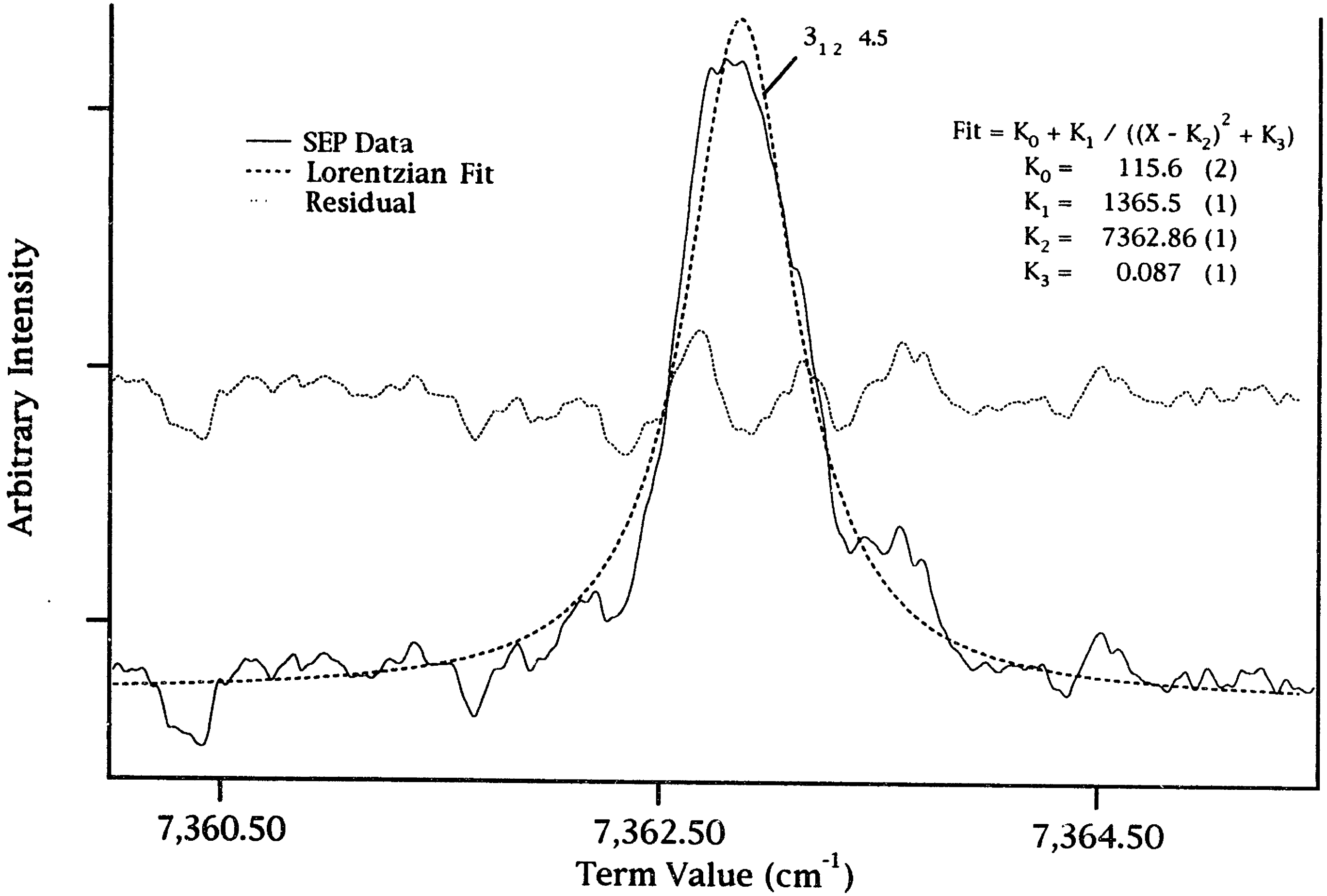

Figure 4.2-3B Line Shape Fit: HCO $\tilde{B} \rightarrow \tilde{X}\ 2_4^0$ SEP Spectrum from the PUMP $\tilde{B} \leftarrow \tilde{X}\ 0_0^0\ {}^{r}Q(4_{04}\ 4.5)$

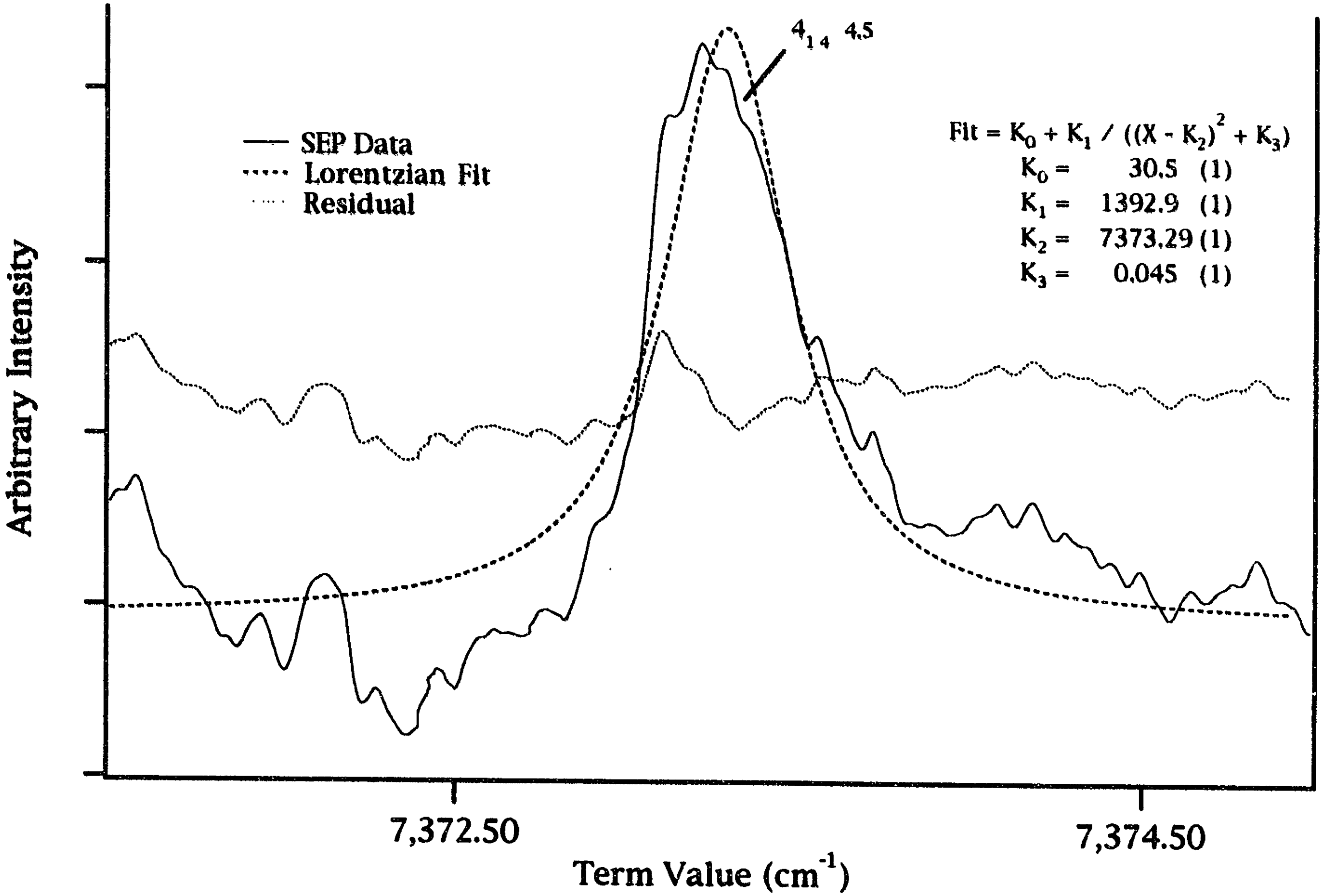

Figure 4.2-3C Line Shape Fit: HCO $\tilde{B} \rightarrow \tilde{X}\ 2^0_4$ SEP Spectrum from the PUMP $\tilde{B} \leftarrow \tilde{X}\ 0^0_0\ {}^rQ(4_{04}\ 4.5)$

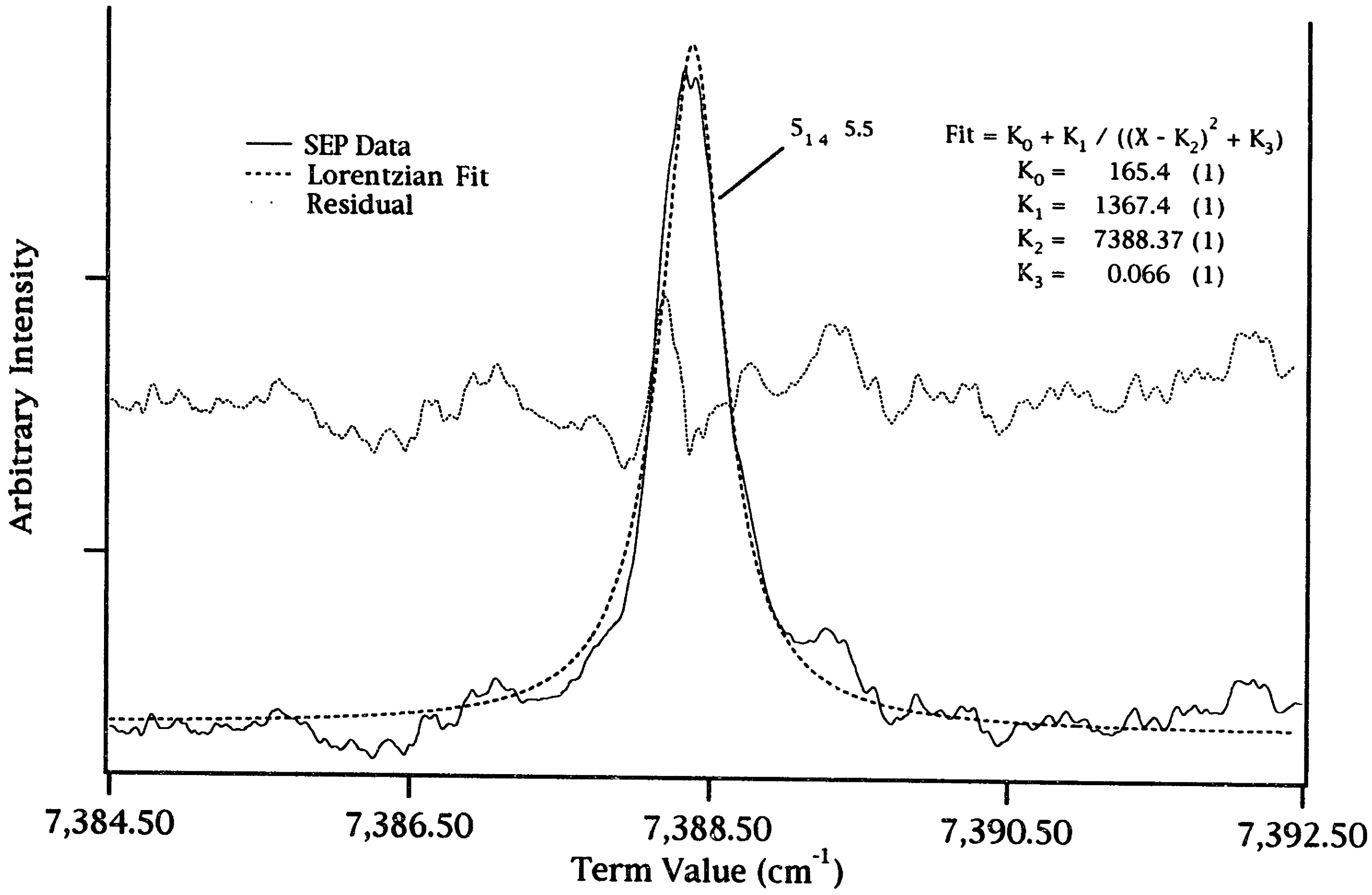

Figure 4.2-3D Line Shape Fit: HCO $\tilde{B} \rightarrow \tilde{X}$ 2_4^0 SEP Spectrum from the PUMP $\tilde{B} \leftarrow \tilde{X}$ 0_0^0 ${}^rQ(4_{04}$ 4.5)

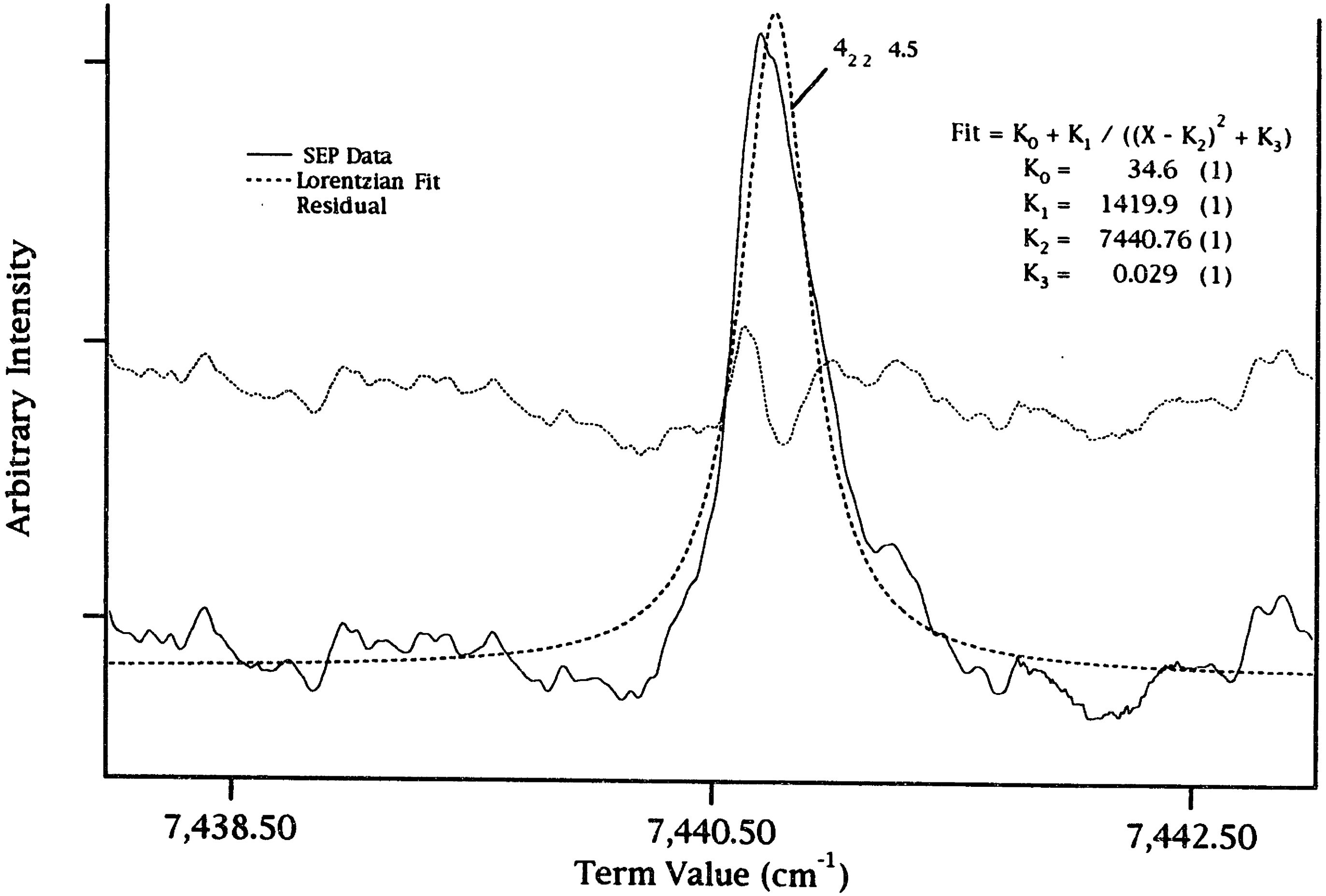

Figure 4.2-3E Line Shape Fit: HCO $\tilde{B} \rightarrow \tilde{X}\ 2_4^0$ SEP Spectrum from the PUMP $\tilde{B} \leftarrow \tilde{X}\ 0_0^0\ {}^rQ(4_{04}\ 4.5)$

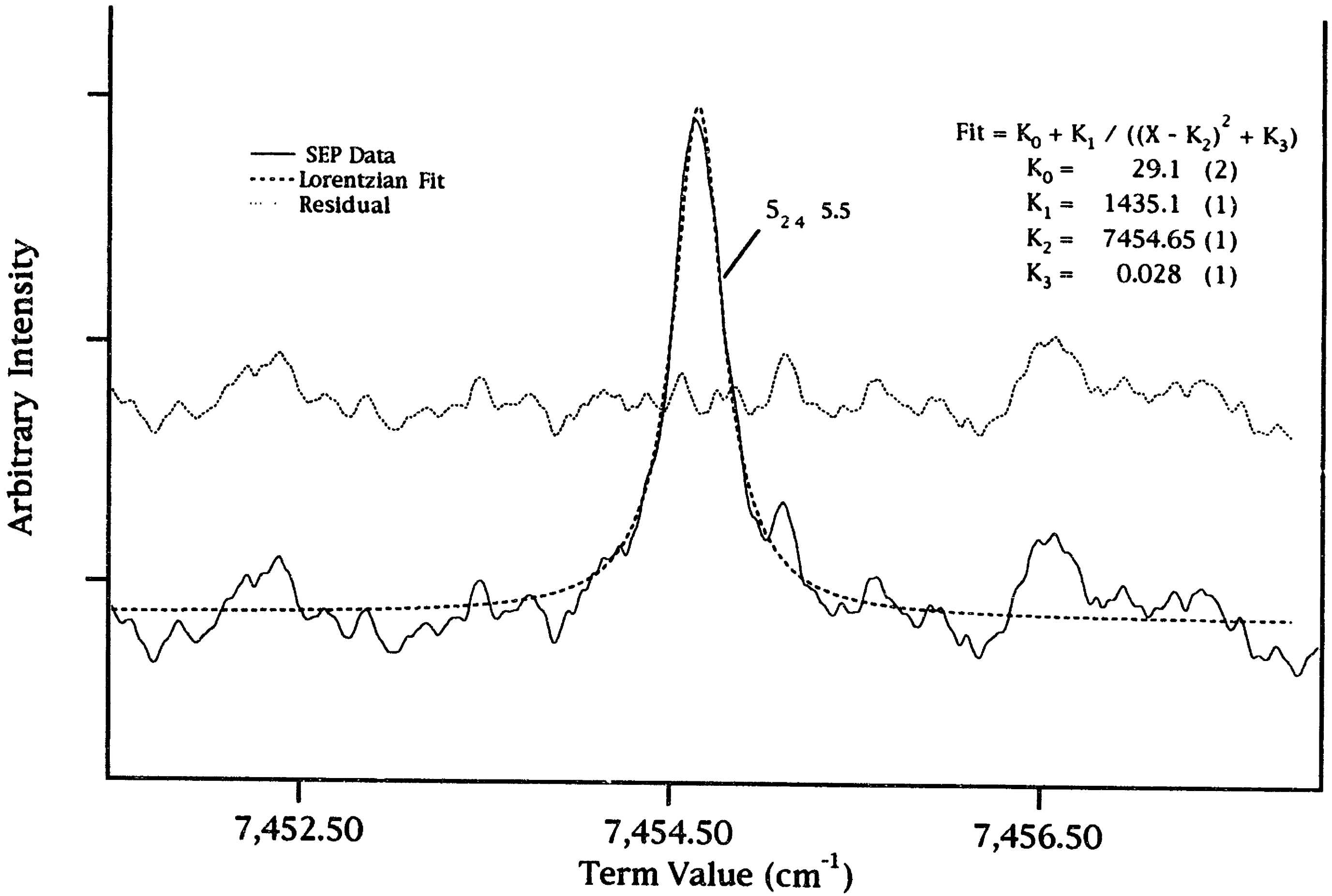

Figure 4.2-3F Line Shape Fit: HCO $\tilde{B} \rightarrow \tilde{X}\ 2_4^0$ SEP Spectrum from the PUMP $\tilde{B} \leftarrow \tilde{X}\ 0_0^0\ {}^rQ(4_{04}\ 4.5)$

Table 4.2-4 Table of $\tilde{X}\,^2A'$-State Molecular Constants and Widths with Resolved Spin-Rotation

(ν_{CH},ν_{CO},ν_{bend})	Term Value	Γ FWHM	A"	0.5*(B"+C")	0.25*(B"-C")	a ③	a_s ③
	cm^{-1}	cm^{-1}	cm^{-1}	cm^{-1}	cm^{-1}	cm^{-1}	cm^{-1}
(0,2,0) ①	3711.56 (7)	0.4 (7)	24.03 (2)	1.423 (3)	0.0226 (8)	④	④
②		0.64 (7)					
(0,3,0) ①	5529.79 (7)	0.4 (1)	23.85 (6)	1.4092 (8)	0.0224 (8)	④	④
②		0.50 (8)					
(0,3,2) ①	7643.84 (3)	0.5 (1)	28.40 (7)	1.4083 (7)	0.287 (9)	-0.1255 (9)	-0.125 (1)
②		0.7 (1)					
(0,4,0) ①	7323.38 (3)	0.50 (9)	23.719 (4)	1.3977 (6)	0.0233 (5)	-0.1252 (7)	-0.1253 (9)
②		0.63 (8)					
(0,4,1) ①	8390.75 (6)	1.6 (8)	25.32 (4)	1.3989 (5)	0,0285 (6)	-0.1260 (8)	-0.1256 (8)
②		2.1 (5)					

① - Constants from the spin-rotation resolved data of Section 4.2

② - Widths from Table 4.1-6 for comparison.

③ - Alternate definitions for the spin-rotation parameters are:

$\kappa = -3a = \varepsilon_{aa} - 0.5\,(\varepsilon_{bb} + \varepsilon_{cc})$ and $\mu = a - a_0 = 0.5\,(\varepsilon_{bb} + \varepsilon_{cc})$

④ - Data set not sufficent to determine

Chapter 5

Discussion

5.1 Rotational Linewidth Trends.

A cursory perusal of the linewidths, tabulated in Tabl 4.1-2 and Table 4.2-2, shows that for each vibrational band observed the widest rotational line is the most intense, and similarly the narrowest is the least intense. The purpose of this section is to determine whether trends indeed exist in the rotational linewidths, measured in Chapter 4, for the HCO $\tilde{B}\,^2A' \rightarrow \tilde{X}\,^2A'$ SEP Spectrum.

In order to determine whether the linewidths depend more upon the rotational intensity directly or the rotational quantum numbers, several statistical measures of correlation were applied. These statistical measures determined which of two possible explanations best accounted for the perceived trends in the rotational linewidths.

For $\tilde{X}$-state vibrational levels below the thermodynamic dissociation limit (approximately ~5050 cm^{-1} for D_0^0 H—CO) [1,20] trends in the rotational width should not exist. Each rotational line below this dissociation limit should have the same linewidth. At energies below the dissociation limit any trends in the linewidths are probably the result of experimental artifacts. The most likely candidate for creating these artifacts is power broadening, meaning that the rotational linewidths would be dependent upon rotational line strength factors [2]. For levels above the dissociation limit there exists the possibility for rotationally dependent perturbations, similar to those observed in the $\tilde{A}$-state of HCO, causing rotational linewidths to depend upon rotational quantum numbers [3]. In light of these two possible mechanisms for rotational linewidth trends, three independent variables were chosen and tested for statistical correlations between the rotational linewidth measured from a-type PUMP transitions. The independent quantities chosen for testing were: peak area, $N'' \cdot (N''+1) - K_a''^2$ and $K_a''^2$. The statistical testing of the SEP spectra recorded from b-type PUMP transitions is discussed later in this Section.

In order to quantify the magnitude of the dependence between the rotational linewidth and each independent variable, a statistical analysis was performed upon the rotational linewidths taken from Table 4.1-2 and Table 4.2-2. The results of these statistical analyses are shown in Tables 5.1-1 through 5.1-3.

The statistical measures used in this analysis were of two types: correlation coefficients and measures for the "goodness" of a least squares fit. The two correlation coefficients calculated were: the linear correlation coefficient (R_ℓ) [4] and the rank order correlation coefficient (R_S) [5]. The two measures for the "goodness" of a least squares fit were: Chi Square (χ^2) and "Q" [7,8]. Each of these statistical tests are described in turn below.

The correlation coefficients are a measure of how well the change in the rotational linewidths could be accounted for by the change in one of the three dependent variables. The value for either of the correlation coefficients can vary between -1 and 1. A value of ±1 shows complete correlation, while a value of 0 shows a complete lack of correlation. The value of the square of the correlation coefficient (R^2) is equal to the fraction of the change in the rotational linewidth that can be accounted for by the change in the independent variable [4,5,6].

The linear correlation coefficient is calculated for a set of data (X_i, Y_i) by first considering a linear fit to the data of the form $Y = a + b \cdot X$. It is also equally valid to make a linear fit of the form $X = a' + b' \cdot Y$. If the data (X_i, Y_i) are perfectly correlated, then the slopes for the two fits are related; $b = 1/b'$. For uncorrelated data this equality does not hold exactly. A measure of how poorly this equality holds is given by the quantity R_ℓ which is defined as $R \equiv \sqrt{bb'}$ [4]. Explicit formulas for computing R_ℓ from a (X_i, Y_i) data set are given by P. R. Bevington [4]. For a data set of a size equal to the typical number of rotational lines measure for each band, a correlation coefficient value of $R = 0.80$ has a probability of occurring randomly from an uncorrelated data set of ~2% [4].

The rank order correlation coefficient (R_S) is similarly calculated for a set of data (X_i, Y_i) by first ranking the X and Y data points separately, and then calculating the linear correlation coefficient from the rank of X versus the rank of Y. The ranks for the X and Y are determined by simply sorting the X data and then the Y data from largest to smallest value [5]. Thus, if the largest value of X corresponds to the largest value of Y and the next largest value of Y continues this trend, then the rank order coefficient will have a value near ±1 showing compleat correlation.

Each of these correlation coefficients has its own strengths and weaknesses. The linear correlation coefficient provides a measure of how much of the change of the rotational linewidth and the chosen independent variable could be accounted for by a linear function $Y = a + b \cdot X$. The linear correlation coefficient is best suited for data sets where there is more than one Y value for a given X value — for example, when the data set (X_i, Y_i) is not single valued. It also works well for data sets where the uncertainties are large relative to the spacings between points. The major limitation of the linear correlation coefficient is that it will only show a large correlation if the linewidths are linearly correlated and not if they are correlated by some other function.

The rank order correlation coefficient, in contrast to the linear correlation coefficient, will show a large correlation if the linewidths are correlated by a monotonic function [5]. The disadvantage of the rank order correlation coefficient is that it cannot be applied directly to a data set that is not single-valued; single valued meaning a data set having tied rankings. The data set is not considerd single valued if more than one value for the Y data ($Y_i \neq Y_j$) exists for a single value for the X data ($X_i = X_j$). It furthermore, calculates a correlation value artificially small for data in which the uncertainties are larger than the spacings between adjacent ranked data points.

The "goodness" of fit statistical measures are used to determine how well any dependence between the rotational linewidths and one of the independent variables (integrated intensity, $N''\cdot(N''+1)-K_a''^2$ and $K_a''^2$) is modeled by a straight line. In this regard the "goodness" measures serve as a check for any conclusions drawn from an examination of the correlation coefficients. The "goodness" measures for the various models are summarized in Table 5.1-1 through 5.1-3. Included in these tables are the slope (a) and intercept (b) for the linear fit of the linewidths $Y = a + b\cdot X$.

The first "goodness" of fit parameter calculated was Chi Squared (χ^2). It was defined in the usual way, as the weighted sum of the squares of the difference between the actual observed data value (Y_i) and the estimated value for that point calculated from the fitting function ($<Y_i>$) [8]. The weights were taken to be the reciprocal of the uncertainty in the linewidth squared ($1/\sigma_i^2$) [8]. The smaller the value of the Chi Squared (χ^2), the better the data set is represented by a linear function.

The second "goodness" of fit statistical calculation was "Q", which is a measure of the believability of the Chi Squared linear fit. The quantity "Q" { $Q = 1 - P((N-2)/2,\ \chi^2/2)$ where N= number of data points, P is the incomplete gamma function} is a measure of how well a linear model represents the actual data [7,8]. A value of "Q" larger than 0.1 indicates that a linear fit model believably represents the data. A value of "Q" between 0.1 and 0.001 indicates that model may be valid, and a value for "Q" less than 0.001 indicates the data cannot be represented by a linear function [7,8].

The first trend that can be drawn from comparing the results of the four statistical tests to the SEP data recorded from a-type

PUMP transitions, discussed above and summarized in Table 5.1-1 through 5.1-3, is that the rotational linewidth is most strongly correlated with intensity and that there exists no clear dependence of the rotational linewidths on rotational quantum number. The second trend that can be inferred is that the dependence of the linewidth on intensity decreases as the average rotational linewidth for each vibrational band increases. Correspondingly, the "goodness" of the linear fit decreases with increasing average rotational linewidths.

These two trends are consistent with the conclusion that the rotational linewidths measured from spin-rotation doubled a-type PUMP transitions are contaminated by power broadening. It should be noted that as the linewidth increases it becomes more difficult to power broaden, which agrees with the observed decrease in correlation. Our SEP data is compared to the SEP data of other groups in Section 5.3.

For levels with a strong rotational linewidth versus intensity correlation a better determination of the vibrational linewidth may be the Y-intercept (*a*), tabulated in Table 5.1-1, instead of the average widths reported in Table 4.1-6.

The statistical test performed on the SEP spectrum recorded via b-type PUMP transitions, where the spin-rotation splitting was resolved (raw data from Table 4.2-2), are also summarized in Tables 5.1-1 through 5.1-3. In all cases the measured linewidths are narrower for SEP transitions measured via b-type PUMP transitions than those measured via a-type PUMP transitions. It is the rotational linewidths measured from SEP spectra recorded using b-type PUMP transitions that are most likely to exhibit rotation dependent widths. The rotational dependence of the spin rotation splitting, for the N, K_a and J levels observed in these SEP spectra, are large and tend to obscure any variations of the homogeneous linewidths. The actual dependence of the splitting observed in the spectrum can be calculated using the expression below for the spin-rotation splitting for each state and the observation that only $\Delta J = \Delta N$ transitions were observed for the $\tilde{B}\,^2A' \leftrightarrow \tilde{X}\,^2A'$ system, [18]

$$\begin{aligned} F_1(\mathrm{N}) &= F_0(\mathrm{N}) + \tfrac{1}{2}\gamma \cdot \mathrm{N} \\ F_2(\mathrm{N}) &= F_0(\mathrm{N}) - \tfrac{1}{2}\gamma \cdot (\mathrm{N}+1) \quad . \\ \gamma &= \kappa \cdot \frac{\mathrm{K}_a^2}{\mathrm{N}\cdot(\mathrm{N}+1)} + \mu \end{aligned} \qquad (1)$$

This variation in the observed splitting produces an artificial dependence of the linewidths on N and K_a rotational quantum numbers in spectra where the spin-rotation splitting is unresolved. The artificially broadened linewidths result since the observed linewidths are the sum of the homogeneous width plus the spin-rotation splitting (see Section 4.2).

The SEP rotational linewidths recorded from b-type PUMP transitions are free from this inhomogeneous broadening mechanism. The rotational widths for the "b-type PUMP" SEP spectra are less correlated with intensity and were more correlated with K_a — instead of being correlated with K_a^2. The results of the statistical tests for correlation with K_a are shown in Table 5.1-4.

These statistical tests indicate that the rotational widths for two different vibrational levels {(0,4,1) and (0,4,0)} were strongly correlated with K_a. The widths for levels lower in energy than these two did not display as strong a K_a dependence. For the level (0,4,0) the statistical results testing for a linear correlation with K_a were: $R_\ell = 0.76$ (2), $Q = 0.14$ and $\chi^2 = 30$. Even more remarkable was the correlation shown by the level (0,4,1), which was the lowest energy level to broaden by more than the instrumental limit. The test results for this level were: $R_\ell = 0.983$ (3), $Q = 1.0$ and $\chi^2 = 0.17$. The constants from the linear fit for this level were: A = 2.73 (9), B = -0.94 (6). A plot of the rotational widths and the linear fit are shown in Figure 5.1-5. For comparison the statistical results for a correlation with K_a^2 are reproduced from Table 5.1-3 for the levels (0,4,0) and (0,4,1), respectively: $R_\ell = 0.08$, $Q = 0.0$, and $\chi^2 = 38.8$; $R_\ell = 0.50$, $Q = 0.0$, and $\chi^2 = 58.2$. It should be noted that the unresolved spin-rotation splitting present in the SEP spectra recorded from a-type PUMP transitions completely masked the rotational dependence of the measured SEP linewidths.

Since the rotational linewidths for the band (0,4,1) depended upon K_a and *not* K_a^2, a Coriolis induced process can be ruled out [18]. A more plausible explanation for the observed K_a dependence of the linewidths is simply a centrifugal barrier [21,27]. The effect of a centrifugal barrier on the dissociation rate is discussed below beginning with a review of the major features of the HCO $\tilde{X}\ ^2A'$-state potential energy surface (see Section 1.1).

The minimum energy point for the ground state ($\tilde{X}\ ^2A'$) of HCO occurs at a bond angle of 124.95°, a C-H distance of 1.125 Å, and a CO distance of 1.175 Å [3]. The classical limit for dissociation ($HCO \rightarrow H + CO$) is approximately (D_0^0) 5058cm^{-1} as determined from the Dunning *ab initio* potential surface [20,24,25]. On the Dunning *ab initio* potential surface, the H—CO saddle point occurs at a C-H distance of ~1.75 Å, a CO bond length of 1.15 Å and a bond angle of ~150° [1,20]. The H—CO saddle point is at an energy of 5757cm^{-1} above the HCO zero point, producing a small barrier to dissociation [20,24,25]. Along the minimum energy path for dissociation the HCO bond angle must change from 124° to 150°. Thus, in order to dissociate, the bond angle for HCO must change by almost 30°.

Since we are examining the effect of rotational excitation about the a-inertial axis on the dissociation rate, we need only consider the vibrational motion which is most strongly affected by rotations about the a-axis which is the bending vibration (v_3). The remaining vibrational degrees of freedom can be accounted for by calculating an adiabatic bending potential [31]. For $K_a = 0$ this adiabatic potential can be used directly to calculate the bending wavefunction. For $K_a > 0$ the effect of a centrifugal barrier at the linear geometry needs to be added to the adiabatic potential [31]. The bending potential including rotations about the a-axis has the functional form (see Section 4.1) [26]

$$V(\theta) = V_{bend}(\theta_0 - \theta) + \frac{\hbar^2 \cdot K_a^2}{2\mu(r_{CH} \cdot \sin(180-\theta))^2}. \qquad (2)$$

Figure 5.1-6 shows a qualitatively correct bending potential for HCO including the centrifugal barrier for K_a =0, 1, and 2 [27].

The crudest approximation of the dissociation rate can be calculated as being proportional to the fraction of a bending vibrational period that the molecule spends with the hydrogen pointing at the exit channel. This fraction is the probability amplitude of the bending wavefunction integrated from the angle corresponding to the inner wall of the exit channel at the saddle point to the angle corresponding to the outer wall of the exit channel. Thus, as the probability amplitude of the bending wave function decreases in the vicinity of the exit channel, the dissociation rate will decrease. This is how the presence of a centrifugal barrier effects the dissociation rate, by making the near-linear (θ=180°) wall of the bending potential more steep. Making this wall more steep skews the probability amplitude of the bending potential away from the nearly linear and usually softer turning point, reducing the dissociation rate.

5.2 Vibrational Linewidth Trends.

Several calculations have predicted the dissociation lifetimes for $\tilde{X}\,^2A'$-state vibrational levels [1,9,10,11,12]. Many of these calculated lifetimes, even near the dissociation limit, were predicted to be short enough (11PS ↔ 100FS) to produce an observed homogeneous broadening of the SEP lines $\{\Gamma(\mathrm{FWHM,\ in\ cm^{-1}}) = 1/(2\pi \cdot \tau \cdot c)\}$. These calculations also predicted that these lifetimes would exhibit mode specificity. In other words, the lifetime of a vibrational state would depend on which vibrational modes were excited. This mode specificity in the HCO ground state lifetimes was first experimentally noted for HCO by R. N. Dixon in the dispersed $\tilde{B}\,^2A' \rightarrow \tilde{X}\,^2A'$ emission of the "hydrocarbon flame bands" [13,14]. The purpose of this section is to provide a discussion of the mode specificity of the dissociation lifetimes inferred from the SEP linewidths measured in Chapters 3 and 4.

In Figures 5.2-1 through 5.2-4 the vibrational level width is plotted in turn versus: the vibrational term values, the number of bending quanta excited, the number of CO stretching quanta excited, and the amount of energy in the CO stretching mode. The vibrational level width used in these figures was the average of the SEP rotational linewidths, shown in Tables 4.1-2 and 4.2-2. These averages are also reported in Tables 4.1-6 and 4.2-4. The error bars on these graphs are ± the standard deviation for the averages of the rotational linewidths.

In Figure 5.2-1 the vibrational level width is plotted versus vibrational term value. For dissociating molecules the vibrational level widths are expected to increase smoothly above the dissociation limit. However, in HCO the widths do not increase as smoothly as is typical because the density of the vibrational states is relatively low (one per hundreds of cm^{-1}) near the dissociation limit. Figure 5.2-1 also indicates that either the previously calculated barrier to dissociation, or the dissociation limit itself, is too small [12,15,16,17,20].

In Figure 5.2-2 the vibrational level widths are plotted versus the number of bending quanta (v_3) excited for a fixed amount of CO stretching (v_2) excitation. The calculation of R. N. Dixon [1] and that of J. M. Bowman et al. [9] predicts that near the dissociation limit, the level width should increase rapidly as the number bending quanta increases for a given excitation in the CO stretch. This trend is roughly evident for the highest energy levels in this SEP data set.

In Figure 5.2-3, the vibrational level widths are plotted against the number of CO stretching quanta for a fixed amount of bend excitation. This figure shows clearly the increase of vibrational level width when the bending mode is excited ($v_3 > 0$). There is also a slow increase in the level widths as the number of quanta of CO stretch increases. This is probably caused by the CO stretching mode providing energy to place a stack of bending levels closer to, or above, the dissociation limit. This is supported by the calculated and observed product state distributions for the HCO dissociation which indicates that energy initially placed in the CO stretch is not available to aid in dissociation [1,28]. In order to get a clearer view of the level width trends with bending excitation, the vibrational level widths are plotted against the energy in the CO stretch for constant bending excitation in Figure 5.2-4. Note the similarity between the trends in Figure 5.2-4 and the trends in Figure 5.2-1.

The dependence of the vibrational level widths on which modes are excited can be rationalized in a way similar to the rotational dependence of the dissociation rate (see Section 5.1 and Section 4.1). The CO stretch basically does not participate in the dissociation as is evidenced by the fact that the widths for pure CO stretching states consistently have the narrowest widths.

The trends in the level widths shown in Figures 5.2-1 through 5.2-4 are not as dramatic as was expected at the beginning of the SEP experiments because so few levels exhibited homogeneous broadening larger than the minimum detectable value (~0.3 cm^{-1}). This is probably a consequence of the limit for dissociation being significantly higher than was previously thought (~5050cm^{-1})[1,20]. Currently, most calculations predict that the first level to be broadened by more than 1cm^{-1} should be at 6960cm^{-1} {(0,2,3) Γ_{calc}=~3.9cm^{-1}, Γ_{obs}=0.65cm^{-1}}; however, the first level observed in our SEP spectra to be broadened by more than 1cm^{-1} is at 8560cm^{-1} {(0,4,1) Γ_{calc}=2.9cm^{-1}, Γ_{obs}=2.7cm^{-1}} [1]. It will be difficult to determine experimentally from level widths the dissociation limit until an apparatus is built to observe widths at higher resolution and better sensitivity, so that even the smallest broadening of

(< 0.1 cm^{-1}) can be measured. Other areas for possible improvement in future experiments are discussed in the next section (Section 5.3)

5.3 Conclusion and Future Experiments

The spectroscopic study of formyl radical (HCO) described in this thesis accomplished direct measurements of the lifetimes for spectroscopically assignable predissociated rovibrational levels of the $\tilde{X}\,^2A'$-state of HCO. Not just vibrational state specific variations in the measured linewidths were observed but vibrational mode specific variations were observed [29]. From the observed trends in the level widths with vibrational excitation, it can be inferred that the CO stretch normal mode affects dissociation by contributing only to the total amount of energy above the barrier [1]. Energy placed in this mode is unavailable to aid in the removing of the hydrogen [1]. However, the bending normal mode was more effective at promoting dissociation. This is probably due to a shift in the probability amplitude of the vibrational wavefunction toward the exit channel with increasing bending excitation (see Sections 5.1 and 5.2). No levels with CH stretch excited were observed in this work. This lack, for purely experimental limitations, has been overcome by another group and is the subject of current experiments by them [2].

For a few vibrational levels the SEP linewidths were found to have a strong linear dependence upon the amount of angular momentum about the a-inertial axis (CO bond axis, K_a''). This correlation with K_a'' is probably the result of a centrifugal barrier at the linear geometry causing the probability amplitude of the bending vibrational wavefunction to be skewed away from the exit channel.

The final observation was that the observed vibrational level widths do not increase as quickly with energy as the current *ab initio* calculations predict, indicating a need to adjust the present *ab initio* potential energy surfaces for HCO.

Table 5.3-1 gives a comparison of the vibrational level position and widths measured here and the most recent experimental and theoretical investigations.

These results open several questions for further investigation. The two most important topics for further investigation are: what is the effect of the CH stretching mode on the dissociation lifetimes, and what vibrational level is the first level above the dissociation limit. Both of these questions are best answered by building a new SEP apparatus. The changes to the experimental apparatus that should be made to overcome current limitations are to have better sensitivity so that spectra can be recorded at lower laser powers eliminating any affects of power broadening [2] and higher resolution in order to detect even slightly broadened levels. Now that the most interesting levels to probe are known, a higher resolution re-examination would be quicker to accomplish. A sub-Doppler technique would be necessary to examine the first few levels above the dissociation barrier which have longer lifetimes and narrower linewidths. Such a technique that would provide higher sensitivity and better resolution would be a sub-Doppler hybrid-FM technique. The most feasible candidate is polarization-rotation pulsed frequency-modulation detected SEP technique. The pulsed frequency modulated laser would be used as the DUMP laser in conjunction with a standard pulsed dye laser used as the PUMP laser. At the very least this SEP technique would remove the limitation of the detection electronics so that $\tilde{B}$-state levels with extremely short lifetimes (i.e. one quantum of $\tilde{B}$-state CH-stretch) could be used as SEP intermediate states so that $\tilde{X}$-state levels with CH-stretch could be observed.

An alternative way to measure the lifetimes of long lived vibrational levels just above the dissociation limit would be by a PUMP-DUMP-PROBE experiment. An SEP PUMP-DUMP sequence would prepare a long lived $\tilde{X}\,^2A'$-state vibrational level Then a third laser would probe the population of this level versus time after the SEP preparation. This would allow the measurement of the lifetimes for vibrational levels that are not significantly broadened. These vibrational levels have lifetimes ranging from several nanoseconds to about 1 microsecond.

A whole set of experiments could also be performed upon DCO (deuterated formyl radical) to provide additional information about the ground state potential and the dissociation dynamics. Experiments on DCO are currently underway in other research groups [2,30]. Measurements on DCO will have the biggest effect upon the rotational dependence of the linewidths proving if the observed dependence in HCO is caused by a centrifugal barrier [31]. The vibrational effect of isotopic substitution are more difficult to predict [31]. The most noticeable vibrational effect is to increase the total number of bound vibrational states since the bending and CH stretching frequencies decrease.

It is hoped that this thesis will stimulate further experimental and theoretical investigations into the dissociation dynamics of HCO as a model for other unimolecular dissociation reactions.

5.4 References

1. R. N. Dixon, *J. Chem. Soc. Faraday Trans.* **88**, 2575-2586 (1992).
2. E. Rohlfing, Private Communication (1994).
3. J. M. Brown and D. A. Ramsay, *Can. J. Phys.* 53, 2232 (1975).
4. P. R. Bevington, "Data Reduction and Error Analysis for the Physical Sciences, Ed. 1", New York: Mc Graw-Hill (1969); Chapter 4, 6 and Appendix C3.
5. L. Ott, "An Introduction to Statistical Methods and Data Analysis, 3rd Ed.", Boston: PWS-Kent (1988), Chapter 8.
6. R. V. Hogg, E. A. Tanis, "Probability and Statistical Inference, 3rd Ed.", New York: Mac Millan (1988), pp. 220-231.
7. "Igor Pro 2.0 Manual", (Data analysis software), Lake Oswego, Oregon: Wavemetrics Inc. (1994); Page 536.
8. P. R. Bevington, "Data Reduction and Error Analysis for the Physical Sciences, Ed. 1", New York: Mc Graw-Hill (1969); Chapter 2.
9. S. W. Cho, A. F. Wagner, B. Gadzy and J. M. Bowman, *J. Chem. Phys.* **96**, 2799-2812 (1992).
10. S. K. Gray, *J. Chem. Phys.* **96**, 6543 (1992).
11. B. Gadzy and J. M. Bowman in "Adv. Mol. Vibr. and Dynamics" (J. M. Bowman and M. A. Ratner, ed. Vol. 1 B, JAI, Greenwich (1992); K. T. Lee, J. M. Bowman, *J. Chem. Phys.* **86**, 215-225 (1987).
12. R. Schinke, Private Communication (1994).
13. R. N. Dixon, *Trans. Faraday Soc.* **65**, 3141-3149 (1969).

14. R. N. Dixon, *J. Mol. Spectrosc.* **30**, 248-252 (1969).
15. J. M. Bowman, J. S. Bittman and L. B. Harding, *J. Chem. Phys.* **85**, 911 (1986).
16. K. Tanaka and E. R. Davidson, *J. Chem. Phys.* 70, 2904-2913 (1979).
17. P. J. Bruna, R. J. Buenker, and S. D. Peyerimhoff, *J. Mol. Struct.* **32**, 217-233 (1976).
18. G. Herzberg, "Electronic Spectra of Polyatomic Molecules," New York: Van Nostrand Reinhold (1966); Pages 244-245.
19. C. B. Dane, D. R. Lander, R. F. Curl, F. K. Tittel, Y. Guo, M. I. F. Ochsner, and C. B. Moore, *J. Chem. Phys.* **88**, 2121-2128 (1988).
20. W. Cho, W. L. Hase and K. N. Swamy, *J. Phys. Chem.* **94**, 7371-7377 (1990).
21. K. K. Murray, T. M. Miller, D. G. Leopold and W. C. Lineberger, *J. Chem. Phys.* **84**, 2520-2525 (1986).
22. J. M. Dyke, N. B. H. Jonathan, A. Morris and M. J. Winter, *J. Chem. Soc, Faraday Trans. 2*, **77**, 667 (1981).
23. J. S. Francisco, A. N. Goldstein and I. H. Williams, *J. Chem. Phys.* **89**, 3044-3049 (1988).
24. T. H. Dunning, *J. Chem. Phys.* **73**, 2304-2309 (1980).
25. J. M. Bowman, J. S. Bitman and L. B. Harding, *J. Chem. Phys.* **85**, 911-921 (1986).
26. R. N. Zare, "Angular Momentum", New York: John Wiely and Sons (1980); Chapter 1.
27. K. Lee and J. M. Bowman, *J. Chem. Phys.* **86**, 215-225 (1987).
28. D. W. Neyer, X. Luo, and P. L. Houston, *J. Chem. Phys.* **98** (1993).

29. W. F. Polik, D. R. Guyer, and C. B. Moore, *J. Chem. Phys.* 92, 3453 (1990); W. F. Polik, D. R. Guyer, W. Miller, C. B. Moore, *J. Chem. Phys.* 92, 3471 (1990); Y. S. Choi, P. Teal, C. B. Moore, *J. Opt. Soc. Am. B*, 7, 1829-1834 (1990).

30. F. Temps, Private Communication (1994).

31. H. Lefebvre-Brion and R. W. Field, "Perterbations in the Spectra of Diatomic Molecules", Orlando, FL: Academic Press (1986), Chapters 2 and 6.

5.5 Chapter 5 Figure Captions

Table 5.1-1 Summary of the Statistical Analysis for the Intensity Dependence of $\tilde{X}\,^2A'$-State Rotational Linewidths

Table 5.1-2 Summary of the Statistical Analysis for the $N\cdot(N+1)-K_a^2$ Dependence of $\tilde{X}\,^2A'$-State Rotational Linewidths

Table 5.1-3 Summary of the Statistical Analysis for the K_a^2 Dependence of $\tilde{X}\,^2A'$-State Rotational Linewidths

Table 5.1-4 Summary of the Statistical Analysis for the K_a Dependence of $\tilde{X}\,^2A'$-State Rotational Linewidths

Figure 5.1-5 The Dependence of $\tilde{X}\,^2A'$ Rotational Linewidths on K_a

Figure 5.1-6 Anharmonic Bending Potential with K_a Dependent Centrifugal Barrier.

Figure 5.2-1 The Dependence of $\tilde{X}\,^2A'$-State Vibrational Width on Energy Above the Zero-Point Vibrational Level

Table 5.1-1 Summary of the Statistical Analysis for the Intensity Dependence of $\tilde{X}\,^2A'$-State Rotational Linewidths

Vibrational Level	Correlation Coefficients		Goodness of Linear Fit		Coefficients for Linear Fit $\Gamma(FWHM) = A + B \cdot x(area)$			
(v_{CH},v_{CO},v_{bend})	R_S	R_ℓ	Q	χ^2	A	σ_A	B x 10^{-4}	σ_B x 10^{-4}
(0,1,2) ①	0.45	0.59	0.66	10.4	0.38 ③	0.07 ③	1.41 ④	0.77 ④
(0,1,3)	0.19	0.37	0.86	6.1	0.46	0.08	1.21	0.98
(0,2,0)	0.55	0.19	0.25	13.8	0.58	0.06	0.43	0.53
(0,2,1)	0.18	0.91	0.67	12.1	0.30	0.06	1.42	0.19
(0,2,2)	0.72	0.72	0.56	6.8	0.31	0.05	1.04	0.39
(0,2,3)	0.02	0.02	0.70	4.7	0.60	0.07	0.36	0.82
(0,3,0)	0.38	0.52	0.15	12.0	0.33	0.06	1.63	0.59
(0,3,0) ②	0.13	0.59	0.32	15.8	0.25	0.04	1.88	0.42
(0,3,1)	0.84	0.76	0.12	19.1	0.65	0.04	1.30	0.23
(0,3,2)	0.10	0.46	0.16	14.3	0.41	0.07	3.43	1.00
(0,3,2) ②	0.39	0.42	0.00	48.5	0.39	0.03	0.83	0.17
(0,4,0)	0.44	0.62	0.21	15.5	0.42	0.05	2.77	0.57
(0,4,0) ②	0.52	0.65	0.00	65.5	0.39	0.02	0.97	0.15
(0,4,1)	0.50	0.52	0.01	23.7	1.14	0.20	5.56	1.40
(0,4,1) ②	0.49	0.86	0.0	121	0.50	0.04	2.87	0.14
(0,4,3)	0.29	0.08	0.00	38.4	1.95	0.10	0.04	0.26
(0,5,1)	0.39	0.59	0.00	74.8	1.07	0.21	2.1	0.27
(0,6,0)	0.53	0.53	0.00	87.8	0.99	0.08	1.3	0.17

① - Data from Table 4.1-2 unless noted, ② - Data from Table 4.2-2,
③ - Units cm^{-1} and ④ - Units cm^{-1} per arbitrary intensity unit

Table 5.1-2 Summary of the Statistical Analysis for the $N \cdot (N+1) - K_a^2$ Dependence of $\tilde{X}\,^2A'$-State Rotational Linewidths

Vibrational Level	Correlation Coefficient	Goodness of Linear Fit		Coefficients for Linear Fit $\Gamma(FWHM) = A + B \cdot x(area)$			
$(v_{CH}, v_{CO}, v_{bend})$	R_ℓ	Q	χ^2	A	σ_A	$B \times 10^{-4}$	$\sigma_B \times 10^{-4}$
(0,1,2) ①	0.26	0.62	10.8	0.45 ③	0.04 ③	8.7 ④	5.0 ④
(0,1,3)	0.11	0.75	7.6	0.56	0.10	0.46	12
(0,2,0)	0.21	0.24	13.9	0.65	0.04	-4.6	6.1
(0,2,1)	0.25	0.00	61.1	0.80	0.05	-11	5.3
(0,2,2)	0.39	0.12	12.9	0.47	0.05	-7.4	6.8
(0,2,3)	0.20	0.69	4.8	0.60	0.08	4.6	13
(0,3,0)	0.35	0.06	15.2	0.36	0.07	14	7.5
(0,3,0) ②	0.25	0.003	32.6	0.35	0.04	29	17
(0,3,1)	0.24	0.00	46.7	0.95	0.04	-8.9	4.4
(0,3,2)	0.62	0.10	16.0	0.48	0.06	24	8.0
(0,3,2) ②	0.19	0.00	70.0	0.51	0.03	12.7	12.5
(0,4,0)	0.48	0.01	25.9	0.81	0.04	-19	5.2
(0,4,0) ②	0.13	0.00	105	0.58	0.02	17.0	8.5
(0,4,1)	0.44	0.00	29.7	2.33	0.16	-65	22
(0,4,1) ②	0.16	0.00	548	1.59	0.10	-142	37
(0,4,3)	0.26	0.00	36.8	2.03	0.06	-9.3	7.3
(0,5,1)	0.37	0.00	111.7	2.17	0.11	64	710
(0,6,0)	0.14	0.00	147.0	1.68	0.09	9.2	10.0

① - Data from Table 4.1-2 unless noted, ② - Data from Table 4.2-2,
③ - Units cm^{-1} and ④ - Units cm^{-1} per arbitrary intensity unit

Table 5.1-3 Summary of the Statistical Analysis for the K_a^2 Dependence of $\tilde{X}\,^2A'$-State Rotational Linewidths

Vibrational Level	Correlation Coefficient	Goodness of Linear Fit		Coefficients for Linear Fit $\Gamma(FWHM) = A + B \cdot x(area)$			
$(\nu_{CH},\nu_{CO},\nu_{bend})$	R_ℓ	Q	χ^2	A	σ_A	B x 10^{-4}	σ_B x 10^{-4}
(0,1,2) ①	0.04	0.40	13.6	0.50 ③	0.03 ③	170 ④	390 ④
(0,1,3)	0.18	0.75	7.6	0.56	0.10	-73	520
(0,2,0)	0.05	0.22	14.3	0.62	0.02	170	410
(0,2,1)	0.42	0.00	57.5	0.75	0.03	-1100	390
(0,2,2)	0.77	0.73	5.3	0.47	0.03	-1200	410
(0,2,3)	0.20	0.69	4.8	0.62	0.03	170	630
(0,3,0)	0.21	0.02	18.5	0.50	0.02	-260	410
(0,3,0) ②	0.21	0.003	32.8	0.45	0.04	29	17
(0,3,1)	0.32	0.00	48.3	0.90	0.18	-450	290
(0,3,2)	0.03	0.01	25.0	0.66	0.03	-200	430
(0,3,2) ②	0.51	0.00	41.6	0.60	0.02	-370	69
(0,4,0)	0.08	0.00	38.8	0.67	0.02	-280	370
(0,4,0) ②	0.83	0.09	32.5	0.60	0.01	-540	62
(0,4,1)	0.50	0.00	26.5	2.15	0.10	-4800	1400
(0,4,1) ②	0.84	0.00	58.2	2.34	0.10	-3800	170
(0,4,3)	0.12	0.00	38.1	1.98	0.04	-450	750
(0,5,1)	0.04	0.00	134.6	2.66	0.05	460	720
(0,6,0)	0.04	0.00	147.0	1.58	0.09	650	530

① - Data from Table 4.1-2 unless noted, ② - Data from Table 4.2-2,
③ - Units cm^{-1} and ④ - Units cm^{-1} per arbitrary intensity unit

Table 5.1-4 Summary of the Statistical Analysis for the K_a Dependence of $\tilde{X}\,^2A'$-State Rotational Linewidths

Vibrational Level	Correlation Coefficient	Goodness of Linear Fit		Coefficients for Linear Fit $\Gamma(FWHM) = A + B \cdot x(area)$			
(v_{CH},v_{CO},v_{bend})	R_ℓ	Q	χ^2	A	σ_A	B	σ_B
(0,3,0) ①	0.16	0.002	34.0	0.45 ②	0.03 ②	-0.025 ③	0.02 ③
(0,3,2)	0.43	0.00	48.2	0.61	0.02	-0.014	0.01
(0,4,0)	0.76	0.14	30.2	0.62	0.01	-0.11	0.01
(0,4,1)	0.98	1.00	0.17	2.73	0.09	-0.94	0.06

① - Data from Table 4.2-2 ② - Units cm^{-1} and

③ - Units cm^{-1} per arbitrary intensity unit

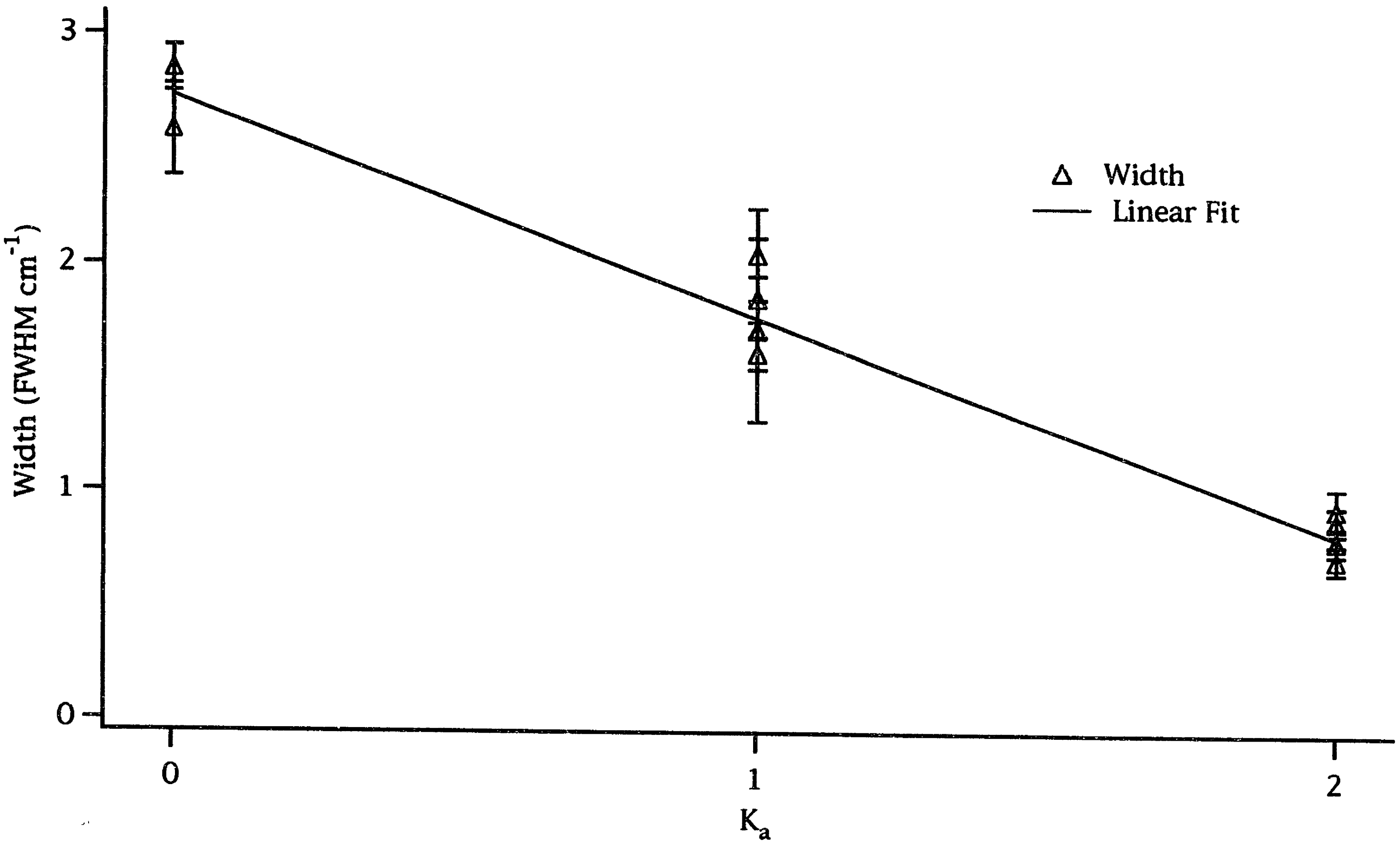

Figure 5.1-5 The Variation of $\tilde{X}$-State (0,4,1) Rotational Linewidths with K_a

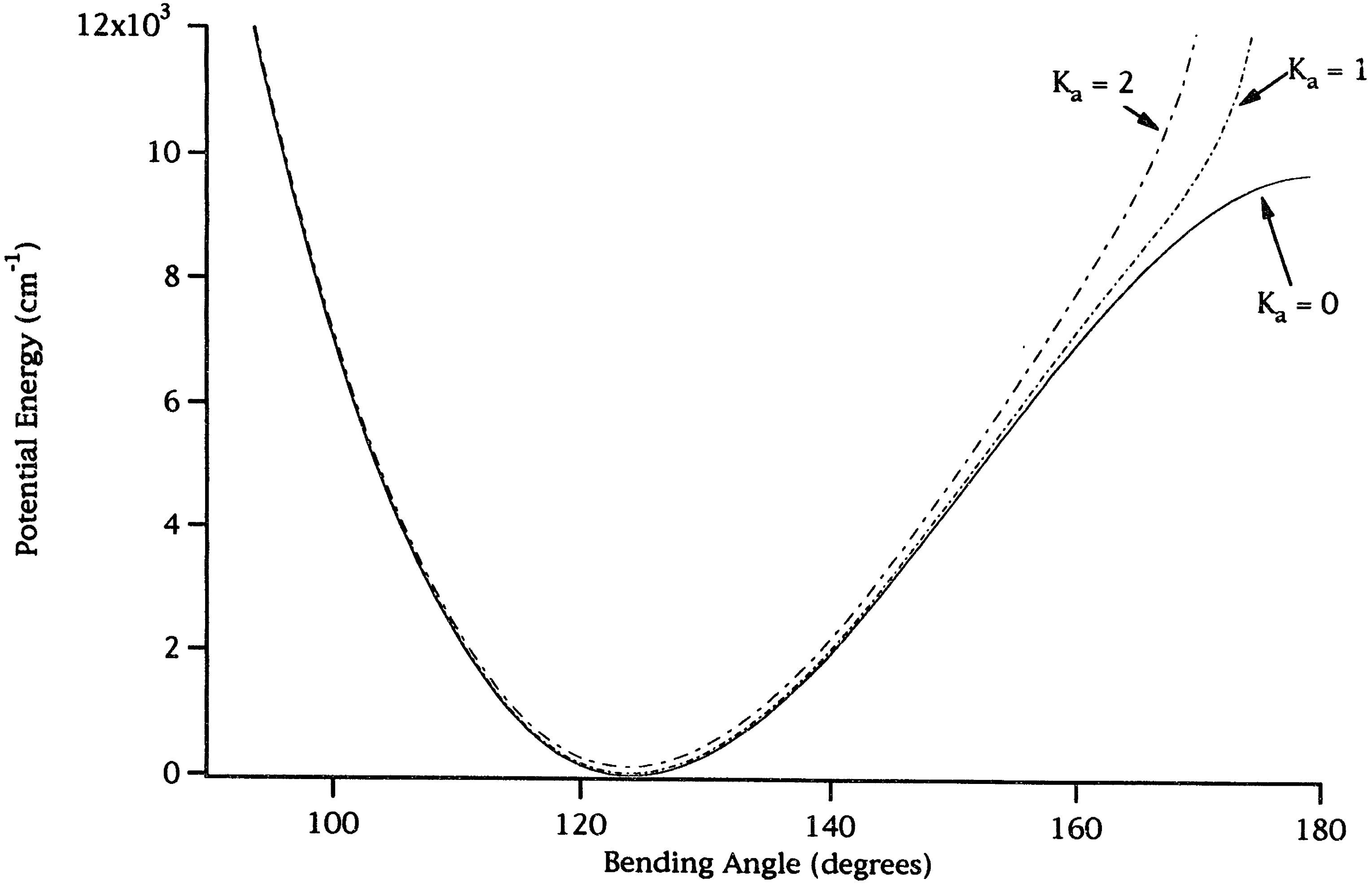

Figure 5.1-6 Anharmonic Bending Potential with Centrifugal Barrier

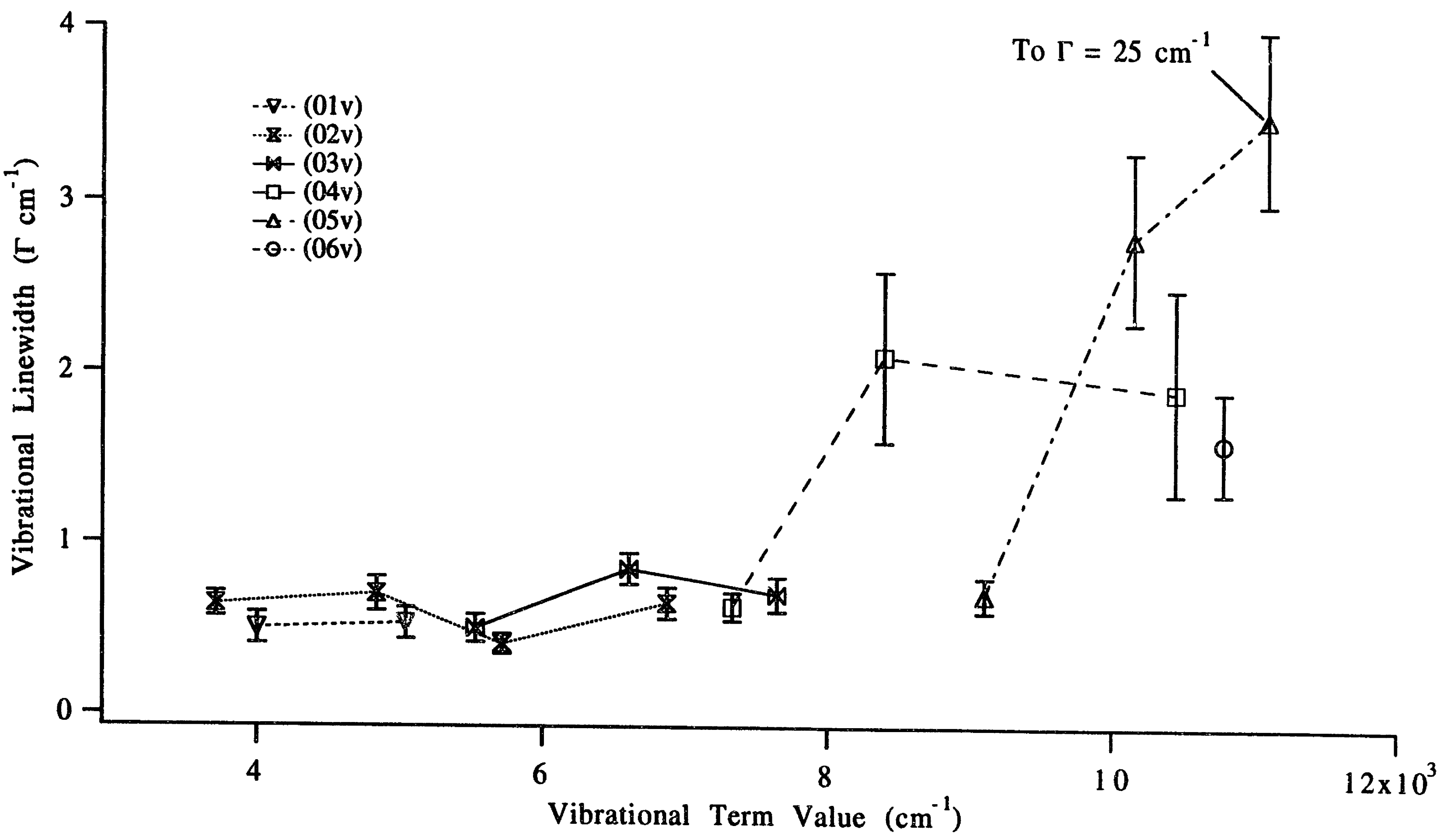

Figure 5.2-1 The Dependence of $\tilde{X}$-State Vibrational Width on Energy Above the Zero-Point Vibrational Level

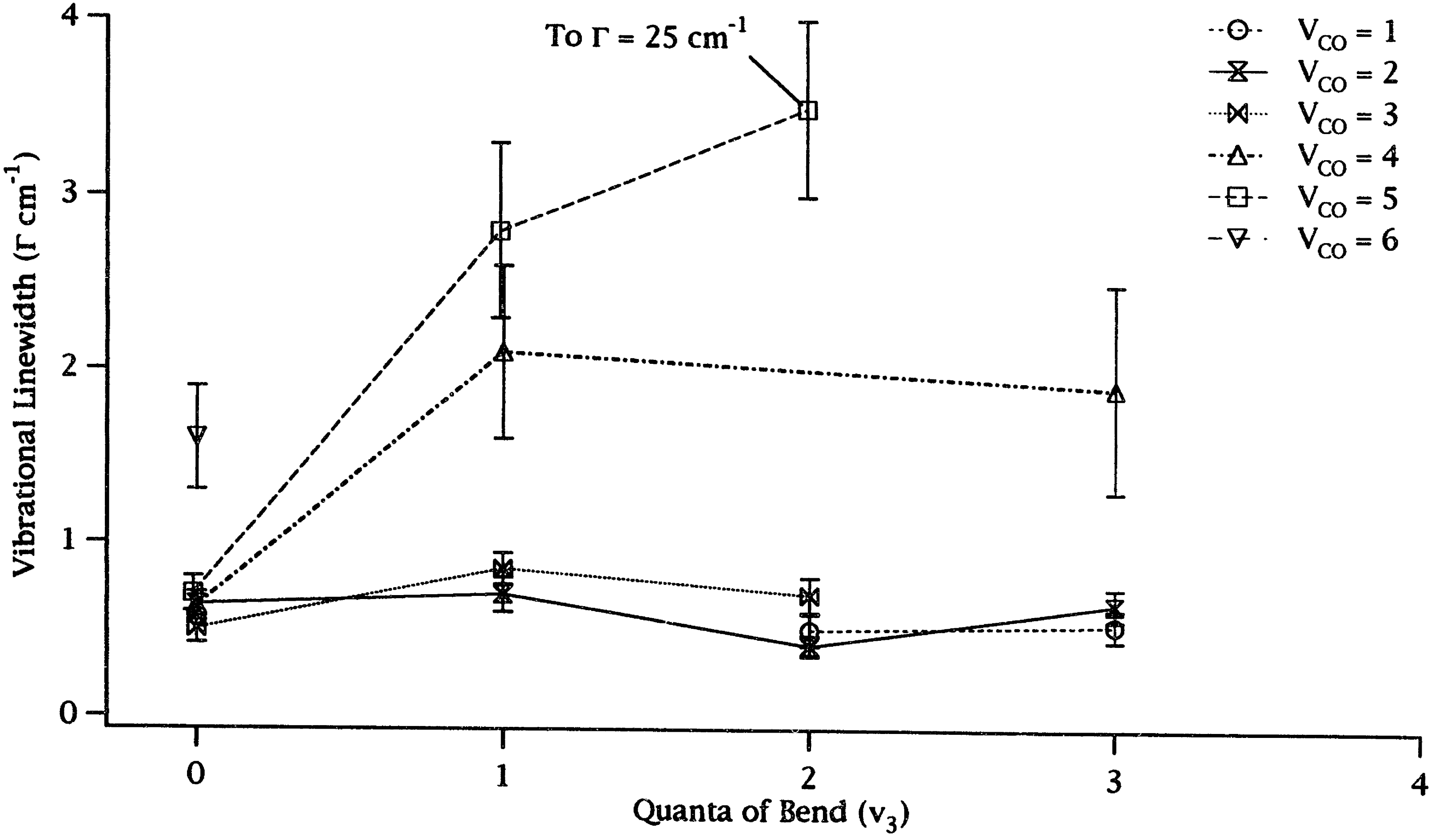

Figure 5.2-2 The Dependence of $\tilde{X}$-State Vibrational Width on Number of Bending Quanta for Constant CO-Stretch Excitation

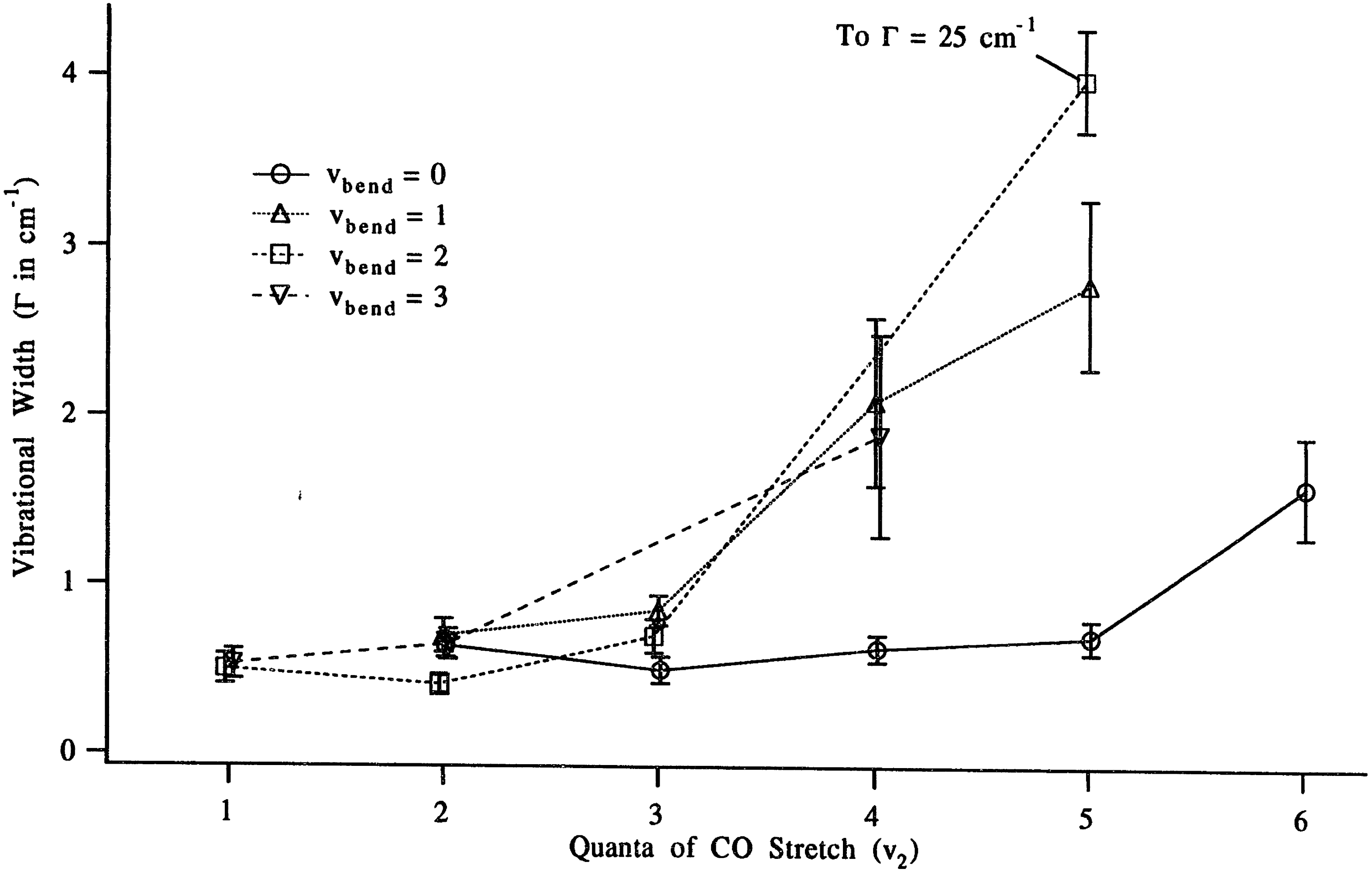

Figure 5.2-3 The Dependence of $\tilde{X}$-State Vibrational Width on Number of CO-Stretching Quanta for Constant Bend Excitation

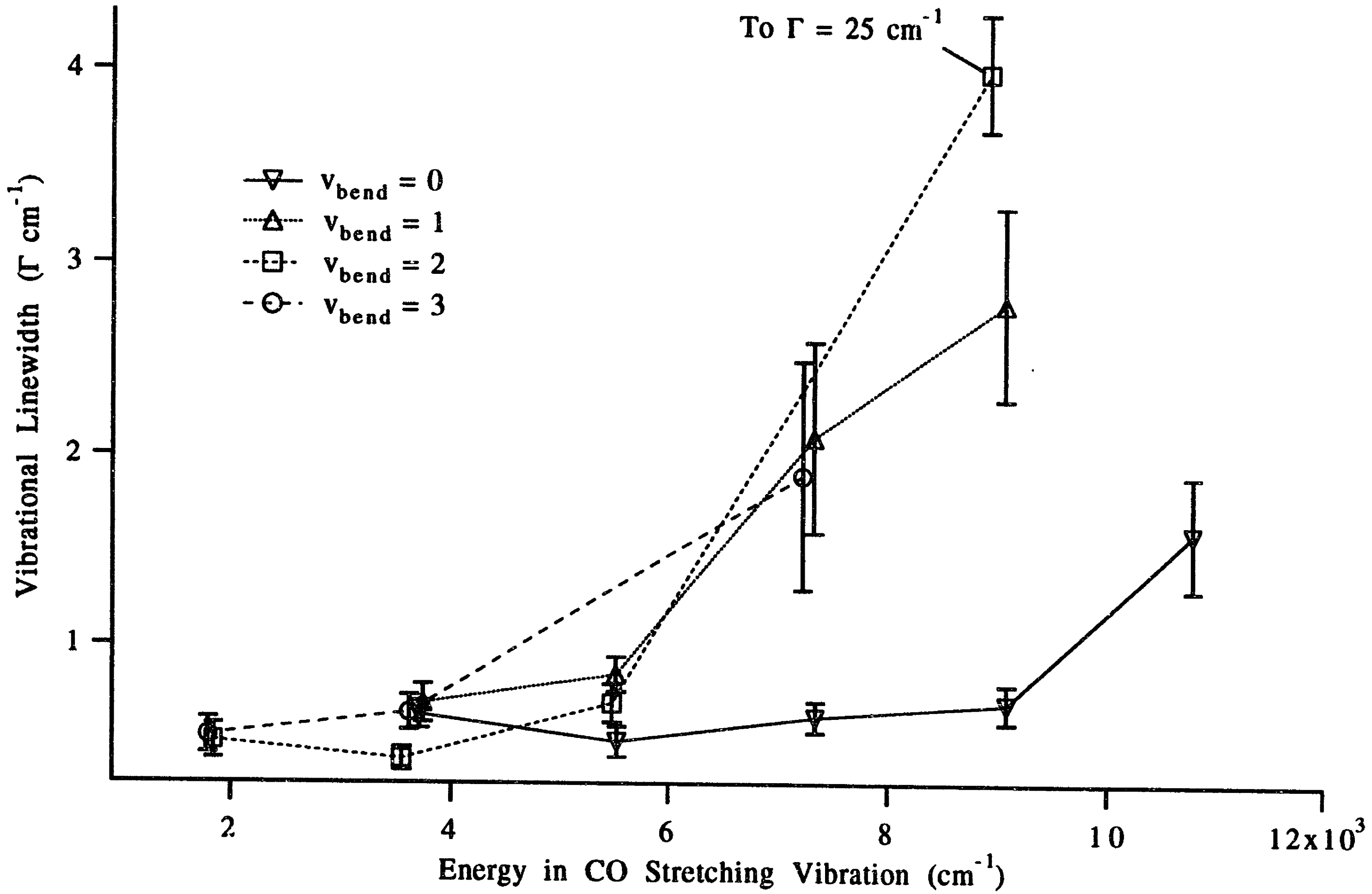

Figure 5.2-4 The Dependence of $\tilde{X}$-State Vibrational Width on Vibrational Energy in CO Stretch for Constant Bend Excitation

Table 5.3-1 Table Comparing $\tilde{X}\,^2A'$-state Term Values and Widths

	Measured This Work		Measured Reference (2)		Calculated Reference (12)	
$(\nu_{CH},\nu_{CO},\nu_{bend})$	Term Value	Γ FWHM	Term Value	Γ FWHM	Term Value	Γ FWHM
	cm^{-1}	cm^{-1}	cm^{-1}	cm^{-1}	cm^{-1}	cm^{-1}
(0,1,2)	3 999.27 (5)	0.50 (9)			3974.9	0.0
(0,1,3)	5 031.65 (2)	0.53 (9)			5006.6	5.6×10^{-5}
(0,2,0)	3 711.40 (4)	0.64 (7)			3664.4	1.5×10^{-5}
(0,2,1)	4,824.27 (4)	0.7 (1)			4735.5	
(0,2,2)	5,715.76 (3)	0.41 (6)			5785.7	0.002
(0,2,3)	6,861.22 (4)	0.65 (9)			6812.5	0.12
(0,3,0)	5 529.81 (7)	0.50 (8)	5530.0	0.23	5460.0	1.3×10^{-4}
(0,3,1)	6 597.65 (4)	0.85 (9)	6597.5	0.46	6529.0	0.66
(0,3,2)	7,643.74 (7)	0.7 (1)	7645.5	0.28	7575.0	0.58
(0,4,0)	7 323.43 (4)	0.63 (8)	7323.4	0.24	7232.0	0.023
(0,4,1)	8 390.71 (9)	2.1 (5)	8388.3	1.7	8290.0	6.5
(0,4,3)	10,448.51 (7)	1.9 (6)				20
(0,5,0)	9,091.97 (3)	0.70 (1)	9090.0	0.18	8980	0.16
(0,5,1)	10 151.5 (3)	2.8 (5)	10147.0	1.0	10037	1.8
(0,5,2)	11 196. (1)	30. (8)	11195.1	33	11067	14
(0,6,0)	10 836.1 (2)	1.7 (3)	10831.7	0.54	10704	0.39

CHAPTER 6

Fabricated Equipment

6.1 Detection Electronics

High Voltage Power Supply

A single high voltage power supply was used to power both photomultiplier tubes used in the SEP apparatus. A variable voltage divider was used to split the single supply into two independent power supplies, Figure 6.1-1. This design allowed a separate voltage adjustment for each of the two photomultiplier tubes which helped match their response. Great care was taken to insulate all high voltage wiring from contact with the chassis. The splitter was constructed in a 4" X 4" X 4" dicast aluminum chassis (Bud) which was electrically insulated from the laser table and the instrument racks. These precautions did not eliminate all grounding problems and it was necessary to wrap the coaxial cables routed from the high voltage splitter to the photomultiplier tubes around separate, large, ferrite balun toroids (Amidon). In addition, forming a choke by coiling 6 feet of the cable from the power supply to the splitter into a 4 inch diameter coil and fastening with cable ties further reduced RF interference.

High Voltage Power Supply Parts List

R1	100kΩ 10 Turn insulated shaft
R2	1.9MΩ 2 Watt
C1	0.1µF 3kV Ceramic

Photomultiplier Tube Housing

The photomultiplier tube (PMT) housing was machined from brass using a previously existing design [1]. Minor modifications were made to allow optimization of the rotational alignment of the tube in the housing and to ease fabrication. The heart of the photomultiplier tube housing was a stock socket which was prewired with the necessary voltage divider components (Hamamatsu). This Hamamatsu base was wired for pulsed operation. The schematics for wiring the other components in the photomultiplier housing are shown in Figure 6.1-2. Only two capacitors (C1, C2) were added inside of the actual photomultiplier housings. The remaining components, a resistor network, was constructed inside a small dicast aluminum box (Pomona) and mounted outside of the photomultiplier tube housing to allow easy removal when necessary.

This resistor network was designed to provide three functions: to resistively terminate the photomultiplier tube, to impedance terminate the signal cable and to provide variable signal attenuation. The termination of the PMT was designed to be 220Ω, which formed an RC circuit with C1 and the stray capacitance (~12pF) of the photomultiplier tube and socket. This low pass RC circuit had a bandwidth (3dB) of approximately 100MHz. The trimmer capacitor in each housing (C1) was set initially to its minimum value and then adjusted to match the pulse responses of the two photomultiplier tubes. During this adjustment each photomultiplier was terminated each with a single 50Ω terminator.

The signal cable terminator has an impedance close to 50Ω but these resistors function more as an attenuator to keep pulses reflected by the preamplifier from being re-reflected by the PMT, causing ringing. The miniature variable resistor (R3) was used as a further adjustment to more closely match the gain responses of the two tubes. Typically, all adjustments to the photomultiplier tube housings and to the high voltage supplies were made while viewing wave forms from HCO fluorescence. The subtraction function of a high speed scope was used to display the differences in the outputs of the two tubes.

Photomultiplier Tube Housing Parts List

R1	1.2kΩ 1/4-Watt
R2	82Ω 1/4-Watt
R3	25kΩ Miniature potentiometer
R4	470Ω 1/4-Watt
R5	12Ω 1/4-Watt
C1	1-5pF Trimmer
C2	0.47µF 3kV Ceramic
SKT	Hamamatsu socket E717-21

Differential Amplifier

The schematic for the differential amplifier is shown in Figure 6.1-3. This amplifier was similar in design to those used in previous SEP experiments [2]. The amplifier was constructed using a point to point wiring or "ugly bug" technique on a piece of perforated board (Vector) [3]. Wire wrap IC sockets were used but the pins were cut short and no wire wrapping was done. All lead wires were kept as short as possible and small diameter 50Ω coaxial cable (RG-174) was used for all signal connections. Ground isolated BNC jacks were used and small copper braid, actually desoldering braid, was used to connect all BNC grounding lugs to a common chassis ground point. The 100Ω resistor (R2) was soldered directly to the potentiometer (R1) which was mounted on the chassis front. The use of a large value potentiometer in parallel with a resistor to provide a 50Ω input termination for the differential amplifier reduced stray input inductance and capacitance . It would have been better to replace the potentiometer and resistor (R1, R2) with one of the now available 50Ω constant impedance attenuators. The 50Ω resistor (R6) at the amplifier output was a 50Ω feed-through terminator mounted externally on the output BNC jack. The 5-pole low pass Butterworth filter on the output was designed for a cut off frequency of 60MHZ (3dB) and was contained in an external dicast box (Pomona) to allow easy substitution and evaluation of other filters [3, 4]. All other components were mounted as close to the chips as possible with grounding buses provided by large gauge bare copper wire with all grounds tied to the common chassis grounding point to minimize grounding loops.

The differential amplifier board was mounted on one side of a 4" X 4" X 4" dicast aluminum chassis (Bud). On the opposite side of the chassis was mounted the board containing the four required linear power supply circuits -- one for each of the four needed voltages. These power supplies are detailed later in this section. An attempt to keep the power supply leads well separated from signal leads was made. The differential amplifier chassis was painted and electrically insulated from the metal laser table.

The completed differential amplifier was aligned by applying a high speed (20ns - 500ns) two volt square wave pulse. The pulse was split by a zero degree hybrid combiner (Mini-Circuits) and fed to the differential amplifier inputs. The output filter was removed during the alignment procedure and *both* ends of the output cable were 50Ω terminated to eliminate ringing. The input cable lengths and the attenuators (R1, R2) were adjusted until the best balance was obtained. One of the attenuators was then glued down and the other roughly calibrated by inserting fixed attenuators into the opposite input and reachieving balance. At large attenuations the differential amplifier would easily break into severe self oscillations. With all fixed attenuators removed and the amplifier again balanced, the trim potentiometers on the differential amplifier board were adjusted for the best shape in the output wave form.

The output of the differential amplifier had a positive three volt DC offset. Ideally, the output of the amplifier should be a flat line even during a pulse provided the two input signals are identical, Figure 6-4. However, a small ring was present at the beginning and end of the pulse. Also during the pulse, the output was not perfectly flat.

Adjustments to the attenuator affected primarily the level during the pulse and the internal trimmers affected mainly skew and ringing. A small capacitor (C4) was added to the output of the video line driver to help reduce this ringing and did not significantly affect other performance characteristics of the amplifier. This ringing could never be eliminated entirely but its minimization and overall symmetrization was sought. A calibrated step attenuator was inserted between the hybrid combiner and one of the inputs and the linearity of the amplifier was checked using 40ns pulses and was found to be in the range of 2-3% [5,6]. The maximum difference between input channels was found to be approximately 200mv and the maximum input signal was 2 volts. The overall voltage gain of the differential amplifier was approximately ten and the broad band output noise was on the order of 10mV-15mV peak to peak.

Differential Amplifier Parts List

U1	μA733M Differential Video Amplifier
U2	OEI9911 Video Line Driver
R1	100Ω 10 turn
R2	110Ω 1/4-Watt
R3	2.7kΩ 1/4-Watt
R4	10kΩ 15 turn trimmer
R5	100kΩ 15 turn trimmer
R6	50Ω 2-Watt Terminator
C1	150pF Ceramic
C2	0.1μF Ceramic
C3	47μF Tantalum
C4	3.4pF Ceramic (see text)
C5	47pF NPO Ceramic
C6	127pF NPO Ceramic
L1	5 Turns @ 8 turns per inch of #22 magnet wire 1.75cm dia. air core

Preamplifier

The preamplifiers incorporated a high bandwidth hybrid pulse amplifier (Le Croy). The connections for the pulse amplifier test board are shown in Figure 6.1-5. The test board for the amplifier was mounted in a 4" X 4" X 4" dicast aluminum chassis (Bud) along with a board containing the three required linear power supplies and filters. The supplied Lemo connectors were removed from the test board and replaced with small diameter coax cable (RG-174). These cables were routed to ground isolated panel mounted BNC jacks. A 51Ω terminating resistor was clipped from the test board allowing the amplifier to drive two 50Ω external loads. A new standard value 51Ω terminating resistor (R1) was soldered directly to each output BNC jack. The alignment procedure in the literature accompanying the pulse amplifier was followed to bring each preamplifier back to specifications after the test board was mounted in the chassis [7].

Preamplifier Parts List

TB	Le Croy VV100BTB test board for the VV100B hybrid pulse amplifier.
R1	51Ω 1/4-Watt

Power Supplies

A doubly regulated scheme was used to power the detection electronics. This scheme was chosen to reduce RF interference and to simplify power distribution. The ±24V power supply, Figure 6.1-6, consisted of two single voltage switching power supplies (24V, Lambda) that were mounted with good thermal contact inside a standard rack mount chassis. The AC power was filtered by an RF interference filter that also incorporated surge and spike suppression (Corcom). The hash chokes (L1) and filter capacitors (C1) were mounted on barrier strips near the rear panel power connectors. These chokes and filter capacitors were retrofitted to the power supply to reduce RF pickup and power supply noise. The power cords from the ±24V power supply to the various detection electronics were made from good quality shielded microphone cable. The output noise under a one ampere load was approximately 200mV peak to peak.

A separate linear power supply, Figure 6.1-7, was constructed for each voltage required by the detection electronics. These power supplies were based on common one ampere voltage regulator chips [3,4,8,9,10]. No heat sinking was required for the regulator, but due to current foldback with a ±24V supply, this design should not be used to provide more that 250mA [8]. Typically three or four of these linear supplies were constructed on a single piece of perforated board (Vector) using point to point wiring. These power supplies were then mounted inside the enclosure for each piece of detection electronics. Note that the schematic in Figure 6.1-7 was drawn for a positive voltage supply. For a negative voltage supply the polarities of the capacitors need to be switched and the different pin outs for negative voltage regulators remembered. For each voltage produced, one RF filter was constructed and inserted at the output to the power supply--on the power supply board for the preamplifiers and on the differential amplifier board for the differential amplifier. The final voltage ripple was approximately 600μV peak to peak. The actual output voltage was within one percent of the specified voltage.

Power Supplies Parts List

PS	24V 2.1A LVS-45 Lambda switching power supply
FL	Corcom AC-line RFI filter with integral surge suppression
FS	3A fast blow fuse
U1	Three terminal 1A voltage regulator 78xx or 79xx
L1	10mH hash choke
RFC1	6 Hole ferrite bead
C1	0.5µF Ceramic
C2	1000µF Electrolytic
C3	1µF Tantalum
C4	47µF Tantalum
C5	2000µF Electrolytic
C6	680pF Ceramic
C7	100µF Tantalum
C8	0.1µF Ceramic

6.2 Auto-Tracker

General Description

The auto-tracker was a servo-control system to adjust the phase matching angle of an optical second harmonic generator crystal. It exploits a phenomenon that occurs when a laser beam passes through a doubling crystal with an angle of incidence different from the optimal phase matching angle. The birefringence of the crystal caused this mismatch in the phase matching angle to produce a lateral displacement of the second harmonic beam.

This displacement of the second harmonic beam was monitored by a 2-channel split photodiode. There are many different schemes for using the differential illumination of these two photodiode channels to drive a motorized crystal mount. However, most of these designs, when put into actual use in a laboratory, had bothersome drawbacks. In an attempt to remedy some of most severe drawbacks, this new auto-tracker was conceived.

The first design goal for the new auto-tracker was to implement as much of the auto-tracker in software as possible. This design relying heavily on software allowed more sophisticated controls to be envisaged for tracking the doubling crystal's phase matching angle. It also made design changes easier, since by changing only a few lines of computer codes the tracker could be adapted to suit differing experimental conditions (e.g. alterations in laser power, laser repetition rate and laser scanning rate); therefore, the increased usage of software decreased the need for operator intervention.

The second design goal was to use a stepping motor controlled crystal mount. A stepping motor controlled crystal mount provided precise, controlled crystal phase matching angle adjustments.

The last design goal was to eliminate the use of sample and hold circuits to acquire photodiode signals. Providing a stable trigger signal for driving these circuits in previous auto-tracker designs was accomplished in the laboratory with difficulty. The photodiode interface, Figure 6.2-3 and Figure 6.2-4, provided for low noise measurements of the photodiode output asynchronous of the laser firing.

A block diagram of the major auto-tracker components is provided in Figure 6.2-1. The computer used in the auto-tracker was a surplus IBM PC-XT with a 12-bit data acquisition (Data Translations DT-2801) card installed. This card provided for 16 channels of single-ended analog to digital (A/D), although only 3 were utilized, and for 16 bits of bi-directional digital I/O. The card was operated in a triggered acquisition mode which caused the board to wait after being issued a software command. This delay ended once an external trigger pulse was received. The trigger interface is more fully described below. The digital to analog ports of the data acquisition card were not used, but a future use for these is mentioned in the section below describing the photodiode interface.

A stepping motor (Hurst, 24V, 32 steps/Rev) was used to drive the mechanical crystal mount. (The details of this mount can be found in Reference 2). The motor was attached to the crystal mount by a 10:1 reduction drive consisting of two toothed pulleys and belt (Pic Wic). The stepping motor was operated by a purchased stepping motor controller board (Hurst, EPC-013). This stepping motor controller board provided flexible control of the motor stepping rate and direction. Additionally, all control inputs were TTL compatible, which made interfacing the stepping motor controller board with the computer simple. Phototransistor opto-isolation were used between the stepping motor controller board and the computer digital I/O ports to prevent noise from the controller board from reaching the computer A/D signal inputs.

Two power supplies provided power for the entire auto-tracker. The first power supply was a triple output linear power supply (Lambda, ±15V, +5V, 2AMP). The ±15V outputs were used to power only the photodiode interface. The +5V output powered the triggering and remote control circuitry. The second power supply (Lambda, +24V, 3AMP), a switching power supply, provided power to the stepping motor controller card and stepping motor. The use of two separate power supplies had the benefit of reducing the amount motor noise entering the computer A/D inputs.

A brief outline of the computer algorithm is shown in Figure 6.2-2. The entire control algorithm was in the software, making it easy to change and embellish the minimal program outlined in this figure. The control sequence begins with the computer, in a hardware wait state caused by the data acquisition card's digitize on trigger command. When a trigger pulse was received from the trigger circuit (Figure 6.2-7) the data acquisition card digitizes three A/D channels, one for each photodiode channel. The length of time since the last trigger was then measured with the computer's hardware clock. The repetition rate for the trigger pulses was then calculated from the timing data. If the repetition rate had changed, then the division ratio of the trigger interface and the photodiode interface was adjusted. The output of the Trigger Interface should provide a trigger pulse train at approximately 1Hz to the data acquisition board.

The next step in the control sequence was to condition the raw digitized photodiode signals and produce a measure linearly proportional to the laser power incident on the photodiodes. The Photodiode Interface did not have a perfectly linear response. Its response was, however, reproducible. The actual response function of the photodiode interface was measured using a 10Hz series of 500nsec square wave pulses and a calibrated step attenuator. This measured response function was then fit to a second order polynomial, and this function was used to correct the raw photodiode signal. The correction function differed slightly for each of the three photodiode channels.

The third photodiode channel was used to provide a monitor of the total power in the doubled laser beam. This provided an additional check on the proper operation of the laser system, and provided a measure for automatically optimizing the phase matching angle. After the linear responses for the photodiode Channel 1 and Channel 2 were determined a normalized error figure was calculated using the formula: (Channel 1 - Channel 2)/(Channel 1 + Channel 2). The sign of the error figure determined the direction of the stepping motor rotation. While, the absolute magnitude of the error figure determined the angle through which the crystal needed to be rotated, in order to bring the crystal back to its optimum phase matching angle. This rotation angle was calculated for a given normalized error signal from an experimentally determined forth order polynomial. This function needed to be determined once for each different doubling crystal used with the auto-tracker. The function was measured by first optimizing the phase matching angle, and then changing the frequency of the dye laser by a small amount. The error figure was then recorded and the stepping motor stepped, noting the number of steps needed to bring the crystal back to its optimum phase matching angle. This procedure was repeated several times, and the number of steps versus the error figure was fit to a fourth order polynomial.

The final stage in the control sequence was to determine if, at the current laser repetition rate, the number of motor steps needed to optimize the phase matching angle could be made before the next trigger pulse. If there was enough time before the next trigger pulse, then the motor could be incrementally adjusted (one step at a time) the required number of steps. If not, then one of the on-board oscillators contained within the stepping motor controller card was enabled for a time to slew the motor. The length of time that one of these free running oscillators remained enabled was determined by dividing the number of motor steps required by the frequency of the oscillator (100Hz or 800Hz). If necessary these oscillators were left on for more than one subsequent trigger pulse.

Photodiode Interface

The schematic for the Auto-Tracker Photodiode Interface is shown in Figure 6.2-3 and Figure 6.2-4. The interface was constructed using point to point wiring on a piece of perforated 5" X 3" (Vector) board. All lead wires were kept as short as possible and the board was mounted in a dicast aluminum box (Pomona 5 1/2" X 4" X 1 1/2"). Three ground isolated BNC jacks, one for each photodiode channel, and a banana jack, to provide +9V to power the photodiodes, were mounted on one side of the chassis. On the other side, a single nine-pin 9mm video connector provided all power and signal connections to the main auto-tracker chassis.

For the three photodiode channels a total of four quad-operational amplifiers (U1) were utilized. One operational amplifier chip was dedicated for each of the three photodiode channels. From the fourth quad-operational amplifier chip, one operational amplifier was used to complete the circuitry of each photodiode channel, Figure 6.2-3 and Figure 6.2-4.

The ±15V power supply lines for each operational amplifier chip were bypassed at each chip with 47μF tantalum capacitors. The main ±15V power supply lines were bypassed with 0.1μF ceramic and 100μF tantalum capacitors upon entering the chassis.

In Figure 6.2-3, the first two operational amplifiers form a peak detector [4] along with two capacitors (C1, C2), a diode (D1) and a resistor (R1). The droop rate of this peak detector was chosen to be approximately 100msec. By choosing this droop rate the output of the peak detector will fall to approximately half the initial value before the next pulse arrives from the photodiode with a 10Hz laser system. This peak detector has the effect of converting the short pulses from the output of the photodiode into a low frequency saw-tooth wave form. The amplitude of this saw-toothed wave form tracked the peak amplitude of the photodiode signal. Scattered light with amplitude less than half the amplitude of the photodiode signal was completely rejected by the peak detector. Although this peak detector will work acceptably at laser repetition rates faster than 10Hz, some laser shots with this rate will be effectively ignored. It would probably be desirable to change the droop rate of the peak detector to more closely matched the laser repetition rate to avoid loosing shots [4]. On a system with variable repetition rates the peak detector's time constant should be set 75-80% the reciprocal of the minimum laser repetition rate. In addition, the photodiode channel software calibration should also be made repetition rate dependent.

The final operational amplifier (U1) on Figure 6.2-3, the remaining resistors (R2, R3, R4) and the capacitor (C3) formed an integration circuit with a time constant of 1 second [4]. This integrator performed a 1 second average of output of the peak detector. The integrator output a DC voltage which tracked the amplitude of the saw-tooth wave form from the peak detector. Again the integrator circuit was optimized for a 10Hz system but may perform acceptably at faster repetition rates. The time constant of the integrator is set by R4, which should be adjusted to average approximately ten laser pulses for use at different repetition rates. For use with variable repetition rate systems R4 should be replaced by a voltage variable resistor. This would allow the time constant of the integrator to be set from software, using one of the data acquisition card's digital to analog converters.

The first operational amplifier along with four resistors (R5, R6) and two capacitors (C4, C5), in Figure 6.2-4 forms a voltage-controlled voltage-source two-pole low-pass Bessel filter with a 3-dB cut-off frequency of 0.6Hz [4]. This type of filter was found to be necessary since the output of the integrator contained a large AC component at the laser repetition rate. This Bessel low-pass filter was experimentally found to be the filter that perform the best in this application. The cut-off frequency for this filter may also need to be adjusted for laser repetition rates of other than 10Hz. For variable repetition rate systems functioning between 10 to 100Hz, it is recommended to set the cut-off frequency at 3 to 5Hz and to change the filter from a 2-pole to a 4-pole response.

The second operational amplifier and R7, seen in Figure 6.2-4, form a unity gain inverting amplifier. This buffer amplifier drives a RC low-pass filter (R8, C6) and the cable to the main auto-tracker chassis.

Photodiode Interface Parts List

U1	TL074 Low Noise JFET Quad Operational Amplifier
D1	1N4148 Small Signal Diode
C1	0.1μF Ceramic
C2	500pF Ceramic
C3	0.47μF Epoxy Dipped Ceramic
C4	1.5μF Tantalum
C5	1.5μF Tantalum
C6	0.1μF Tantalum
R1	560kΩ 1/4-watt
R2	1.0MΩ 1/4-watt
R3	5.1kΩ 1/4-watt
R4	1.0MΩ 1/4-watt
R5	82kΩ 1/4-watt
R6	22kΩ 1/4-watt
R7	1.0kΩ 1/4-watt
R8	10Ω 1/4-watt

Auto-Tracker Photodiode

The circuit schematic for the auto-tracker's split photodiode is shown in Figure 6.2-5. The photodiode (PD) and the discrete parts (R1, R2 and C5) were housed in a small (2" X 2" X 1 1/2") chassis mounted on a stainless steel post (Newport, SP-4). The signals from the two photodiodes independently excited the chassis through ground isolated BNC jacks. The 9V power for the photodiode was brought into the chassis from the Photodiode Interface through a single conductor shielded cable.

The small 9V power supply for the split photodiode (shown in Figure 6.2-5) consisted of: U1, C1, C2, C3 and C4. This power supply was powered by the main +15V power rail of tne Photodiode

Interface and was housed in the Photodiode Interface's chassis. This supply provided up to 100mA of current.

Auto-Tracker Photodiode Parts List

U1	LM78L09AC 9 volt Regulator
PD	FND-100Q Split Photodiode
C1	0.1µF Ceramic
C2	4.7µF Tantalum
C3	10µF Tantalum
C4	220µF Tantalux
C5	100pF Ceramic
R1	1.0kΩ 1/4-watt
R2	300kΩ 1/4-watt

Remote Control

Complete manual control of the auto-tracker's stepping motor functions was provided by the Remote Control pendent. The pendent was mounted remotely from the rest of the auto-tracker assembly. A long 9 conductor shielded computer cable connected the pendent to the main auto-tracker chassis.

The schematic for the pendent is shown in Figure 6.2-6. The many switches were mounted in a small (5" X 4" X 2") dicast aluminum box. Each stepping motor function, controlled manually by the pendent, was also automatically controlled by the computer through the data acquisition card's digital I/O lines. Opto-isolators between the computer's digital I/O lines and the stepping motor controller card were necessary in the elimination of motor noise reaching the A/D inputs.

Auto-Tracker Trigger Circuit

The auto-tracker was synchronized with the laser repetition rate by TTL pulses sent to the Trigger Input. These pulses could arrive at any time relative to the laser firing, since these pulses only provide a measure of the laser's repetition rate. This circuitry (pictured in Figure 6.2-7) allowed for the division of the repetition rate of the raw trigger signals by a factor of 5 or 10. This division factor was determined by the computer through one of the digital I/O lines of the data acquisition card. The trigger circuitry was also capable of manually producing of a single trigger pulse. This manual trigger pulse, used in trouble shooting, was activated by a push button mounted on the front panel of the Auto-Tracker chassis.

Auto Tracker Trigger Parts List

U1	SN74LS176 Decade Binary Counter
U2	SN74LS08 Quad Positive-AND Gates
U3	SN74LS32 Quad Positive-OR Gates
U4	SN74LS121 Retriggerable Monostable Multivibrator
C1	0.1μF Ceramic
R1	27kΩ 1/4-watt

6.3 Laser Triggering

AC Line Synchronizer

Several times during the course of these experiments it was useful to synchronize the firing of the lasers with the 60 Hz of the AC power line. This phase locking helped reduce noise picked up from other pieces of laboratory equipment. The synchronizer, Figure 6.3-1, consisted of three units: an input attenuator and Schmitt-Trigger, divide by six counter and a TTL pulse generator. The AC line wave form was sampled through a power transformer (120VAC to 18VAC). The synchronizer circuitry was built using point to point wiring on a piece of perforated board (Vector) and housed with a miniature 5V DC power supply in a small aluminum enclosure. The 10µsec 10Hz TTL pulse output was then used as the master triggering clock for the experiment.

AC Line Synchronizer Parts List

U1	SN74LS04 Hex inverter
U2	SN74LS09 Quad AND gate
U3	SN74LS74 Dual flip-flop
U4	SN74LS121 Dual Monostable
U5	SN74LS128 50Ω Line driver
R1	4.8kΩ 1/4-Watt
R2	1.5kΩ 1/4-Watt
R3	6.8kΩ 1/4-Watt
R4	1.0kΩ 1/4-Watt
R5	27kΩ 1/4-Watt

Variable Pulse Delay Generator

Variable time delay for the various TTL trigger pulses for the lasers was provide by a circuit based on a dual monostable multivibrator integrated circuit with Schmitt-trigger inputs (SN74LS221) [11]. Six separate delay circuits were built with variable delays and housed in a single rack mounted chassis containing a power supply [12]. The time constants for the monostables were set by a single external resistor and capacitor. The first of the dual monostables were triggered by an external pulse applied to the Schmitt-trigger input. The capacitor for this first monostable had been chosen to set the range of the delay generated (0-45μsec, 0-900μsec and 0-2300μsec). A ten turn potentiometer was used to adjust the delay within the range fixed by the capacitor. Even though temperature stable capacitors (NPO type) the delay circuit exhibited significant warm up drift. The drift was minimized in practice by always leaving the delay generator powered up.

The second monostable stage was used to provide a clean 500nsec square wave output pulse delayed from the leading edge of the input pulse by the delay set from the first monostable. In order to drive the long coaxial cables (35 feet) leading to the lasers the output of the second monostable was routed through a 50Ω line driver (SN74LS128). The amplitude of the output was found to be slightly too low to reliably trigger the laser when the circuit was powered by 5 volts. After the power supply was adjusted to provide 5.8 volts, the maximum the chips could tolerate, no further triggering problems were experienced. The total pulse to pulse jitter in the delay period was on the order of several nanoseconds.

Laser Triggering Interfaces

In order to interface the pulse delay generator with the inputs and outputs of the lasers, two small circuits were required. The first of these circuits, Figure 6.3-2, was used to attenuate and stretch the output pulse of the DCR-2 "Q-switch Sync". This attenuation was necessary to keep from burning out the inputs of the delay generator. This pulse stretcher was built in a small dicast aluminum box (Pomona) and mounted in the cable from the laser. The output from the DCR-2 "Q-switch Sync" was a 10nsec 9 volt pulse which was stretched and attenuated to a 200nsec 6.3 volt pulse.

The second circuit was needed to produce a pulse capable of driving the CMOS "Blank" input of the DCR-1A laser from TTL signal from the pulse delay generator. This circuit was taken directly from the DCR-1A manual [13].

Pulse Shaper Parts List

C1	0.001µF Ceramic
C2	100pF Ceramic
R1	150Ω 1/4-Watt
R2	330Ω 1/4-Watt
R3	86Ω 1/4-Watt
R4	300Ω 1/4-Watt

6.4 References

1. New shop plans were redrawn from an existing housing original design probably by Carter Kittrel (1989).
2. Y. Chen, "Ph.D. Thesis," Massachusetts: MIT (1988).
3. A.R.R.L., "Handbook for the Radio Amateur," Newington, CT: American Radio Relay League (1990); Chapters 24-27 and 34-35.
4. P. Horowitz and W. Hill, "The Art of Electronics," 2nd edition, Cambridge: Cambridge University Press (1989); Chapters 4-7, 12 and 13.
5. Private communication, USA: OEI, Inc. (1992).
6. D. M. Jonas, "Ph.D. Thesis," Massachusetts: MIT (1988).
7. Data sheet for VV100BTB, USA: LeCroy Inc. (1993).
8. "Linear Circuits Data Book," Vol. 1 and 3, Texas: Texas Instruments, Inc. (1990).
9. W. Hayward and D. DeMaw, "Solid State Design for the Radio Amateur," Newington, CT: American Radio Relay League (1986); Chapter 7.
10. P. Lancaster, "TTL Cookbook," Indianapolis, Indiana: Howard W. Sams and Company (1979).
11. "TTL Data Book," Vol. 2, Texas: Texas Instruments, Inc. (1990).
12. C.M. Gittins, "Ph.D. Thesis," Massachusetts: MIT (1994).
13. "DCR-1A Laser Technical Manual," USA: Quanta-Ray Inc. (1981).

6.5 Chapter 6 Figure Captions

Figure	
6.1-1	High Voltage Power Supply Schematic. Diagram shows wiring of a variable high voltage divider to power photomultiplier tubes.
6.1-2	Photomultiplier Tube Housing Schematic. Diagram shows wiring for a home built photomultiplier tube housing.
6.1-3	Differential Amplifier Schematic. Diagram shows wiring for a home built wideband differential amplifier used in the normalization of SEP spectra.
6.1-4	Differential Amplifier Alignment. Plots displays applied waveform for adjusting differential amplifier and output waveforms before and after alignment.
6.1-5	Preamplifier Schematic. Diagram shows the wiring of the Le Croy Corp. pulse amplifiers for use as preamplifiers.
6.1-6	±24 Volt Power Supply Schematic. Diagram shows wiring of Lambda Electronic Inc. power supplies for use as main detection electronics DC power supplies.
6.1-7	Linear Power Supply Schematics. Figure shows wiring of three terminal regulators for providing various DC voltages.
6.2-1	Auto-Tracker Block Diagram. Figure diagrams the major components of the doubling crystal auto-tracker.
6.2-2	Auto-Tracker Logic Flow Chart. Figure shows logic diagram of doubling crystal auto-tracker control algorithm.
6.2-3	Photodiode Interface Schematic: Part 1. Figure shows the heart of the auto-tracker, the analog circuits for pulses from the photodiode into a DC signal for the computer.

6.2-4 Photodiode Interface Schematic: Part 2. Figure shows the heart of the auto-tracker, the analog circuits for pulses from the photodiode into a DC signal for the computer.

6.2-5 Split Photodiode Schematic. Figure shows wiring of the split photodiode housing for auto-tracker.

6.2-6 Auto-Tracker Remote Control Schematic. Figure displays wiring for the auto-tracker remote control pendent.

6.2-7 Auto-Tracker Trigger Circuit Schematic. Figure shows the triggering circuitry for the auto-tracker.

6.3-1 AC Line Synchronizer Schematic. Diagram shows the wiring of a circuit to derive a 10Hz TTL pulse train from the 60Hz AC line.

6.3-2 Q-switch Sync Pulse Shaper. Figure shows a passive circuit for converting the a Quanta-Ray DCR-2 Q-switch output to a TTL compatible signal.

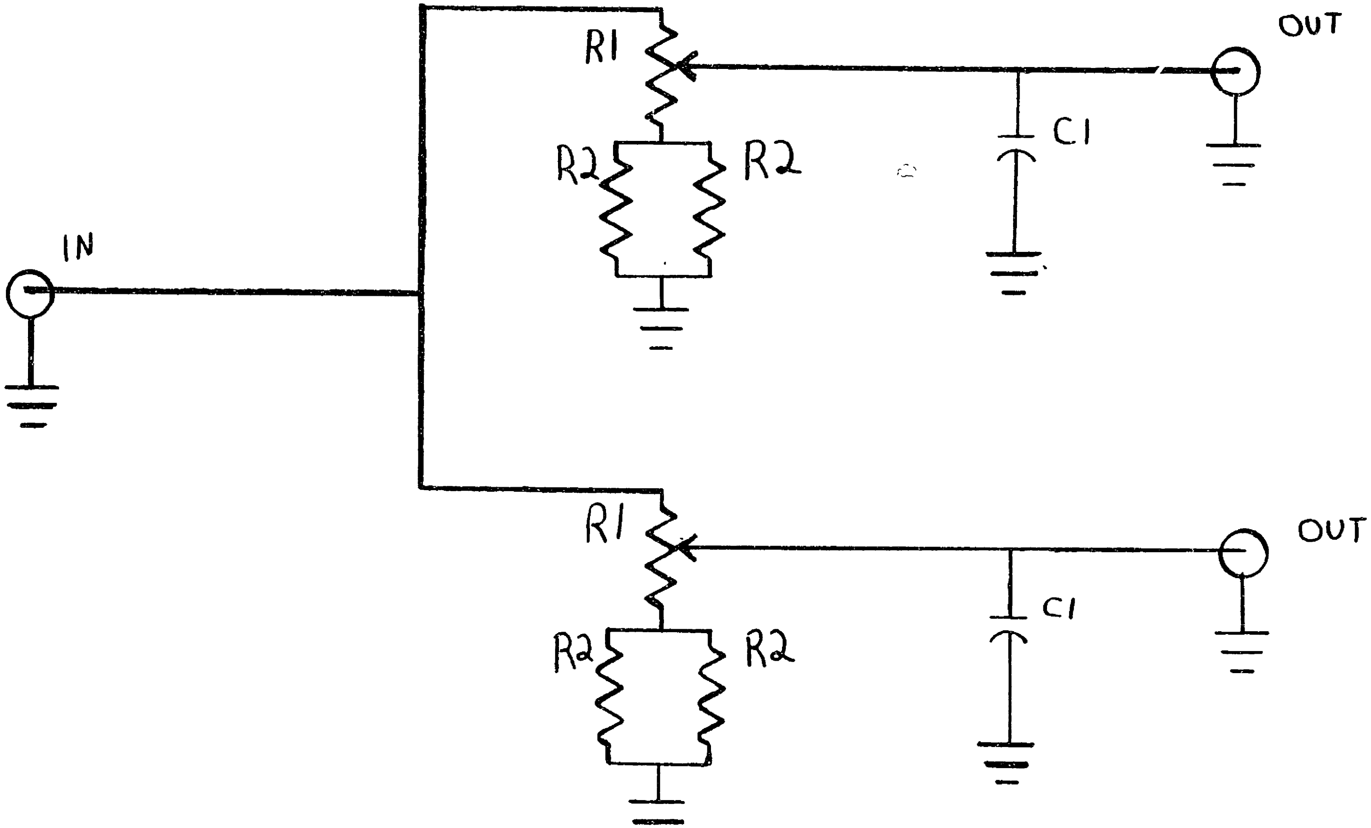

Figure 6.1-1 High Voltage Power Supply Schematic.

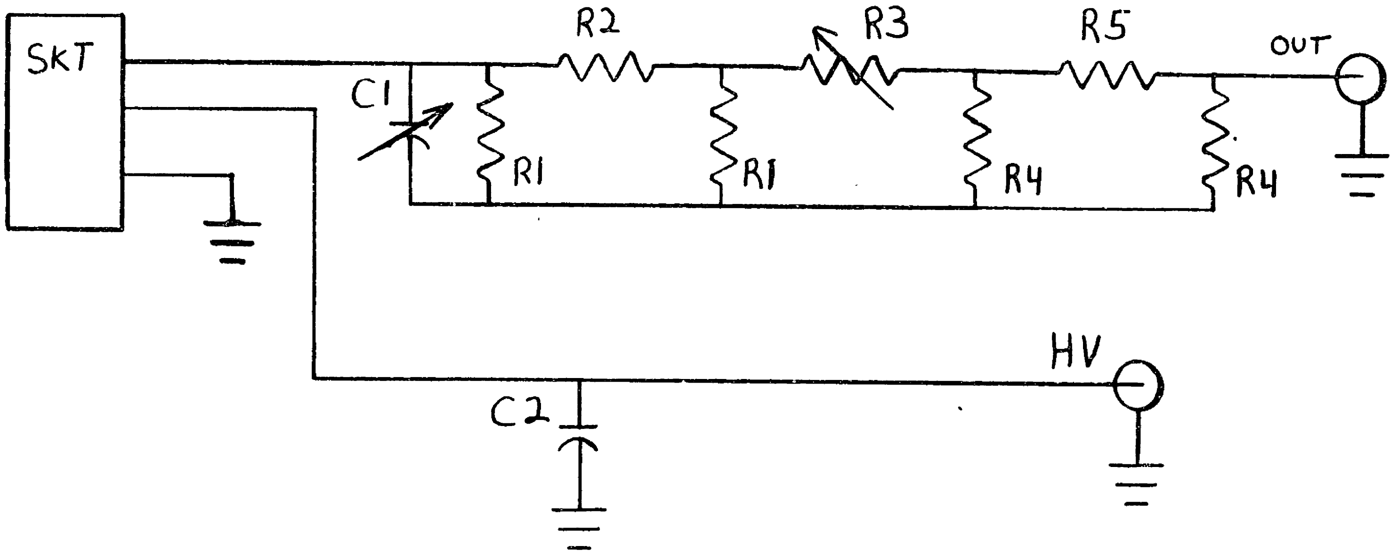

Figure 6.1-2 Photomultiplier Tube Housing Schematic.

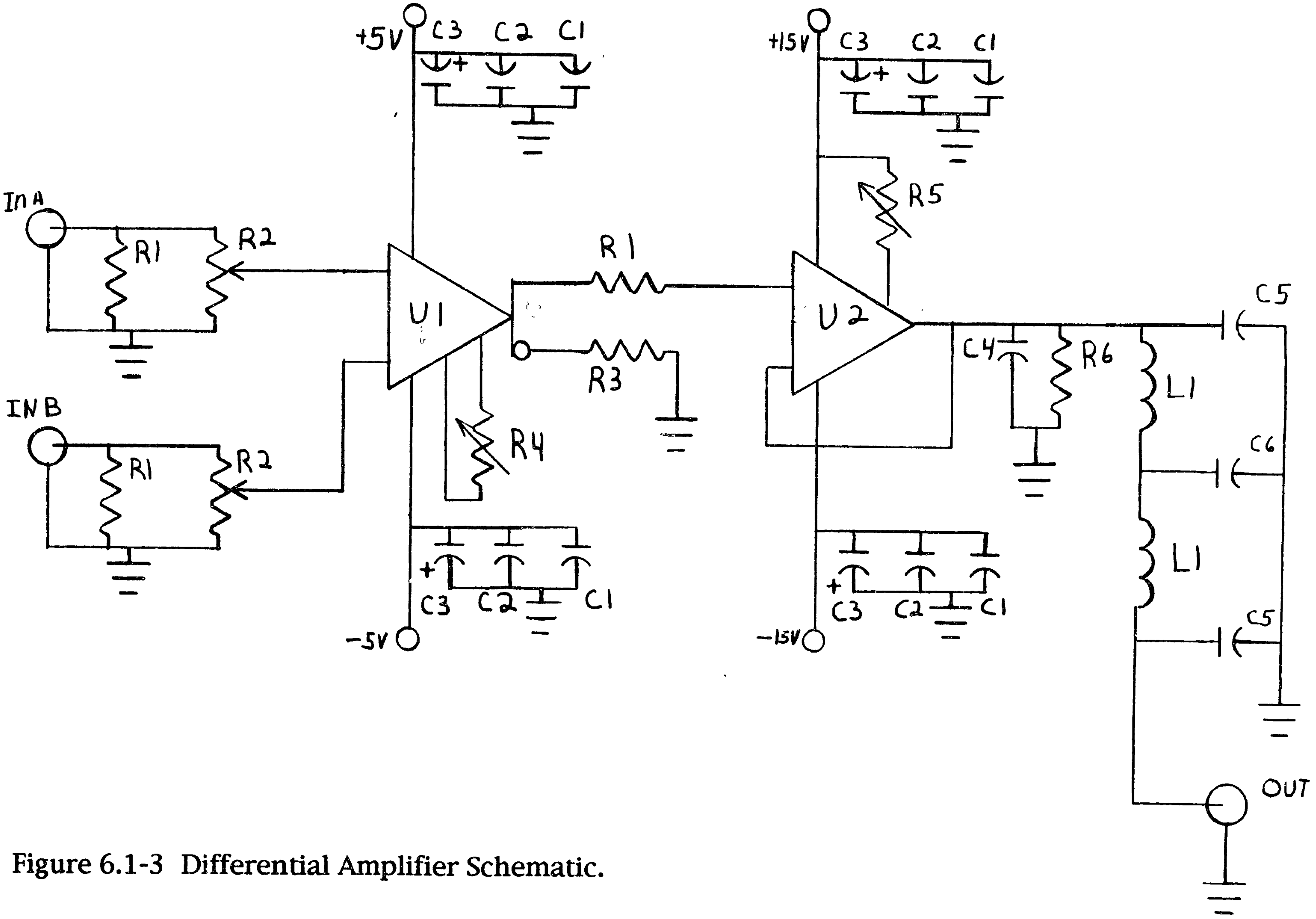

Figure 6.1-3 Differential Amplifier Schematic.

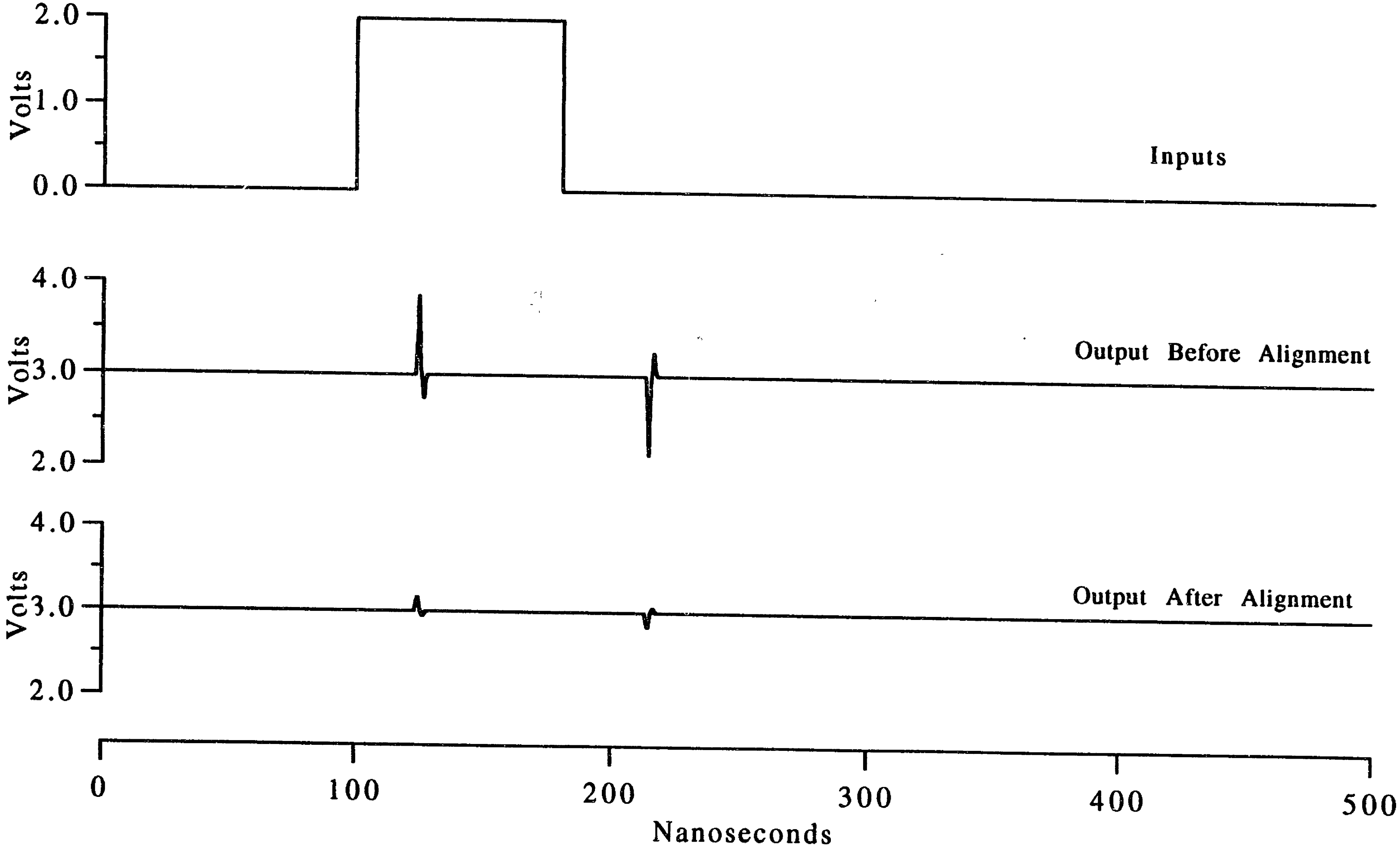

Figure 6.1-4 Differential Amplifier Alignment.

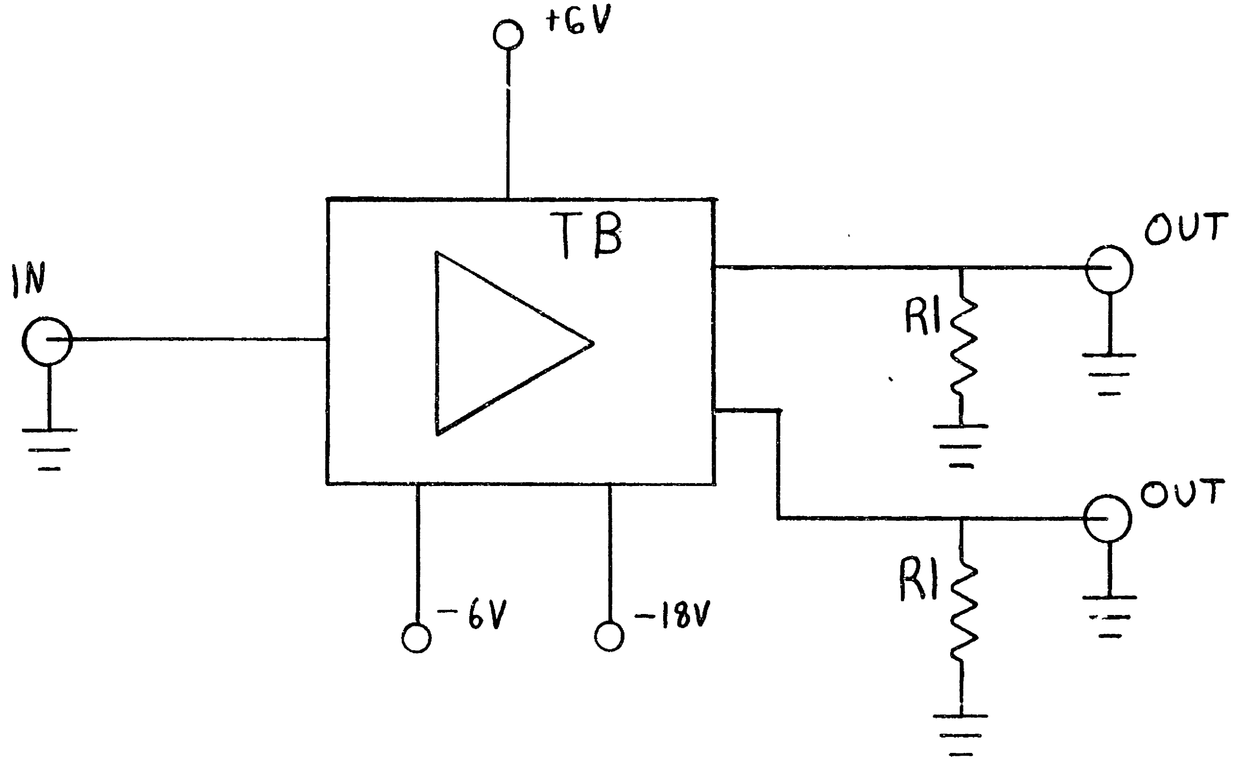

Figure 6.1-5 Preamplifier Schematic.

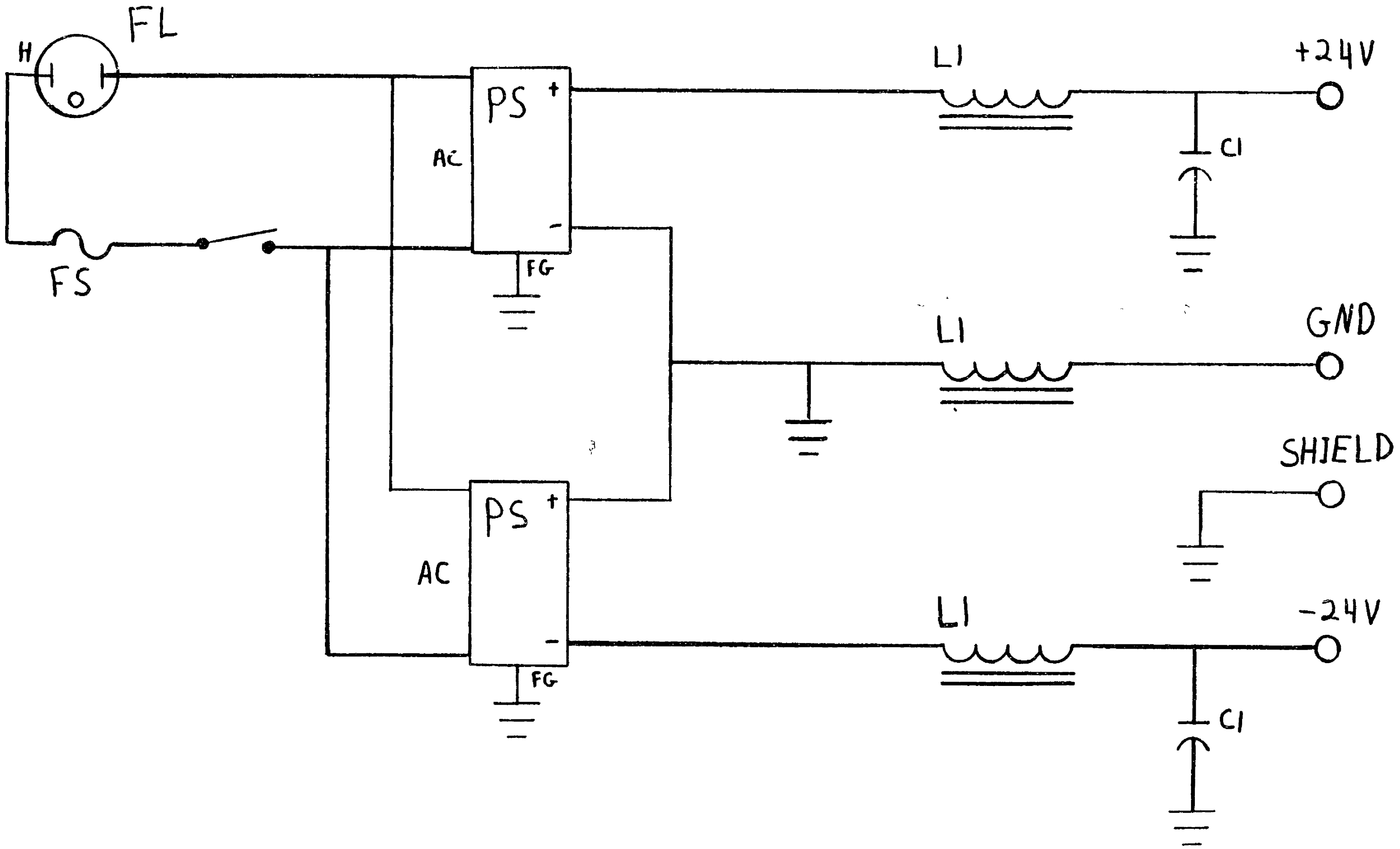

Figure 6.1-6 ±24 Volt Power Supply Schematic.

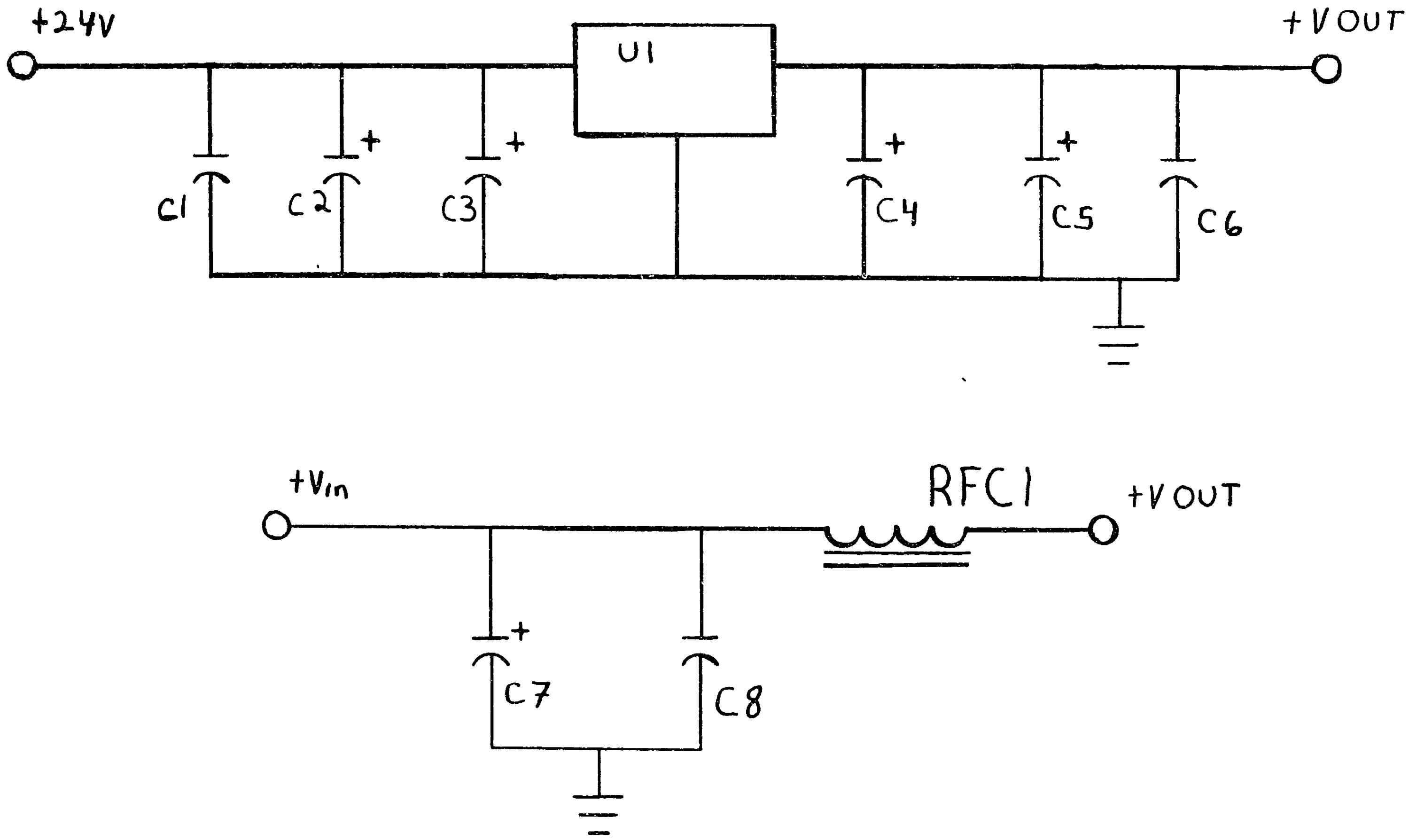

Figure 6.1-7 Linear Power Supply Schematics.

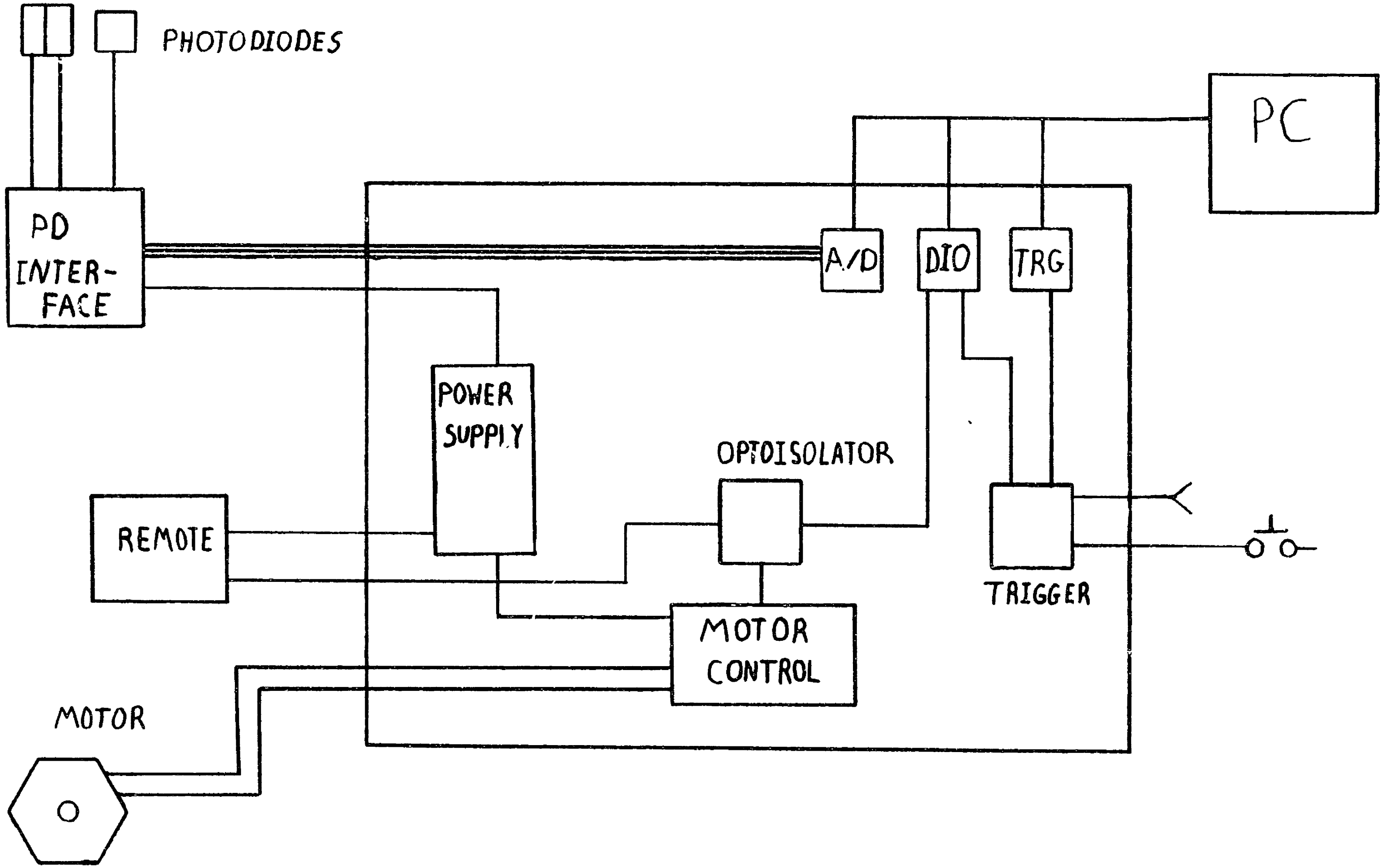

Figure 6.2-1 Auto-Tracker Block Diagram.

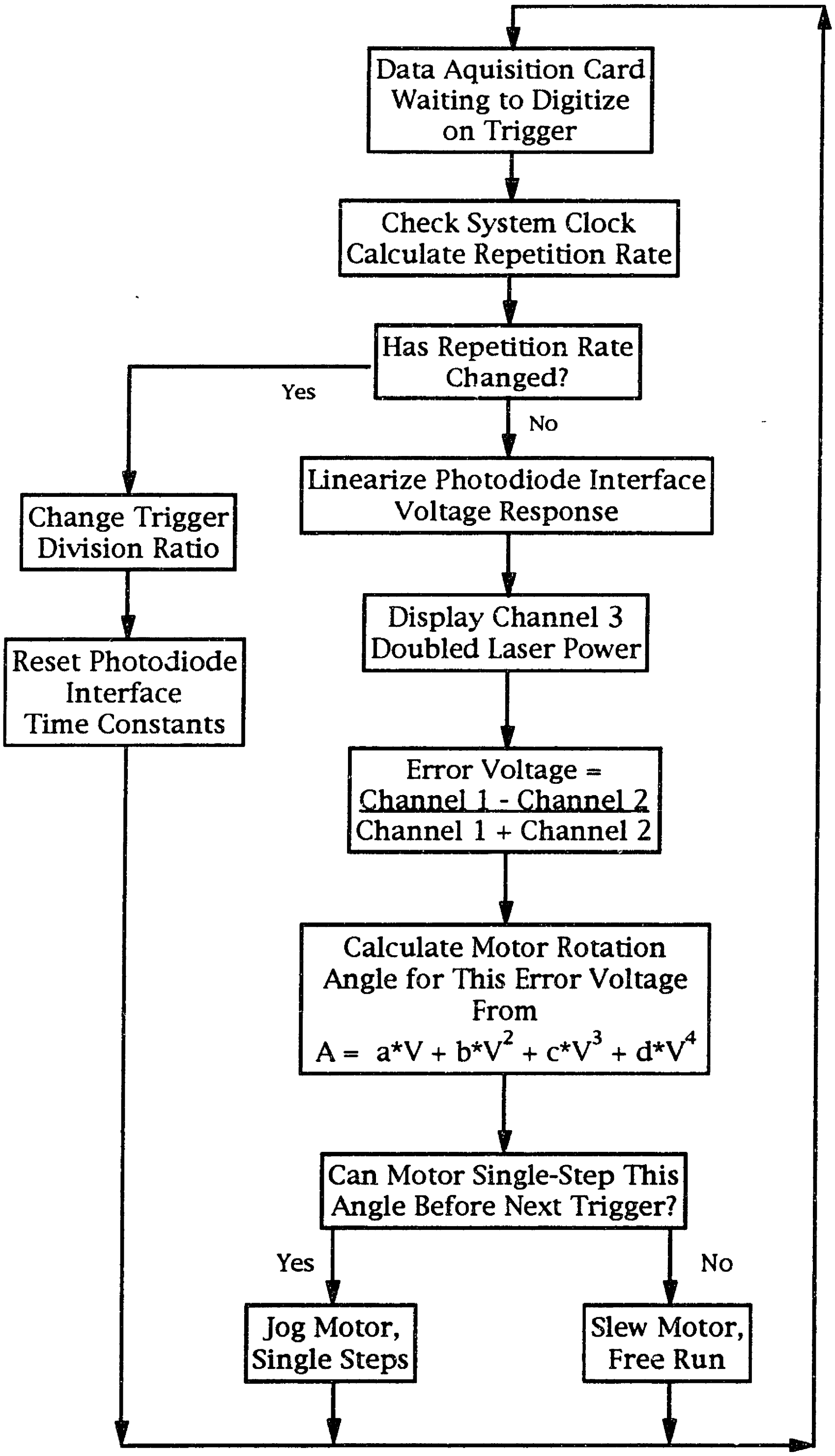

Figure 6.2-2 Auto-Tracker Logic Diagram

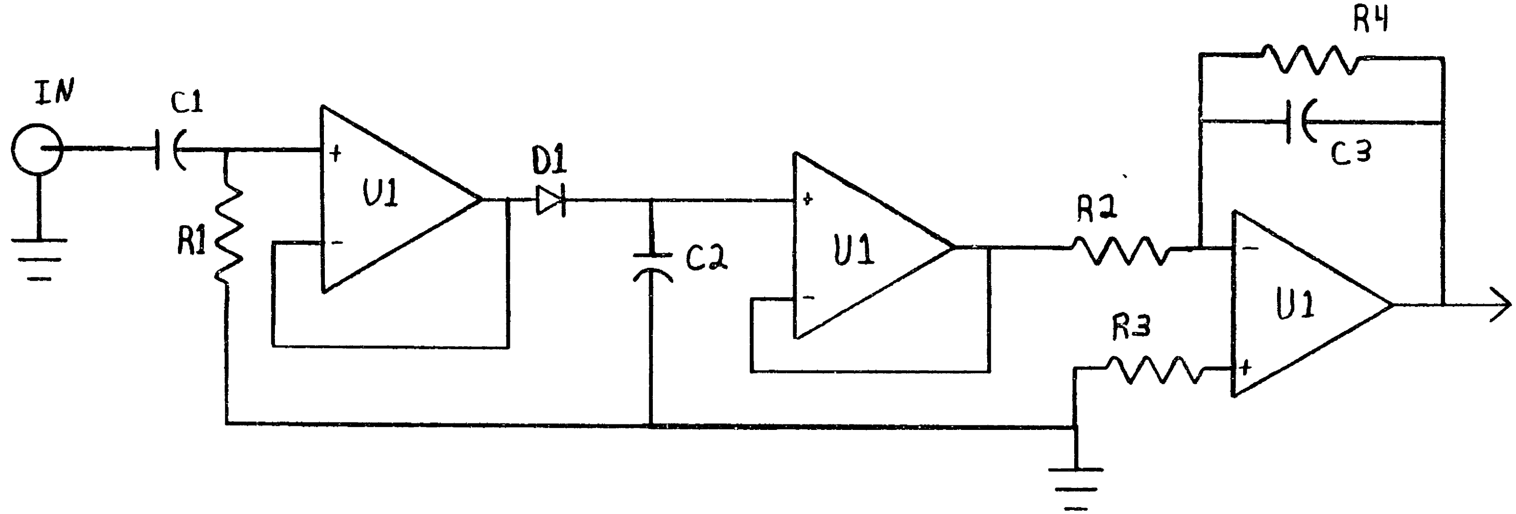

Figure 6.2-3 Photodiode Interface Schematic, Part 1.

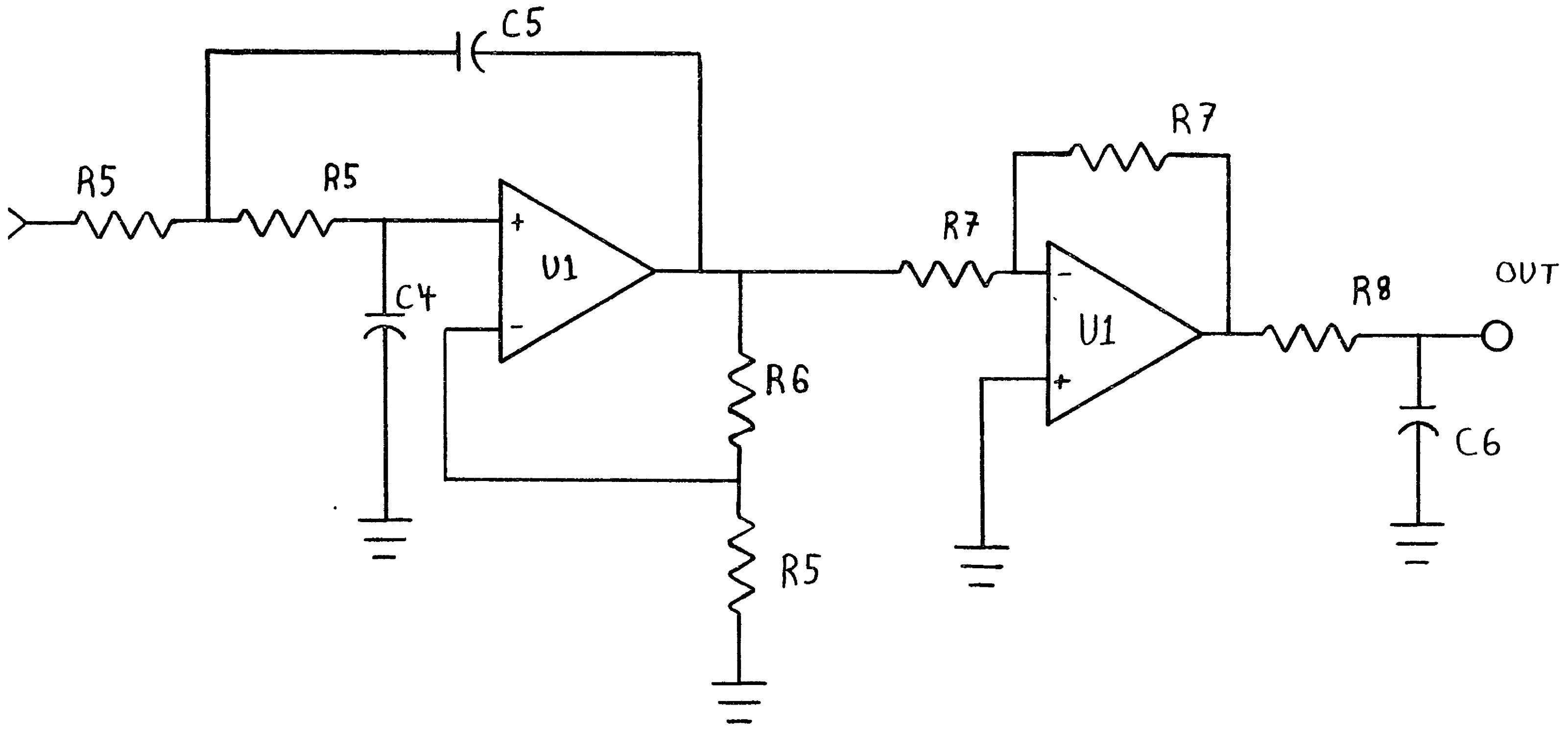

Figure 6.2-4 Photodiode Interface Schematic, Part 2.

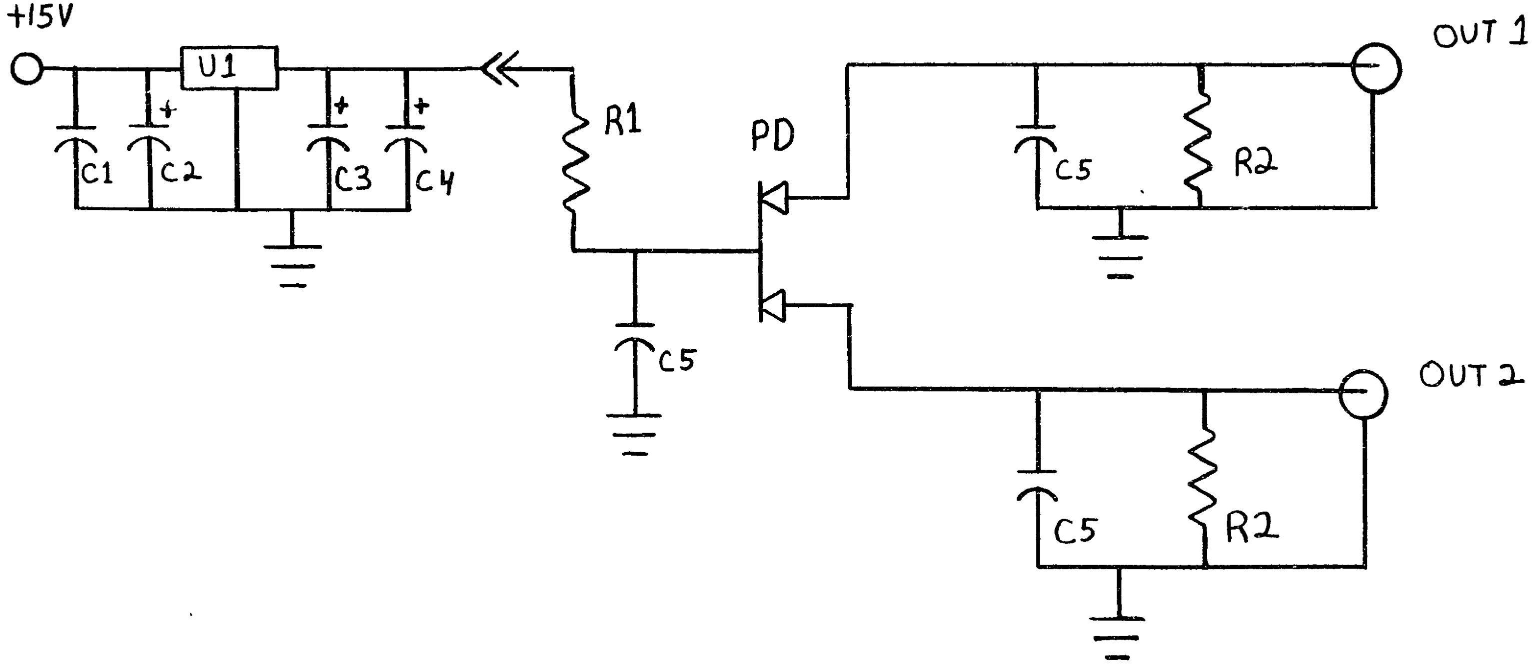

Figure 6.2-5 Split Photodiode Schematic.

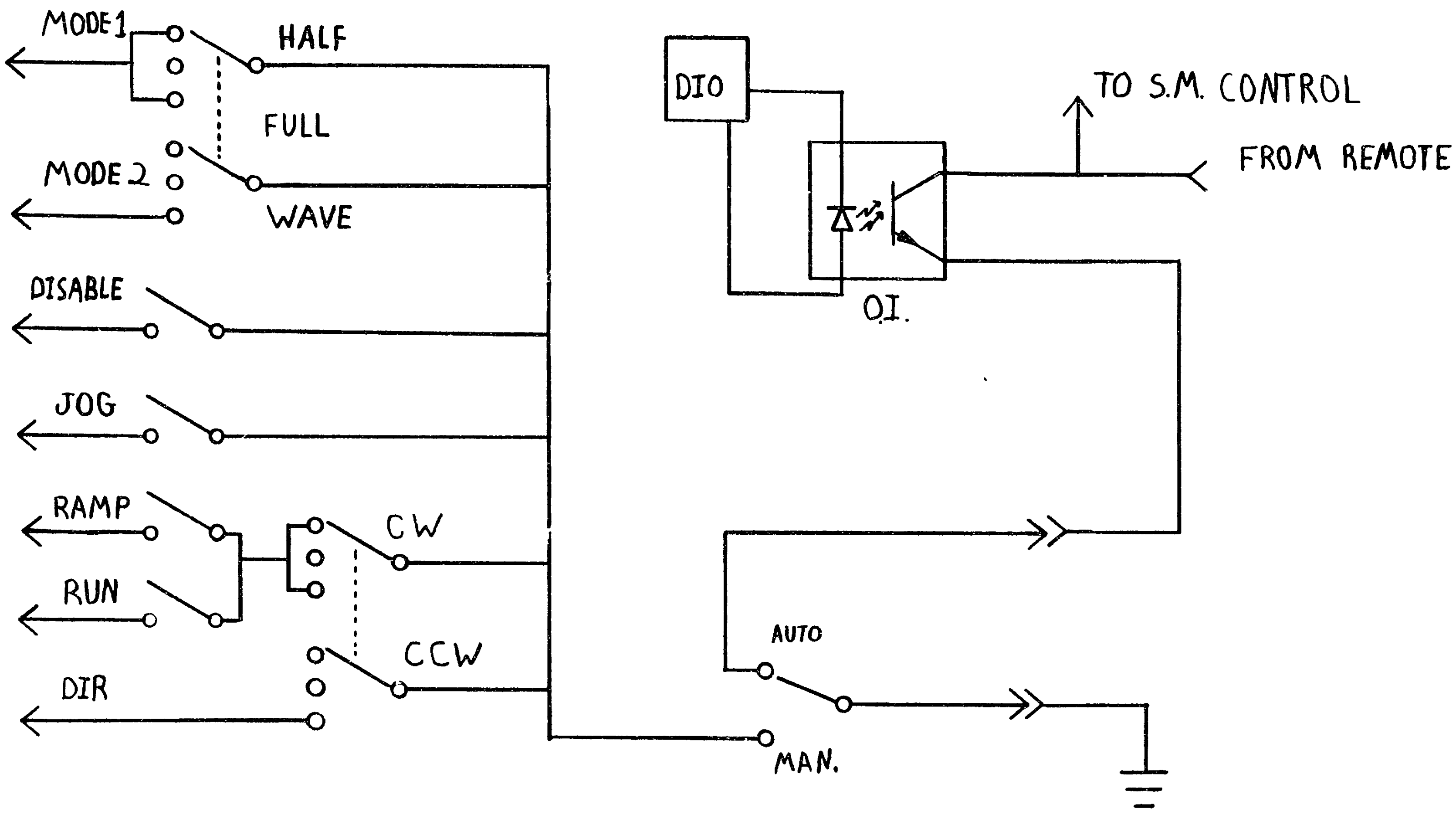

Figure 6.2-6 Auto-Tracker Remote Control Schematic.

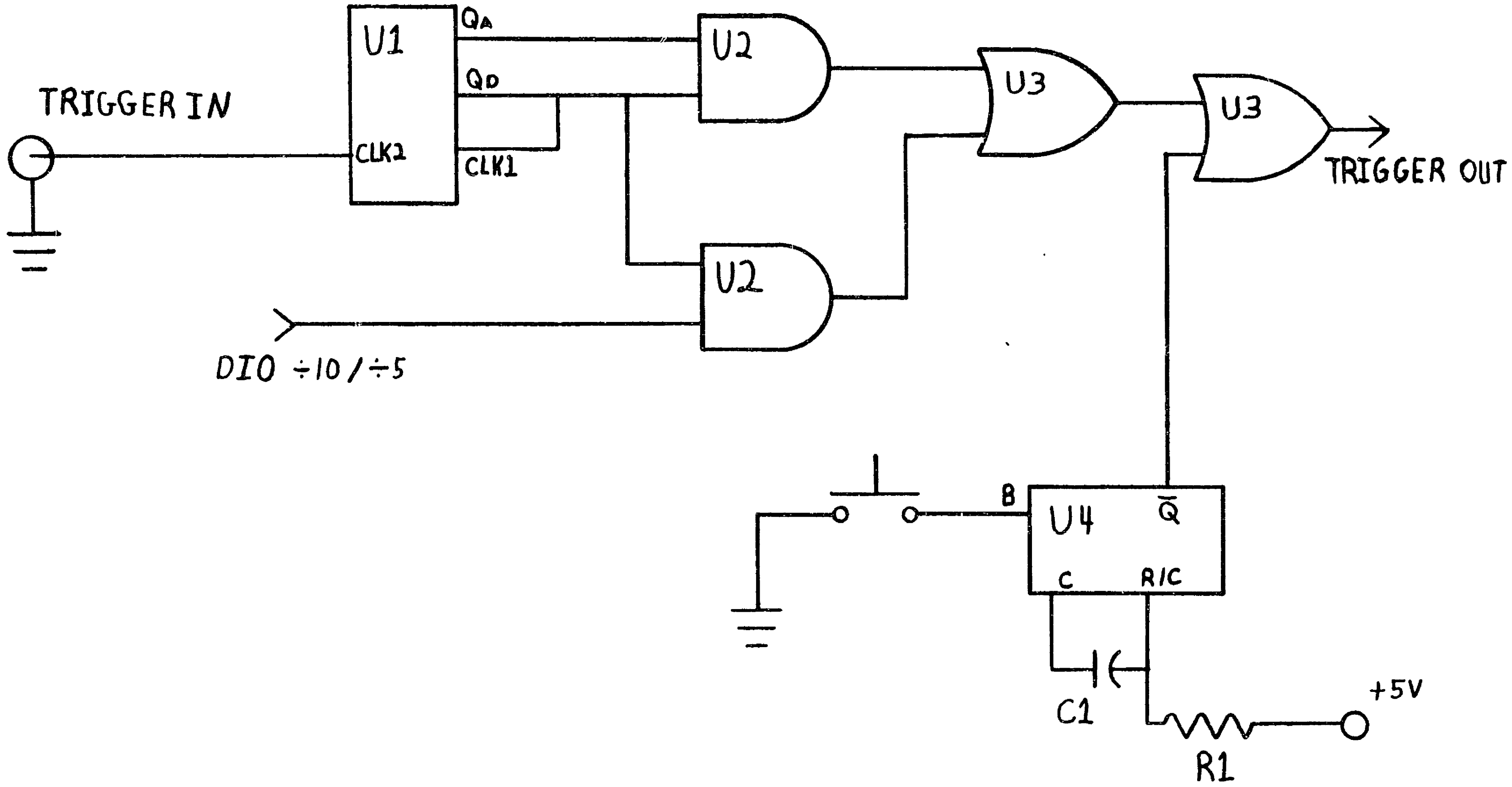

Figure 6.2-7 Auto-Tracker Trigger Schematic.

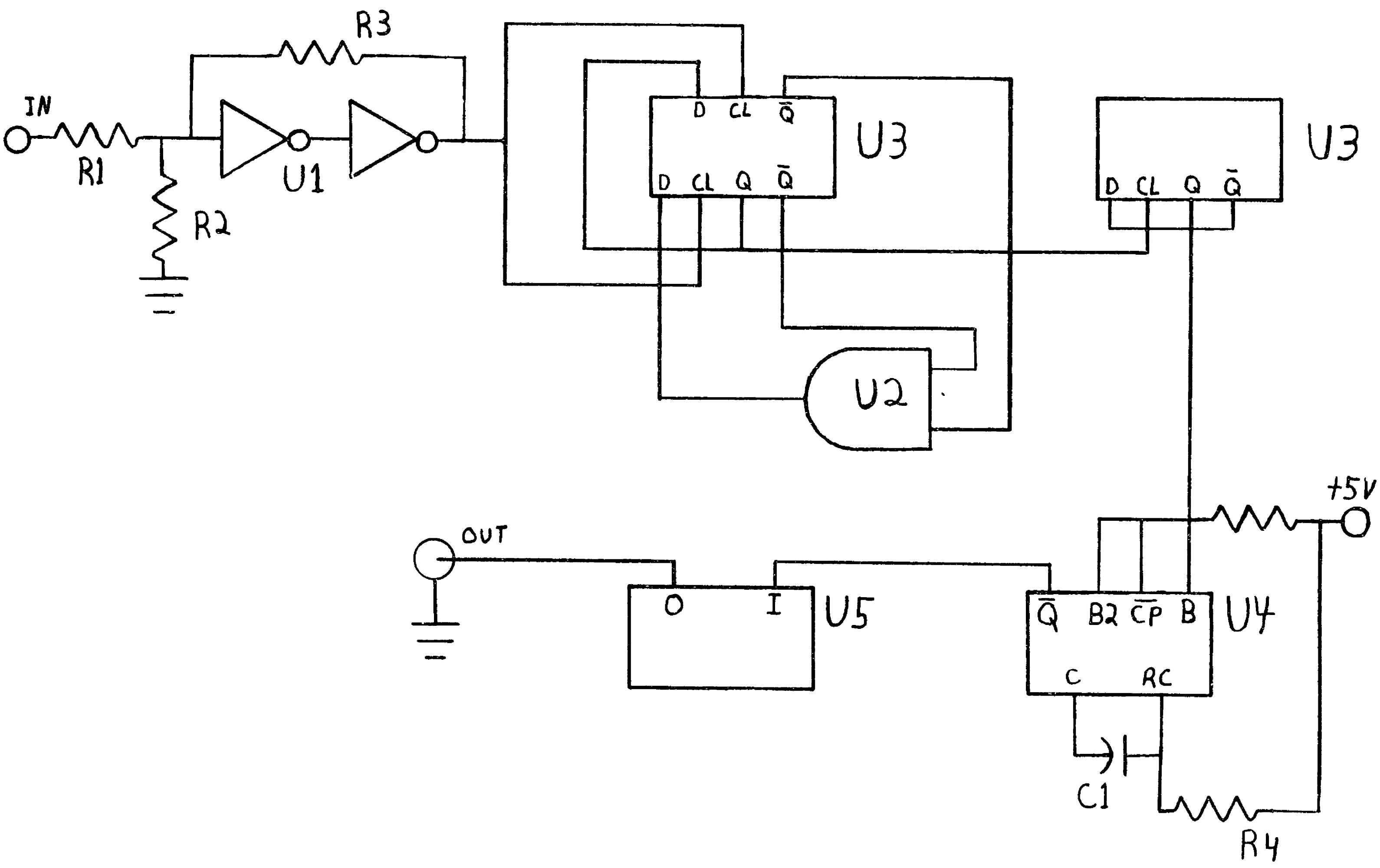

Figure 6.3-1 AC Line Synchronizer Schematic.

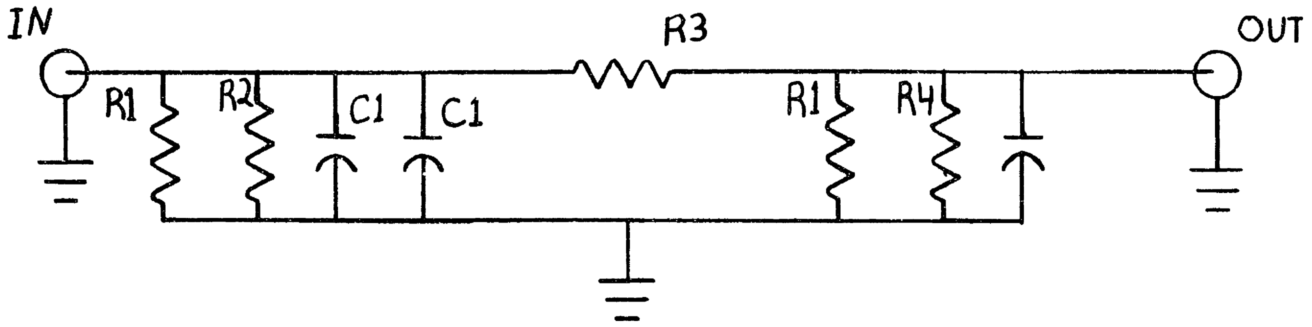

Figure 6.3-2 Q-switch Pulse Shaper Schematic.

Appendix

A.I Calculation of Rotational Transition Moment

As noted in Section 4.2, an a-type Q-branch (K_1^1) was observed in the SEP spectra recorded from b-type PUMP transitions. It is possible to exploit the appearance of this type of Q-branch to determine the absolute sign of the angle that the $\tilde{B}\,^2A' \leftrightarrow \tilde{X}\,^2A'$ transition dipole moment makes with the molecule's a-inertial axis (the axis is nearly collinear to the CO bond axis). The magnitude of the angle made by the transition moment with the a-axis was determined from the fluorescence excitation spectrum, as described in Section 3.1 and is further discussed here. The procedure for determining the sign (whether the transition dipole lies more nearly parallel or perpendicular to the CH bond) of this angle is also discussed below.

For the HCO $\tilde{B}\,^2A' \leftrightarrow \tilde{X}\,^2A'\,0_0^0$ band, the relative intensities of the a-type and b-type subbands indicate that the transition dipole moment is tipped approximately 31.1±1° away from the a-inertial axis[1]. The following discussion follows closely the calculation of the transition dipole moment of Reference (1). Although it should be noted that there are several typographical errors in the equations of this reference. The angle made by the transition dipole moment with the a-inertial axis may be calculated from the intensity ratio as follows: the line strength for an electronic transition can be expressed, within the Born-Oppenheimer approximation, by three factors, assuming isotropic excitation by unpolarized light as [2]

$$S(N',K_a',V',\psi';N'',K_a'',V'',\psi'') = q_{V'V''} \cdot \left|\mu_{\psi'\psi''}\right|^2 \cdot S_\alpha(N',K_a';N'',K_a''). \quad (1)$$

Since we are interested in taking the ratio of two rotational line intensities belonging to the same electronic and vibrational state, the Franck-Condon factor, $q_{v'v''}$,and the electric dipole transition moment ($\mu_{\psi'\psi''}$)can be ignored for this discussion. This leaves only the rotational line strength factor, $S_\alpha(N',K_a';N'',K_a'')$, to consider

$$S_\alpha(N',K_a';N'',K_a'') = \sum_{M'}\sum_{M''}\left|\langle N',K_a',M'|\mu|N'',K_a'',M''\rangle\right|^2; \; \alpha = a,b.$$

(2)

For light linearly polarized along the laboratory Z direction, M'=M" and the electric-dipole transition moment, μ, can be expressed in terms of its body-fixed (x, y, z) components

$$\mu = \mu_Z = 1/2(\phi_{Zx} - i\phi_{Zy}) \cdot (\mu_x + i\mu_y) + 1/2(\phi_{Zx} + i\phi_{Zy}) \cdot (\mu_x - i\mu_y) + \phi_{Zz}\mu_z. \quad (3)$$

μ_x, μ_y, and μ_z, are the projections of the transition moment on the x, y, and z internal molecular fixed axes. For an a-, b-type (in the plane of the molecule) transition in a planar symmetric top, Eq. (3) can be rewritten (in the I^r representation for symmetric tops [3]) as

$$\mu_Z = \mu_a \phi_{Za} + \mu_b \phi_{Zb}, \tag{4}$$

where μ_a, and μ_b, are the projections of the transition moment on the a- and b-inertial axes of the initial state. The direction cosine matrix elements, ϕ_{Za}, and ϕ_{Zb} , are tabulated in several references [2,3,5]. They are the projections of the transition dipole moment onto the laboratory Z-axis. Since we are only interested in comparing the intensities of two rovibronic transitions between the same initial and final vibronic states, we need only consider the rotational line strength factors, which are

$$S(N', K_a'; N'', K_a'') = \sum_{M'} \sum_{M''} \left| \langle N', K_a', M' | \phi_{Z\alpha} | N'', K'', M'' \rangle \right|^2 . \tag{5}$$

In order to evaluate the rotational line strength expressions for a prolate symmetric top, it is convenient to convert the usual symmetric top basis functions into a signed-K_a parity conserving basis set. The symmetrized symmetric top rotational wave function is then written as:

$$|N,K_a,K_c,M\rangle = 2^{-1/2}(|N,K_a,M\rangle + (-1)^{N-K_a-K_c}|N,-K_a,M\rangle) \qquad |K_a|>0 \tag{6a}$$

$$|N,K_a,K_c,M\rangle = |N,0,M\rangle \qquad K_a = 0, \tag{6b}$$

where the phase convention of Condon and Shortley has been used [5,6]

$$\sigma_{ab}|N,K_a,M\rangle = (-1)^{N-K_a}|N,-K_a,M\rangle. \tag{7}$$

In the group C_S, the operator σ_{ab} (reflection through the plane containing the body fixed a and b axes) corresponds to the parity operator (E^*), which for a planar molecule is equivalent to R_c^π, a rotation about the c-axis by π [7]. The parity of the symmetric top wave function is then given by [7,11]

$$\sigma_{ab}|N,K_a,K_c,M\rangle = R_c^\pi|N,K_a,K_c,M\rangle = (-1)^{K_c}|N,K_a,K_c,M\rangle. \tag{8}$$

When the wave function from Eq. (6) is used to evaluate the expression for the rotational line strengths in Eq. (5) the following equation results,

$$S_\alpha(N',K_a';N'',K_a'') = \frac{1}{4}\cdot\mu_\alpha^2\left\{\sum_{M'}\sum_{M''=M'}\left|\begin{matrix}\langle N',K_a',M'|\phi_{Z\alpha}|N'',K'',M''\rangle \\ +(-1)^P\langle N',-K_a',M'|\phi_{Z\alpha}|N'',-K_a'',M''\rangle\end{matrix}\right|^2\right\};\ \alpha = a,b\cdot \tag{9}$$

In Eq. (9) the quantity P is given by

$$P = (N' + N'') - (K_a' + K_a'') - (K_c' + K_c''). \tag{9a}$$

Using tabulated direction cosine matrix elements and explicit formulas for the summations over M, explicit expressions for the rotational line strengths can be derived [2,3,5]. These expressions must follow the sum rules for rotational intensities, a fact that is useful in verifying the accuracy of the intensity expressions. This sum, over all rotational transition intensities of a given transition type, a or b, which originates from a specific rotational eigenstate of the lower electronic state, has been explicitly given by Zare for a symmetric top [2]

$$\frac{1}{|\mu_\alpha|^2} \sum_{N',K_a'} S_\alpha(N',K_a';N'',K_a'') = 1/3(2N''+1) \qquad \alpha = \mathrm{a,b}\ . \tag{10}$$

If one extends the summation in Eq. (10) to include all transitions originating from both asymmetry components of the lower state, then one obtains the sum rules given previously for diatomic molecules by Whiting et al. [8], since for linear molecules the b- and c-axes are indistinguishable.

Taking the ratio of intensities between a pair of rotational lines originating from the same rotational eigenstate of the lower electronic state but belonging to different transition types, a or b, one obtains

$$\frac{S_a(N',K'_a=K''_a;N'',K''_a)}{S_b(N',K'_a=K''_a\pm 1;N'',K''_a)}=$$

$$\left(\frac{\mu_a}{\mu_b}\right)^2\cdot\left(\frac{\sum\limits_{M'}\sum\limits_{M''}\left|\langle N',K'_a=K''_a,M'|\phi_{Za}|N'',K'',M''\rangle\right|^2}{\sum\limits_{M'}\sum\limits_{M''}\left|\langle N',K'_a=K''_a\pm 1,M'|\phi_{Zb}|N'',K'',M''\rangle\right|^2}\right). \tag{11}$$

The expression in brackets depends only on the rotational quantum numbers (N'',K''_a) and type $(\Delta N'',\Delta K''_a)$, and can be evaluated using the tabulated direction cosine matrix elements [3,5]. For example, for the intensity ratio for a prolate symmetric top a-type transition ${}^qR(N_{0N})$, with that of the prolate symmetric top b-type transition, ${}^rQ(N_{0N})$, the bracketed expression, D, becomes

$$\mathrm{D}=\frac{4N''(N''+K''_a+1)(N''-K''_a+1)}{(N''+1)(N''-K''_a)(N''-K''_a-1)}. \tag{12}$$

The ratio of the components of the transition moment then becomes

$$\frac{\mu_a^2}{\mu_b^2}=\mathrm{D}\cdot\frac{S_b(N'=N'',1;N'',0)}{S_a(N'=N''+1,0;N'',0)}. \tag{13}$$

The angle θ between the a-axis and the symmetric top transition moment is then

$$\tan\theta=\frac{\mu_b}{\mu_a}. \tag{14}$$

In order to apply this expression correctly to the observed HCO $\tilde{B}\,^2A' \leftarrow \tilde{X}\,^2A'$ 0^0_0 fluorescence excitation spectrum, an allowance must be made for the spin-rotation interaction and each N' or N'' in Eq. (12) must be replaced by the half integral J' or J''. For transitions where the spin-rotation splitting is unresolved, the intensity expressions for $\Delta N = \Delta J$ transitions involving both J components must be summed explicitly rather than ignored. This can be accomplished for the quantity D, by substituting $J = N \pm 1/2$ into Eq. (12). Adding the two spin-rotation components results in the following alternative expression for D,

$$\mathrm{D} = \frac{4(N''+1/2)(N''+1/2+K_a''+1)(N''+1/2-K_a''+1)}{(N''+1/2+1)(N''+1/2-K_a'')(N''+1/2-K_a''-1)} + \frac{4(N''-1/2)(N''-1/2+K_a''+1)(N''-1/2-K_a''+1)}{(N''-1/2+1)(N''-1/2-K_a'')(N''-1/2-K_a''-1)} \,. \qquad (15)$$

Equation (15) corrects the typographical error in Equation (9) of Reference (1).

However, since HCO is an asymmetric top, the wave function used in Eq. (6) to calculate the rotational line strength should really be a linear combination of symmetric top basis functions with K_a differing by two (for an a-reduced Hamiltonian) [4]. For the two branches chosen for comparison, the above asymmetry effects would cause some K_a=2 character to be admixed into the K_a=0 lower rotational state of each branch. For the ground state of HCO with a (B"-C")/4 = 0.082cm^{-1} and an A" rotational constant of 24.2cm^{-1} the fractional K_a=2 character in the $|N, K_a = 0, K_c = N\rangle$ eigenstate is small. After accounting for asymmetry effects in both states, the change in the intensity ratio given in Eqs. (12) and (15) is only ~1%. Thus, for the HCO $\tilde{B}\,^2A' \leftarrow \tilde{X}\,^2A'$ transition, neglect of asymmetry effects has negligible effects on the observed body-fixed direction of the transition moment.

The absolute body-fixed direction of the tipping of the transition moment in the a, b plane, whether more nearly parallel or perpendicular to the CH bond axis, cannot be determined from the fluorescence excitation intensity data of Section 3.1. However, the absolute direction of the $\tilde{B}\,^2A' \leftarrow \tilde{X}\,^2A'$ transition moment can, in principle, be determined by the observation of departures from the rotational line strengths predicted by Eq.(5) that are brought about by interference effects [9]. Such interference effects occur when the intensity for a transition arises from two independent sources. In the case of HCO, the two interfering intensity mechanisms are the intrinsic a-type transition strength and a-type (i.e. ΔK_a=even,

ΔK_C=odd) intensity borrowed from the b-type transition moment through axis switching effects [10].

Recently, Held et al. discussed the possibility of using such an interference effect to determine the molecule-fixed orientation of a transition moment in 2-pyridone. The ideal scheme would involve a normally weak a-type transition, such as a $5 \leq N \leq 10$ $^{q}Q(N_{1N})$ line, and a member of the strongest possible class of axis switching transitions that derives its intensity as a constructive interference between two strong b-type transition amplitudes (e.g. $^{r}Q(N_{0N})$ and $^{p}Q(N_{2N-2})$). In order to infer the absolute orientation of the HCO $\tilde{B}\,^2A' \leftrightarrow \tilde{X}\,^2A'$ transition moment, only the sign (not the magnitude) of the a~b interference effect must be determined experimentally. Since the axis-switching contribution to the intensity of the $^{q}Q(N_{1N})$ line is much larger than for corresponding P- and R-lines, $^{q}P(N_{1N-1})$ and $^{q}R(N_{1N-1})$, a comparison of the relative intensities of two SEP transitions originating from the same upper level, combined with the *a priori* known sign of the axis switching angle, would determine whether the HCO $\tilde{B}\,^2A' \leftrightarrow \tilde{X}\,^2A'$ transition dipole moment lies more nearly parallel or perpendicular to the CH bond.

The axis switching and interference effects arise as follows: in order to perform the integral over all space implied in the expression for the rotational line strength, Eq. (5), the rotational wave functions must first be expressed in the same coordinate system [9,10]. The rotational wave functions in Eq. (5) are written in the coordinates of the upper and lower electronic state's inertial axis system,

$$S_\alpha(N',K_a';N'',K_a'') = \mu^2{}_\alpha \sum_{M'}\sum_{M''}\left|\iiint \psi^*_{N'K_a'M'}(a',b',c')\phi_{Z\alpha}\psi_{N''K_a''M''}(a'',b'',c'')\,\mathrm{d}a'\,\mathrm{d}b'\,\mathrm{d}c'\right|^2; \quad \alpha = a,b. \tag{16}$$

Since there is a marked geometry change between the $\tilde{X}\ {}^2A'$ and $\tilde{B}\ {}^2A'$ -state of HCO, the inertial axes of the two electronic states do not exactly coincide and the rotational wavefunction of the lower electronic state must be rewritten as a linear combination of upper state rotational wavefunctions before the integration in Eq. (16) can be performed

$$\psi_{N''K_a''M''}(a'',b'',c'') = \sum_{K_a'=-J}^{J} s_{K_a'} \cdot \psi_{N'K_a'M'}(a',b',c'). \tag{17}$$

This rotation of basis functions is characterized by the axis switching angle which is determined from the geometries of the upper and lower electronic states.

After substituting Eq. (17) into Eq. (16) and collecting terms and applying the selection rules for dipole radiation, the term inside the sums over M in Eq. (16) becomes,

$$\left| \begin{array}{l} \mathbf{D}_{K_a''=K_a'} \cdot \mu_a \langle N', K_a', M' | \phi_{Za} | N'', K_a'' = K_a', M'' \rangle \\ \qquad\qquad + \mathbf{D}_{K_a''=K_a'\pm 1} \cdot \mu_b \langle N', K_a', M' | \phi_{Zb} | N'', K_a'' = K_a' \pm 1, M'' \rangle \end{array} \right|^2 . \tag{18}$$

It is the relative signs of the two mixing coefficients that give rise to the interference effect [9].

In order to determine the absolute direction of transition moment within the plane, the intensities of the a-type transitions (${}^{q}Q(4_{14})$ and ${}^{q}P(5_{14})$) observed in the SEP spectrum, shown in Figure 4.2-1, were compared to intensity expressions calculated both including and neglecting axis-switching. As in the determination of the tipping angle for the SEP spectrum (Section 3.2) the intensity effects of the PUMP laser were neglected. This approximation did not significantly effect the results of the tipping angle determination. An expression for the intensity of these P-, Q-, and R-branch lines observed in Figure 4.1-1, similar to that obtained by A. Held et al. [9], was obtained by multiplying out Eq. (18) and performing the sums over M:

$$
\begin{aligned}
S_{\mathrm{a}}(N', K_a'; N'', K_a'' = K_a') = {} & \left| \mathbf{D}_{K_a'=K_a''} \cdot \mu_a \langle N', K_a', M' | \phi_{Za} | N'', K_a'' = K_a', M'' \rangle \right|^2 \\
& + \left| \mathbf{D}_{K_a'=K_a''-1} \cdot \mu_b \langle N', K_a' | \phi_{Zb} | N'', K_a'' = K_a' + 1 \rangle \right|^2 \\
& + 2\mathbf{D}_{K_a'=K_a''} \cdot \mathbf{D}_{K_a'=K_a''-1} \cdot \mu_a \cdot \mu_b \cdot \\
& \langle N', K_a', M' | \phi_{Za} | N'', K_a'' = K_a', M'' \rangle \cdot \langle N', K_a' | \phi_{Zb} | N'', K_a'' = K_a' + 1 \rangle
\end{aligned}
\tag{19}
$$

All interference effects in the above intensity expressions arise in the last term of Eq. (19) and are determined by the relative signs of the axis-switching rotation elements and the relative signs of the transition moments. Approximate values for the axis-switching rotation elements in Eq. (19) are given for the case of a planar molecule by J. T. Hougen and J. K. G. Watson [10],

$$
\begin{aligned}
\mathbf{D}^{(N)}_{K_a'=K_a''} &= 1 - \rho^2 [N(N+1) - K_a'] \\
\mathbf{D}^{(N)}_{K_a'=K_a''-1} &= +\rho \left[(N + K_a')(N - K_a' + 1) \right]^{1/2} \\
\mathbf{D}^{(N)}_{K_a'=K_a''+1} &= -\rho \left[(N - K_a')(N + K_a' + 1) \right]^{1/2} \\
\rho &= \tan\left(\tfrac{1}{2}\theta\right) \quad .
\end{aligned}
\tag{20}
$$

In the above equation theta (θ) is defined as the axis switching angle for a planar molecule, an expression for which is given by J. T. Hougen and J. K. G. Watson [10]. For HCO this angle is calculated at +1.5°, using the expression in Reference (10).

In order to analyze the SEP spectrum in Figure 4.2-1 the line strength ratio between the ${}^{q}Q(4_{14})$ and the ${}^{q}P(5_{14})$ lines, neglecting axis-switching, is 0.094 (0.15 : 1.6 = 0.094). The line strength ratio for the same two lines including axis-switching is calculated by starting with Eq. (19) and inserting numerical values for the axis-switching elements computed using Eq. (20). Then numerical values for the cosine matrix elements were computed. The line strength expression for the $^{q}Q(4_{14})$-line, assuming the orientation of the transition moment is positive, becomes:

$$S_a(4,1;4,1) = 0.15 \cdot \mu_a^2 + 0.0023 \cdot \mu_b^2 + 0.037 \cdot \mu_a \cdot \mu_b. \qquad (21)$$

Similarly, the line strength expression for the $^{q}P(5_{14})$ line becomes:

$$S_a(4,1;5,1) = 1.57 \cdot \mu_a^2 + 0.0005 \cdot \mu_b^2 + 0.0055 \cdot \mu_a \cdot \mu_b. \qquad (22)$$

Comparing Equations (21) and (22) shows that axis-switching make a much larger contribution to the Q-branch intensity than the P-branch; thus, the intensity ratio of the two lines should be larger than the intensity ratio neglecting axis-switching. If the orientation of the transition moment were negative, then the last term in Equation (21) and (22) would be negative and the intensity ratio would be smaller than predicted neglecting axis-switching. For these two lines in Figure 4.1-1 (from Table 4.2-2) the observed intensity ratio is 0.23. This indicates that the absolute sign of the transition moment is positive, which agrees with the *ab initio* calculation by Yarkony [12].

References

1. G. W. Adamson, X. Zhao, and R. W. Field, *J. Mol. Spec.* **160**, 11-38 (1993).
2. R. N. Zare, "Angular Momentum,"pp.283-293, New York: Wiley (1988).
3. J. T. Hougen, "The Calculation of Rotational Energy Levels and Rotational Line Intensities in Diatomic Molecules," Washington, D. C.: NBS Monograph 115 (1970).
4. J. K. G. Watson, in "Vibrational Spectra and Structure," (J. R. Durig, Ed.), Vol. 6, New York: Dekker (1977).
5. C. H. Townes and A. L. Schawlow, "Microwave Spectroscopy," pp. 83-114, New York: Dover (1975).
6. E. U. Condon and G. H. Shortley, "The Theory of Atomic Spectra," pp. 45-78, Cambridge: Cambridge University Press (1964).
7. P. R. Bunker, "Molecular Symmetry and Spectroscopy", p. 349, San Diego: Academic Press (1979).
8. E. E. Whiting, A. Schadee, J. B. Tatum, J. T. Hougen, and R. W. Nicholls, *J. Mol. Spectrosc.* **80**, 249-256 (1980).
9. A. Held, B. B. Champagne, and D. W. Pratt, *J. Chem. Phys.* **95**, 8732-8743 (1991).
10. J. T. Hougen and J. K. G. Watson, *Can. J. Phys.* **43**, 298-320 (1965).
11. D. M. Jonas, "Ph.D. Thesis," Massachusetts: MIT (1988).
12. M. R. Manaa and D. R. Yarkony, *J. Chem. Phys.* preprint (1993).